UNIVERSITÀ DEGLI STUDI DI TRIESTE

XXXVII CICLO DEL DOTTORATO DI RICERCA IN

Fisica

This work was funded by the ERC under HORIZON 2020 grant agreement No. 866026

Multimodal 2D and 3D X-ray Directional Dark-Field Imaging: Development and Applications

Settore scientifico-disciplinare: **FIS/07**

DOTTORANDA
Ginevra Lautizi

COORDINATORE
PROF. Francesco Longo

SUPERVISORE DI TESI
PROF. Pierre Thibault

ANNO ACCADEMICO 2023/2024

CONTENTS

ABSTRACT

The thesis focuses on the development and application of advanced X-ray imaging techniques, specifically modulation-based dark-field imaging and X-ray scattering tensor tomography. Most of the measurements presented in this thesis have been performed at synchrotron facilities, including the ID19 beamline at the European Synchrotron Radiation Facility (ESRF), the SYRMEP beamline at Elettra Sincrotrone Trieste, and the TOMCAT beamline at the Swiss Light Source (SLS). In addition, some datasets have been acquired in the newly-established OPTimal IMAging and TOmography (OPTIMATO) laboratory at Elettra Sincrotrone Trieste.

Modulation-based imaging (MBI) exploits heterogeneous illumination patterns to encode locally the X-ray interaction with a sample. While a uniform illumination can normally reveal only the attenuating properties of the sample, a non-uniform X-ray illumination is also altered by refraction and ultra-small-angle scattering effects. MBI is commonly implemented using a periodic grating array (grating-based imaging or GBI) or a random diffuser (speckle-based imaging or SBI). MBI enables simultaneous access to absorption, phase contrast, and small-angle scattering (or dark-field) signals from a single dataset, offering a multi-modal view of a sample's internal structure.

Combining high signal sensitivity with a simple experimental implementation, SBI is particularly suitable for biological soft tissues, where small density differences in the specimen are highlighted thanks to the differential-phase signal, enabling a higher contrast compared to absorption imaging without the need for a contrast agent. A multimodal study on ovarian and hepatic tissues is carried out in this thesis, providing insights into microstructural changes during follicular maturation of the ovaries and exploring hepatic tissue to reveal lipid aggregate distribution in the liver. The combination of phase contrast and transmission signals offered a detailed, non-destructive analysis of bovine ovaries and human liver samples.

Samples with strongly oriented microstructural features often exhibit an anisotropic X-ray scattering profile. In these cases, the directionality of the scattering can also be extracted to reveal information about their orientation, e.g., of fibres in a composite material. In this thesis, we demonstrate the capability of speckle-based dark-field imaging to detect barely visible impact damage in carbon fibre reinforced polymers. This approach offers a valuable tool for non-destructive testing of composite structures.

By collecting two-dimensional projection images with small-angle scattering signals at various orientations of the sample, two-dimensional directional scattering signals can be combined to reconstruct tomographically the local scattering tensor of the sample using X-ray tensor tomography (XTT). XTT

provides information on the sub-structures' orientations in a macroscopic sample, even when their dimensions are smaller than the image pixel resolution, enabling the exploration of microstructural organisation in a macroscopic volume. A universal reconstruction method for XTT is presented in this thesis, which is compatible with different wavefront modulation techniques.

In addition, we present a robust method for the extraction of the directional dark-field signal from data acquired with random diffusers. We demonstrate this approach on experimental measurements to obtain the first reconstruction of speckle-based tensor tomography. To optimise experimental parameters and predict the scattering behaviour, we developed a numerical wave-optics simulation model for SBI. We validate its effectiveness simulating a SBI measurement and an X-ray tensor tomography experiment.

The work presented in this thesis aims to establish X-ray scattering tensor tomography with a random modulator, making it more accessible for a broader range of applications, from industrial non-destructive testing to advanced biomedical diagnostics, and cultural heritage. We show several application cases, ranging from aerospace-type carbon-epoxy materials, to human middle ear ossicles, to fossil human remains. These various applications demonstrate the versatility and power of the imaging techniques developed in this work, with significant potential to impact different fields of ongoing research.

Finally, this thesis paves the way for method validation in a laboratory setting. During this PhD project, a significant contribution was made to the development of the OPTIMATO laboratory. The thesis presents the optimisation of acquisition settings and the first successful implementation of the proposed dark-field signal extraction method within the laboratory environment.

1 INTRODUCTION

1.1 MOTIVATION

X-ray imaging has recently become an indispensable tool for applications ranging from industrial quality control and biomedical diagnostics to cultural heritage preservation. However, conventional imaging techniques, such as micro-CT, face a trade-off between spatial resolution and the imaged field of view. As a result, micron-sized structures cannot be visualised if the field of view is on the order of centimetres. This limitation hinders fully characterising complex materials, such as biological tissues, industrial composites and archaeological remains, where microstructural information is critical for functional and structural assessment.

To tackle this problem, this PhD project aims to contribute to full-field small-angle X-ray scattering using modulation-based imaging. The main goal is to introduce novel formalisms and computational methods that enable the extraction and reconstruction of directional information in both 2D and 3D. By integrating theoretical developments, numerical simulations, and experimental validations, this research enables the non-destructive characterisation of oriented microstructures.

The motivation for this research comes from the need to:

1. Enhance the detection of defects and damage in industrial materials, particularly carbon fibre-reinforced polymers (CFRPs), which are critical for sustainable and lightweight engineering applications.

2. Characterise microstructural changes in biological tissues, enabling advancements in diagnostic techniques for soft tissue analysis.

3. Improve the analysis of archaeological and cultural heritage samples, such as fossilised materials, by extracting directional features like tubule orientations that provide valuable insights into their structure and history.

In addition, this research addresses practical challenges in laboratory-based X-ray systems, developing and testing a new X-ray imaging device based on a high-brilliance liquid-metal-jet source. This system paves the way for a broader use of new X-ray imaging methods in both scientific and industrial settings.

The outcomes of this work will enable a new class of imaging tools to visualise microstructural orientations in 3D. This has the potential to impact

various fields, including non-destructive testing, biomedical imaging, and archaeological research, driving innovation in material characterisation.

1.2 RESEARCH OUTCOMES

The focus of this PhD project is to introduce a new formalism for small-angle scattering in modulation-based imaging. Starting from theoretical and numerical developments, a new scattering-aware X-ray imaging formalism has been developed, validated and applied to study objects smaller than the resolving power of the imaging apparatus.

Moreover, a versatile reconstruction method for X-ray full-field tensor tomography has been implemented and validated, exploiting small-angle X-ray scattering, reconstructing tomograms of oriented microstructures acquired at the synchrotron. In addition, a robust method has been developed for the extraction of the directional dark-field signal from data acquired with random diffusers. Using this novel approach, it was possible to obtain the first reconstruction of X-ray speckle-based tensor tomography.

A numerical wave-optics simulation model for speckle-based imaging was developed to design new experiments and to better understand the small-angle scattering contribution in the imaging context.

Finally, a new X-ray imaging device based on a high-brilliance liquid-metal-jet source has been developed and tested. To effectively apply dark-field extraction methods, a large field-of-view high-energy photon-counting detector and a 6-axis robotic arm have been added to the laboratory. Industrial and biomedical samples have been analysed in the laboratory in order to assess the capabilities of the system.

The outcomes of this PhD project will have a major impact on the X-ray imaging users, both at the synchrotron and in the laboratory. Multiple applications stemming from the outcomes of this project are envisioned and presented, ranging from industrial non-destructive testing to advanced biomedical diagnostics, and cultural heritage. For instance, dark-field imaging and tensor tomography will provide new tools to detect defects in the manufacturing process of carbon reinforced polymers. Since composites are a critical part of future lightweighting strategies, the impact translates to green and sustainable engineering. The methods used in this project are also based on the extraction of phase-contrast signal, therefore employing refraction as a contrast mechanism to detect small density differences in unstained soft tissues. Also archaeology can benefit from a deeper understanding of the small-angle scattering mechanism, leading to a robust imaging technique capable of extracting the orientations of dentinal tubules.

1.3 THESIS OUTLINE

- **Chapter 2** introduces the background theory of X-ray physics, such as the Kramers-Kronig relations, and the small-angle scattering. In addition, the principal X-ray sources used in this project are presented: synchrotron sources and X-ray liquid-metal-jet sources.
- **Chapter 3** introduces the basics and the principles of two X-ray imaging methods that rely on phase-sensitive mechanisms: propagation-based imaging and modulation-based imaging, either with circular diffractive optics or with random diffusers. The Unified Modulated Pattern Analysis (UMPA) algorithm is also presented in details, along with a synthetic review of speckle-based directional dark-field imaging.
- **Chapter 4** introduces the principles of scalar computed tomography, starting from the Radon transform and filtered back-projection to iterative methods and quantitative interpretation of the tomograms. In this chapter, X-ray tensor tomography is also introduced.
- **Chapter 5** presents the results of a dark-field radiography analysis to detect barely visible impact damage on CFRP materials, with both matrix-cracking and delamination damages.
- **Chapter 6** shows a multimodal X-ray tomography study of two biological tissues, ovarian tissue and hepatic tissue, using modulation-based imaging and propagation-based imaging.
- **Chapter 7** presents a fast and versatile omnidirectional dark-field extraction method, along with a novel reconstruction method for X-ray scattering tensor tomography. The software architecture of both algorithms is also presented, as long as unit tests, simulation results and experimental validations.
- **Chapter 8** presents a robust method for the extraction of the directional dark-field signal tailored for data acquired with random diffusers. The model, the software architecture, and the experimental validation are presented. The first reconstruction of speckle-based tensor tomography is also shown in this chapter.
- **Chapter 9** presents a numerical wave-optics simulation model for speckle-based imaging. The physical model of the simulation, the software architecture and some examples of applications are presented. The effectiveness of the simulation is validated with three examples: an SBI measurement of a carbon fibre cross and an X-ray tensor tomography experiment on a cube containing three fibre bundles along three different orientations.
- **Chapter 10** presents three main applications of the X-ray tensor tomography model described in this thesis: an industrial application on carbon-fibre composites, a medical application on human middle ear

ossicles, and a cultural heritage application on a fossil tooth and a fossil femur.

- **Chapter 11** presents a description of the newly-established OPTIMATO laboratory, the study for the optimisation of the acquisition settings, and some speckle-based imaging reconstructions with UMPA. In addition, the first results in the laboratory of the proposed omnidirectional dark-field signal extraction method are presented.
- **Chapter 12** concludes this thesis work and provides an outlook for possible future developments.

2 FUNDAMENTALS OF X-RAY IMAGING

In this chapter, we introduce the basics and principles of X-ray physics, and the principal X-ray sources used in the rest of the thesis.

2.1 INTERACTION OF X-RAYS AND MATTER

2.1.1 Kramers-Kronig relations

To describe the energy-dependent interaction between X-rays and matter, resonant scattering has to be introduced. In quantum mechanics, resonant scattering happens when an incoming photon excites an electron from a lower energy level to a higher one. The electron subsequently returns to its original state, releasing a photon with the same energy as the incoming photon. This behaviour can be represented by a driven harmonic oscillator model.

The scattering amplitude of the atom can be written as follows:

$$f(\mathbf{Q}, \hbar\omega) = f^0(\mathbf{Q}) + f'(\hbar\omega) + if''(\hbar\omega). \tag{2.1}$$

where $f^0(\mathbf{Q})$ is the atomic form factor, and f' and f'' are known as the dispersion corrections. They are functions of the X-ray energy $\hbar\omega$, since their behaviour is dominated by tightly bound inner-shell electrons **[Nielsen2011]**. In Eq. 2.1 Q is the wave-vector transfer $Q = k - k'$ from the incident to the scattered wave.

The real (f') and the imaginary (f'') parts of the dispersion corrections are related through the Kramers-Kronig relations. It can be demonstrated, based on Cauchy's theorem **[Nielsen2011]**, that f' and f'' are related by the principal integral $\mathcal{P}$:

$$i\pi \left(f_s'(\omega) + if_s''(\omega) \right) = \mathcal{P} \int_{-\infty}^{\infty} \frac{f_s'(\omega') + if_s''(\omega')}{\omega' - \omega} d\omega'. \tag{2.2}$$

Eq. 2.2 leads to the Kramers-Kronig relations for a single oscillator:

$$f'(\omega) = \frac{1}{\pi} P \int_{-\infty}^{\infty} \frac{f''(\omega')}{\omega' - \omega} d\omega' \tag{2.3}$$

$$f''(\omega) = -\frac{1}{\pi} P \int_{-\infty}^{\infty} \frac{f'(\omega')}{\omega' - \omega} d\omega' \tag{2.4}$$

As a result, if the energy dependence of f'' is known, then f' can be calculated.

2.1.2 Complex index of refraction

In the case of elastic scattering ($\mathbf{Q} = 0$), Eq. 2.1 becomes

$$n = 1 - \delta + i\beta = 1 - \frac{r_0}{2\pi}\lambda^2 \sum_i \rho_a^i f_i(Q = 0), \tag{2.5}$$

where δ and β are the real and imaginary parts of the refractive index n, respectively. We can therefore express δ and β of a given i-th element as

$$\delta = \frac{r_0}{2\pi}\lambda^2 \sum_i \rho_a^i \left(f_i(0,\omega) + f'(\omega)\right) \tag{2.6}$$

$$\beta = \frac{r_0}{2\pi}\lambda^2 \sum_i \rho_a^i f''(\omega) \tag{2.7}$$

where r_0 is the Thomson scattering length, ρ_a^i is the atomic density of the i-th element, and $f_i(0,\omega)$ is the scattering factor.

A transmitted beam through a material of thickness s, can be expressed using the index of refraction:

$$I(s,\omega) = I_0 \exp\left\{\frac{i\omega}{c}\int [1 - \delta + i\beta]\, ds\right\} \tag{2.8}$$

The phase of the transmitted wave is affected by the real part of the scattering factor ($1 - \delta$), whereas the imaginary part of the scattering factor (β) is related to the absorption term.

We can rewrite β in Eq. 2.7 in terms of the attenuation coefficient μ, which depends on the atomic number:

$$\beta = \frac{\lambda\mu}{4\pi}\,. \tag{2.9}$$

In addition, we can rewrite δ in Eq. 2.6 in terms of atomic density $\rho_a = f_0(0)$ and atomic scattering length r_0, neglecting the dispersion corrections **[Nielsen2011]**:

$$\delta = \frac{2\pi\rho_a f_0(0) r_0}{k^2}\,. \tag{2.10}$$

Therefore, the phase shift $\Delta\Phi$ that the X-rays that encounter when travelling through matter with respect to vacuum can be easily calculated, as function of the X-ray wavelength λ, the thickness s of the material and δ.

$$\Delta\Phi = \frac{2\pi\delta s}{\lambda}\,. \tag{2.11}$$

An object with varying thickness or δ causes a deviation in an initially planar wavefront. This curvature in the wavefront results in the refraction of the X-ray beam (phase shift $\Delta\Phi$). The angular deviation α can be calculated in the plane perpendicular to the direction of propagation of the incident beam **[Nielsen2011; Paganin2006]**:

$$\alpha_x = \frac{\lambda}{2\pi}\frac{\partial\phi(x,y)}{\partial x} \quad \text{and} \quad \alpha_y = \frac{\lambda}{2\pi}\frac{\partial\phi(x,y)}{\partial y} \tag{2.12}$$

2.1.3 Small-angle X-ray scattering

When describing scattering from matter, it is necessary to account for a vast number of electrons and their scattered waves. However, since we are interested in the small-angle scattering, the scattering angles $2\theta << 1^\circ$, and many simplifications can be made. For the description of the small-angle scattering, we refer to **[Nielsen2011]**.

The limit of the wave-vector transfer $Q \to 0$ corresponds to large distances in real space, and since $Q \propto \sin(\theta)$, this occurs at small scattering angles near the forward direction. The small-angle X-ray scattering (SAXS) region gives information on the size and morphology of large-scale structures, such as polymers, rather than precise positional details of individual atoms. Therefore, for small wave-vector transfers, that is to say for small scattering angles, the intensity of the scattering signal can be written as:

$$I^{SAXS}(Q) = f^2 \sum_n \int_V \rho_a e^{iQ\cdot(r_n - r_m)} dV_m = f^2 \sum_n e^{iQ\cdot r_n} \int_V \rho_a e^{-iQ\cdot r_m} dV_m, \tag{2.13}$$

where f is the atomic or molecular form factor, ρ_a is the average of the electron density, and dV_m is a volume element located at a position $r_m - r_n$ with respect to the reference atom at r_n.

The sum over the reference atoms can be replaced by an integral:

$$I^{SAXS}(Q) = f^2 \int_V \rho_a e^{iQ\cdot r_n} dV_n \int_V \rho_a e^{-iQ\cdot r_m} dV_m. \tag{2.14}$$

For sufficient averaging, as typically occurs in small-angle scattering, Eq. 2.14 becomes:

$$I^{SAXS}(Q) = \left| \int_V \rho_s e^{iQ\cdot r} dV \right|^2, \tag{2.15}$$

where $\rho_s = f\rho_a$ which, when multiplied by the Thomson scattering length r_0, gives the scattering length density. From Eq. 2.15 it is possible to see how the intensity distribution observed in the far-field is similar to the square of the Fourier transform of the electron density distribution within an object.

2.2 X-RAY SOURCES

2.2.1 Synchrotron sources

Most of the measurements presented in this thesis have been acquired with synchrotron sources. We can define as synchrotron light the electromagnetic radiation emitted by relativistic charged particles that are accelerated along curved trajectories **[Paganin2006]**. When electron accelerator were first realised in the 1920s, the synchrotron light was considered a mere inconvenience. A century later, fourth-generation synchrotrons are being built all over the world.

In a synchrotron, relativistic electrons are accelerated in a storage ring, and emit electromagnetic radiation, ranging from infrared to hard X-rays. To reach a very high brightness, the electrons are produced in an electron gun, packed in several bunches, separated by a few ns, and then accelerated and injected into the booster. In the booster, the electrons are accelerated to the order of GeV and injected in the storage ring every time there is a refill. The storage ring (Fig. 2.1) is a tube, maintained at 10^{-9} mbar, where the electrons circle at relativistic speed for hours. In each curved section of the storage ring, two bending magnets force the path of the electrons and in each linear section, focusing magnets maintain the electron in the orbital path.

The radiation is emitted in correspondence to bending magnets or insertion devices. Bending magnets (Fig. 2.2) generate a constant magnetic field. When electrons pass through a bending magnet at relativistic speed, they emit radiation tangentially to the trajectory of the electron beam and with a continuous spectrum. An undulator, or insertion device, (Fig. 2.3) is an array of magnets with alternating poles. The electrons passing thorough an undulator are forced to follow a wavy trajectory, generating a focused, brilliant beam of radiation. The gap between the magnets of the undulator can be adjusted to change the spectrum of the emitted radiation. Both undulators and bending magnets have been used to acquire the data presented in this thesis.

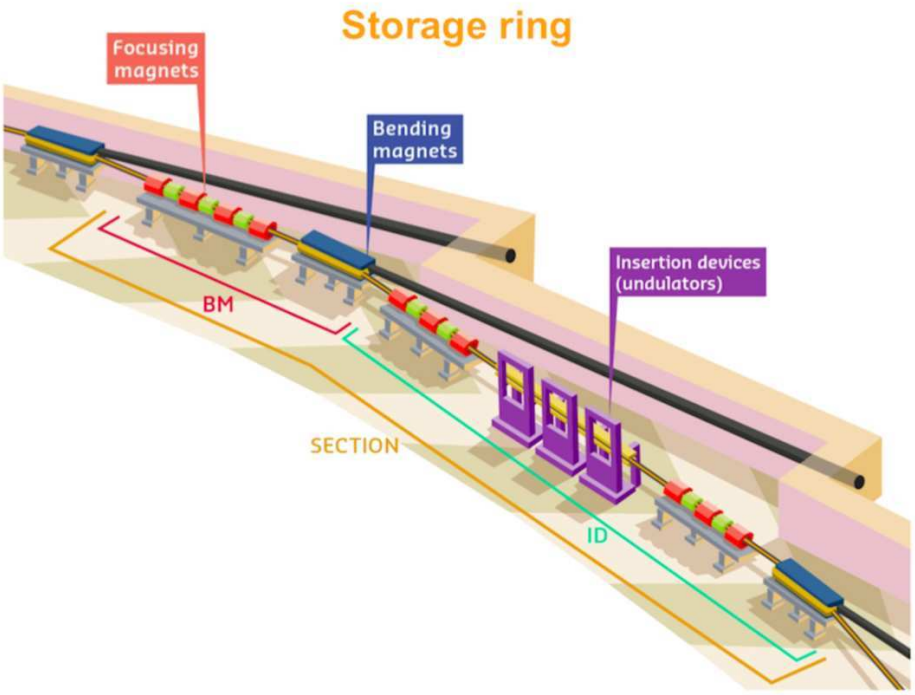

Figure 2.1: Outline of a curved section of the storage ring, showing a bending magnet (BM) and insertion devices (ID). Reprinted from **[ESRF]**.

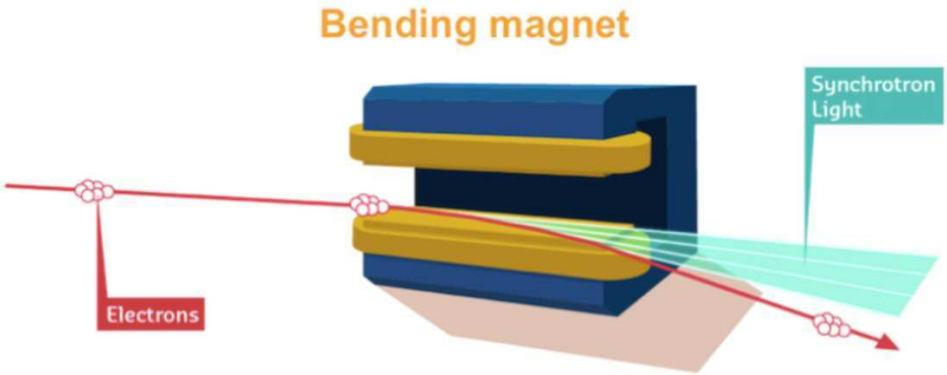

Figure 2.2: Outline of a bending magnet. Reprinted from **[ESRF]**.

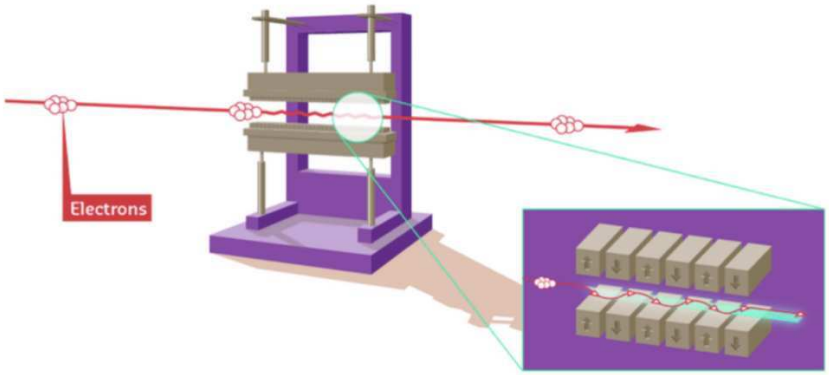

Figure 2.3: Outline of an insertion device or undulator. Reprinted from **[ESRF]**.

2.2.2 X-ray liquid-metal-jet sources

Part of this PhD project consisted in developing the OPTIMATO (OPTimal IMAging and TOmography) laboratory, a new laboratory hosted at Elettra, and test our techniques. For a detailed description of the laboratory, the reader is referred to chapter 11.

To obtain X-ray in a laboratory, an X-ray tube source is needed. In an X-ray tube source, electrons, generated in the cathode, are accelerated towards the anode by a high voltage bias. The electron beam, interacting with the anode material, emits a continuous bremsstrahlung spectrum. The maximum energy of the photons corresponds to the maximum electron energy, and characteristics lines are emitted due to X-ray fluorescence of the anode material.

By increasing the electron current, the X-ray brightness increases. The achievable X-ray brightness reaches its limit when the electron current melts the anode locally. With a liquid-metal-jet source, like the one in the OPTIMATO laboratory, the liquid anode is continuously regenerated (Figs. 2.4, 2.5). In this way, very high electron beam power densities can be handled. Achieving significantly higher brightness and smaller spot sizes than other commercial X-ray sources, a liquid-metal-jet source can generate very brilliant and small beams. Therefore, a liquid-metal-jet source is the closest possible solution to a synchrotron performance in the laboratory, enabling a major increase of the image acquisition speed with maintained resolution **[Excillum]**. Alloys like gallium and indium are used for different X-ray emission properties.

In the OPTIMATO laboratory, X-rays are generated by a microfocal, high-brilliance liquid-metal-jet source (MetalJet D2+, Excillum, Sweden), having a maximum voltage of 160 kV, a power of 250 W, and adjustable focal spot sizes ($\geq$ 15 µm).

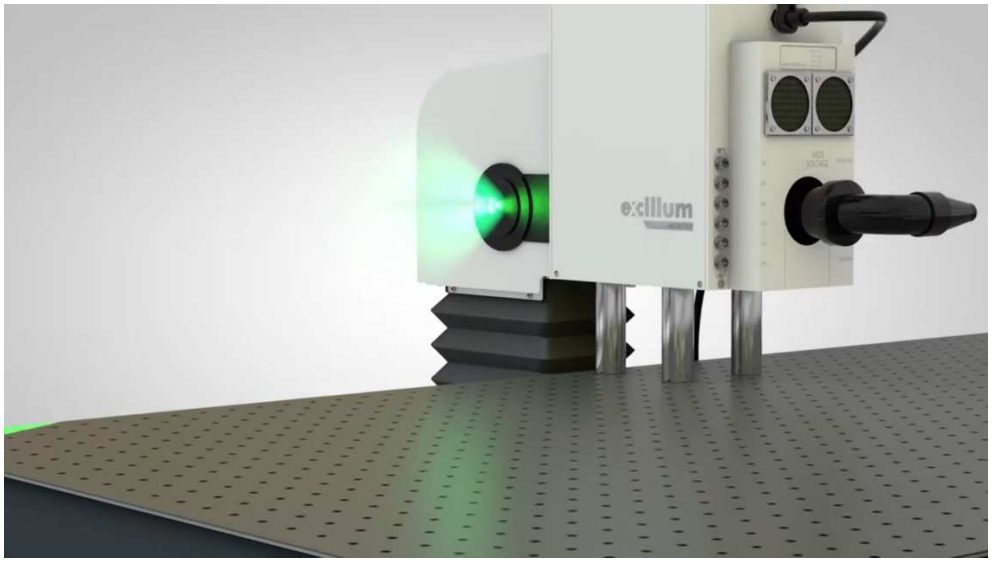

Figure 2.4: An outline of the Excillum liquid-metal-jet source. Reprinted from **[Excillum]**.

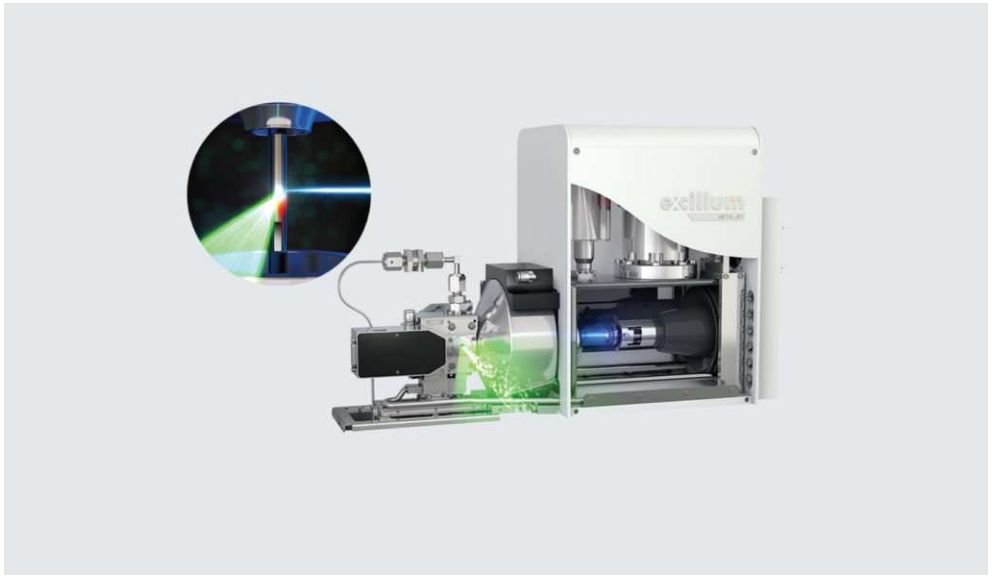

Figure 2.5: An outline of a section of the Excillum liquid-metal-jet source. In the inset, the generation of X-rays (green) from the electron beam (blue) is visible. Reprinted from **[Excillum]**.

3 IMAGING METHODS

This chapter introduces two X-ray imaging methods that rely on phase-sensitive mechanisms: propagation-based imaging (PBI) and modulation-based imaging (MBI), either with circular diffractive optics or with random diffusers. These techniques allow for the retrieval of complementary image signals, such as absorption, phase contrast, and dark field, enabling comprehensive visualization of complex structures in a sample.

3.1 PROPAGATION-BASED PHASE-CONTRAST IMAGING

Propagation-based imaging (PBI) is probably the most used phase-sensitive technique. It exploits free-space propagation to convert phase variations over a plane into intensity variations in a registered image without using any optical element (Fig. 3.1) **[Paganin2002; Paganin2006]**. A PBI setup consists of a source and a detector, given high spatial coherence and enough propagation distance from the sample and the detector. PBI relies on the spatial coherence of the source, otherwise the phase contrast is destroyed, but it is rather insensitive to polychromaticity in the source.

The intensity of the propagation-base phase contrast image, recorded over the plane $z = \Delta$ depends on the phase and the intensity variations at $z = 0$ **[Paganin2006]**:

$$\begin{aligned} I_\omega(x,y,z=\Delta) =& I_\omega(x,y,z=0) \\ &- \frac{\Delta}{k}\nabla_\perp \cdot \left[I_\omega(x,y,z=0)\nabla_\perp \phi_\omega(x,y,z=0) \right]. \end{aligned} \tag{3.1}$$

In Eq. 3.1, k is the radiation angular wave-vector, ω is the angular frequency of the radiation, z is the propagation distance, $\phi_\omega(x,y,z=0)$ is the phase of the radiation, and x and y are the Cartesian coordinates over planes parallel to the optic axis. Eq. 3.1 is a form of the transport-of-intensity equation **[Teague1983]**.

If the transverse intensity gradient and the transverse phase gradient are not too strong, then Eq. 3.1 becomes identical to

$$I(x,y,z+\delta z) \approx I(x,y,z) - \frac{\delta z}{k}\nabla_\perp \cdot \left[I(x,y,z)\nabla_\perp \phi(x,y,z) \right], \tag{3.2}$$

where δz is the propagation distance, sufficiently small for the evolution of intensity to be linear in z, and $\nabla_\perp$ indicates the gradient. The second term

on the right side of this equation represents the local increase or decrease in intensity, which is due to the local curvature of the phase in a plane at a constant z **[Paganin2006]**.

The second term of Eq. 3.2 can be written as:

$$\nabla_\perp \cdot [I(x,y,z)\nabla_\perp \phi(x,y,z)] = I(x,y,z)\nabla_\perp^2 \phi(x,y,z) + \nabla_\perp I(x,y,z) \cdot \nabla_\perp \phi(x,y,z). \tag{3.3}$$

where the first term is the edge enhancement term, and the second term is the phase gradient term. The phase gradient term can be neglected in the case of small intensity variations compared to phase variations.

The most common method to perform phase retrieval has been proposed by Paganin et al. **[Paganin1998; Paganin2002]** and it is based on the transport-of-intensity equation. The proposed method assumes a single-material sample and a constant ratio of the real and imaginary part of the refractive index (δ/β). In the mentioned algorithm, the following Fourier representation for the Laplacian and gradient operators are used:

$$\begin{cases} \nabla_\perp^{-2} = -\mathcal{F}^{-1} \dfrac{1}{k_x^2 + k_y^2} \mathcal{F} \\ \nabla_\perp = i\mathcal{F}^{-1}(k_x, k_y)\mathcal{F} \end{cases} \tag{3.4}$$

where k_x, k_y are the coordinates in Fourier space. Using the Fourier representations and the single-material approximation, the phase signal of a sample placed in the near field becomes:

$$\Phi(x,y) = \frac{\delta}{2\beta} \ln \left(\mathcal{F}^{-1} \left\{ \frac{\mathcal{F}\{I(x,y)/I_0(x,y)\}}{1 + [\lambda z \delta/(4\pi\beta)] \left(k_x^2 + k_y^2\right)} \right\} \right), \tag{3.5}$$

where $\mathcal{F}$ and $\mathcal{F}^{-1}$ indicate the Fourier transform and the inverse Fourier transform operators, respectively. $I(x,y)$ and $I_0(x,y)$ are the intensities measured by the detector placed at a distance z with and without the sample in the beam, and λ is the X-ray wavelength.

If the approximations are not met, for instance the sample is not placed at a near-field distance, or the δ/β ratio is not exactly known, then this phase-retrieval algorithm still provides excellent qualitative results.

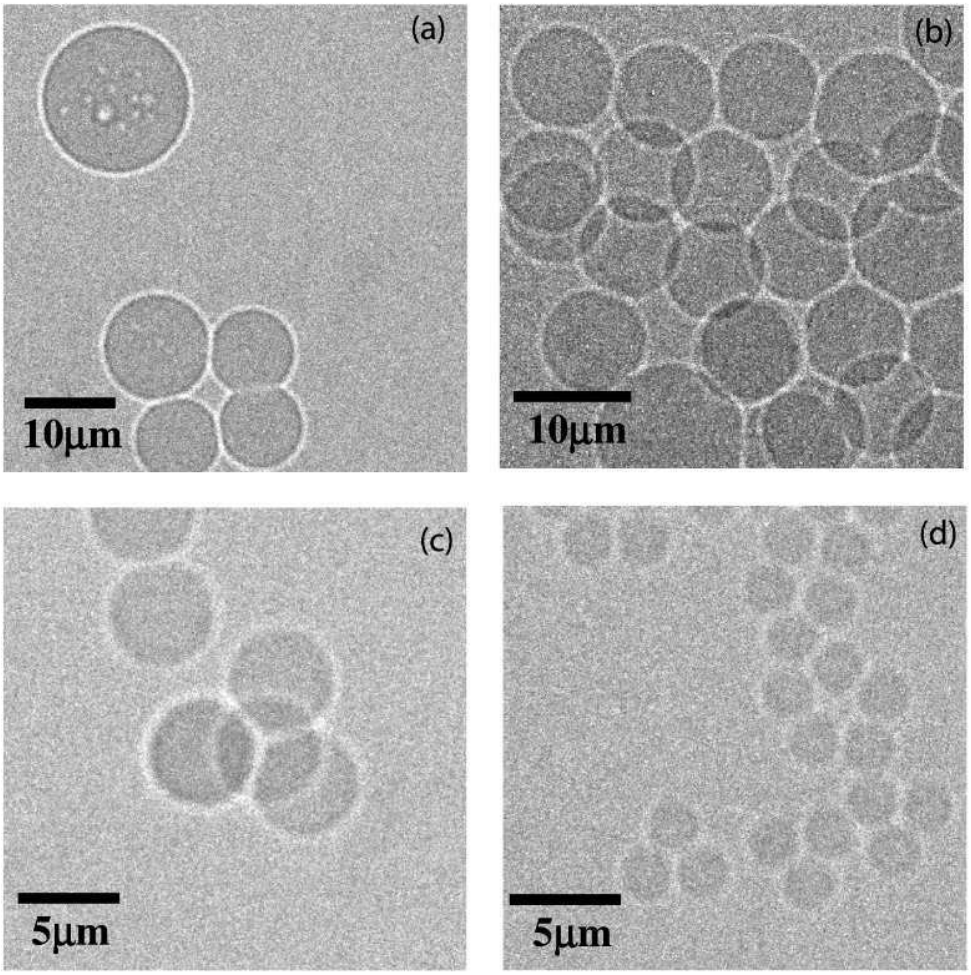

Figure 3.1: Phase contrast X-ray images of latex spheres of varying size: (a) 9 μm, (b) 9 μm, (c) 5.2 μm; (d) 2.3 μm. Exposure times were 25 min, 10 min, 35 min and 25 min, respectively. Image reproduced from **[Paganin2002]**.

3.2 MODULATION-BASED IMAGING

Modulation-based imaging (MBI) is a multi-modal X-ray imaging technique that retrieves absorption, phase, and small-angle scattering (dark-field) signals in a single shot by analysing modulations in a reference wavefront pattern **[Pfeiffer2008; Wang2015; Kagias2019; Olivo2021]**. An X-ray beam modulator, either periodic or random, is employed to create a non-uniform illumination on the detector. While uniform X-ray illumination normally reveals the attenuation properties of a sample, non-uniform illumination can also detect refraction and ultra-small-angle scattering effects. When a sample is placed in the modulated X-ray beam, it modifies the pattern through absorption, refraction, and scattering, allowing the extraction of the three complementary image signals: absorption, phase, and dark-field signals.

Grating interferometry (GI) and speckle-based imaging (SBI) are the principal MBI techniques. Grating interferometry uses phase and absorption gratings to create periodic interference patterns. It is highly sensitive to phase changes.

Speckle-based imaging, in contrast, uses a random pattern generated by a diffuser, for instance one or more layers of sandpaper, offering flexibility in setup and cost-effectiveness. This technique requires smaller detector pixels due to the fine resolution of speckle patterns but works well with polychromatic X-ray sources **[Morgan2012; Berujon2012]**.

To assess the performance of a technique for a given setup, the visibility quantity can be defined as follows **[Zdora2018]**:

$$V = \frac{\sigma}{\langle I \rangle} = \frac{\sqrt{\langle I^2 \rangle - \langle I \rangle^2}}{\langle I \rangle}, \tag{3.6}$$

where σ and $\langle I \rangle$ are the standard deviation and the mean intensity value of the reference image of the pattern. The visibility map can be calculated using a Gaussian filter with a kernel size which is slightly bigger than the marking structures.

3.2.1 X-ray imaging with circular diffractive optics

Circular diffractive optics (CDO) enables simultaneous omnidirectional sensitivity to small-angle X-ray scattering (SAXS) in a single shot, without the need for mechanical scanning of the sample or of the optical components. This is in contrast to traditional grating interferometry (GI), which requires multiple directional acquisitions to obtain the scattering information **[Kagias2016; Kagias2019]**.

The basic principle behind CDO is the use of a 2D periodic array of unit cells, each formed by concentric circular gratings. This arrangement allows for isotropic sensitivity to scattering angles in the imaging plane, which is crucial for detecting structures with unknown or variable orientations. The periodicity of the array defines both the feature sizes that can be imaged and the sensitivity of the system to small-angle scattering.

The X-rays scattered from the circular grating create a circular pattern that can be measured at a distance L from the diffractive optics, also known as the Talbot distance **[Kagias2016]**. For a grating with period P, the Talbot distance is defined as:

$$L_m = m\frac{P^2}{2\lambda}, \tag{3.7}$$

where λ is the wavelength of the X-rays, and m is an integer representing the Talbot order. At the Talbot distance, a self-image of the grating is formed, which contains information about the scattering properties of the sample.

The system is sensitive to structural variations in the sample with a characteristic length scale ξ, known as the autocorrelation length, given by:

$$\xi = \frac{\lambda L}{P}. \tag{3.8}$$

The autocorrelation length defines the sensitivity of the system to specific feature sizes in the sample. Therefore, by tuning the parameters of the system,

it becomes possible to image features smaller than the resolution limit of the detector by detecting changes in the visibility of the interference fringe, caused by scattering within the sample.

When X-rays interact with a sample, the microstructures in the material induce small-angle scattering. This scattering broadens the angular distribution of the X-rays, reducing the visibility of the interference fringe. The visibility reduction is related to the scattering strength and orientation of the microstructures. The intensity of the scattered signal can be described as:

$$I(r,\gamma) = A(\gamma)\left[1 + V(\gamma)\cos\left(\frac{2\pi r}{P}\right)\right], \tag{3.9}$$

where r is the radial distance from the centre of the unit cell, γ is the angular coordinate, $A(\gamma)$ is the average intensity, and $V(\gamma)$ is the visibility of the fringe pattern **[Kagias2019]**. A reduction in visibility can indicate the presence of small-angle scattering, which is related to the anisotropic features of the material (Fig. 3.2).

To extract the scattering signal, Fourier analysis is applied to the recorded interference pattern, allowing for the reconstruction of the scattering properties in all directions within the imaging plane. This is a significant improvement over traditional methods, which only provide directional sensitivity in a few angles, requiring rotation or scanning **[Kagias2016]**.

The scattering anisotropy can be quantified by fitting the angular distribution of the visibility reduction to a cosine function:

$$D(\gamma) = a_0 + a_1\cos(\gamma - \gamma_{\text{main}}), \tag{3.10}$$

where a_0 is the isotropic scattering component, a_1 represents the anisotropic contribution, and γ_{main} is the primary direction of the scattering **[Kagias2019]**.

Thanks to its omnidirectional sensitivity, single-shot acquisition and broad applicability, CDO has demonstrated significant potential in various fields, including biomedical imaging, materials science, and non-destructive testing. The ability to capture scattering information from multiple directions in a single acquisition makes CDO particularly useful for dynamic studies and real-time imaging applications. For instance, the visualization of the evolving microstructures of complex materials subject to mechanical stress **[Kagias2021]**.

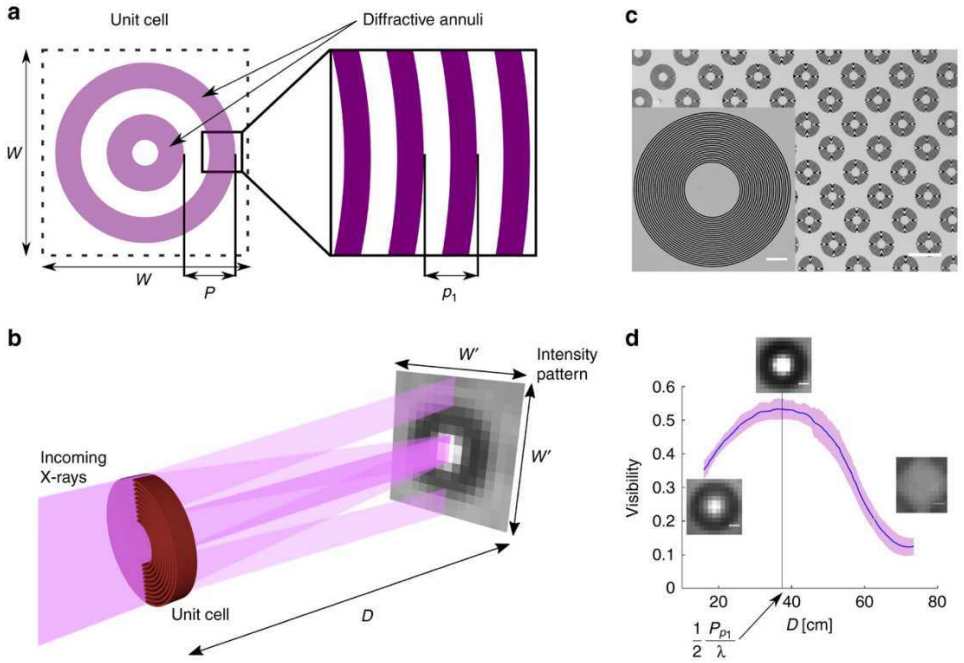

Figure 3.2: Fringe formation for a single unit cell. (a) Schematic of a single unit cell containing two diffractive annuli. (b) The substructures of the annulus cause diffraction of the incoming X-rays. (c) Fabricated grating. (d) Measured visibility for the grating shown in (c) as a function of the propagation distance. Image reproduced from **[Kagias2019]**.

3.2.2 X-ray speckle-based imaging

X-ray speckle-based imaging is a special case of modulation-based imaging, where the modulator consists of one or more layer of sandpaper. It was first introduced by Morgan **[Morgan2012]** and Berujon **[Berujon2012]**. The patter on the detector consists of a random speckle-like intensity distribution.

Commercially available sandpaper, typically composed of silicon carbide grains, is used as a diffuser to create a speckle pattern and finer grit sizes are chosen to produce a speckle pattern with a smaller speckle size. The size of the speckle pattern is mainly determined by the grit of the sandpaper, while the visibility of the speckle pattern is influenced also by the beam properties and the type of the detection system. The visibility of the speckle pattern can be enhanced by adding multiple layers of sandpaper or increasing the distance from the diffuser to the detector. The speckle size of the diffuser at the detector stage should be bigger than the pixel size, so to be resolved.

Several acquisition methods are available, including single-shot speckle-tracking **[Berujon2012; Morgan2012]** and multi-frame 1D and 2D scanning **[Wang2016]**, with advanced mixed approaches simplifying the process **[Berujon2017]**. Various algorithmic methods have been developed to extract information from X-ray patterned data. The majority of these methods utilize a pattern- or speckle-tracking approach **[Berujon2012; Zdora2017]**, while some rely on implicit tracking methods **[Pavlov2021]**. The algorithm used in this PhD thesis is the Unified Modulated Pattern Analysis (UMPA) **[Zdora2017;**

DeMarco2023], which explicitly models local distortions of the reference pattern caused by the sample.

The drawback of speckle-based imaging is that it needs a high detector resolution to image the interference patterns. On the other hand, SBI provides a high phase sensitivity, quantitative output, and it is compatible with laboratory sources. Thanks to its benefits and relaxed setup constraints, SBI has become increasingly popular in the imaging community.

3.2.3 Unified Modulated Pattern Analysis

The Unified Modulated Pattern Analysis (UMPA) **[Zdora2017; DeMarco2023]** is an algorithm that allows to extract transmission, phase and dark-field signals from a modulation-based imaging (MBI) dataset. UMPA is an explicit tracking model that allows signal retrieval from single shot acquisitions, modelling the local intensity variations in a near-field speckle pattern when a sample is inserted in the beam.

In a single-shot acquisition scheme, a single reference image $I_0(\mathbf{r})$ is acquired with only the modulator, but not the sample, in the beam. When the sample is introduced in the beam, a sample image $I(\mathbf{r})$ is acquired. UMPA performs a comparison between $I_0(\mathbf{r})$ and $I(\mathbf{r})$ for every pixel $\mathbf{r}$, by centring an analysis window of size $(2N+1) \times (2N+1)$ pixels on $I(\mathbf{r})$, and seeking the most similar match of this window in the reference image $I_0(\mathbf{r})$ **[DeMarco2023]**. The attenuation of the sample is described by a uniform decrease of intensity, the refraction induced by the sample is modelled with a local transverse translation $\mathbf{u}$, and the dark-field is modelled as a decrease in the modulation amplitude. The effect of the sample is modelled as follows:

$$I^{\text{model}}(\mathbf{r}; \mathbf{u}, T, D) = T(\mathbf{r}) \cdot \{D(\mathbf{r}) \cdot [I_0(\mathbf{r} - \mathbf{u}) - \langle I_0(\mathbf{r} - \mathbf{u}) \rangle] + \langle I_0(\mathbf{r} - \mathbf{u}) \rangle\}, \tag{3.11}$$

where $T(\mathbf{r})$, $D(\mathbf{r})$ and $\mathbf{u}(\mathbf{r})$ correspond to the transmittance, dark-field, and differential-phase signals. $\langle I_0(\mathbf{r}) \rangle$ is the local mean of I_0 in the vicinity of $\mathbf{r}$.

A better image quality and a higher spatial resolution can be achieved by acquiring different sets of sample and reference images with a relative lateral displacement between the sample and the modulator.

UMPA attempts to minimize the sum of squared differences between the reference and sample images in a window $\Gamma(\mathbf{w})$:

$$L(\mathbf{r}) = \sum_{m=1}^{M} \sum_{w_x=-N}^{N} \sum_{w_y=-N}^{N} \Gamma(\mathbf{w}) \cdot \left[I_m^{\text{model}}(\mathbf{r} + \mathbf{w} - \mathbf{S}_m; \mathbf{u}, T, D) - I_m(\mathbf{r} + \mathbf{w} - \mathbf{S}_m) \right]^2, \tag{3.12}$$

where M pairs of images contribute to the final cost function $L(\mathbf{r})$. A Hamming window $\Gamma(\mathbf{w})$ function is used to decrease the weight of the pixels at the edges of the window.

Two stepping modalities can be employed to acquire different pairs of sample-reference images: the diffuser-stepping mode, and the sample-stepping mode (Fig. 3.3). In the diffuser-stepping approach, the diffuser is shifted transversely to the beam, typically in a spiral pattern, and different pairs of sample-reference images are acquired at different diffuser positions. An instability of the motors can cause artefacts in the images that can be corrected considering a drift of the modulator. In the sample-stepping mode, the sample is moved relatively to the diffuser and the difference in sample position between the different steps is taken into account so that identical regions of the sample add to the local minimization. With the sample-stepping approach, the field of view can be extended, being limited only by the travel range of the motors (Fig. 3.4).

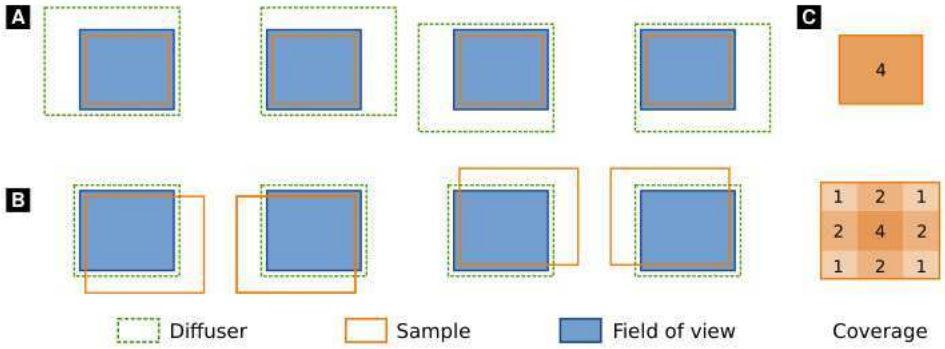

Figure 3.3: An outline of the two possible stepping methods used for UMPA. (a) Diffuser-stepping method. (b) Sample-stepping method. (c) Coverage maps of the sample for the two stepping methods. Image reproduced from **[DeMarco2023]**.

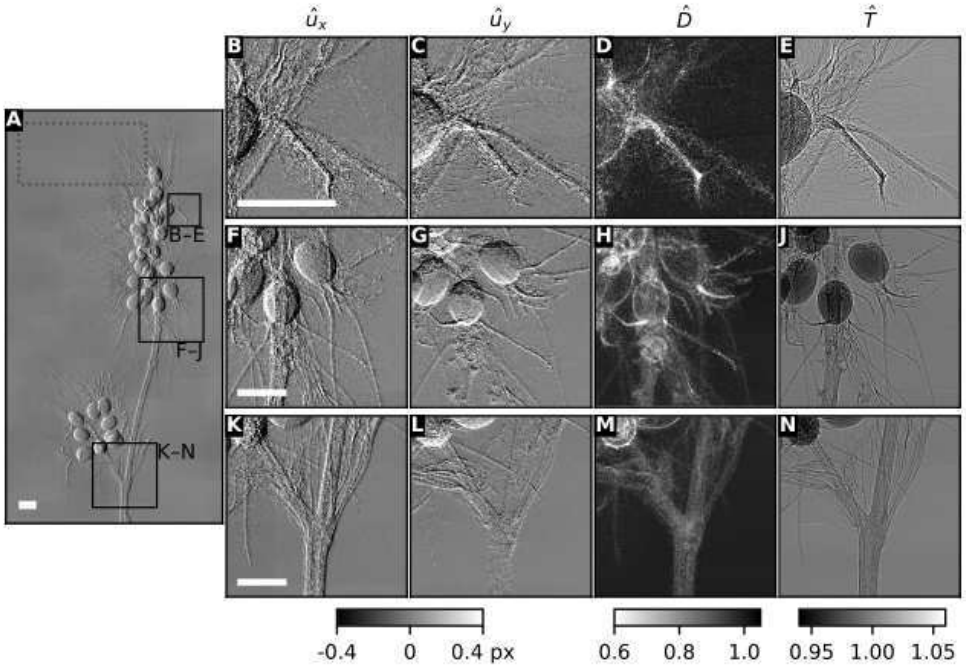

Figure 3.4: Flower acquired with speckle-based imaging and analysed using UMPA with the sample-stepping approach and a window of size 5×5. (a) Overview of the whole sample (differential-phase shift signal). The dashed rectangle represents the size of the detector field of view (3.48 mm $\times$ 7.25 mm). Three regions of interest are shown in the insets on the right, for all four modalities. Image reproduced from **[DeMarco2023]**.

3.2.4 Speckle-based directional dark-field imaging

Samples with strongly oriented microstructural features often exhibit an anisotropic X-ray scattering profile. In these cases, the directionality of the scattering can also be extracted to reveal information about their orientation. Directional dark-field (DDF) can detect and quantify the orientation of anisotropic structures. X-ray speckle-based DDF imaging was first introduced by Wang et al. **[Wang2015]** at synchrotron sources. The proposed method required the precise movement of a diffuser across the X-ray beam in small, equidistant steps. While effective, this technique required an extremely stable setup and high-precision scanning motors, which made it time-consuming and prone to artefacts. In addition, hundreds of scanning points were needed to achieve adequate angular resolution, limiting its application in real-world scenarios requiring faster imaging.

To address these challenges, Zhou et al. **[Zhou2018]** suggested a tracking method that significantly simplified the imaging process. Their approach required the acquisition of only two images, a reference image and a sample image, and used the visibility loss across line profiles taken at various angles. This allowed for a more efficient and robust reconstruction of the DDF signal with less stringent setup requirements and it was also tested on images acquired with a laboratory source.

Later, Pavlov et al. **[Pavlov2021]** introduced a novel approach based on the Fokker-Planck equation. Their approach presented an explicit model of the X-ray energy flow through a sample, allowing for the extraction of the dark-field signal directly from the speckle pattern. However, this technique operated under the assumption that the dark-field signal varied slowly throughout the sample, potentially limiting its applicability to cases where rapid changes in scattering properties occur.

Wang et al. **[Wang2021]** expanded the concept of angular analysis by implementing a spiral scanning pattern. This allowed for a more comprehensive sampling of the scattering directions, improving the angular sensitivity. Although this represented a significant advancement, the technique was still limited by analysing a finite number of discrete angles, leaving room for further refinement in angular resolution. This approach was demonstrated only with synchrotron radiation, but it can be potentially transferred to laboratory X-ray microfocus sources.

The key challenges related to scan time, angular resolution, and equipment stability have been tackled by the work of Smith et al. **[Smith2022]**. In this approach, UMPA is refined, enabling the extraction of mean scattering width, directionality, and orientation of the DDF signal. In their work, it is shown how the reconstruction parameters can be tuned to increase accuracy at the expense of spatial resolution. However, the model converges very slowly, and it is not suitable for a tensor tomography setup, where thousands of projections have to be analysed in real time.

X-ray speckle-based DDF imaging has been recently demonstrated also using a low-coherence X-ray source **[Magnin2023]**. This approach foresee implementing both imaging and scattering measurements within the same setup.

4 COMPUTED TOMOGRAPHY

4.1 SCALAR TOMOGRAPHY

The previous chapters described the interaction of X-rays with matter and how it is possible to extract 2D information on attenuation, phase-shift or scattering in a sample using modulation-based imaging. For thin samples, a 2D image can provide sufficient information on the sample. However, for most applications, 3D samples are studied and 3D volumetric information is necessary to overcome inaccuracies due to superposition effects in planar images. This chapter introduces the principles of scalar computed tomography and tensor tomography.

4.1.1 Radon transform and filtered back-projection

A tomographic acquisition consists in a collection of planar images at various angular orientations of the sample around a rotation axis perpendicular to the beam (Figs. 4.1-4.2). If we consider a parallel beam approximation, each projection will be the line integral through the sample of the spatial distribution function $f(x, y, z)$ of the sample for a given angular view.

We consider the rotation axis long the z axis and with $f(x, y)$ we indicate a slice of the object perpendicular to the rotation axis, along the xy plane. In this case, the 1D projection of the spatial distribution function at a given angle ϕ is called the Radon transform.

$$\tilde{f}(p, \phi) = \int_{-\infty}^{+\infty} f(p\cos\phi - s\sin\phi, p\sin\phi + s\cos\phi)\, ds. \tag{4.1}$$

Where we expressed the Radon transform using a coordinate system with axes p and s rotated by an angle ϕ with respect to x and y.

The reconstruction of the projection is obtained by a back-projection of the Radon transform for all the angles ϕ.

$$[\mathcal{B}(f)](x, y) = \int_0^{\pi} f(x\cos\phi + y\sin\phi, \phi)\, d\phi. \tag{4.2}$$

It can be demonstrated **[Deans1983]** that the 2D spatial distribution function of a slice of the sample, can be recovered using the back-projection of the Radon transform. However, since using the simple back-projection would lead to a blurred reconstructed image, the projections are filtered with a

ramp filter before the back-projection step in Fourier space. The filtered back-projection (FBP) method is the most commonly used method to reconstruct a tomographic dataset. It consists of filtering of the measured projection data followed by a back-projection step.

$$f(x,y) = \mathcal{B}f^* = \int_0^\pi f^*(x\cos\phi + y\sin\phi, \phi)\, d\phi, \tag{4.3}$$

where f^* is defined as follows:

$$f^*(s,\phi) = \mathcal{F}^{-1}\left\{|k|\mathcal{F}\{(f(k,\phi))\}\right\}. \tag{4.4}$$

$\mathcal{F}$ and $\mathcal{F}^{-1}$ are the Fourier transform and inverse Fourier transform, respectively, and k is the coordinate in Fourier space.

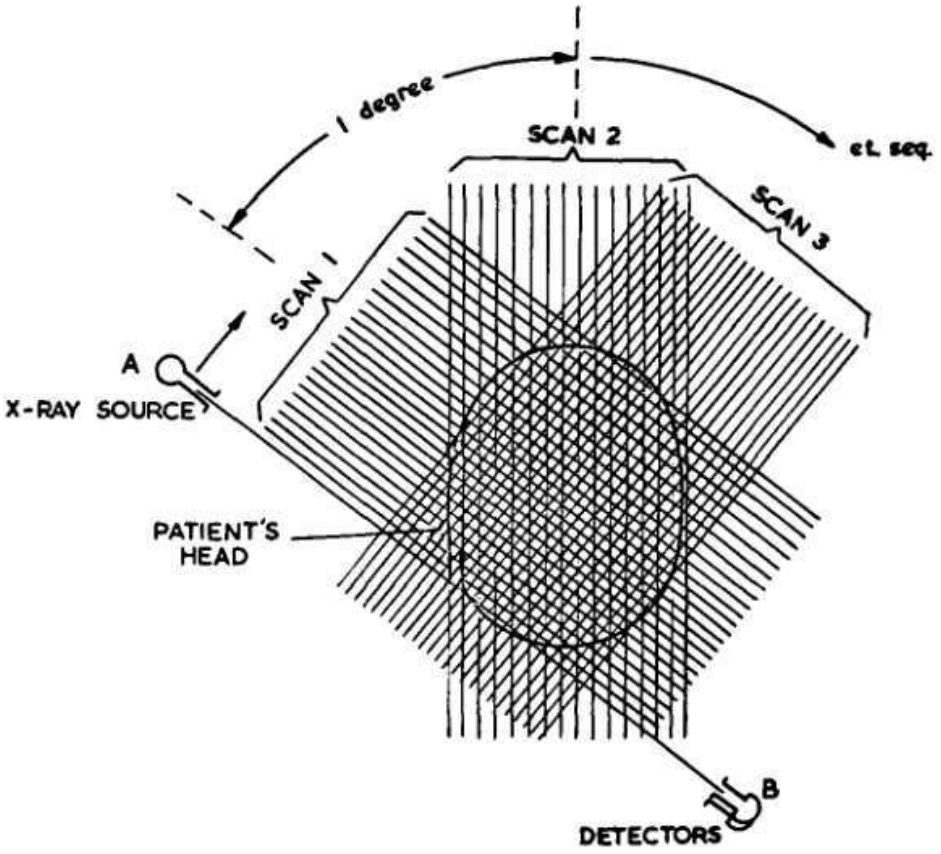

Figure 4.1: Simplified illustration of the scanning sequence of the first computed tomography scanner. Image reproduced from **[Hounsfield1973]**.

4.1.2 Iterative methods

Even though direct reconstruction methods are computationally efficient, they rely on the inversion of a continuous model, and thus they require a sufficiently large number of noise-free projections. When reconstructing sparse datasets, direct inversion methods (such as FBP) result in significant

Figure 4.2: A sample in position in the first computed tomography scanner. Image reproduced from **[Hounsfield1973]**.

artefacts in the reconstructed volume. To overcome these problems, iterative methods are used. Unlike direct methods, iterative approaches refine the solution over successive iterations, enabling better convergence towards a realistic and artifact-free reconstruction even with limited projection data.

Iterative algorithms solve a system of linear equations of the form $AX = B$, where A is a rectangular $M \times M$ matrix and X and B are $M \times 1$ column vectors. The matrix A s a sparse matrix: it is usually quite large, with dimensions of the order of 10^4, but with many of its entries being zero. Even if solving a system of linear equations might seem a trivial problem, the number of unknowns and the number of equations is large and the number of available equations from the projection data can be fewer than the number of unknowns.

Different iterative reconstruction methods exist, such as the algebraic reconstruction technique (ART), and the simultaneous iterative reconstruction technique (SIRT), and the simultaneous algebraic reconstruction technique (SART), a hybrid method **[Kak1988]**.

In ART techniques, the method computes an approximation of the solution of the linear systems of equations. Each projection in a tomographic acquisition is a linear equation, and the unknowns are the pixel (or voxel) values of the image to reconstruct. ART iteratively refines the estimates of these pixel values to fit the projection data. In each iteration, ART computes the new iteration vector such that one of the equations in the system is satisfied. This is achieved by projecting the current iteration vector X on one of the hyperplanes.

The update formula for ART is given by:

$$x^{(k+1)} = x^{(k)} + \frac{b_i - A_i \cdot x^{(k)}}{\|A_i\|^2} \cdot A_i^T, \tag{4.5}$$

Where $x^{(k)}$ is the solution vector at iteration k, b_i is the measured projection value for the i-th ray, A_i is the i-th row of the system matrix, representing the contribution of each pixel to the i-th projection. $\|A_i\|^2$ is the squared norm of the i-th row of A.

ART reconstructions usually suffer from salt and pepper noise, caused by the approximations introduced to solve the system of equations. SIRT, on the other hand, updates all pixel values only at the end of each iteration, after considering all the projections, where the change for each pixel being the average value of all the computed changes for that pixel.

In SART, it is possible to have reconstructions of good quality in only one iteration. Instead of the pixel basis, bilinear elements are used. Unlike ART, SART applies correction terms simultaneously for all rays in one projection. Additionally, a Hamming window is used to reduce noise.

4.1.3 Absorption, phase and dark-field tomograms

As described in chapter 3, from a modulation-based imaging measurement, three kinds of signals are obtained: absorption, phase-contrast and dark-field.

The absorption tomogram, reconstructed from the absorption projections, provides a 3D map of the sample's attenuation coefficient, μ, which represents its attenuation properties. According to the Beer-Lambert Law, transmission T through the sample is:

$$T = \exp\left(\int -\mu(x, y, z)dz\right) \tag{4.6}$$

To obtain the attenuation coefficient of a sample, we apply the logarithm to the absorption projections and multiply them by -1. Filtered back-projection is then used to generate the absorption tomogram.

The phase tomogram describes the 3D distribution of the refractive index decrement, δ, which is proportional to the electron density, ρ_a. The phase tomogram is therefore a 3D electron density map of the specimen.

As we described in Eq. 2.11, the phase shift ($\Delta\Phi$) of X-rays is related to δ. While in propagation-based imaging (PBI), the phase signal is recovered computationally, in modulation-based imaging (MBI), the first derivative of the phase signal ($\partial\Phi/\partial r$) is reconstructed. The approaches to reconstruct the phase projections differ from PBI and MBI.

For PBI, the phase projections are reconstructed similarly to absorption, without taking the logarithm, and the phase volume is multiplied by $\lambda/2\pi$ to obtain δ, which can be converted to ρ_a **[Zdora2021]**. On the other hand, for MBI, the first derivative of the phase-signal is obtained:

$$\frac{2\pi}{\lambda}\frac{\partial\Phi}{\partial x} = \frac{2\pi}{\lambda}\frac{\partial}{\partial x}\int \delta(x,y,z)dz \tag{4.7}$$

Integration of the differential phase signal in the projections, followed by conventional filtered back-projection, is necessary to obtain the 3D electron density map.

The electron density map can be converted to the mass density map multiplying it by $A/N_A Z$, where A is the molecular mass, N_A the Avogadro number and Z the atomic number. The mass density map, combined with absorption data, helps distinguish different materials in the specimen **[Zanette2015]**.

For MBI, a dark-field tomogram can be obtained from the same tomographic acquisition using filtered back-projection, similar to the case of the absorption tomogram. It has been demonstrated **[Wang2009; Bech2010; Wang2016]** that the dark-field signal is related to the linear diffusion coefficient ε:

$$\varepsilon = \frac{\sigma^2}{\Delta s}, \tag{4.8}$$

where σ is the total scattering width and Δs is the thickness of a slice. For speckle-based imaging, the following expression holds:

$$\int \varepsilon(s)ds = -\frac{\zeta_a^2}{8\pi^4 z^2} ln\gamma_{max}, \tag{4.9}$$

where ζ_a is the average speckle size, z is the propagation distance and γ_{max}, is the maximum cross-correlation coefficient, quantifying the visibility of the speckle pattern.

4.2 TENSOR TOMOGRAPHY

After a conventional tomographic scan, a scalar (i.e., the attenuation coefficient) is reconstructed for each voxel. On the other hand, a different model is necessary to extract the scattering tensor. In X-ray tensor tomography (XTT) two-dimensional projection images, with small-angle scattering signals, are acquired at various orientations of the sample. The two-dimensional directional scattering signals can be combined to reconstruct tomographically the local scattering tensor of the sample.

Different tensor tomography models have been suggested in recent years, both for scanning SAXS and full-field imaging with circular diffractive optics.

It has been demonstrated **[Malecki2014]** that the X-ray directional dark-field signal $D(x,y)$ can be expressed like a weighted Beer-Lambert law:

$$D(x,y) = \exp\left[-\int \sum_{\alpha=1}^{\infty} \left((|e_\alpha(x,y,z)||t|)^2(|\hat{s}\times\hat{e}_\alpha|\langle\hat{e}_\alpha,\hat{t}\rangle)^2\,dz\right)\right], \tag{4.10}$$

where $\hat{e}_\alpha$ is the normalized scattering vector along the sampling direction, $\hat{s}$ is the normalized beam direction vector, and $\hat{t}$ is the sensitivity unit vector of the grating interferometer. For a given geometry, the values of the weight factor $(|\hat{s}\times\hat{e}_\alpha|\langle\hat{e}_\alpha,\hat{t}\rangle)^2$ can be precalculated.

Another tensor tomography model, alternative to Eq. 4.10, does not use a fixed number of scattering sampling direction, but instead it defines a 2-rank symmetric scattering tensor **T [Gao2019]**. We can write $D(x,y)$ with the same formalism of Eq. 4.10.

$$D(x,y) = \exp\left[-\int (\mathbf{s}\times\mathbf{t})^T\cdot\mathbf{T}(z)(\mathbf{s}\times\mathbf{t})\,dz\right], \tag{4.11}$$

where

$$\mathbf{T} = \begin{bmatrix} T_{xx}(z) & T_{xy}(z) & T_{xz}(z) \\ T_{xy}(z) & T_{yy}(z) & T_{yz}(z) \\ T_{xz}(z) & T_{yz}(z) & T_{zz}(z) \end{bmatrix} \tag{4.12}$$

Both models assume that the local scattering distribution is modelled as an ellipsoid. It is also possible to model the scattering distribution using spherical harmonics **[Liebi2015]**. However, this model is beyond the scope of this PhD project.

To find the scattering tensor, we can build a system of linear equation, solvable using iterative solvers, like least squares (LS) or conjugate gradients (CG).

A non-iterative approach for tensor tomography was recently presented **[Kim2022]**. The suggested filtered back-projection method is based on algebraic filters and enables rapid tensor tomographic reconstructions (Fig. 4.3). The measured scattering signal $p_{m\gamma}$ is the measured scattering signal with measurement index m and sensitivity angle index γ:

$$p_{m\gamma} = -ln(D_{m\gamma}) = \sum_\alpha v_{m\gamma\alpha}\int_{L_m}\mu(\mathbf{x})d\mathbf{x} = \sum_\alpha v_{m\gamma\alpha}\int_{\mathbb{R}}\mu_\alpha(x_m+q_{lm})dq. \tag{4.13}$$

The scalar term $v_{m\gamma\alpha}$ is the weight factor of Eq. 4.10. To reconstruct μ_α, the squared magnitude of the scattering vector $\hat{e}_\alpha$ along the sampling channel α, the iterative reconstruction in **[Kim2020]** can be approximated by a filtered back- projection (FBP) with a precalculated algebraic filter:

$$\mu_\alpha = \bar{\mathbf{W}}^T\mathbf{H}_{\mathbf{q}_\alpha}\mathbf{p}. \tag{4.14}$$

In Eq. 4.14 the matrix $\mathbf{W}$ represents the discrete beam path integral operation, $\mathbf{H}_{\mathbf{q}_\alpha}$ is the convolution matrix of the algebraic filter $\mathbf{q}_\alpha$. The entire volume can be expressed as the back-projection of the convolution of $\mathbf{q}_\alpha$ with the measurement vector p.

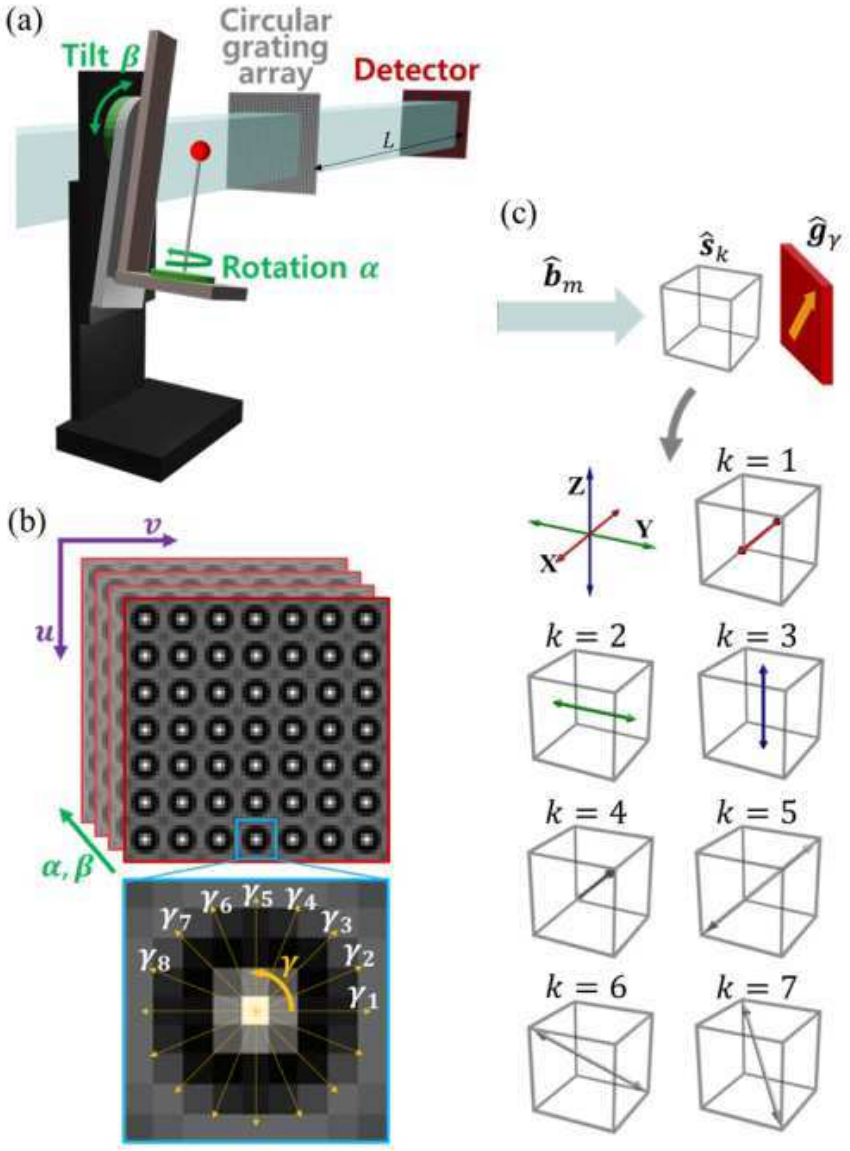

Figure 4.3: (a) An outline of the setup of X-ray scattering tensor tomography. The X-rays are diffracted by a circular grating array and form (b) a circular pattern at the detector stage. The directional scattering signal is extracted along the sensitivity vectors. In (c) the seven scattering sampling direction channels are shown **[Kim2022]**. Image reproduced from **[Kim2022]**.

5 SPECKLE-BASED DARK-FIELD DAMAGE DETECTION IN CFRP

In this chapter we detect Barely Visible Impact Damage in composite materials, particularly carbon fibre reinforced plastics (CFRPs), using modulation-based dark-field imaging with a sandpaper diffuser. We demonstrate the capability of speckle-based dark-field imaging to detect these critical failure mechanisms in CFRPs, offering a valuable tool for non-destructive testing of composite structures. This chapter was done in collaboration with Gregor Borstnar, Mark Mavrogordato, Ian Sinclair and Mark Spearing of Southampton University, who provided the samples. The project and the analysis of the results were supervised by Ronan Smith.

5.1 INTRODUCTION

The term "composite material" refers to any material made from multiple component materials to enhance its mechanical properties. Among these, carbon fibre reinforced plastics (CFRPs) consist of carbon fibres ($5 - 7\,\mu m$ radius) embedded in an epoxy-based matrix **[Soutis2005; Huang2009]**. Various forms of CFRPs exist: different layers with unidirectional fibres, two- and three-dimensional woven layups, and materials with short/discontinuous fibres of varying degrees of alignment. The applications of these materials are countless in the automotive, construction, aerospace, and biomedical industries.

While manufacturing CFRPs, different defects may occur, such as porosity, fibre waviness and wrinkling, and delamination **[Chen2022]**. In addition, throughout their life cycle, CFRPs may potentially suffer damage, for instance from impacts. As a consequence, the mechanical properties of the CFRP laminated panels can experience a significant degradation, often without leaving visible signs on the surface. This type of damage is known as Barely Visible Impact Damage (BVID) **[Richardson1996]**. BVID is the result of several damage mechanisms **[Bouvet2012]** that reduce the material's strength, causing sub-surface damages. The two main damage mechanisms behind BVID are delaminations of the plies and interlaminar matrix cracks. The most common types of delamination are indicated as Mode I and Mode II (Fig. 5.1). Mode I delamination (or opening) consists in a separation of the layers, with the cracks running through the layers. On the other hand, Mode II delamination (or shearing) is induced by shear stresses pushing the layers in opposing directions relative to each other along the interface plane as a result of material bending.

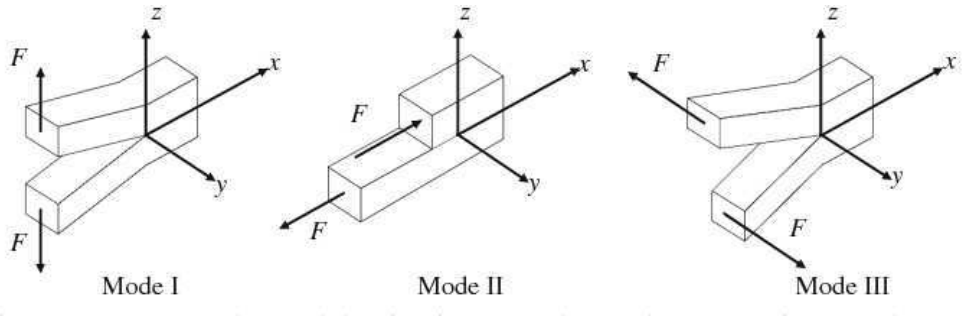

Figure 5.1: The three modes of delamination: Mode I or opening, Mode II or shearing, and Mode III or tearing. Image from **[Kormanikova2015]**.

Since delamination is one of the most common failure mechanisms in composite laminates, extensive study has been conducted to detect the damages and develop computational models. Indeed, understanding and detecting what kind of damage happened is fundamental to prevent failures in safety critical structures.

Several techniques have been used to detect BVID, such as ultrasound **[Wronkowicz2018]** and X-ray radiography **[Garcea2018]**. The latter is extensively used to detect damages in several materials. However, detecting small damages measuring only the attenuation of the X-ray beam on a large sample can be hard, especially for a BVID that extends in the beam direction. X-ray micro-computed tomography (µ-CT) can overcome the limitations of X-ray radiography. Nevertheless, the majority of CFRPs that undergo non-destructive testing are large, plate-like objects. For these object, the µ-CT is not suitable, since many artefacts form when the sharp edges of the sample align with the beam **[Yu2016]**. Computed Laminography (CL) overcomes this problem by tilting the sample towards the beam **[Helfen2007]** and it is thus often used to evaluate cracking in CFRP plates **[Moffat2010]**.

Compared to CL, X-ray radiography has the advantage of being much faster both in the acquisition and in the analysis. If attenuation signal is often not sufficient for the detection of BVID, dark-field signal can be exploited. Different studies have shown the feasibility of damage detection using dark-field imaging, using a Talbot-Lau interferometer **[Senck2018; Rus2020]** or an Edge-Illumination system **[Endrizzi2015; Shoukroun2022]**. The surfaces and voids created by delaminations and matrix cracks interact with X-rays in different ways, due to their different orientations and geometries, producing distinct dark-field signals.

In this chapter, we present the results obtained using speckle-based dark-field signal to study both the delamination of the plies and the matrix cracking.

5.2 EXPERIMENTAL SETUP AND DATA ACQUISITION

5.2.1 Sample preparation

Two samples have been realised for this study by Solvay (Belgium) by adding particles to the matrix to modify the damage processes observed in BVID **[Bull2014]**. The first sample was meant to have more matrix cracking, therefore we will refer to it as matrix-cracking sample, and the other to have delamination as the primary damage mechanism, from now on the delamination sample. The samples were manufactured utilizing a 24 ply layup with a $[45/0/-45/90]_{3s}$ stacking sequence, in compliance with ASTM D7137M requirements. The cured composite sheet had a thickness of $4.5\,\text{mm} \pm 0.2\,\text{mm}$. The coupons were waterjet cut and end-mill finished into $150\,\text{mm} \times 100\,\text{mm}$ sections. Two types of secondary phase thermoplastic particles, comprising 13% of the pre-cure weight of the interlayer, were dispersed in the interlayers. Both materials used the same base epoxy resin and intermediate modulus carbon fibre. To induce the necessary damage for imaging, the samples were placed over a $125\,\text{mm} \times 75\,\text{mm}$ window and subjected to a quasi-static impact. Both were indented to a depth of 4 mm by using an indenter with a radius of 8 mm.

5.2.2 Experimental setup

Dark-field radiography was performed at the ID19-ESRF beamline. An outline of the experimental setup is shown in Fig. 5.2. We used a polychromatic beam a with mean photon energy of 37.7 keV. As a wavefront modulator, we used a diffuser made of 6 sheets of *P*180 grit silicon-carbide sandpaper. As a detector, we used a PCO.edge sCMOS detector coupled to a Gadox scintillator and a $0.3X$ objective. The pixel size in the sample plane was 21.6 µm. The sample-diffuser distance was 1.89 m, while the sample-detector distance was 6.65 m. We used a sample-stepping acquisition procedure, stepping the sample through the beam with 5 ms exposure time. For each sample position, 50 images were averaged to reduce noise. The total FOV encompassing all the 560 frames was $122\,\text{mm} \times 137\,\text{mm}$, where the FOV of each overlapping frame was $41.6\,\text{mm} \times 7.99\,\text{mm}$.

Synchrotron-based computed laminography at the ID19-ESRF beamline has been used to validate the results. We used a polychromatic beam with a mean energy of 19 keV. The pixel size was 1.4 µm in the sample plane, and the field of view (FOV) was $2.8\,\text{mm} \times 2.8\,\text{mm}$. We acquired 2400 projections with an exposure time of 100 ms. For each sample, we acquired four scans, giving reconstructed volumes of $7.6\,\text{mm} \times 2.0\,\text{mm} \times 1.0\,\text{mm}$.

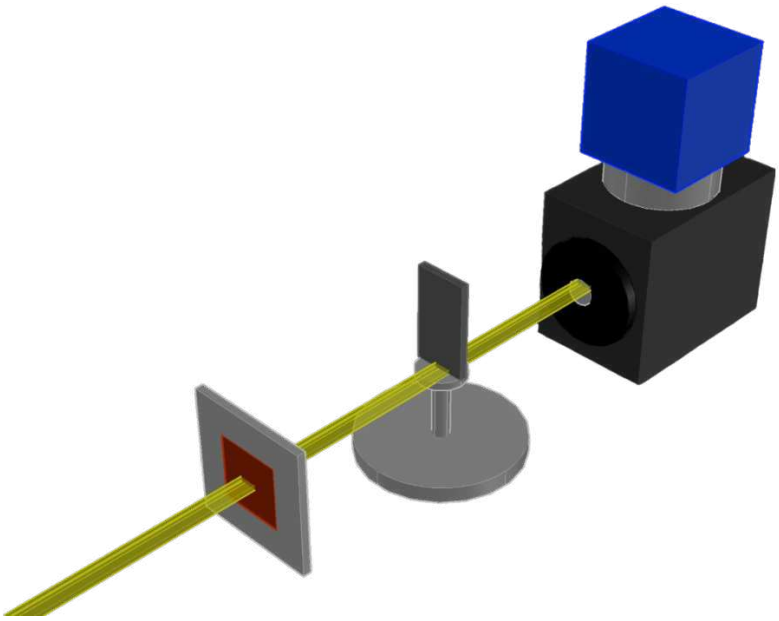

Figure 5.2: Schematic overview of the experimental setup. The X-ray beam is modulated by a diffuser mounted on a scanning stage upstream of the rotator. The detector system consists of a sCMOS camera with an X-ray microscope.

5.3 ANALYSIS OF THE RESULTS

We analysed the radiographs using UMPA algorithm with an analysis window of 7×7 pixels. We used a mask made of dark-corrected flats in UMPA, instead of simply flat-correcting the images before performing the analysis. This expedient guaranteed a better quality in the reconstructed images, due to instabilities in the flat images. The positions of the diffuser and sample motors were optimised using cross-correlation to avoid artefacts due to motors instabilities. We extracted and compared both transmission and dark field from UMPA and validated the results using CL segmentations performed by Gregor Borstnar.

Fig. 5.3 shows the matrix-cracking sample. Fig. 5.3a shows the transmission of the sample, placed on an aluminium holder, with the crack area highlighted in the green region of interest (ROI) and shown in Fig. 5.3c. By looking at the transmission image, it is difficult to identify the extent of the damage. On the other hand, in Fig. 5.3b and in the ROI in Fig. 5.3d, the dark-field images show the extent of the matrix-cracking damage. From the dark-field images, it is therefore possible to recognise that the matrix-cracking sample has a crack-like failure under the indentation site, with several cracks propagating from it. The results were validated with CL. The yellow ROIs in Fig. 5.3c-d show the regions where the segmentation of CL volumes was performed. From the segmented volume in Fig. 5.3e, it is possible to recognise different matrix cracks, caused by an increased toughness. On the left-hand side of the volume, the matrix cracks are more numerous, since this region is closer to the impact site.

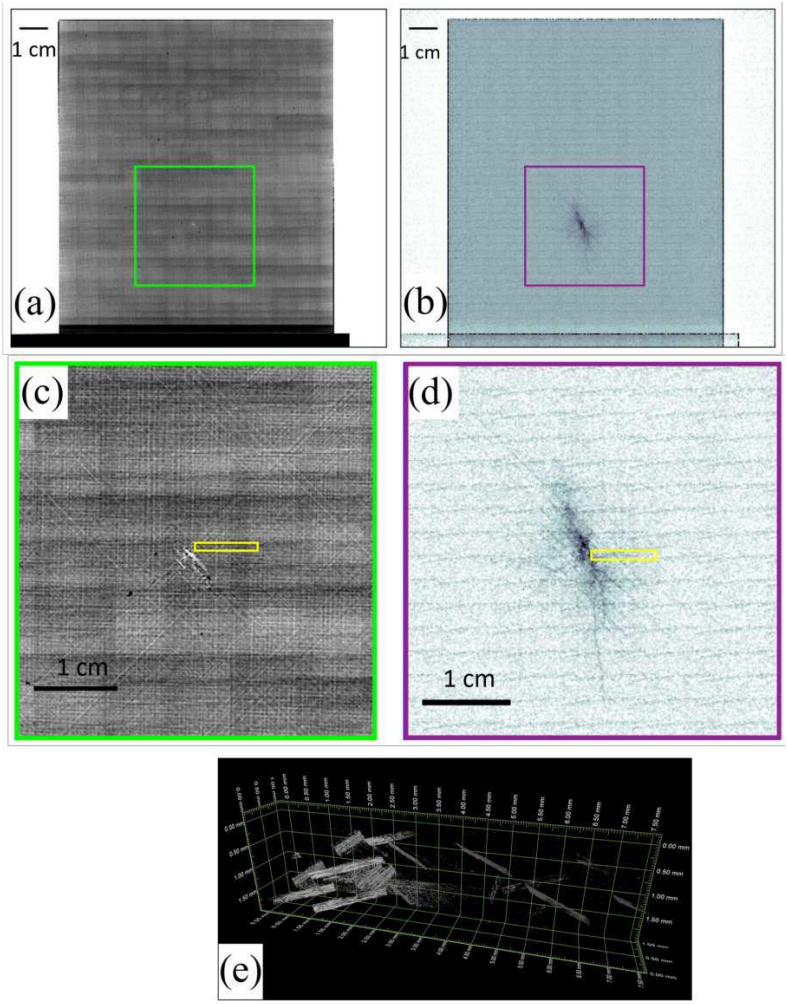

Figure 5.3: Radiographs of the matrix-cracking sample. In (a) a transmission radiograph of the whole sample and in (c) a ROI in the damaged area. In (b) a dark-field radiograph of the whole sample and in (d) a ROI in the damaged area. In (e) the segmented laminography volume performed in the yellow region. The segmentation was performed by Gregor Borstnar.

Fig. 5.4 shows the delamination sample. Fig. 5.4a shows a transmission radiograph of a ROI in the damaged area of the sample, while Fig. 5.4b shows a dark-field radiograph in the same region. Even more clearly than before, the dark-field radiograph allows a visual inspection of the damage, which is not possible only by looking at the transmission radiograph. Figure 5.4c shows the segmentation for the delamination sample, where the segmented damage is following two planes corresponding to the region where plies meet. In this sample, the main damage mechanism is clearly delamination. However, a matrix crack is also visible in the left-hand side of the lower delamination layer. This crack may also be one of the cracks visible in Fig. 5.4b.

In both transmission and dark field images, horizontal and vertical faint lines are visible. These lines are caused by variations in the X-ray beam's intensity across the various frames that were used to produce the final images. Since the beam location on the detector was also fluctuating, any intensity correction was unfruitful. The lines are not periodic, so a Fourier correction

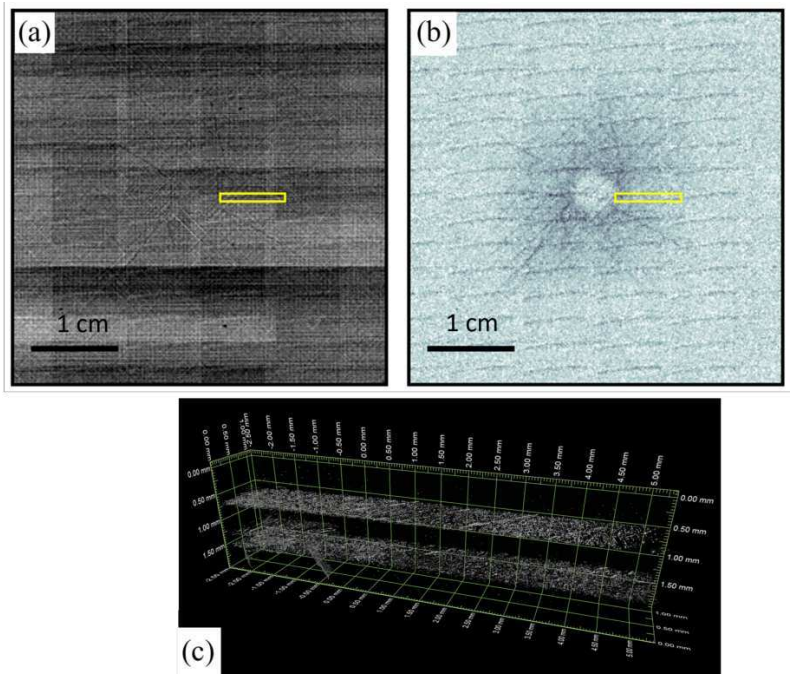

Figure 5.4: Radiographs of the delamination sample. In (a) a transmission radiograph of a ROI in the damaged area of the sample. In (b) a dark-field radiograph of ROI in the damaged area of the sample. In (c) the segmented laminography volume performed in the yellow region. The segmentation was performed by Gregor Borstnar.

was also not useful. To perform an automatic threshold segmentation using only dark-field radiographs, we removed the lines by subtracting a region without the damage to the image. In Fig. 5.5 a comparison of the dark-field radiograph of the matrix-cracking sample before and after the correction (Fig. 5.5a-b) and a triangular segmentation before and after the correction (Fig. 5.5c-d). This segmentation can be performed directly on the dark-field radiographs, allowing a fast and reliable way of detecting damages in CFRP materials.

5.4 CONCLUSIONS

In conclusion, we have shown that by using dark-field radiography, it is possible to visualise barely visible impact damage on CFRP materials. We analysed two samples, one with mostly matrix-cracking damage, and the other with delamination as the primary damage mechanism. In both cases, the transmission radiographs showed almost no sign of damage except for the impact point, while in the dark-field radiographs, the damage was easily recognisable. This study is the first demonstration of visualizing barely visible impact damage using speckle-based dark-field imaging. By using the UMPA algorithm and its ability to combine frames taken with the sample in various positions into a single image, the FOV is limited only by the range

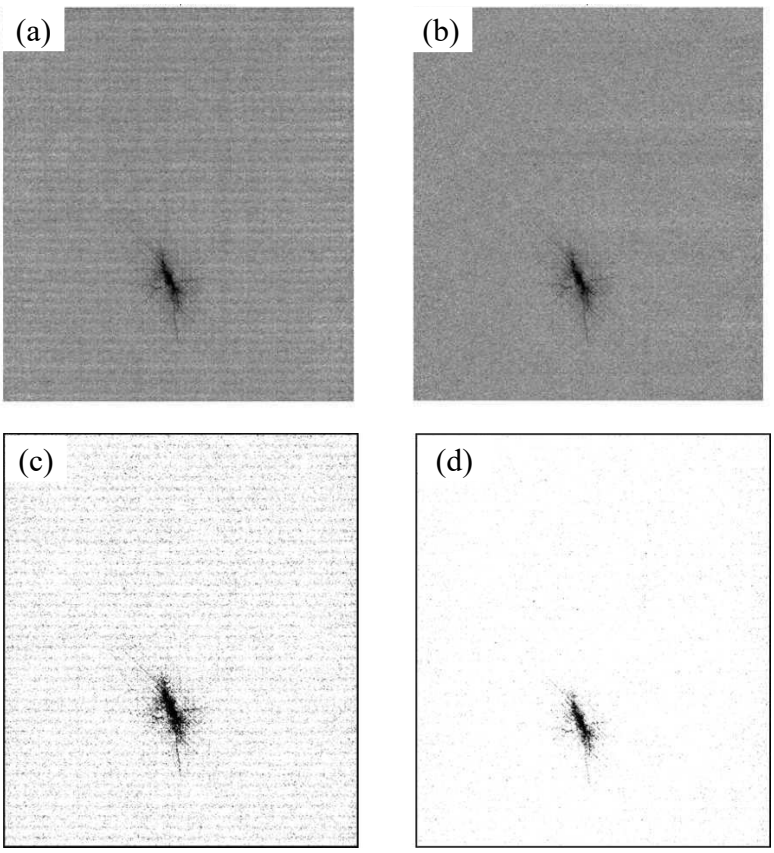

Figure 5.5: Dark-field radiograph of the matrix-cracking sample (a) before and (b) after the correction. (c) A triangular segmentation before and (d) after the correction.

of travel on the sample motors. In the future, this analysis could become a routine in the laboratory for fast non-destructive testing.

6 A MULTIMODAL X-RAY TOMOGRAPHY STUDY FOR THE EVALUATION OF THE MICROSTRUCTURAL CHANGES IN BIOLOGICAL TISSUES

This chapter explores advanced imaging techniques for studying biological tissues at the sub-micrometer scale, focusing on phase-contrast methods like modulation-based imaging (MBI) and propagation-based imaging (PBI). A multimodal study on ovarian tissues provides insights into microstructural changes during follicular maturation and after cryopreservation (vitrification), which is crucial for advancing reproductive technologies like ovarian tissue cryopreservation. Additionally, the chapter explores hepatic tissue imaging to reveal lipid aggregate distribution in the liver, providing valuable insights for diagnosing conditions like steatosis. This chapter was done in collaboration with Lorella Pascolo and Giuseppe Ricci from IRCCS Burlo Garofalo, who provided the samples. It includes segmentation work from the Erasmus+ Traineeship project of Michèle-Louise Regner, who was supervised by Ginevra Lautizi as part of this thesis.

6.1 INTRODUCTION

When it comes to biological tissues, the sub-µm length scale plays a fundamental role in understanding tissue changes, whether it is caused by tumours or other organ-specific pathologies. Revealing the microstructures in human and animal tissues requires imaging methods with high spatial resolution and high contrast for soft tissue. The current biomedical standard is conventional histology. However, reconstructing a 3D volume of the sample is time-consuming, and the reconstruction is affected by artefacts due to sample preparation and sectioning **[Ourselin2001; Pichat2018]**. To overcome these problems, X-ray absorption-based µ-CT is widely employed. However, the contrast in absorption is typically too low for biomedical applications, particularly for soft tissue discrimination and vessel visualisation **[Muller2018; Hlushchuk2018]**, requiring contrast agents that may alter tissue structure and are incompatible with other imaging techniques. Alternative X-ray techniques are based on the extraction of phase-contrast signal, employing refraction as a contrast mechanism to detect small density differences in unstained soft tissues.

Among these, modulation-based imaging (MBI) has recently seen increased interest, combining high signal sensitivity with a simple experimental im-

plementation (see chapter 3). MBI is particularly suitable for biological soft tissues, where small density differences in the specimen are highlighted thanks to the differential-phase signal, enabling a higher contrast compared to absorption imaging without the need for a contrast agent. In addition, MBI provides information about small-angle scattering, known as dark field. With the dark-field signal, it is possible both to improve the visualisation of sub-resolution microstructure alterations and to quantitatively detect the orientation of anisotropic structures.

In this chapter, we show the results obtained using both MBI and PBI methods on unstained biological samples, showing similar results and providing supplementary information for distinguishing tissues.

6.2 BOVINE OVARY

6.2.1 Motivation

In this section, we show a multimodal study on ovarian tissues for a deeper understanding of the local changes in the microstructures during follicular maturations as well as those resulting from a cryopreservation procedure (vitrification). An enhanced understanding of the ovary's architecture is critical to supporting developments in reproductive technology such as ovarian tissue cryopreservation to preserve fertility. There is no complete agreement on an optimal protocol for cryopreservation **[Boccaccio2012; Pascolo2018; Gianoncelli2023]**. Therefore, identifying which freezing procedure better preserves tissue integrity is important in order to allow proper revascularization after transplantation. The effectiveness of transplantation and subsequent fertilization heavily relies on the integrity of the tissues and on proper revascularization after cryopreservation.

Studying ovarian tissues with a combination of high-resolution propagation-based imaging (PBI) and modulation-based imaging (MBI) without the need for a contrast agent, we may gain insightful knowledge on follicle position and dynamics in various circumstances, such as ageing, pathologies, and hormone/drug administration. We could also help to improve the setting of clinical cryopreservation protocols. The findings in this field would find application to improve fertility preservation procedures, particularly for young women and prepubertal girls at risk of infertility due to chemotherapeutic treatments.

6.2.2 Sample preparation

The human tissues used for analyses at ESRF in Grenoble in the frame of the collaboration "Synchrotron-based microscopy at ESRF to unravel is-

sues of reproductive medicine and environmental toxicology" are obtained from bovine ovaries. The tissue was embedded into a paraffin block after an ethanol-dehydration series at the Institute for Child and Maternal Health–IRCCS Burlo Garofolo of Trieste.

6.2.3 Experimental setup and data acquisition

We scanned previously frozen bovine ovary samples both with synchrotron light at ESRF and with a high-brilliance microfocus liquid-metal-jet X-ray source.

The experiment with synchrotron light was performed at the beamline ID19 of the European Synchrotron Radiation Facility (ESRF). An outline of the experimental setup is shown in Fig. 6.1. To compare the tissue structure at different length scales, the specimens were scanned using two configurations: one at medium spatial resolution (MR) for MBI, and another at high spatial resolution (HR) for PBI.

For the HR setup, we used the U17 single-harmonic undulator in combination with 0.7 mm of aluminium to generate an X-ray beam with a mean energy of 19 keV. As a detector, we used a PCO.edge sCMOS detector coupled to a scintillator and a magnifying objective. The pixel size in the sample plane was 1.3 µm. The HR setup was used for PBI measurements with a propagation distance (sample-detector distance) of 0.05 m. The sample was mounted on a tomographic stage. Tomography was performed by acquiring 3000 projections over 180°. Before the scan, 10 dark images (with a closed X-ray shutter) were obtained and averaged. The flat-field was calculated by averaging 20 frames taken without the sample in the beam. The exposure time per frame was 100 ms.

For the MR setup, we used the U17 single-harmonic undulator in combination with 0.7 mm of aluminium to generate an X-ray beam with a mean energy of 26.5 keV. We used the same detector as for the HR setup, but adjusting the magnification to have a pixel size in the sample plane of 3.1 µm. The MR setup was used for MBI measurements with sandpaper (SBI). Two layers of *P*800 sandpaper were used to generate a near-field speckle pattern. The sandpaper modulator was mounted on translation stages for stepping in the plane transverse to the beam direction. The sample-modulator distance was 0.7 m, while the sample-detector distance was 0.06 m. The sample was mounted on a tomographic stage. Tomography was performed by acquiring 3000 projections over 180°. Before the scan, 10 dark images (with a closed X-ray shutter) were obtained and averaged. The flat-field was calculated by averaging 20 frames taken without the sample and the modulator in the beam. The exposure time per frame was 100 ms. This process was repeated for 20 modulator positions, which were scanned in a spiral trajectory to prevent incorrect pattern-tracking effects and grid-like visual artefacts. A reference imagine was obtained for each modulator position by averaging a series of

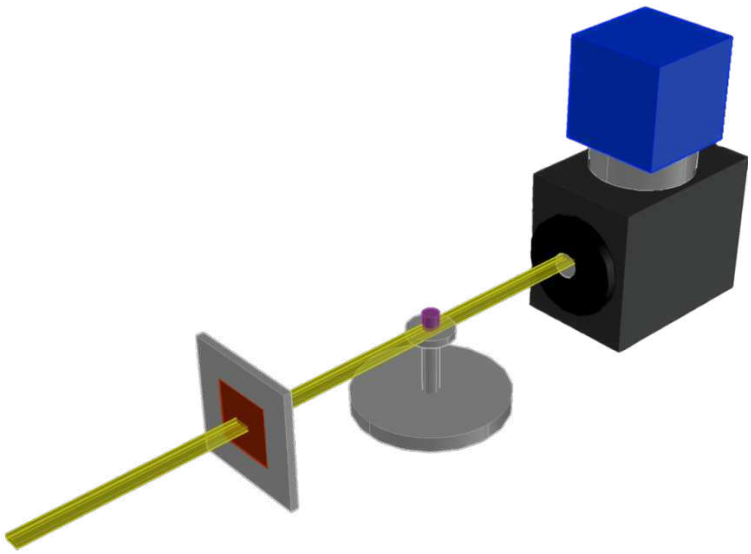

Figure 6.1: Schematic overview of the experimental setup. The X-ray beam is modulated by a diffuser mounted on a scanning stage upstream of the rotator. The detector system consists of a sCMOS camera with an X-ray microscope.

20 reference images that were acquired with the modulator in the beam but without the sample.

The experiment with a laboratory source was performed at the OPTIMATO laboratory. We will call the data analysed with this setup the LAB dataset. For the LAB dataset, X-rays were generated by a microfocal, high-brilliance liquid-metal-jet source (MetalJet D2+, Excillum, Sweden), with a maximum acceleration voltage of 160 kV, a maximum power of 250 W, and adjustable focal spot sizes ($\geq$ 15 µm). The mean energy was 24 keV. As a detector, we used an FPD (Varex Imaging's 1512 CMOS camera) with a 200 µm thick micro columnar CsI scintillator. This detector has an effective area of $145 \times 115\,\mathrm{mm}^2$ and a pixel pitch of 74.8 µm. The LAB setup was used for PBI measurements with a source-sample distance of 0.16 m and a source-detector distance of 1.5 m. The effective pixel size at this magnification was 7.98 µm. The sample was mounted on a tomographic stage. Tomography was performed by acquiring 1441 projections over 360°. Before the scan, 30 dark images (with a closed X-ray shutter) were obtained and averaged. The flat-field was calculated by averaging 20 frames taken without the sample in the beam. The exposure time per frame was 60 s.

6.2.4 Analysis of the results

HR dataset

The HR dataset, without the use of a modulator, was processed with the transport-of-intensity equation-homogeneous-sample (TIE-Hom) algorithm

[Paganin2002], assuming a constant δ/β value for the volume. The ratio δ/β was estimated, using tabulated value as $(\delta_{softtissue} - \delta_{wax})/(\beta_{softtissue} - \beta_{wax})$ **[Schoonjans2011]**. An example of one of the 3000 projections is visible in Fig. 6.2, whee the sample (soft tissue) is visible inside the paraffin (wax) block.

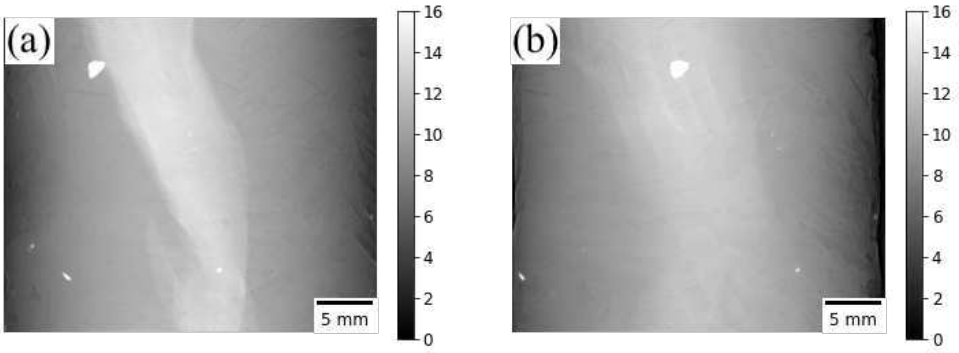

Figure 6.2: Two of the 3000 projections of the tomographic scan of a bovine ovary in paraffin with the HR setup, obtained with PBI.

While it was difficult to recognise any structure in the PBI projections, 3D information can only be obtained from the tomographic volume. Tomographic reconstructions of the projections were carried out with the FBP method from the ASTRA toolbox, after an accurate centre of rotation correction. In Fig. 6.3 three slices of the volumes are shown: axial, coronal, and sagittal, respectively. The coloured lines indicate the planes where the slices were taken. Some features of this sample, such as the corpora lutea, the follicles, and the blood vessels are visible in the slices.

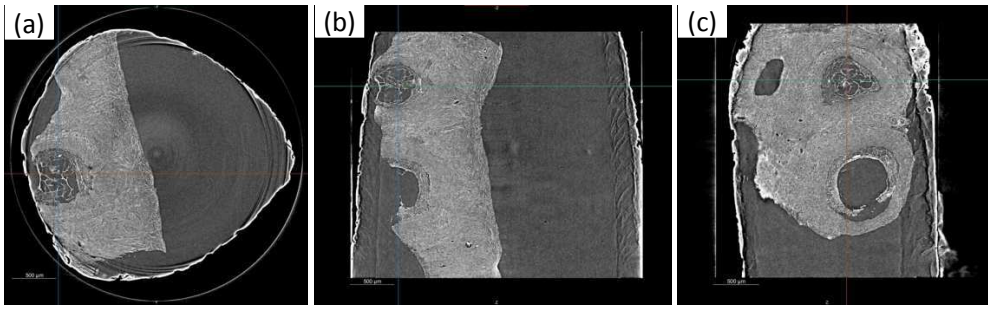

Figure 6.3: Bovine ovary volume (HR) acquired with propagation-based imaging. (a) An axial slice of the volume, (b) a coronal slice and (c) a sagittal slice. The scale bar is 500 µm.

Some additional slices through the volume are visible in Fig. 6.4. Previously observed structures can be identified, such as corpora lutea (Fig. 6.4a-b). Two other slices reveal additional features: a blood vessel (Fig. 6.4c) and several follicles (Fig. 6.4d). The blood vessels and the antrum of the follicles have a lower density and hence appear darker, while the oocytes appear lighter due to their higher density.

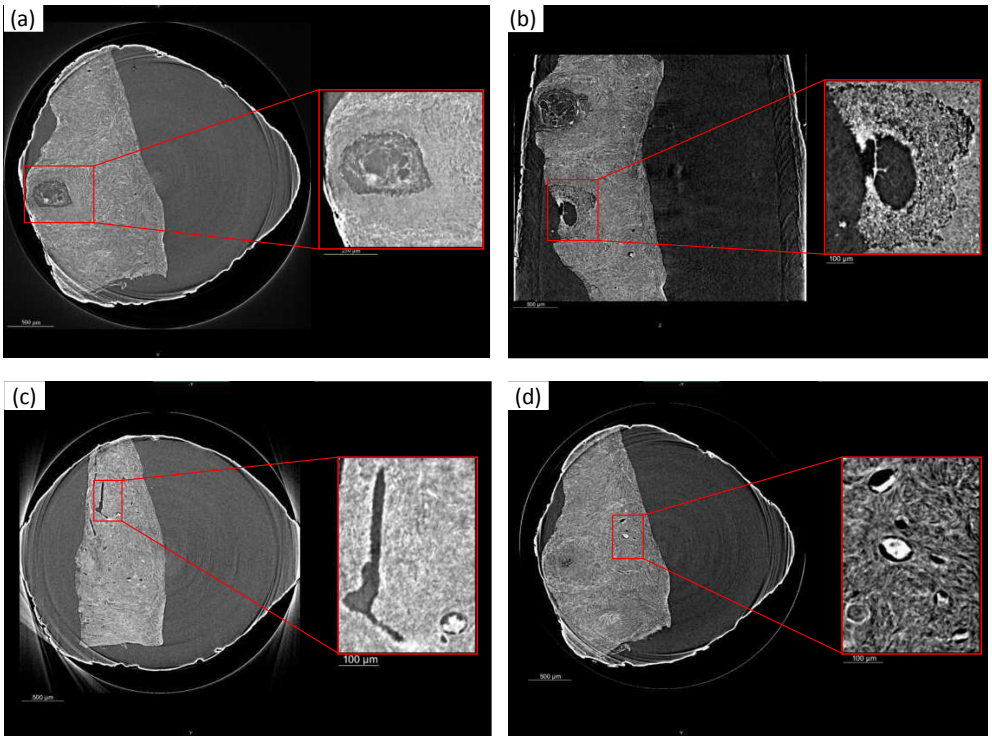

Figure 6.4: Additional slices through the bovine ovary volume (HR) acquired with propagation-based imaging. (a) An axial slice where a corpus luteum is visible, and (b) a coronal slice with a mature corpus luteum. In (c) an axial slice where a blood vessel and a small follicle are visible with high contrast. In (d) an axial slice where several follicles are visible. The scale bar of the slices is 500 µm, while the scale bar of the insets is 100 µm.

The 3D volume was downsampled by binning by two the neighbouring voxel, with a resulting voxel size of 2.6 µm. This operation lowered the volume size, accelerating the segmentation. Although the binning procedure lowered the resolution, the segmentation was still possible since the interesting features are bigger than the final pixel size.

The segmentation was done in Dragonfly ORS **[Dragonfly2022]**, mainly by hand using the segmentation wizard. Four labels were used for the segmentation: follicles (yellow), corpora lutea (orange), vessels (red) and all the rest of the soft tissue (pink). In Fig. 6.5a a ROI of the segmented volume is shown, while in Fig. 6.5b-c two axial slices are presented with superimposed the segmented features.

The segmentation helped us to visualise the structures in the bovine ovary and allowed us to perform an accurate analysis of the follicle mean diameter. In Fig. 6.6 the results of the follicle diameter analysis are shown. Fig. 6.6a shows the segmented follicles colour-coded depending on their diameter, while Fig. 6.6b shows the distribution of diameter values in the segmented follicles. The mean follicle diameter resulted to be 41.89 µm $\pm$ 15.61 µm.

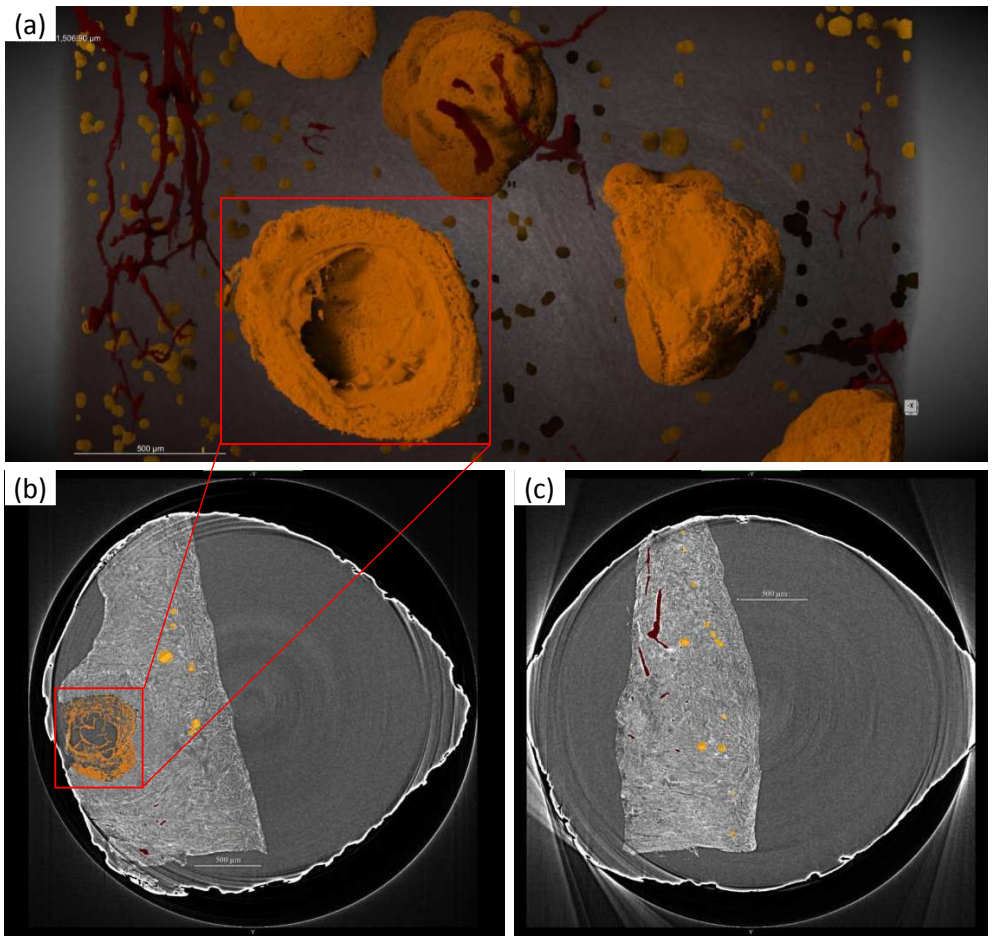

Figure 6.5: (a) A ROI of the segmented volume with follicles (yellow), corpora lutea (orange), vessels (red) and all the rest of the soft tissue (dark pink). (b) An axial slice with a corpus luteum (orange) and some follicles (yellow). (c) An axial slice with a vessel (red) and some follicles (yellow). The scale bar is 500 µm.

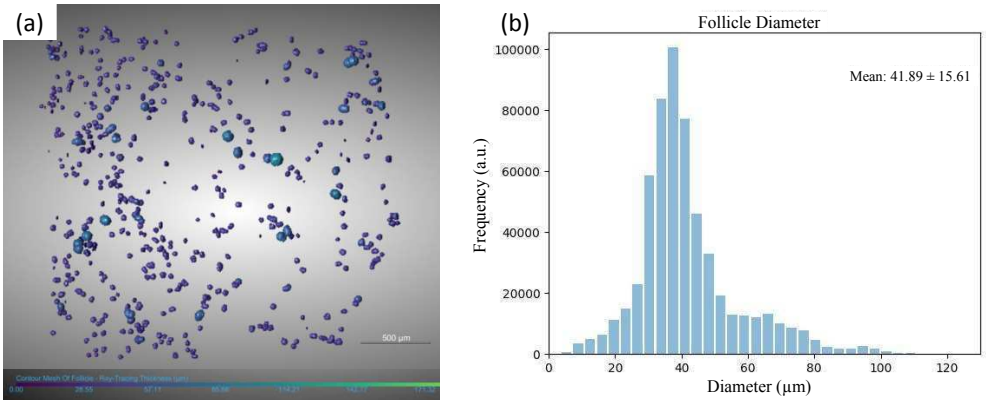

Figure 6.6: Results of the follicle diameter analysis. In (a) the segmented follicles colour-coded depending on their diameter. In (b) the distribution of diameter values in the segmented follicles. The scale bar is 500 µm.

MR dataset

PBI is the simplest experimental method for qualitatively visualising phase information. However, with MBI, the different quantitative signals add value to the biological interpretation of sample composition (e.g., attenuation coefficient, electron density, diffusion coefficient).

To obtain the 3D volumes with SBI, all sample images and reference images underwent dark- and flat-field correction. Each frame was also normalized for the beam current. Any dead and bright pixels in the corrected frames were replaced with the median values of their neighbouring pixels. We used UMPA algorithm to process the sets of 20 sample frames captured at identical angles but different modulator positions, along with the 20 reference frames taken at corresponding modulator positions. Before applying UMPA, the drifts and instabilities of the modulator were adjusted for by matching the reference speckle images to the appropriate sample images by using cross-correlation in an air region without the sample, where the two images should agree. Even though the observed displacements in this correction process were almost negligible, this correction enhanced the image quality. The images were then processed using UMPA. This processing produced the transmission, dark-field, and refraction angle signals for each projection in both the vertical and horizontal directions. An example of one of the 3000 projections is visible in Fig. 6.7. In the projections, it is difficult to distinguish between the tissue and the paraffin due to the rough surface of the paraffin block. However, it is visible that the dark-field signal is dominated by noise.

We analysed the projections using UMPA algorithm with an analysis window of 5×5 pixels. This window is a good compromise between a high spatial resolution and a low noise level in the images. The differential-phase signal from UMPA was bias-corrected **[DeMarco2023]** to reduce the bias-induced noise.

To characterize the performance of a modulator, its visibility and mean speckle size can be calculated. In Fig. 6.8 a flat-corrected reference image is shown, together with its visibility analysis. The visibility is calculated as the ratio of the standard deviation and the mean intensity value of the reference image, and the visibility map is calculated using a Gaussian filter with a kernel size equal to the analysis window used in UMPA (7 pixels in this analysis). The visibility map shown in Fig. 6.8b is not homogeneous all over the field of view, and its mean value is 11%.

In Fig. 6.9 the mean speckle size of the modulator, which is determined by calculating the full width at half maximum (FWHM) of the radial profile from the 2D auto-correlation function of a reference image. The speckle size is 3.9 pixel or 12.1 µm.

Quantitative phase images were created by integrating the differential-phase images in both horizontal and vertical directions (Fig. 6.7c-d). Before reconstructing the tomogram, we applied a ring correction to each slice's sinogram. This correction is necessary to minimize ring artefacts, which primarily result

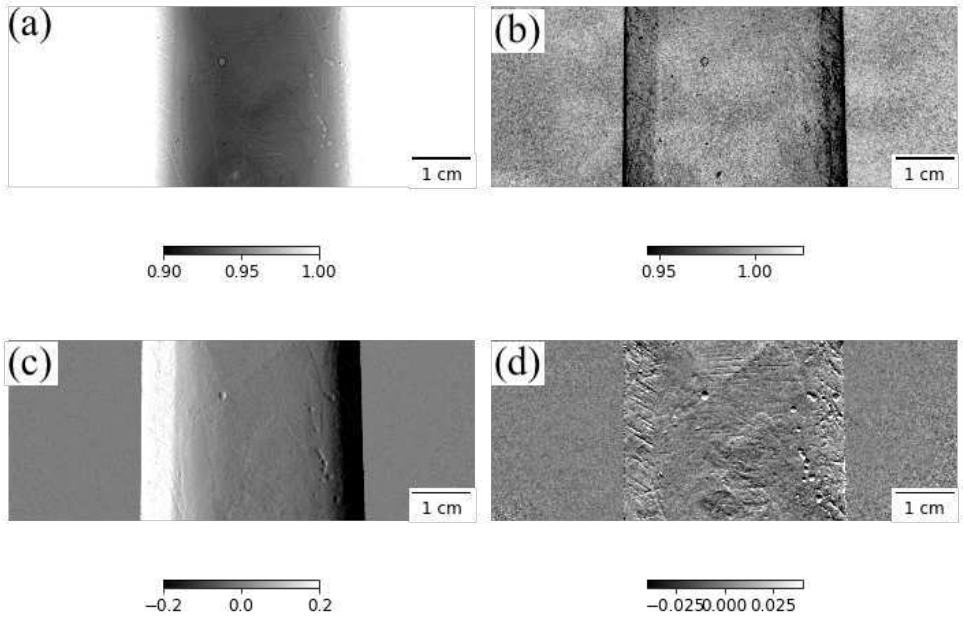

Figure 6.7: One of the 3000 projections of the tomographic scan of a bovine ovary in paraffin with the MR setup, obtained with SBI using UMPA algorithm. (a) Transmission, (b) dark-field signal and (c) the differential-phase signal in the horizontal and (d) vertical direction reported in pixels.

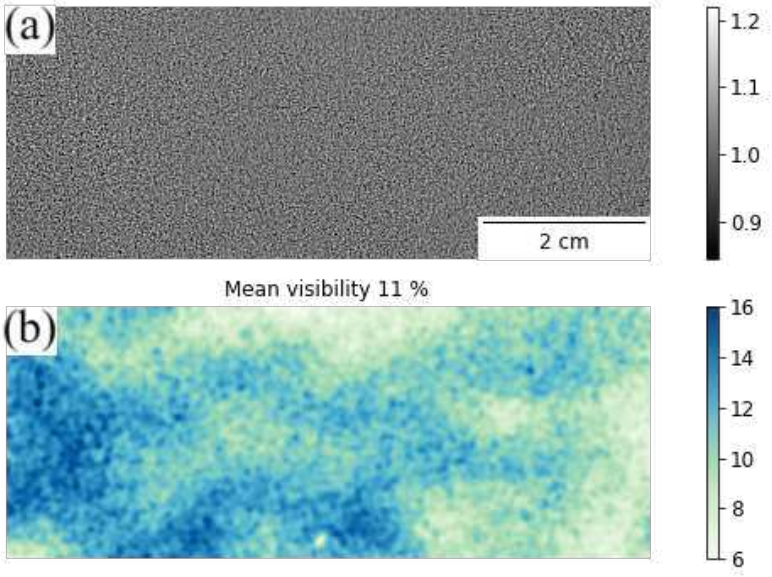

Figure 6.8: A flat-corrected reference image (a) and (b) its visibility analysis.

from scintillator defects, noise, beam instabilities, and estimation biases in the UMPA algorithm. The correction we decided to apply was a low-pass Butterworth filter. A Butterworth filter, with its smooth frequency response, is used in ring correction to suppress low-frequency ring artefacts while

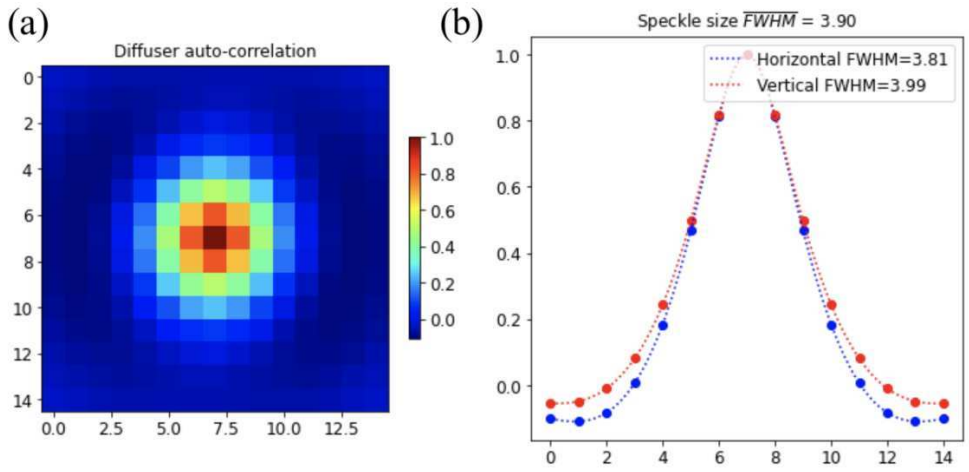

Figure 6.9: A 3D representation of the speckle size auto-correlation function in (a) and its radial profile in (b).

preserving important structural details. Tomographic reconstructions using phase and transmission projections were carried out with the FBP method from the ASTRA toolbox.

The phase volume shows the distribution of the refractive index decrement δ. In Fig. 6.10 three slices of the phase volume are shown: axial, coronal, and sagittal, respectively. The coloured lines indicate the planes where the slices were taken. Some features of this sample, such as the corpora lutea, the follicles, and the blood vessels are visible in the slices.

Figure 6.10: Bovine ovary volume (MR) acquired with modulation-based imaging. (a) An axial slice of the volume, (b) a coronal slice and (c) a sagittal slice. The scale bar is 500 µm.

A closer look at the tissue structure of this bovine ovary sample is presented in Fig. 6.11, where some additional slices through the phase volume are shown, together with some ROIs highlighting interesting structures. Previously observed structures can be identified, such as two follicles in different maturation stages (Fig. 6.11a-d), and two blood vessels (Fig. 6.11b-c).

Comparing the same slices with the transmission volume (Fig. 6.12) by visual inspection, it is evident how the contrast between the layers is significantly lower for the transmission slices than for the corresponding phase slices.

Due to the high contrast of interesting features, the phase volume allows for an easier segmentation. The segmentation of the phase volume was done

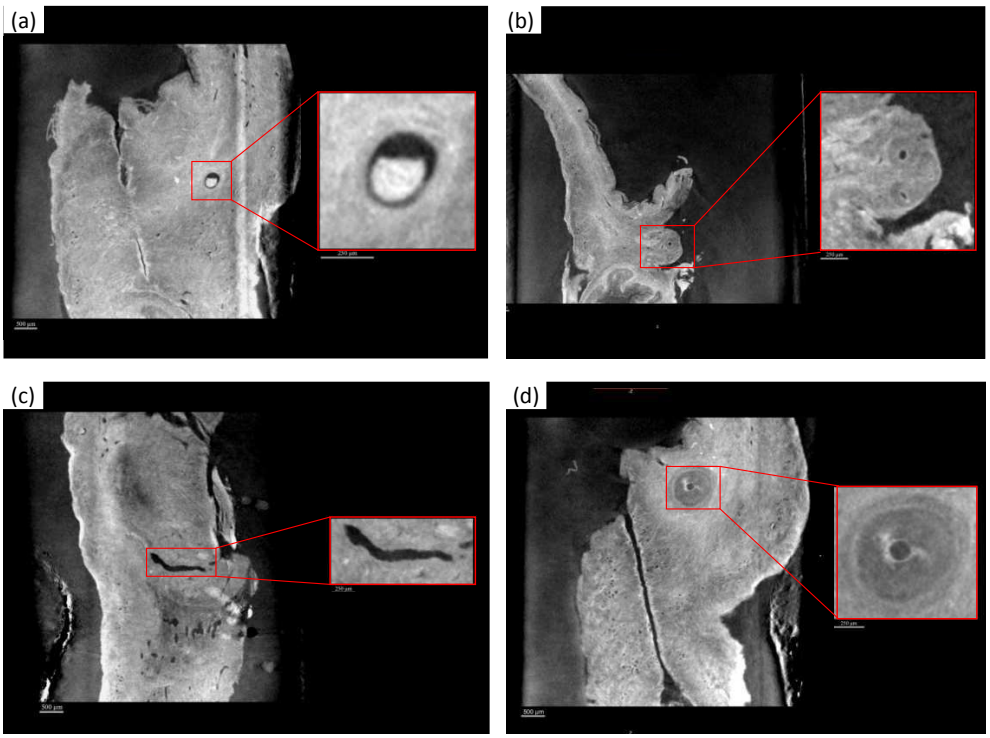

Figure 6.11: Additional slices through the bovine ovary phase volume (MR) acquired with modulation-based imaging. (a) An coronal slice where a follicle is visible, and (b) a sagittal slice with two blood vessels. In (c) a coronal slice where a blood vessel is visible with high contrast. In (d) a coronal slice where a follicle is visible. The scale bar of the slices is 500 µm, while the scale bar of the insets is 250 µm.

in Dragonfly ORS **[Dragonfly2022]**, mainly by hand using the segmentation wizard. Four labels were used for the segmentation: follicles (yellow), corpora lutea (orange), vessels (red) and all the rest of the soft tissue (pink). In Fig. 6.13 two axial slices of the segmented volume are presented with superimposed the segmented features.

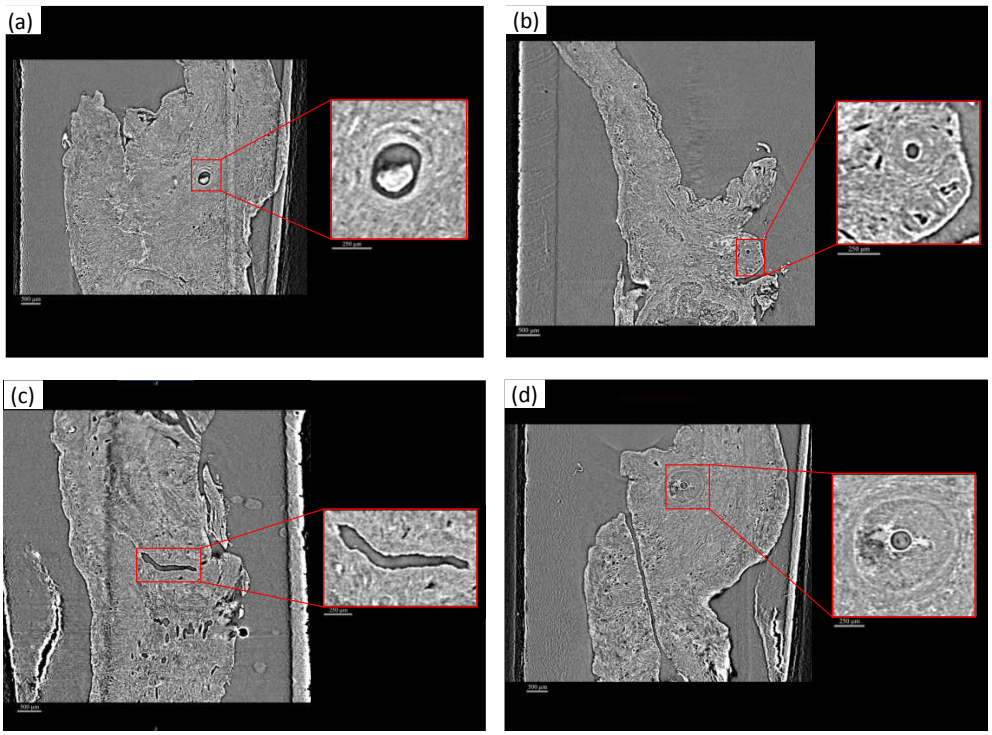

Figure 6.12: Some slices (the same of Fig. 6.11) through the transmission volume. The scale bar of the slices is 500 µm, while the scale bar of the insets is 250 µm.

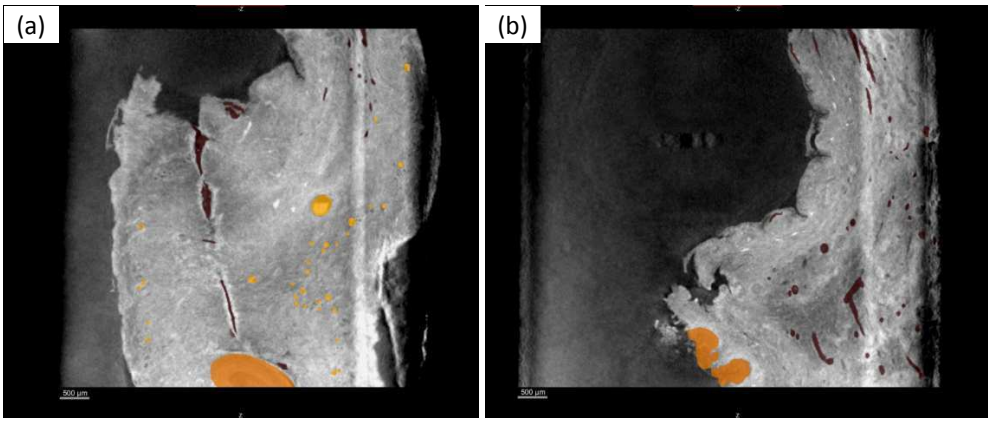

Figure 6.13: (a) A coronal slice with a corpus luteum (orange), a follicle (yellow) and some blood vessels (red). (c) A coronal slice with a vessel (red) and some corpora lutea (orange). The scale bar is 500 µm.

LAB dataset

The results reported until now were obtained using a synchrotron source. However, PBI phase tomography is being used at laboratory X-ray sources with little effort or expensive equipment.

Tomographic reconstructions of the projections were carried out with the FDK method from the TIGRE library for cone-beam geometry reconstructions, after an accurate centre of rotation correction. Before reconstructing the tomogram, we applied a ring correction (a low-pass Butterworth filter) to

each slice's sinogram. This correction is necessary to minimize ring artefacts, mainly resulting from scintillator defects, noise, and beam instabilities.

Fig. 6.14 displays three slices through the volume: axial, coronal, and sagittal. The coloured lines represent the planes from which the slices were obtained. The slices show some of the sample's characteristics, including the corpora lutea, follicles and blood arteries.

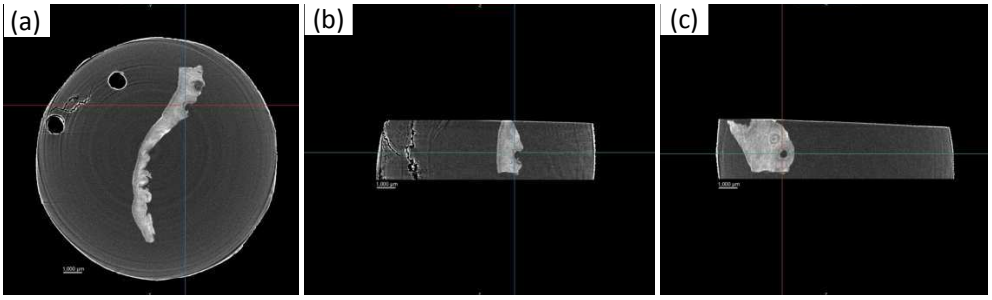

Figure 6.14: Bovine ovary volume (LAB) acquired in the laboratory with propagation-based imaging. (a) An axial slice of the volume, (b) a coronal slice and (c) a sagittal slice. The scale bar is 1 mm.

Some additional slices through the volume are visible in Fig. 6.15. Previously observed structures can be identified, such as a corpus luteum (Fig. 6.15b), two blood vessels (Fig. 6.15a) and a follicle (Fig. 6.15a).

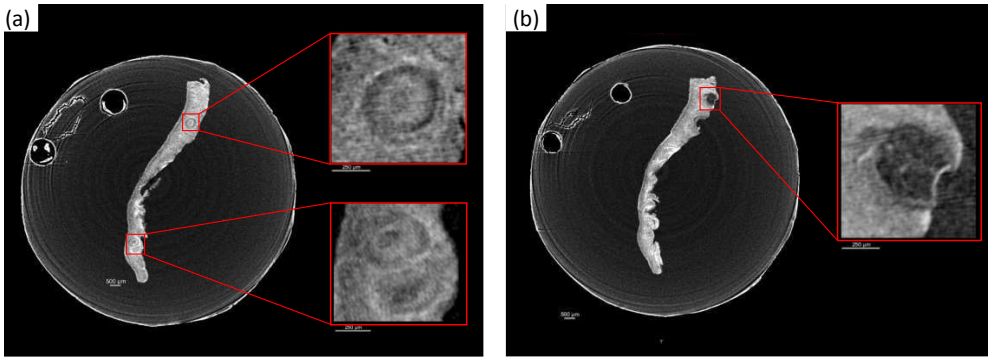

Figure 6.15: Additional slices through the bovine ovary volume (LAB) acquired in the lab with propagation-based imaging. In (a) an axial slice where a blood vessel and a follicle are visible. In (b) an axial slice with a mature corpus luteum. The scale bar of the slices is 500 µm, while the scale bar of the insets is 250 µm.

This volume was segmented using Dragonfly ORS **[Dragonfly2022]**, mainly by hand using the segmentation wizard. Four labels were used for the segmentation: follicles (yellow), corpora lutea (orange), vessels (red) and all the rest of the soft tissue (pink). In Fig. 6.16a a ROI of the segmented volume is shown, while in Fig. 6.16b-c two slices are presented with superimposed the segmented features.

Even though in the laboratory setup, the resolution is lower compared to the synchrotron scans, it was still possible to segment corpora lutea and vessels. Using a laboratory source will make the study more widely available for

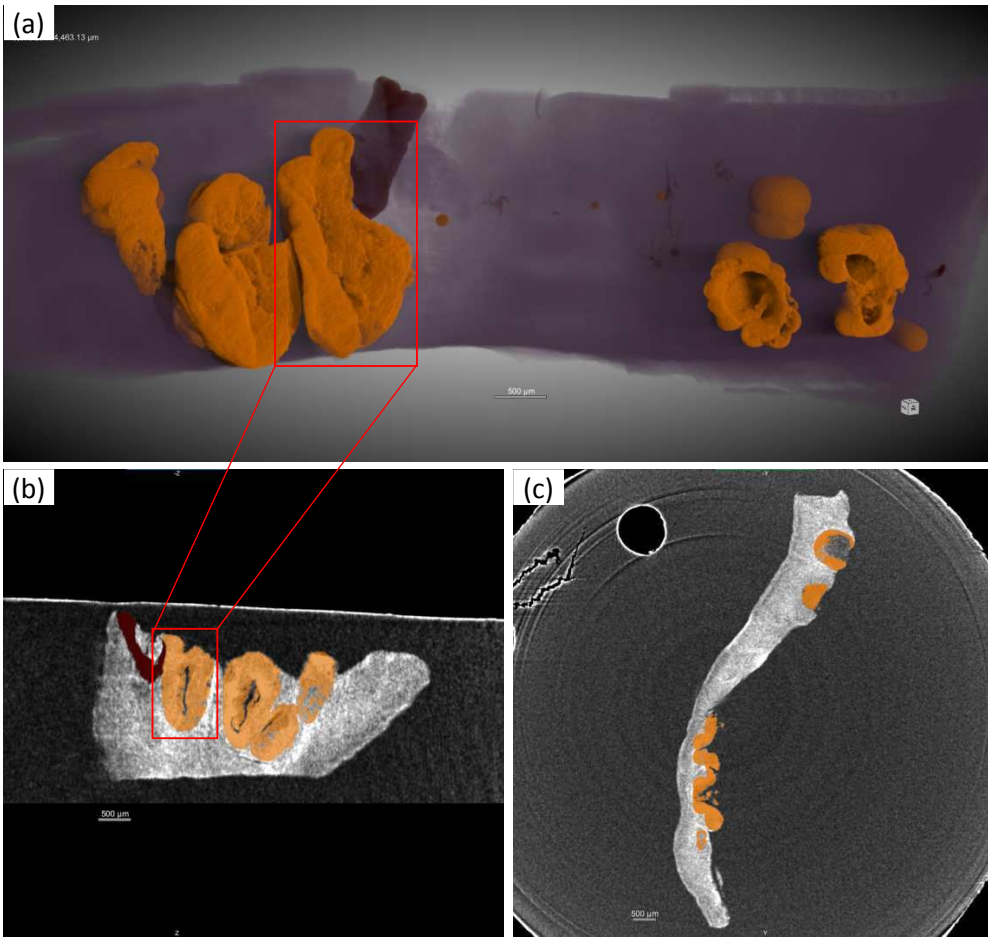

Figure 6.16: (a) A ROI of the segmented volume (LAB) with corpora lutea (orange), vessels (red) and all the rest of the soft tissue (dark pink). (b) A sagittal slice with a vessel (red) and corpora lutea (orange). (c) An axial slice with some corpora lutea (orange). The scale bar is 500 µm.

advanced clinical histopathology and research applications for a complete picture of ovary function and pathology.

6.2.5 Conclusions

As shown in this chapter, with a combined study of PBI and MBI, we were able to perform virtual histology of ovarian tissue. Using the phase tomogram, we were able to identify tissue structural information and to perform a further structural analysis on the size of various functional parts of the organ, such as the follicles. With this study, we were able to better understand the microvasculature and the anatomy of the tissues, and to reveal the effects produced by current clinical cryopreservation protocols. Therefore, we believe that the presented approach could help to unravel important aspects of microanatomy and structural changes of the ovary tissue during maturation or clinical procedures.

6.3 HUMAN LIVER

6.3.1 Motivation

In this section, we show a multimodal study on hepatic tissue for a deeper understanding of the distribution of lipidic aggregates in a human liver. Studying the hepatic tissue with a combination of high-resolution propagation-based imaging (PBI) and modulation-based imaging (MBI) without the need for a contrast agent, we may gain insightful knowledge on the lipidic aggregates position and distribution, leading to an unprecedented diagnosis of the severity of steatosis. This measurement was planned for a dark-field analysis of the sub-micrometer lipidic aggregates, however the dark-field signal was severely affected by instabilities in the beam.

6.3.2 Sample preparation

The human hepatic tissues used for analyses have been collected from a post-mortem specimen of a human liver donated to the Institute for Child and Maternal Health–IRCCS Burlo Garofolo of Trieste. The tissue was conserved in ethanol.

6.3.3 Experimental setup and data acquisition

We scanned human liver samples with synchrotron light at ESRF. The experiment with synchrotron light was performed at the beamline ID19 of the European Synchrotron Radiation Facility (ESRF). To compare the tissue structure at different length scales, the specimens were scanned using two configurations: one at medium spatial resolution (MR) for MBI, and another at high spatial resolution (HR) for PBI.

The two setups are analogous to what described in Section 6.2.3, with one difference in the HR setup: in this case, the X-ray beam had a mean energy of 26.5 keV. We opted for this higher energy to minimise damages in the human samples.

The MR setup and the way MBI images were acquired are identical to what described in Section 6.2.3. The interested reader is therefore referred to Section 6.2.3 for a detailed description of the setup and measurement conditions.

6.3.4 Analysis of the results

HR dataset

The HR dataset, without the use of a modulator, was processed with the transport-of-intensity equation-homogeneous-sample (TIE-Hom) algorithm **[Paganin2002]**, assuming a constant δ/β value for the volume. The ratio δ/β was estimated, using tabulated value as $(\delta_{softtissue} - \delta_{ethanol})/(\beta_{softtissue} - \beta_{ethanol})$ **[Schoonjans2011]**.

Tomographic reconstructions of the projections were performed using the ASTRA toolbox with the FBP approach, after an appropriate centre of rotation correction. Fig. 6.17 displays three slices of the volume: axial, coronal, and sagittal. The coloured lines represent the planes from which the slices were obtained.

Some features of this sample, such as the blood vessels and the lipidic aggregates, are visible in the slices.

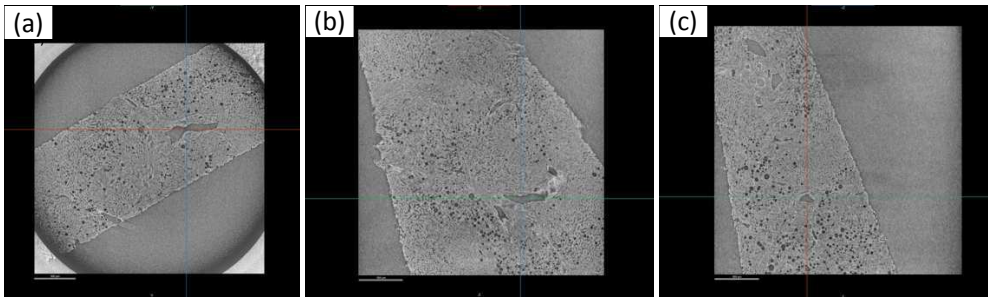

Figure 6.17: Human liver volume (HR) acquired with propagation-based imaging. (a) An axial slice of the volume, (b) a coronal slice and (c) a sagittal slice. The scale bar of the slices is 500 µm.

Figs. 6.18-6.19 show further slices of the volume. Identified structures include bile ducts (Fig. 6.18a and Fig. 6.19b-d), blood vessels (Fig. 6.18c and Fig. 6.19a) and multiple lipidic aggregates (Fig. 6.18b-d).

By binning the adjacent pixels by two, the 3D volume was downsampled, resulting in 2.6 µm voxel size. This process sped up the segmentation, by reducing the volume size. Since the important features are larger than the final pixel size, segmentation was still achievable even if the binning method reduced resolution.

The segmentation was done in Dragonfly ORS **[Dragonfly2022]**, mainly by hand using the segmentation wizard. Three labels were used for the segmentation: bile ducts (yellow), vessels (red) and lipidic aggregates (cyan). In Fig. 6.20a a ROI of the segmented volume is shown, while in Fig. 6.20b-c two axial slices are presented with superimposed the segmented features.

The segmentation helped us to visualise the structures in the human liver and allowed us to perform an accurate analysis of the lipidic aggregates mean diameter. In Fig. 6.21 the results of the lipidic aggregates diameter

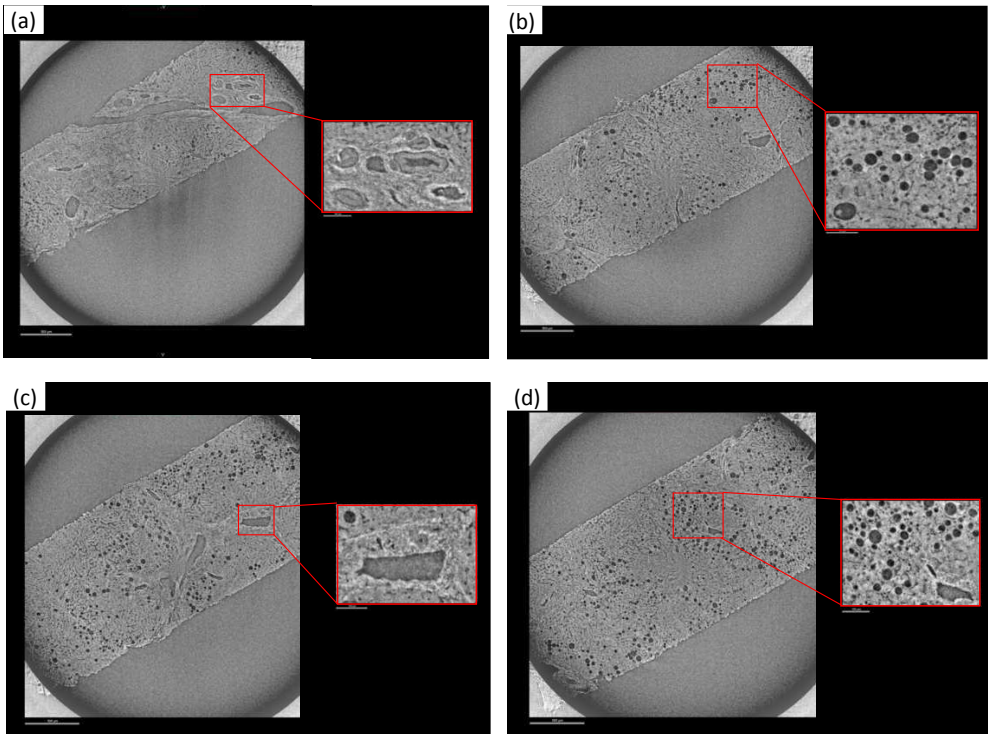

Figure 6.18: Additional axial slices through the human liver volume (HR) acquired with propagation-based imaging. In (a) a bile duct is visible, in (c) a blood vessel is visible with high contrast. In (b) and (d) several lipidic aggregates are visible. The scale bar of the slices is 500 µm, while the scale bar of the insets is 100 µm.

analysis are shown. Fig. 6.21a shows the segmented lipidic aggregates in cyan. Fig. 6.21b displays the contour of the lipidic aggregates in a single axial slice, colour-coded depending on their diameter. Fig. 6.21c shows the distribution of diameter values in the segmented lipidic aggregates. The mean lipidic aggregate diameter resulted to be 25.40 µm $\pm$ 18.25 µm.

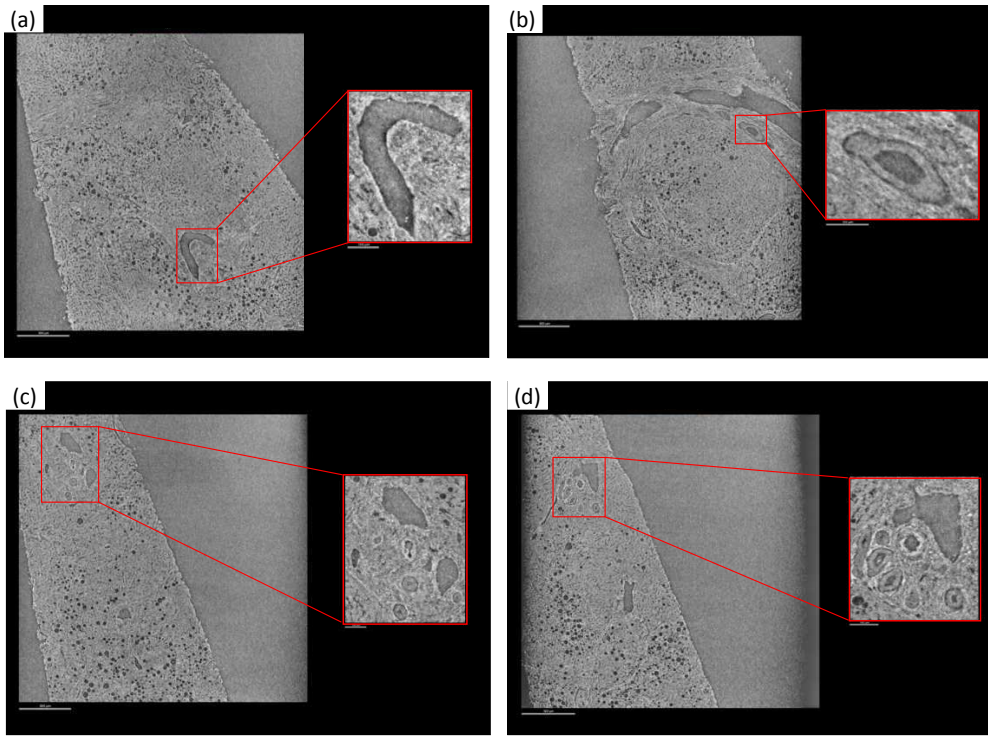

Figure 6.19: Additional coronal slices through the human liver volume (HR) acquired with propagation-based imaging. In (a) and (c) blood vessels are visible. In (b) and (d) several bile ducts are visible. The scale bar of the slices is 500 µm, while the scale bar of the insets is 100 µm.

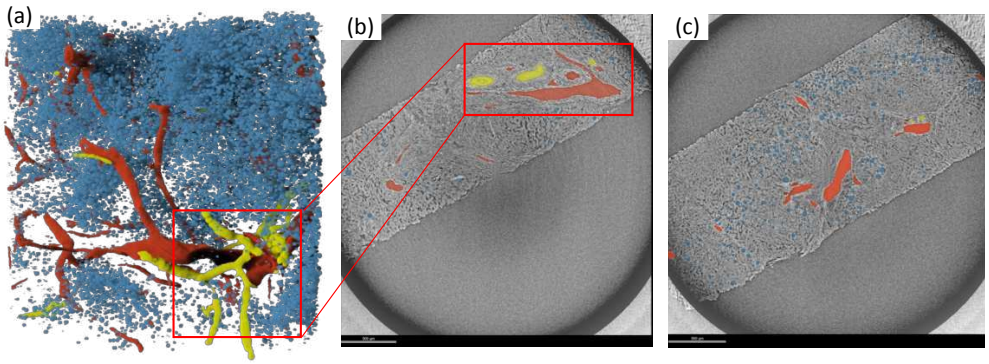

Figure 6.20: (a) A ROI of the segmented volume with bile ducts (yellow), vessels (red) and lipidic aggregates (cyan). (b) An axial slice with a blood vessel (red) and bile ducts (yellow). (c) An axial slice with some vessels (red) and some lipidic aggregates (cyan). The scale bar of the slices is 500 µm.

MR dataset

All the reference and sample images underwent flat-field and dark-field correction in order to obtain the 3D volumes with SBI. Each frame was also normalized for the beam current. Any dead and bright pixels in the corrected frames were replaced with the median values of their neighbouring pixels. We used UMPA algorithm to process the sets of 20 sample frames captured at identical angles but different modulator positions, along with the 20 reference

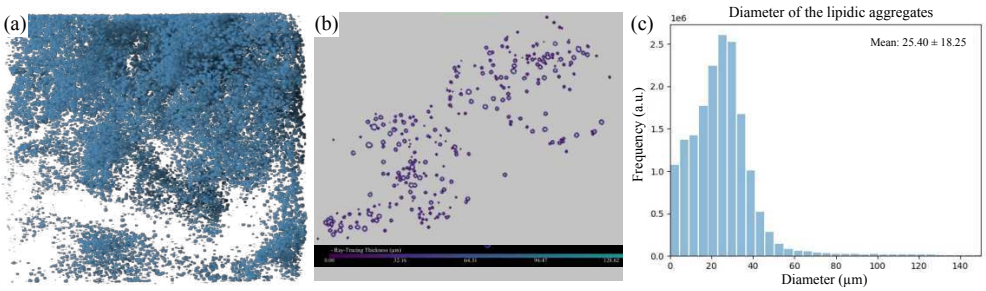

Figure 6.21: Results of the lipidic aggregate diameter analysis. In (a) the segmented lipidic aggregates in cyan. In (b) the contour of the lipidic aggregates in a single axial slice, colour-coded depending on their diameter. In (c) the distribution of diameter values in the segmented lipidic aggregates.

frames taken at corresponding modulator positions. Prior to applying UMPA, the modulator's drifts and instabilities were compensated for by employing cross-correlation in an air region, where the sample is not present, to match the reference images to the corresponding sample images, where the two images should agree. This adjustment improved the image quality. UMPA was then used to process the images. The transmission, dark-field, and refraction angle signals for each projection in both the vertical and horizontal directions were generated by this procedure. A 3000 projection example may be seen in Fig. 6.22. Nonetheless, it is evident that noise dominates the dark-field signal.

We analysed the projections using UMPA algorithm with an analysis window of 5×5 pixels. This window allows a good balance between minimal noise level and high spatial resolution in the images. To mitigate bias-induced noise, the UMPA differential-phase signal was bias-corrected **[DeMarco2023]**.

By integrating the differential-phase images in both horizontal and vertical directions, quantitative phase images were produced (Fig. 6.22c-d). We applied a low-pass Butterworth filter as ring correction to each slice's sinogram prior to reconstructing the tomogram.

Tomographic reconstructions based on phase and transmission projections were performed using the ASTRA toolbox with the FBP approach.

The phase volume shows the distribution of the refractive index decrement δ. In Fig. 6.23 three slices of the phase volume are shown: axial, coronal, and sagittal, respectively. The coloured lines indicate the planes where the slices were taken.

A closer look at the tissue structure of this human liver sample is presented in Fig. 6.24, where some additional slices through the phase volume are shown, together with some ROIs highlighting interesting structures. In Fig. 6.24a a bile duct can be identified, while in Fig. 6.24b-d two blood vessels are visible. In Fig. 6.24c the lipidic aggregates are shown in the inset.

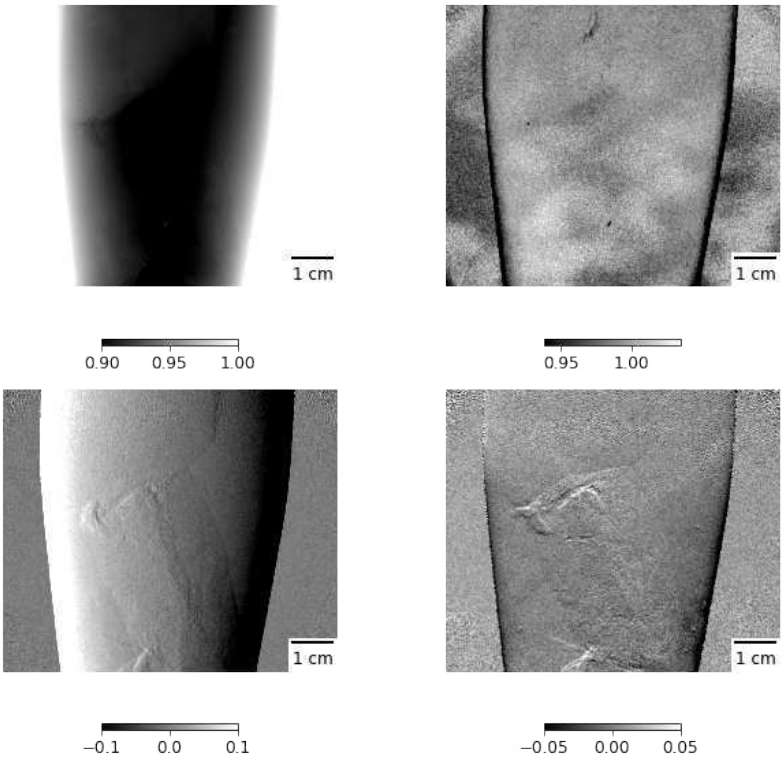

Figure 6.22: One of the 3000 projections of the tomographic scan of a human liver in ethanol with the MR setup, obtained with SBI using UMPA algorithm. (a) Transmission, (b) dark-field signal and (c) the differential-phase signal in the horizontal and (d) vertical direction reported in pixels.

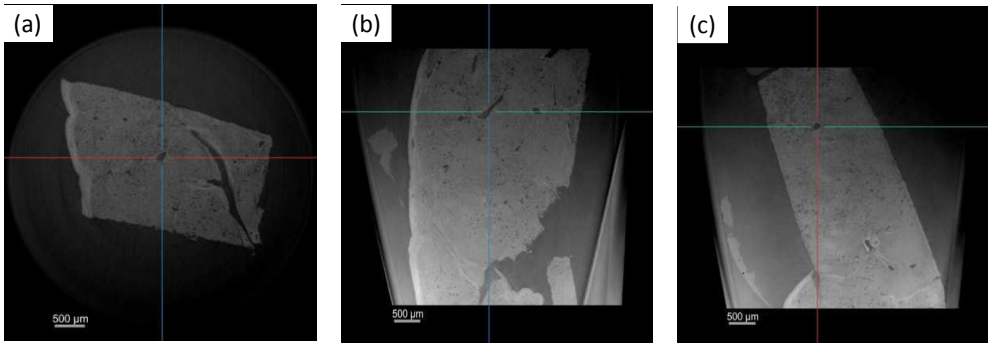

Figure 6.23: Human liver volume (MR) acquired with modulation-based imaging. (a) An axial slice of the volume, (b) a coronal slice and (c) a sagittal slice. The scale bar of the slices is 500 µm.

In Fig. 6.25 the same slices of Fig. 6.24 are shown in the transmission volume. By visual inspection, it is not easy to judge the advantage of the phase images in this specific case.

The segmentation of the phase volume was done in Dragonfly ORS **[Dragonfly2022]**, mainly by hand using the segmentation wizard. Three labels were used for the segmentation: bile ducts (yellow), vessels (red) and lipidic aggregates (cyan). In Fig. 6.26 two axial slices of the segmented volume are presented with superimposed the segmented features.

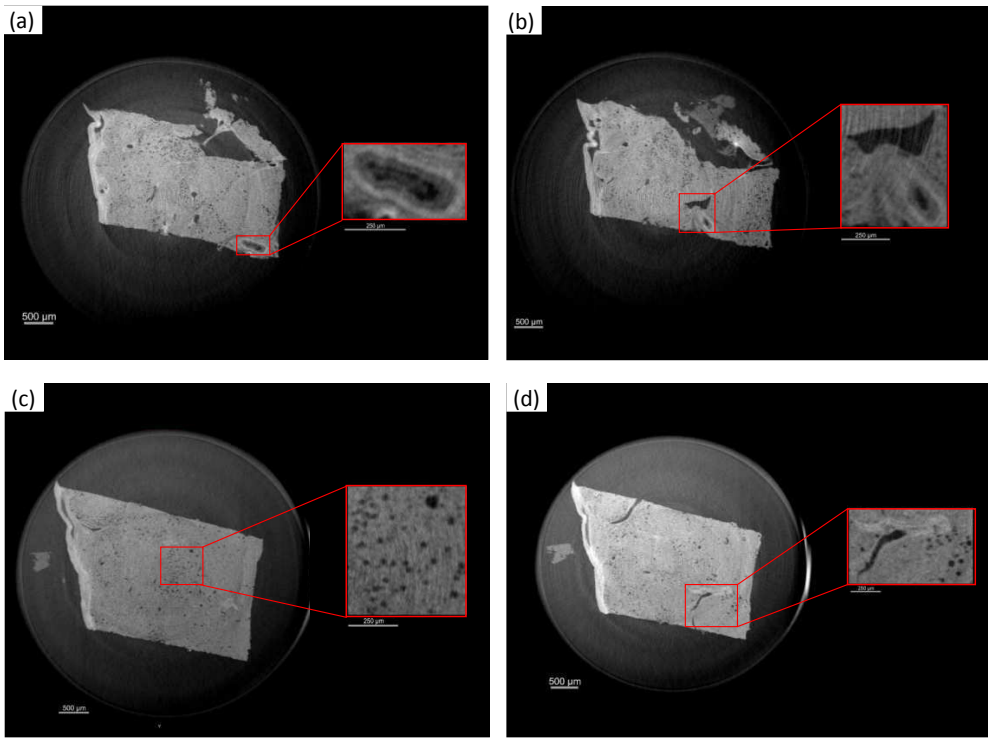

Figure 6.24: Additional axial slices through the human liver phase volume (MR) acquired with modulation-based imaging. (a) A slice where a bile duct is visible, and (b) a slice with a blood vessel and a bile duct. In (c) a slice where the lipidic aggregates are visible. In (d) a slice where a blood vessel and some lipidic aggregates are visible. The scale bar of the slices is 500 µm, while the scale bar of the insets is 250 µm.

6.3.5 Conclusions

As seen in this chapter, using a combination of PBI and MBI, we were able to perform virtual histology on hepatic tissue. Using the phase tomogram, we were able to detect tissue structural information and do further structural analysis on the size of various functional organ sections, such as lipidic aggregates. This investigation allowed us to gain a better understanding of the microvasculature and tissue architecture. As a result, we believe that this study will aid in the understanding of critical features of microanatomy and structural changes in hepatic tissue, as well as the diagnosis of the degree of steatosis. In the future, it would be interesting to try again a dark-field analysis of the sub-micrometer lipidic aggregates with a different sample and a different resolution, trying to minimise the instabilities in the beam.

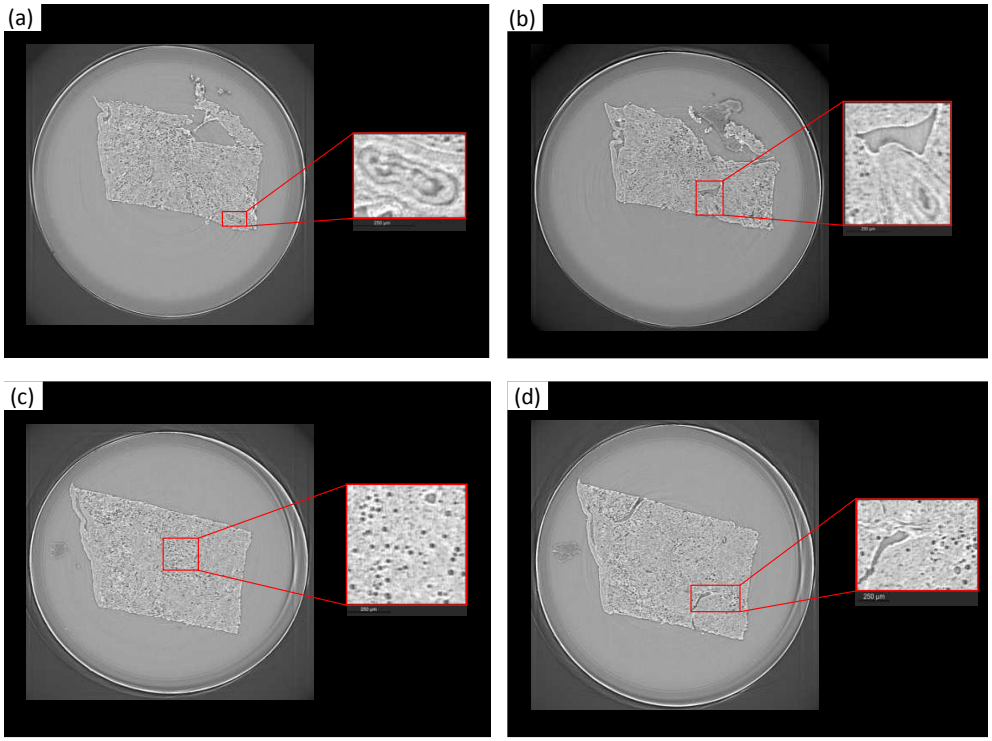

Figure 6.25: Some slices (the same of Fig. 6.25) through the transmission volume. The scale bar of the slices is 500 µm, while the scale bar of the insets is 250 µm.

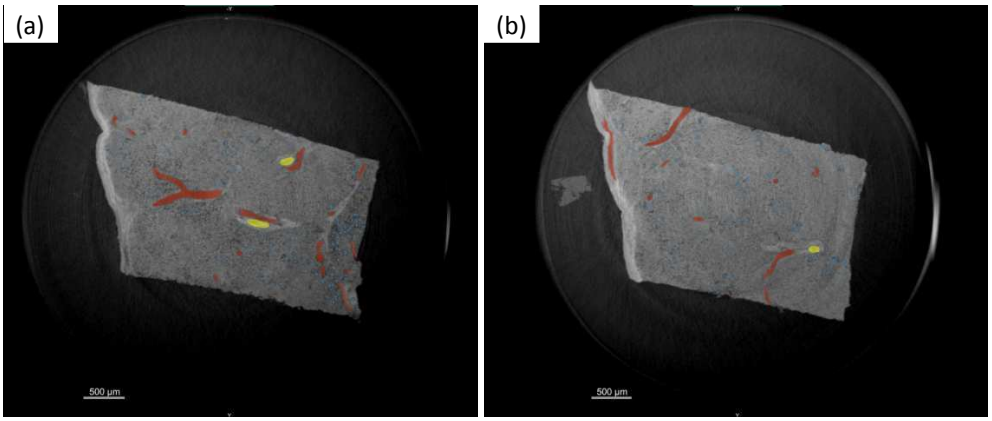

Figure 6.26: Two axial slices with bile ducts (yellow), vessels (red) and lipidic aggregates (cyan). The scale bar of the slices is 500 µm.

7 A UNIVERSAL RECONSTRUCTION METHOD FOR X-RAY SCATTERING TENSOR TOMOGRAPHY BASED ON WAVEFRONT MODULATION

This chapter discusses a reconstruction method for X-ray scattering tensor tomography, which is applicable to data obtained using different wavefront modulators. This chapter is a revised and expanded version of a paper published in Physical Review Applied: "Universal reconstruction method for x-ray scattering tensor tomography based on wavefront modulation" by Ginevra Lautizi, Alain Studer, Marie-Christine Zdora, Fabio De Marco, Jisoo Kim, Vittorio Di Trapani, Federica Marone, Pierre Thibault, and Marco Stampanoni.

7.1 INTRODUCTION

The micro- and nanostructures inside a macroscopic object play a fundamental role in its characteristics and properties. For instance, the mechanical properties of bones are closely linked to the alignment of collagen fibres at a local level **[Fratzl2008]**. Likewise, the mechanical characteristics of fibre-reinforced polymers and composites are significantly influenced by the local orientation of synthetic fibres **[Pipes1982]**.

Small-angle X-ray scattering (SAXS) tensor tomography can provide information about the alignment of microstructures of non-crystalline samples on a sub-micron length scale, often not resolvable with conventional approaches such as micro-CT **[Schaff2015; Liebi2015; Liebi2018; Gao2019; Skjonsfjell2016]**. However, scanning SAXS requires long acquisition times due to drastic reduction in flux to create a narrow beam that has to be scanned over the sample at different sample angular poses. The long acquisition times of scanning SAXS, combined with long analysis times, limit its applications, in particular for large samples. For these reasons, the established approaches require experimental times in the order of several hours, even for small sample volumes.

Full-field X-ray imaging methods capable of delivering directional information about sub-structures in a sample, such as speckle-based imaging (SBI) and grating interferometry (GI), have been actively investigated in recent years. Both GI and SBI techniques make use of a wavefront-marking element, such as gratings and sandpaper respectively, to generate intensity fluctua-

tions in the recorded detector image **[Momose2003; Weitkamp2005]**. The local distortion of the pattern, introduced by the sample, is then analysed to retrieve attenuation, phase contrast, and scattering (dark-field) information **[Pfeiffer2008]**. SBI has become more and more common in recent years. It is based on a similar principle as GI and it has shown similar scattering sensitivities, without the need of tailored phase optical elements **[Morgan2012; Berujon2012; Zanette2015; Zdora2018; Zhou2018; Zdora2021]**. Compared to SAXS imaging, these full-field techniques allow for larger fields of view (FOVs) to be investigated in shorter measurement times. Moreover, access to the dark-field information is not directly limited by the beam properties, such as size, monochromaticity and transverse coherence **[Yashiro2010; Lynch2011; Strobl2014]**. Given that the directional dark-field signal provides information on the sub-structures' orientations in a sample, it becomes possible to detect these structures, even when their dimensions are smaller than the image pixel resolution, enabling a reliable reconstruction of the prevalent orientations of microstructural features **[Malecki2014; Vogel2015; Jensen2010; Kim2022b; Smith2022]**.

Recently, 2D omnidirectional X-ray scattering sensitivity in a single shot has been demonstrated using circular gratings, paving the way for time-resolved studies **[Kim2020; Kim2021; Kim2022]**. These studies combine an improved acquisition speed based on circular diffractive optics with an optimised data acquisition protocol. A tomographic reconstruction method based on a filtered back-projection with algebraic filters has also been introduced. However, in the mentioned approaches, the extraction of dark-field signal relies on a tailored circular phase-grating array that requires specialized facilities and knowledge to be fabricated. Moreover, the use of such a grating array does not allow for easy tuning of the X-ray energy and spatial resolution of the scattering images. A general reconstruction method is therefore needed, where the dark-field signal extraction is not strictly dependent on the type of wavefront marker used.

In this chapter, we suggest a general reconstruction method that can be applied both to GI and SBI X-ray scattering approaches to obtain tensor tomography volumes. Unlike existing algorithms **[Felsner2019; Graetz2021]**, our method is based on the mathematical rotation of the scattering tensor and can therefore be applied to different techniques. Moreover, we reformulated the reconstruction problem directly and intuitively, leading to the reconstruction of the full tensor field, not only the scattering signal along predefined directions.

7.2 OMNIDIRECTIONAL DARK-FIELD SIGNAL EXTRACTION

7.2.1 Model

Our method is based on energy conservation: it assumes that the intensity of the photon distribution not absorbed by the sample is conserved by the scattering process. The model considers a wave field intensity distribution generated by an ideal point source.

The scattering can be modelled, on a first approximation, as a Gaussian probability distribution. The process underlying the X-ray dark-field image modality is ultra-small angle X-ray scattering (USAXS), which is a coherent process. In SAXS/USAXS theory, the scattered fields from all regions of a given microstructure are integrated, which leads to a certain distribution of scattered fields as a function of the scattering vector $\boldsymbol{q}$, or equivalently, the scattering angle θ. The squared magnitude of the field gives the scattered intensity as a function of the scattering angle. The relationship with $\boldsymbol{q}$ or θ is not generally a Gaussian, but often resembles one. In SAXS, if sufficiently small $\boldsymbol{q}$ values are probed, approximating $I(\boldsymbol{q})$ with a Gaussian, the Guinier approximation, is often used to retrieve the radius of gyration, a measure for the particle size. While the Guinier approximation does not accurately model the behaviour at large scattering vectors $\boldsymbol{q}$, using the approximation is almost always appropriate in imaging, because the relative scattering intensities at high scattering vectors are very small ($< 10^{-3}$). In an imaging geometry, scattered and unscattered beams overlap spatially, and thus high-$\boldsymbol{q}$ scattering is effectively invisible.

The covariance matrix of the Gaussian distribution can be interpreted as the scattering tensor of the sample. The physical model used can be derived from the Photon Diffusion equation **[Aronson1999]** combined with the Fokker-Planck model for X-ray imaging **[Paganin2019]**. Therefore, if we label the incident beam with I_0 and the transmitted beam leaving the voxel with I_s, for each unit cell we can write

$$I_s(\boldsymbol{r}_\perp) = I_0(\boldsymbol{r}_\perp) e^{-\mu(y)\Delta y} * |\Sigma_y|^{-\frac{1}{2}} e^{-\frac{1}{2}\boldsymbol{r}_\perp^\top \Sigma_y^{-1} \boldsymbol{r}_\perp} \tag{7.1}$$

where Σ_y is the 2D scattering tensor (covariance matrix) of a thin slice at a position y in the beam, if we consider that the beam propagates along the y direction. The 2D pixel coordinates in each unit cell are indicated as $\boldsymbol{r}_\perp$, where $\boldsymbol{r}_\perp$ represents the 2D coordinates transverse to the beam direction. The convolution operator is indicated as $*$, $\mu(y)$ is the absorption coefficient for each unit cell at a given position y, and Δy is the thickness of the unit cell. The unit cell is given by the period of the pattern for the grating array and by an arbitrary window for a non-periodic wavefront modulator, such as

sandpaper. Performing the Fourier transform on Eq. 7.1, taking the absolute value, and the natural logarithm, it follows that

$$\frac{1}{2}\boldsymbol{k}_\perp \Sigma_y \boldsymbol{k}_\perp + \mu(y)\Delta y = -\ln \frac{|\hat{I}_s(\boldsymbol{k}_\perp)|}{|\hat{I}_0(\boldsymbol{k}_\perp)|}. \tag{7.2}$$

The right-hand side of Eq. 7.2 is always non-negative, hence the left-hand side must be a positive definite bilinear form in the variable $\boldsymbol{r}_\perp$. For each projection the 2D scattering tensor can be extracted in Fourier space, fitting each arbitrarily defined analysis window with a positive definite bilinear form, using a multislice version of Eq. 7.2.

Eq. 7.1 can be generalized to a multislice version, considering one additional convolution per voxel:

$$I_s(\boldsymbol{r}_\perp) = I_0(\boldsymbol{r}_\perp) \cdot e^{-\int_0^y \mu(y')\,dy'} \cdot e^{-\frac{1}{2}\boldsymbol{r}_\perp^\top \Sigma_0^{-1} \boldsymbol{r}_\perp} * \cdots * e^{-\frac{1}{2}\boldsymbol{r}_\perp^\top \Sigma_y^{-1} \boldsymbol{r}_\perp}, \tag{7.3}$$

yielding the magnitude of the Fourier transform

$$|\hat{I}_s(\boldsymbol{k}_\perp)| = |\hat{I}_0(\boldsymbol{k}_\perp)| e^{-\int_0^y \mu(y')dy'} e^{-\frac{1}{2}\boldsymbol{k}_\perp \int_0^y \Sigma(y')dy' \boldsymbol{k}_\perp}. \tag{7.4}$$

Since we cannot see scattering in beam direction, the full 3D Σ needs to be corrected by a projection operator P_y, $P_y\Sigma := P_B \Sigma P_B^T$ such that

$$\frac{1}{2}\boldsymbol{k}_\perp \int_0^y P_y \Sigma(y')dy'\, \boldsymbol{k}_\perp + \int_0^y \mu(y')dy' = -\ln \frac{|\hat{I}_s(\boldsymbol{k}_\perp)|}{|\hat{I}_0(\boldsymbol{k}_\perp)|}. \tag{7.5}$$

The derivation of the projection operator

The projection operator P_y can be derived as follows. Starting from Eq. 7.1 and considering only one scattering layer:

$$I_{scatter} = I_0 *_{3D} MVG(\Sigma) \tag{7.6}$$

where MVG stands for Multi Variate Gaussian and $I_{scatter}(\boldsymbol{r})$ can be seen as the 3D intensity distribution arriving at the detector, after having exited the thin monolayer sample.

The intensity measured at the detector reads

$$I_{det}(x,z) = \int I_{scatter}(x,y,z)dy = \int\int I_0((x,y,z) - \boldsymbol{r'})dy\, MVG(\boldsymbol{r'};\Sigma)\, d\boldsymbol{r'}, \tag{7.7}$$

where we have explicitly written the convolution integral. Since the support of the blurring probability density function is much smaller than the size of the unit cell support, we can approximate $I_0(x-x', -y', z-z')$ as a constant with respect to y' (evaluated at zero) such that

$$I_{det}(x,z) \simeq \int\int I_0(x-x',y,z-z')dy \left\{ \int MVG(\boldsymbol{r}';\Sigma)dy' \right\} dx'dz'. \quad (7.8)$$

Defining the projection operator as $P_y\Sigma := P_B\Sigma P_B^T$, it holds that a MVG probability density function is still a MVG, with dimension reduced accordingly:

$$\int MVG(x,y,z;\Sigma)dy = MVG(x,z;P_y\Sigma). \quad (7.9)$$

From this we see that

$$I_{det} = I_0 *_{2D} MVG(P_y\Sigma), \quad (7.10)$$

where $I_0(x,z) = \int I_0(x,y,z)dy$.

The derivation of the phase contrast

One could argue that the phase contrast is not taken into account in the model. However, a potential phase shift effect would lead to a translation of the intensity in real space, which means adding a phase to the Fourier intensity. Since we take the magnitude of the Fourier transformed intensity to calculate the scattering contribution, the phase shift contribution is not present in the term $|\hat{I}(\boldsymbol{k}_\perp)|$ of Eq. 7.5.

Since developing an alternative method to calculate the phase shift is not the purpose of this thesis, the focus in the experimental results will be mainly on the scattering tensor. However, the derivation of the phase contrast signal in this new model is included here for completeness.

The phase-contrast signal can also be calculated, modifying the model in Eq. 7.1. If the effect of the sample is modelled as $I_0(\boldsymbol{r}_\perp)e^{-\mu(y)\Delta y}e^{i\phi(\boldsymbol{r}_\perp)}$, then, in the Fresnel regime, the intensity within a unit cell is shifted by an amount $\boldsymbol{r}_{\perp s}$ proportional to $\nabla\phi$. Hence, if we Taylor expand $\phi(\boldsymbol{r}_\perp)$ as

$$\phi(\boldsymbol{r}_\perp) = \phi(0) + \nabla\phi(0)\cdot\boldsymbol{r}_\perp + \ldots, \quad (7.11)$$

with 0 being the centre of the unit cell, we can think of the first order term as the refraction term, and all other terms as the scattering contributions summarized in Σ_y.

To take the differential phase-contrast (DPC) signal into account, we modify the Fourier transform of Eq. 7.1 as follows:

$$\hat{I}_s(\boldsymbol{k}_\perp) = \hat{I}_0(\boldsymbol{k}_\perp)\underbrace{e^{-i\boldsymbol{k}_\perp\cdot\boldsymbol{r}_{\perp s}}}_{\text{DPC}}\underbrace{e^{-\mu(y)\Delta y}}_{\text{absorption}}\underbrace{e^{-\frac{1}{2}\boldsymbol{k}_\perp^\top\Sigma_y^{-1}\boldsymbol{k}_\perp}}_{\text{dark field}}. \quad (7.12)$$

Therefore, the phase shift can be calculated as $\boldsymbol{k}_\perp\cdot\boldsymbol{r}_{\perp s} = \text{phase}\left[\hat{I}_s(\boldsymbol{k}_\perp)/\hat{I}_0(\boldsymbol{k}_\perp)\right]$.

7.2.2 Software architecture

```
Input Data:
 - Load "Sample" and "Reference" detector images
 - Load Tensor Sinogram (HDF5 file)
  |
  v
Preprocessing:
 - Rearrange images into blocks (blockshaped)
 - Apply Fourier Transform on blocks (blockwiseFFT)
  |
  v
Compute Scattering Tensor:
 - Least Squares Fit (blockwiseFit)
 - Ensure positive-definite tensors
 - Parallelize across angles
   (calculateTensorSinogramPerProjectionPara)
  |
  v
Postprocessing:
 - Eigendecompose tensors
 - Extract mean scattering, fibre orientation
   (FiberOrientationExtraction)
 - Optionally calculate Differential Phase-Contrast (DPC)
  |
  v
Save Results:
 - Save reconstructed tensor field as a file
```

The code to calculate the scattering tensor field of a sample was developed in Python and designed in collaboration with Alain Studer from Data Processing Development and Consulting Group, Paul Scherrer Institut. The input is a detector image encoding the dark-field signal of the slice (the "sample" image) and a "reference" detector image, showing the reference intensity of the unit cells. Only 2D radiography is involved in this part of the reconstruction process.

Firstly, the projection image is rearranged as an array of blocks. This operation is encoded in the function `blockshaped` which converts the input array to a block-wise equivalent, given the rows and the column. Each block is defined by the chosen analysis window. The inverse function `unblockshaped` converts back the block-wise array to its original form. The, we developed a function `blockwiseFFT`, which returns an array of blocks which are Fourier-transformed and centred. Only the magnitude of the signal is returned. With these three functions, we can calculate the right-hand side of Eq. 7.2. We use this as input to calculate Σ_y using a least square fit (from `scipy.optimize`) of the bilinear form in k-space. So here we calculate

$$\Sigma_y^* = \underset{\Sigma}{\operatorname{argmin}} \left\| \ln\left(\frac{|\hat{I}_s(k_\perp)|}{|\hat{I}_0(k_\perp)|}\right) + \frac{1}{2}\langle k_\perp, \Sigma_y k_\perp\rangle + \mu(y)\Delta y \right\|^2 . \tag{7.13}$$

In the function `blockwiseFit` we fit the scattering tensor from data in Fourier space, per block, according to the model. For each block, the absorption is calculated as the zero frequency ($k = 0$) term of the Fourier-transform. The block structure is useful to loop over all the blocks and parallelize the process. We find a Σ_y for each block and for each image. Σ_y is a 2×2 symmetric, positive-definite matrix. We make sure that the non positive-definite terms are discarded by excluding the values for which the trace or the determinant of Σ_y are negative.

We call `blockwiseFit` in the function `calculateTensorSinogramPerProjection` to calculate the tensor sinogram data for each projection, for fixed β and α angle, and `calculateTensorSinogramPerProjectionPara` to run the partial function in parallel over all the α angles.

Now that the scattering tensors are available, we can eigendecompose them and extract the following quantities: mean scattering, and 2D preferential fibre orientation. The mean of the eigenvalues represents the mean scattering, while the eigenvector with the lowest eigenvalue represents the preferential local fibre orientation, since the scattering is typically the weakest along the fibre orientation. The scattering angle is calculated as the angle between the two components of the smallest eigenvector and converted to degrees. Then, the result is taken as modulo 180 to ensure the angle is within the range $[0°, 180°]$, which confines the angle to a half-circle, as the principal axis direction is symmetrical in this context. This analysis is performed in the function `FiberOrientationExtraction`, which uses `np.linalg.eig` to eigendecompose the matrices. An example of the application of this reconstruction code can be found in subsection 7.4.1.

For completeness, the extraction of the differential phase-contrast signal is also implemented. The code to extract the DPC shifts is similar compared to extracting the scattering tensor, except that here a linear form is fitted in k space. So here we calculate

$$\boldsymbol{r}_{\perp s}^* = \underset{\boldsymbol{r}_{\perp s}}{\operatorname{argmin}} \left| \boldsymbol{k}_\perp \cdot \boldsymbol{r}_{\perp s} + \operatorname{phase}\left[\hat{I}_s(\boldsymbol{k}_\perp)/\hat{I}_0(\boldsymbol{k}_\perp)\right] \right|^2 \tag{7.14}$$

Therefore, the function `blockwiseFit` is modified with this new model and the function `blockwiseFFT` in this case return the complex Fourier transform and not the magnitude.

7.3 THE MATHEMATICS OF TENSOR TOMOGRAPHY

7.3.1 Definition of Tensor Field and System Matrix

After having extracted the omnidirectional dark-field signal for each projection, we need to introduce a new mathematical model to reconstruct the tensor tomogram. Let F be a symmetric, positive definite tensor field, $F : \mathbb{R}^3 \to \mathbb{R}^{3\times3}$. For any rotation $R^{axis}_{angle} \in SO(3)$, $D(R^{axis}_{angle})$ maps a tensor field F to the rotated tensor field. For positions $\boldsymbol{r} = (x, y, z)$ and for our specific scan protocol, we can write

$$D(R^x_\beta)D(R^z_\alpha)[F](\boldsymbol{r}) = (R^x_\beta R^z_\alpha) \cdot F\big((R^x_\beta R^z_\alpha)^{-1}\boldsymbol{r}\big) \cdot (R^x_\beta R^z_\alpha)^{-1}. \tag{7.15}$$

Having defined how a tensor field transforms, the definition of a tensor sinogram is straightforward. The 2-axes sinogram $S = A[F]$ is defined as

$$A[F](P_B\boldsymbol{r}, \alpha, \beta) = \int_{\mathbb{R}} P_B D(R^x_\beta)D(R^z_\alpha)[F](x, y, z)P_B dy, \tag{7.16}$$

where P_B is the projection operator along the beam propagation direction.

Reconstructing the tensor tomogram means solving the linear system $AX = B$, where X denotes the tensor field to be reconstructed, B is the measured tensor sinogram and A the linear operator defined above. This linear system can be solved with conjugate gradient method (CG) or least squares (LS). Both the forward tensor operator A and the adjoint A^* are needed for the reconstruction. It can be proven (7.3.2) that A^* equals

$$\begin{aligned} A^*[S](\boldsymbol{r}) = \int_0^{2\pi} \int_0^{\pi/2} (R^x_\beta R^z_\alpha)^{-1} S(P_B R^x_\beta R^z_\alpha \boldsymbol{r}, \alpha, \beta) R^x_\beta R^z_\alpha \\ \times \cos\beta d\beta d\alpha. \end{aligned} \tag{7.17}$$

With the method we present, it is possible to retrieve the tensor tomogram also using a single tilt axis. However, having multiple tilt axes, shrinks the nullspace of the tensor tomography forward operator, enhancing the convergence of the reconstruction algorithm **[Kim2021]**.

Once the scattering tensor field is reconstructed, it is then eigendecomposed. Knowing the eigenvalues of the scattering tensor for each voxel, the following quantities can be defined. The mean of the three eigenvalues represents the mean scattering $\mathrm{MS} = (\lambda_1 + \lambda_2 + \lambda_3)/3$. The fractional anisotropy (FA) **[Basser1996]**, which represents the scattering anisotropy, describes how well-aligned the fibres are in each voxel:

$$\mathrm{FA} = \frac{\sqrt{(\lambda_1 - \lambda_2)^2 + (\lambda_2 - \lambda_3)^2 + (\lambda_3 - \lambda_1)^2}}{\sqrt{2(\lambda_1^2 + \lambda_2^2 + \lambda_3^2)}}. \tag{7.18}$$

Areas characterized by a high volume fraction of well-aligned fibres will exhibit a high FA. Finally, the eigenvector with the lowest eigenvalue represents the preferential local fibre orientation, since the scattering is typically the weakest along the fibre orientation. We will therefore show the above-mentioned quantities, as meaningful indicators accessible through tensor tomography for assessing the level of fibre scattering, alignment, and orientation.

7.3.2 Adjoint operator

As stated in the previous subsection (7.3.1), the adjoint operator $A^* : L^2(\mathbb{R}^4, \mathbb{R}^{3\times3}) \rightarrow L^2(\mathbb{R}^3, \mathbb{R}^{3\times3})$ equals

$$A^*[S](\boldsymbol{r}) = \int_0^{2\pi} \int_0^{\pi/2} (R_\beta^x R_\alpha^z)^{-1} S(P_B R_\beta^x R_\alpha^z \boldsymbol{r}, \alpha, \beta) R_\beta^x R_\alpha^z \cos\beta d\beta d\alpha. \quad (7.19)$$

It can be proved as follows. The inner product in both spaces is defined as $\langle X, Y\rangle = \int tr(XY^T)$. Hence, for a sinogram S and a tensor field F, the inner product $\langle S, A[F]\rangle$ equals

$$\int_{\mathbb{R}^2} \int_0^{2\pi} \int_0^{\pi/2} tr\big\{ S(P_B \boldsymbol{r}, \alpha, \beta) \int_{\mathbb{R}} [P_B D(R_\beta^x) D(R_\alpha^z)[F](\boldsymbol{r}) P_B]^T dy \big\}\, d\beta d\alpha dz dx. \quad (7.20)$$

Using the linearity of the trace and the transformation rule for tensor fields

$$\int_{\mathbb{R}^3} \int_0^{2\pi} \int_0^{\pi/2} tr\big\{ S(P_B \boldsymbol{r}, \alpha, \beta) P_B R_\beta R_\alpha F^T(R_\alpha^T R_\beta^T \boldsymbol{r}) R_\alpha^T R_\beta^T P_B \big\}\, d\beta d\alpha d\boldsymbol{r}. \quad (7.21)$$

The trace is cyclic, such that

$$\int_{\mathbb{R}^3} \int_0^{2\pi} \int_0^{\pi/2} tr\big\{ R_\alpha^T R_\beta^T P_B S(P_B \boldsymbol{r}, \alpha, \beta) P_B R_\beta R_\alpha F^T(R_\alpha^T R_\beta^T \boldsymbol{r}) \big\}\, d\beta d\alpha d\boldsymbol{r}, \quad (7.22)$$

shifting the rotations to the sinogram and again skipping the projector, since the sinogram is already projected.

$$\int_{\mathbb{R}^3} \int_0^{2\pi} \int_0^{\pi/2} tr\big\{ R_\alpha^T R_\beta^T S(P_B R_\beta R_\alpha \boldsymbol{r}, \alpha, \beta) R_\beta R_\alpha F^T(\boldsymbol{r}) \big\}\, d\beta d\alpha d\boldsymbol{r}. \quad (7.23)$$

Due to linearity of the trace, we can rearrange this as

$$\int_{\mathbb{R}^3} tr\Big\{ \Big(\int_0^{2\pi} \int_0^{\pi/2} R_\alpha^T R_\beta^T S(P_B R_\beta R_\alpha \boldsymbol{r}, \alpha, \beta) R_\beta R_\alpha d\alpha d\beta \Big) F^T(\boldsymbol{r}) \Big\}\, d\boldsymbol{r}. \quad (7.24)$$

This must equal by definition

$$\langle A^*[S], F\rangle = \int_{\mathbb{R}^3} tr\Big\{A^*[S](\boldsymbol{r})F^T(\boldsymbol{r})\Big\}\, d\boldsymbol{r}, \tag{7.25}$$

from which we see that

$$A^*[S](\boldsymbol{r}) = \int_0^{2\pi}\int_0^{\pi/2} (R_\beta^x R_\alpha^z)^{-1} S(P_B R_\beta^x R_\alpha^z \boldsymbol{r}, \alpha, \beta) R_\beta^x R_\alpha^z \, d\beta d\alpha. \tag{7.26}$$

Instead of choosing the simple integral measure $d\beta$, we can as well chose the measure $\cos\beta d\beta$.
Indeed, for $\beta = \pi/2$, the sample is rotated around the beam axis, making tomography redundant. One single α value, e.g $\alpha = 0$, is sufficient to capture all information available. This fact is covered with the $\cos\beta$ factor, by which the number of α rotations can be decreased while increasing β. This completes the proof.

7.3.3 Software architecture

The code to simulate and to reconstruct a tensor tomography scan was developed in Python and designed in collaboration with Alain Studer from Data Processing Development and Consulting Group, Paul Scherrer Institut. The emphasis is on a concise and straightforward software architecture. Most of the mathematical formulae and equations that are used are derived from basic principles, therefore no element of the code should be seen as a black box. Furthermore, it is possible to see the reconstruction technique as an extension of the well-known scalar iterative back projection algorithm. The reconstruction algorithm discussed here reconstructs the full tensor field, unlike other algorithms where a principle axes (vector-) field or "projections/extractions" that yield only a "partial" tensor field are reconstructed. Additionally, this algorithm can be applied to any reference pattern. It is not required to map a standard grid structure in the Talbot regime, simple sandpaper works perfectly.

Understanding tensor tomography hinges on the accurate definition of a symmetric, positive definite tensor field and its transformation under the SO(3) representation, i.e., how a tensor field rotates. The next crucial aspect is the precise definition of the measurement process (how a tensor tomogram is defined). Lastly, for the iterative reconstruction algorithm used here (conjugate gradient), deriving the adjoint of the system operator is necessary. This is because the conjugate gradient method requires the system operator to be symmetric and positive definite, which is achieved by left-multiplying the original equation with the adjoint operator.

In order to explain how the code is structured, we will divide it in five parts: conjugate gradient, forward and backward operators, tensor field rotation, parallelization, and simulation.

Conjugate gradient

The conjugate gradient (CG) based iterative reconstruction of an intrinsically acquired tensor tomography scan is implemented in `tensorTomoRecAlgorithmCG.py`, which contains the function `reconstruct(tensorTomogram, maxNumIter)`. The basis for the algorithm are the forward and the backward operators relating the sample and its tomogram (simulated or measured). Note that CG expects a symmetric positive definite system matrix, this is achieved by left-multiplying the original equation with the adjoint operator. Usually $5 - 10$ iterations are enough. The `cg` function from `scipy.sparse.linalg` is used. A linear least squares alternative version of this function can be found in `tensorTomoRecAlgorithmLSQ.py`. In `tensorTomoReconstruction.py` the tensor tomogram is finally reconstructed and a sphere mask is applied.

Forward and backward operators

The Python code in `twoAxesTensorFieldProjectors.py` contains the operators necessary to iteratively reconstruct a tensor tomogram: the forward projection operator A and the adjoint operator A^T. The line integration is outsourced to C code for performance reason. Shared library is loaded at runtime via ctypes. Several functions are contained in this Python file. The function `projectTensorFieldOnPhysicalSubset(tf)` takes a tensor field (numpy array) as input and projects it onto the set of physically valid tensor fields. The function `rotateTensorFieldz(tf, alpha)` rotates a tensor field around the z-axis by an angle α, while the function `rotateTensorFieldx(tf, beta)` rotates a tensor field around the x-axis by an angle β. The tensor sinogram for a specific beta angle (Eq. 7.16) is calculated in the function `intrinsicAxesTensorForward(tf, beta, numberOfAlphaAngles)` which returns a sinogram as 5D numpy array with shape = (numberOfAlphas, projected xz-support, 3, 3). The tensor sinogram is then rotated in `rotateTensorTomogramxy(beta, tt)` according to the reconstruction formula in Eq. 7.17 to prepare for line integration. The line integral in α is then performed in `intrinsicAxesTensorBackward(beta,intrinsicAxesTomogram)`.

The function `tensorFieldForwardProject(tensorField, scanprotocol)` implements the forward projector A, while `tensorTomogramBackwardProject(sinogram)` implements the adjoint operator A^T by calculating the β integral in Eq. 7.16 since the α integral was already calculated before. The integration over β is an outermost for loop in C code.

Tensor field rotation

The Python code in `singleAxisTensorFieldRotation.py` is useful to rotate a tensor field around a single Cartesian coordinate axis. This is the basis for implementing the forward operator and uses `scipy.ndimage` function `rotate`. Two functions are contained in this Python file. The function `rotationMatrix(eta, theta)` creates a rotation matrix defined by the Carte-

sian axis η and the rotation angle θ, while the function `rotateTensorField(tf, eta, theta)` rotates a tensor field around the coordinate axis η and angle θ. It takes as input the tensor field `tf` as 5D numpy array, the Cartesian axis η and the rotation angle θ. The tensor field is computationally rotated in two steps: firstly, all the components of the field are transformed as if scalar fields via the SciPy `rotate` function, and then the components are rotated (each matrix is transformed as if in a basis change).

Parallelization

The forward operator is parallelized in a multiprocessing way (using Python's `multiprocessing` module), whereas the backward operator is parallelized in a multithreaded way (via OpenMP). This different parallelization was chosen according to the way the two operators are implemented. The function `tensorFieldForwardProjectParallel(tensorField, scanprotocol)` is the equivalent of `tensorFieldForwardProject(tensorField, scanprotocol)`, but it runs in parallel over β. One β value is calculated locally, the remaining β angles are sent to the servers in network terms. Connections have been established in the CG part of code.

The forward operator's parallelization is realised in two different versions: The `twoAxesTensorFieldForwardProjectorPara.py` code is based on the `multiprocessing` package and runs fine for moderately large datasets, while the code in file `twoAxesTensorFieldForwardProjectorParaSHM.py` uses the `concurrent.futures.process` package to start a pool of workers and additionally shares the tensor tomogram memory between the different processes. The choice depends on the size of the datasets. For larger input datasets (tensor field support of size ≈ 300 pixels), the `multiprocessing` module fails to allocate the memory and processes stall.

Single-node parallelization of the forward operator is based on the fact that, for a fixed β angle, the for loop on the α angles can be easily parallelized. Indeed, we can independently calculate different α values in a β sinogram. Therefore, the α angular range is divided equally and assigned to different processes, with each process computing its share of the result.

For memory-intensive arguments (like the tensor field), having all the arguments serialized by the "master" process and then sent to the "worker" processes to be deserialized and loaded into memory leads to a CPU burden and a high memory usage. Indeed, in this way, each process holds its own copy of the input tensor field. This problem was mitigated by defining the input array as global. In this way, each process has its own virtual address space, avoiding physical memory copying unless necessary, thereby allowing processes to share the globally-defined input variables implicitly. Similarly, the output array was defined as a shared-memory array, allowing each process to write directly to it, thus avoiding serialization and some memory duplication. Additionally, the `concurrent.futures.process` package provides better exception handling for high memory consumption compared to the `multiprocessing` package.

Simulation

Several tensor fields have been simulated to test the reconstruction code before acquiring experimental datasets. In `tensorFieldExample.py` we simulated some examples of specific tensor fields to test reconstruction quality. The function `initTensorfield` creates an example tensor field. There are two possible examples: letters elongated along the third dimension, and different oscillating functions for each component. The output is a tensor field as 5D numpy array. In `initUnityTensorField` a unity tensor field (identity matrix for all coordinates) is initialized, while in `init2LayersTensorField` a two-layer tensor field is initialized, and analogously in `init3LayersTensorField` for a three-layer tensor field. A more complicated use case is implemented in the `initKJTensorField` function, where the sample described in Ref. **[Kim2020]** (Fig. 2a) is simulated. In this case, in the first (lower half plane) and last layer (right half plane), the scattering tensor has the smallest eigenvector along the z-axis, the middle layer is empty, and in the orthogonal layer the scattering tensor has the smallest eigenvector along the y-axis and along the x-axis. In `tensorTomoSimulation.py` a tensor tomography scan is simulated and the subsequent reconstruction of the simulated data is performed.

The following chain is therefore simulated: tensor field $\rightarrow$ tensor tomogram $\rightarrow$ raw dataset (sample projections and reference projections) $\rightarrow$ Reconstruction (tensor field) $\rightarrow$ eigendecomposition. `simulateProjections.py` is the Python script to simulate raw data as obtained at the beamline. It transforms a tensor field into a corresponding simulated raw dataset, creating a hdf5 file containing data plus metadata. The class `SimulateProjections` contains a `initHDF5file` function to define the datasets that are later filled with simulated values, a `calculateTensorTomogram` function which calculates the tensor tomogram from the simulated tensor field. The simulated projections are derived from the tensor tomogram by reverting the algorithm which extracts a integrated/projected 2D tensor from a unit cell. The function `calculateFlat` is used to calculate the reference image by repeating the unit cell data several times, while `calculateSandPaperFlat` calculates the reference image as random intensities that follow a Poisson distribution. Then, `transformTensorTomogramSlice2Projection` is used to calculate a projection image from a fixed (β, α) tensor tomogram slice, and finally `calculateProjections` calculates the full simulated scan data for all angles.

7.3.4 Unit tests

In this subsection, we consider two specific cases (i.e., no β or no α rotations) as unit tests for the reconstruction of the tensor tomogram.

No β rotation

We restrict ourselves to the special case $R^x = 1$, so no β rotation (no tilt). Let $F(\boldsymbol{r}) = diag\big(\lambda_1(\boldsymbol{r}), \lambda_1(\boldsymbol{r}), \lambda_2(\boldsymbol{r})\big)$ label the tensor fields that form the centre of the subgroup SO(2), i.e. $[F(\boldsymbol{r}), R^z_\alpha] = 0 \; \forall \, R^z_\alpha \in \mathrm{SO}(3)$ and for all eigenvalue fields $\lambda_1(\boldsymbol{r}), \lambda_2(\boldsymbol{r})$. For these tensor fields, the tensor sinogram in Eq. 7.16 becomes $diag\big(\mathcal{R}[\lambda_1](x,z,\alpha), \mathcal{R}[\lambda_2](x,z,\alpha)\big)$ where $\mathcal{R}$ is the standard scalar Radon transform. If we skip the projector P_B in the tomogram definition (which is only possible for a simulation), the tomogram becomes $diag\big(\mathcal{R}[\lambda_1], \mathcal{R}[\lambda_1], \mathcal{R}[\lambda_2]\big)$, such that the adjoint tensor operator in Eq. 7.17 equals a component-wise scalar adjoint, like for the tensor forward operator. Hence

$$A^*A[F](\boldsymbol{r}) = diag\big(\mathcal{R}^T\mathcal{R}[\lambda_1](\boldsymbol{r}), \mathcal{R}^T\mathcal{R}[\lambda_1](\boldsymbol{r}), \mathcal{R}^T\mathcal{R}[\lambda_2](\boldsymbol{r})\big) \tag{7.27}$$

Thus, we can compare the scalar unfiltered backprojection of the diagonal components of the tensor sinogram for any specific slice z with the left side of Eq. 7.27. This unit test was run successfully.

No α rotation

For the scan protocol $\beta = 90$; $\alpha = 0$, the summation in the adjoint operator in Eq. 7.17 collapses to a single value, such that for the according tensor sinogram $S_{90,0}$

$$A^*[S_{90,0}](\boldsymbol{r}) = (R^x_{90})^{-1} S_{90,0}(P_B R^x_{90}\boldsymbol{r}, 0, 90) R^x_{90} \tag{7.28}$$

The function argument $P_B R^x_{90}\boldsymbol{r}$ equals (y,x), hence for the tensor sinogram of the form

$$S_{90,0}(x,0,z,90) = \begin{pmatrix} t_{11} & 0 & t \\ 0 & 0 & 0 \\ t & 0 & t_{33} \end{pmatrix} (z,x) \tag{7.29}$$

the rotated tensor sinogram is

$$A^*[T_{90,0}](x,y,z) = \begin{pmatrix} 0 & 0 & 0 \\ 0 & t_{33} & t \\ 0 & t & t_{11} \end{pmatrix} (y,x) \tag{7.30}$$

So if we select an arbitrary z in the adjoint and flip coordinates ($x \leftrightarrow y$), the (11) element in the adjoint matrix field will equal the (11) component in the tensor tomogram. Analogous for (00) and (22) component and (12) and (23) component. This equality is implemented as a unit test.
Both unit tests verify the correctness of the system operator and its adjoint.

7.3.5 Null space analytical analysis

In order to analyse to which extent the tensor forward operator A can be inverted, it is useful to determine the null space of the mapping. The size of the nullspace serves as a measure of non-invertibility or ill-posedness of the problem. For an iterative reconstruction algorithm, the back projection step might explore the nullspace of the operator extensively, maybe decreasing the quality of reconstruction without increasing the error measure. This makes it hard to find the halting point of the algorithm. In this subsection, we discuss the null space analytically and for the special case $R^x = 1$. For a numerical analysis of the null-space, see Ref. **[Kim2021]**.

To calculate the null space, it is important to first define the domain of the mapping. Every scattering field can be mathematically described as a positive definite self-adjoint matrix field F. Decomposing F into its singular value fields $F = \sum_i \lambda_i \boldsymbol{v_i} \otimes \boldsymbol{v_i}, \lambda_i > 0$, it follows that $A[F] = 0 \Rightarrow F = 0$. Unfortunately, the null-set being zero does not mean that the mapping is one-to-one, since the set of positive definite symmetric fields S is not a vector space. Indeed, S is closed under addition but not under scalar multiplication. Hence, the proof for $ker(A) = 0 \Rightarrow A\, injective$ does not hold: s_1 and s_2 may have the same tomogram if $s_1 - s_2 \in Ker(A)$.

Nevertheless, if the reconstruction algorithm going back and forth between sample space and measurements space is defined on the full vector space domain, the deviation F_μ from the true solution F^* can be arbitrarily large as long as $A[F_\mu] = 0$ and hence $A[F^* + F_\mu] = A[F^*]$ is compatible with the measurements.

Analytical results for the special case $R^x = 1$

Here, we characterize the vectors in the null space for the special case of no tilt angle (no β rotations): $R^x = 1$. Since the zz component of the tensor field transforms as a scalar field and the scalar Radon transform is injective, it must equal zero for $A[F] = 0$. The (zx, xy) component of the tensor transforms as a 2D vector field, hence the null-space consists of either curl-free or divergence-free fields (here curl-free). This can be proven doing a Helmholtz decomposition of the vector field. For a vector field, $\nabla \times \boldsymbol{v} = -\partial_y v_x + \partial_x v_y$ such that $\nabla \times \nabla\phi = 0$ and $\nabla \cdot \nabla \times A = 0$, as expected.
For the remaining 2D matrix field (embedded in the 3×3 matrix field), we set $F = \begin{pmatrix} 0 & v_{zx} & v_{zy} \\ v_{zx} & d_1 & t \\ v_{zy} & t & d_2 \end{pmatrix}$

such that the transformed xx component becomes $D(R^z_\alpha)[F]_{xx} = d_1 \sin^2\alpha + d_2 \cos^2\alpha - 2t \sin\alpha \cos\alpha$. We set $d_1 = d_2 = d$ such that $d - 2t \sin\alpha \cos\alpha$ is supposed to be zero. The scalar Radon transform of the equation is then $\mathcal{R}[d] = 2\mathcal{R}[t] \sin\alpha \cos\alpha$ or, inverting the Radon transform $d = \mathcal{R}^{-1}\left[\mathcal{R}[t] \sin\alpha \cos\alpha\right]$. The term t can in principle be an arbitrary scalar field, except that we must

make sure that $\mathcal{R}[t](y,\alpha)\cdot\sin\alpha\cos\alpha$ is a proper sinogram. As mentioned, for the vector-like components, it must hold
$\nabla_{xy}\times\left(v_{zx}(\boldsymbol{r}),v_{zy}(\boldsymbol{r})\right)=0\quad\forall z$ in $\boldsymbol{r}=(x,y,z)$.

7.3.6 Simulation results

Two simulations will be shown, which were realised following the protocol described in 7.3.3 with a cube size of 40 pixels, 40 α angles over 360° and 5 β angles, with $\beta\in[0°,40°]$ with an angular step of 10°.
The first simulated sample consists of three layers of parallel rods perfectly aligned in a staple of planes and orthogonal to the rotation axis. Three axial slices through the simulated tensor field and the reconstructed tensor field, respectively. The results are displayed in Fig. 7.1. The colour is an RGB representation of the local structure orientation. The colour ball is symmetric with respect to the $x-y$, $x-z$, and $y-z$ planes. In this case, the reconstructed tensor field perfectly reproduce what simulated in the original tensor field.

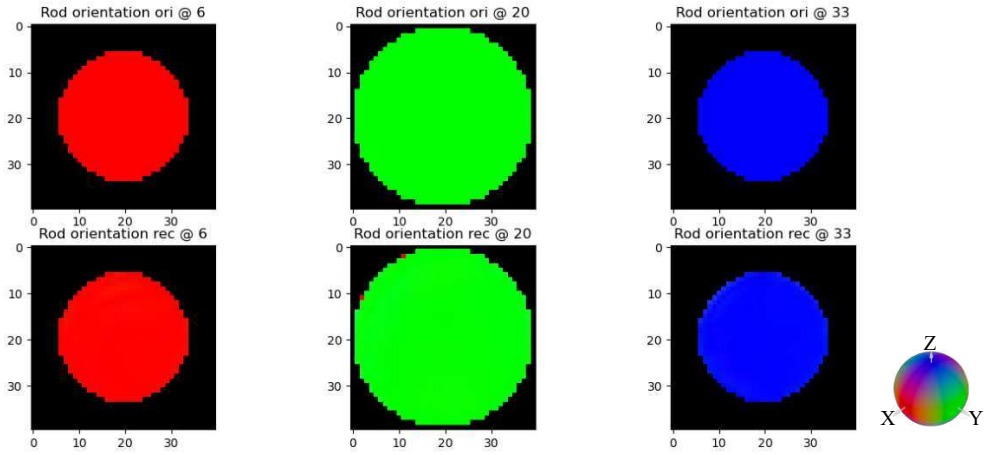

Figure 7.1: Three axial slices through the simulated tensor field (top) and the reconstructed tensor field (bottom) of a simulated sample made of three layers of parallel rods perfectly aligned in a staple of planes and orthogonal to the rotation axis. The colour is an RGB representation of the local structure orientation. The colour ball is symmetric with respect to the $x-y$, $x-z$, and $y-z$ planes.

The second simulated sample is like the validation sample described in Ref. **[Kim2020]**, and it consists of three main orientation: a top layer with two bundles, one here all the parallel fibres aligned along the x-axis, and a smaller one with all the parallel fibres aligned along the z-axis. In the middle layer, the small bundle with the z-axis orientation continues, to finish in the bottom layer, where another bundle, with fibres aligned along the y-axis is present. In Fig. 7.2 three axial slices through the simulated tensor field and the reconstructed tensor field, respectively.

In the case of mixed orientations within planes, ghost reconstructions and missing data occur, but reconstructed values are mostly correct. These

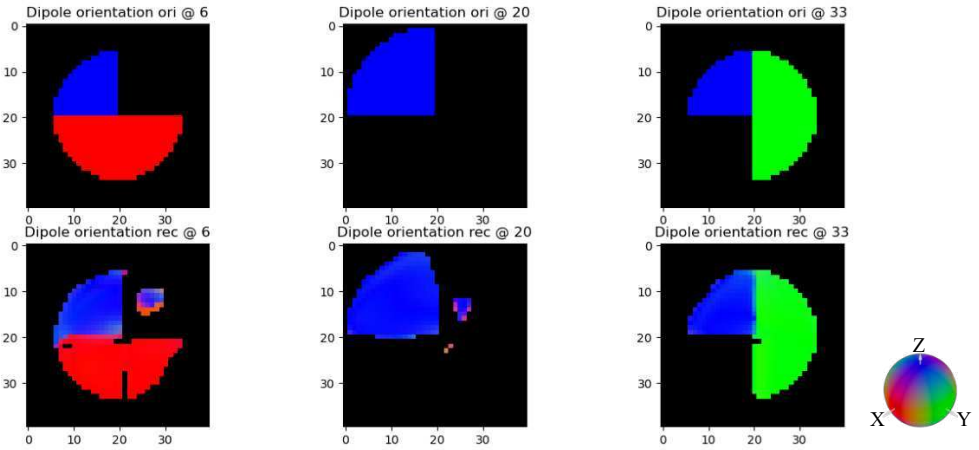

Figure 7.2: Three axial slices through the simulated tensor field (top) and the reconstructed tensor field (bottom) of a simulated sample that reproduces the validation sample described in Ref. **[Kim2020]**. The colour is an RGB representation of the local structure orientation.

inaccuracies are localized outside the sample volume and at the edges, so they can be masked post-processing with an attenuation mask.

7.4 EXPERIMENTAL DEMONSTRATION

We validated the method for use with full-field imaging methods utilizing three different wavefront markers: a circular phase-grating array, a fractal wavefront modulator **[Shi2022]**, and a sandpaper diffuser. The projection images with both the gratings and the fractal pattern were acquired at the TOMCAT beamline (Swiss Light Source, Paul Scherrer Institut) following the stair-wise acquisition protocol described in **[Kim2020; Kim2021]**, using a monochromatic X-ray beam of 17 keV. For each tilt angle β, we acquired 1000 projections with a continuous rotation of the sample over $\alpha \in [0°, 360°]$, while $\beta \in [0°, 24°]$ with an angular step of 2° (Fig. 7.3).

We fabricated two test samples, shown in Fig. 7.4. The samples have a size of $4 \times 4 \times 4$ mm^3, and are composed of two superimposed PMMA blocks with cavities, which contain bundled carbon fibres with a diameter of 12 µm, with different orientations, as visible in Fig. 7.4.

7.4.1 Omnidirectional dark-field signal extraction

Circular gratings array

The first scan was carried out using a π-shifting circular gratings array **[Kagias2016; Kagias2019]** with a unit cell period $P = 49.5$ µm and a fine grating period $g = 1.46$ µm. We used the CMOS-based GigaFRoST **[Mokso2017]**

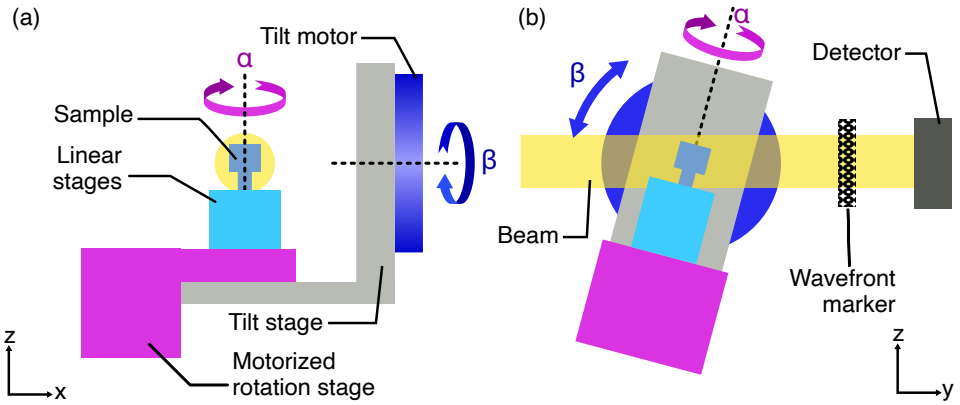

Figure 7.3: (a) Experimental setup outline viewed from the side and (b) from the side

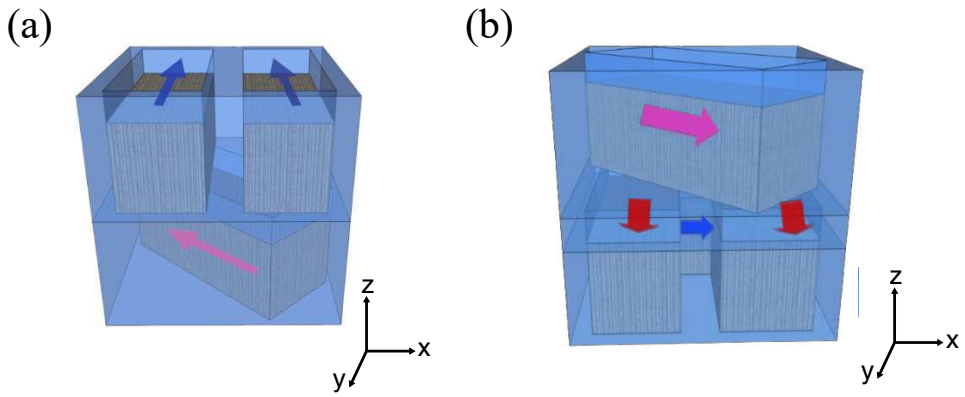

Figure 7.4: A schematic illustration of two artificial validation samples (sample 1 in (a) and sample 2 in (b)), where carbon fibre bundles lie in a PMMA box. The arrows represent the main directions of the fibres in the bundles.

detector coupled with a high-numerical-aperture tandem 1:1 microscope optic, leading to an effective pixel size of 11 µm. The detector was placed at a distance of 49.5 cm downstream of the grating array, while the grating-sample distance was 46.3 cm. The exposure time for each projection was 12 ms and the FOV was 460 × 1008 pixels. The unit cell for the analysis, i.e. the image spatial resolution, corresponds to a square whose size is the diameter of a single circular grating: 9 pixels or 99 µm. The computation time per projection was 20 s.

A raw transmission image of the validation sample 1, obtained with a single shot, is shown in Fig. 7.5a. In the image, the circular fringes of the gratings are visible, and their blurring due to strong scattering from the sample can be observed. The extracted absorption image is shown in Fig. 7.5b, while the mean scattering (Fig. 7.5c) is calculated starting from Eq. 7.2, as the mean of the eigenvalues of the scattering tensor. The main orientation (Fig. 7.5d) is the HSV representation of the 2D eigenvectors with the shortest lengths, where the hue (colour shade) is the fibre orientation projected onto the detector plane, the saturation is the fractional anisotropy, and the value (brightness) is the mean scattering intensity. The main orientation of the fibres in the bottom

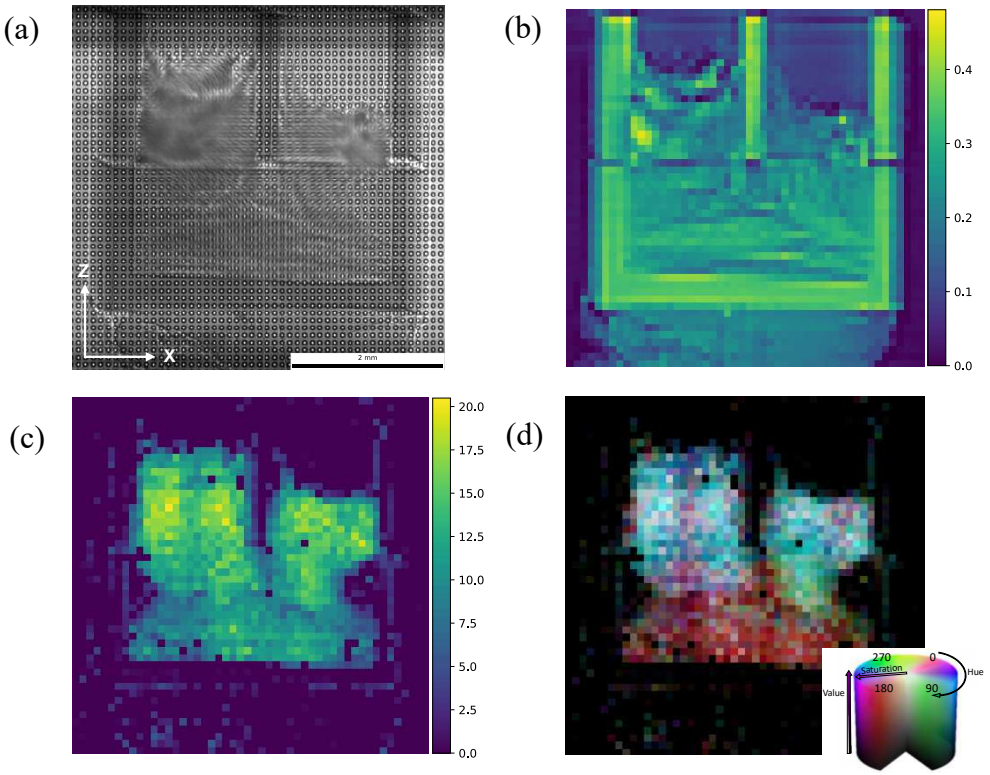

Figure 7.5: (a) Raw transmission image of the validation sample 1 with a grating array at $\alpha = 0°$, $\beta = 0°$. (b) Extracted absorption image, (c) mean scattering in arbitrary units and (d) main orientation signals. Each pixel corresponds to one unit cell. 0° (red) corresponds to the horizontal direction (x) in (a).

part of sample 1 is clearly recognizable. In the top part of sample 1, the fibres are mainly oriented perpendicularly to the plan of the image, with some bundles escaping upwards at the borders. This information is reproduced by a high mean scattering (Fig. 7.5c and high brightness in Fig. 7.5d), but low fractional anisotropy indicated by the low saturation in Fig. 7.5d (colour tending to white).

In Fig. 7.6 the same analysis has been performed on sample 2. For this sample, two field of views have been stitched to include the full sample in all the projections. Even though it is difficult to judge in a single projection the effective fibre orientations, hence the need for tensor tomography, we can clearly recognize where the lower bundle turns to make the U-shape visible in Fig. 7.6d.

Fractal pattern array

The second scan was performed using an in-house fabricated fractal pattern array, featuring structures with different shape and size, which allows tuning of the analysis window (i.e., the image spatial resolution) to focus on a desired feature size. The fractal pattern array can be used as an alternative wavefront modulator. For this scan, images were collected using a PCO.edge 5.5 sCMOS

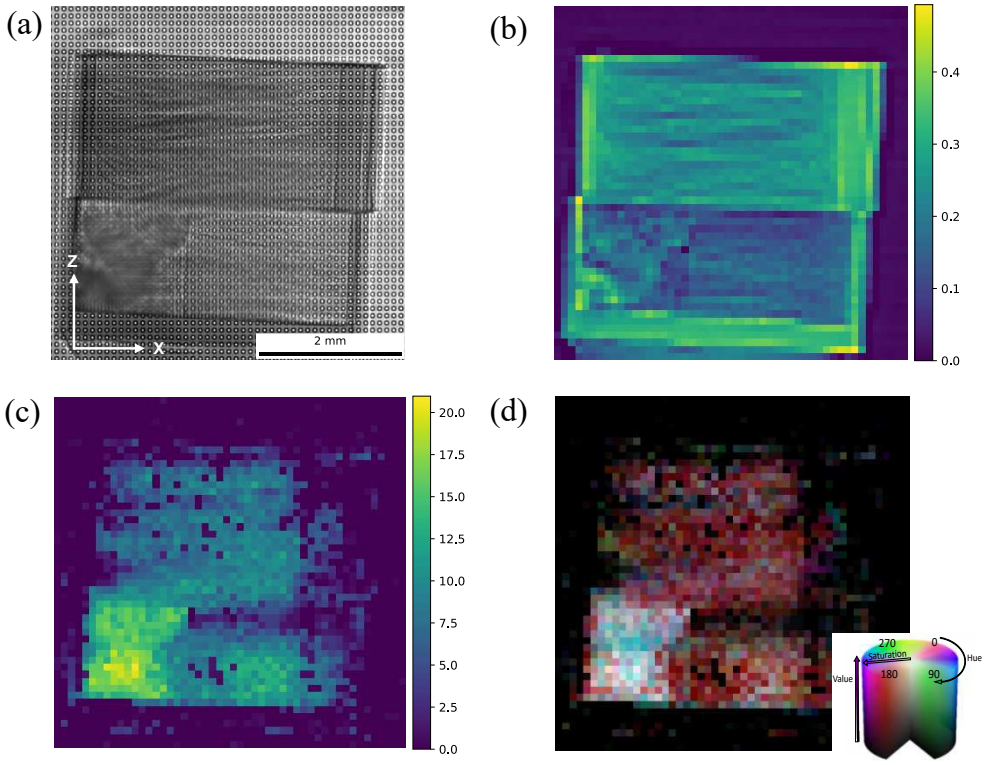

Figure 7.6: (a) Raw transmission image of the validation sample 2 with fractal array at $\alpha = 0°$, $\beta = 0°$. (b) Extracted absorption image, (c) mean scattering in arbitrary units and (d) main orientation signals.

camera, coupled with a 1:1 microscope optic, giving an effective pixel size of 6.5 µm. The exposure time for each projection was 100 ms and the FOV was 802×2560 pixels. In this case, the analysis window corresponds to a square whose size is 24 pixels or 156 µm. The computation time per projection was 20 s. The results in Fig. 7.7 demonstrate that, despite the lower visibility of the pattern compared to the grating scan, the proposed method allows for the extraction of both scattering and main orientation signals also for this kind of reference pattern. Fig. 7.8 is the result of the Fourier-space analysis on sample 2, obtained extracting the 2D scattering signal of two FOVs then stitched in a single image.

Random diffuser

Moving to a setup even easier to implement, sandpaper has proven to be an effective wavefront-marker for dark-field signal extraction. SBI images using three layers of P320 sandpaper as a wavefront marker were acquired at the SYRMEP beamline (Elettra Sincrotrone Trieste). For this application, the test sample was made of two sheets of unidirectional carbon fibres (10 µm diameter), glued together to form an angle of 90°. We used a filtered white beam with a mean energy of the detected photon beam of 37.6 keV. SBI scans were performed using the diffuser-stepping method, where the diffuser is laterally translated (20 different positions), while the sample remains

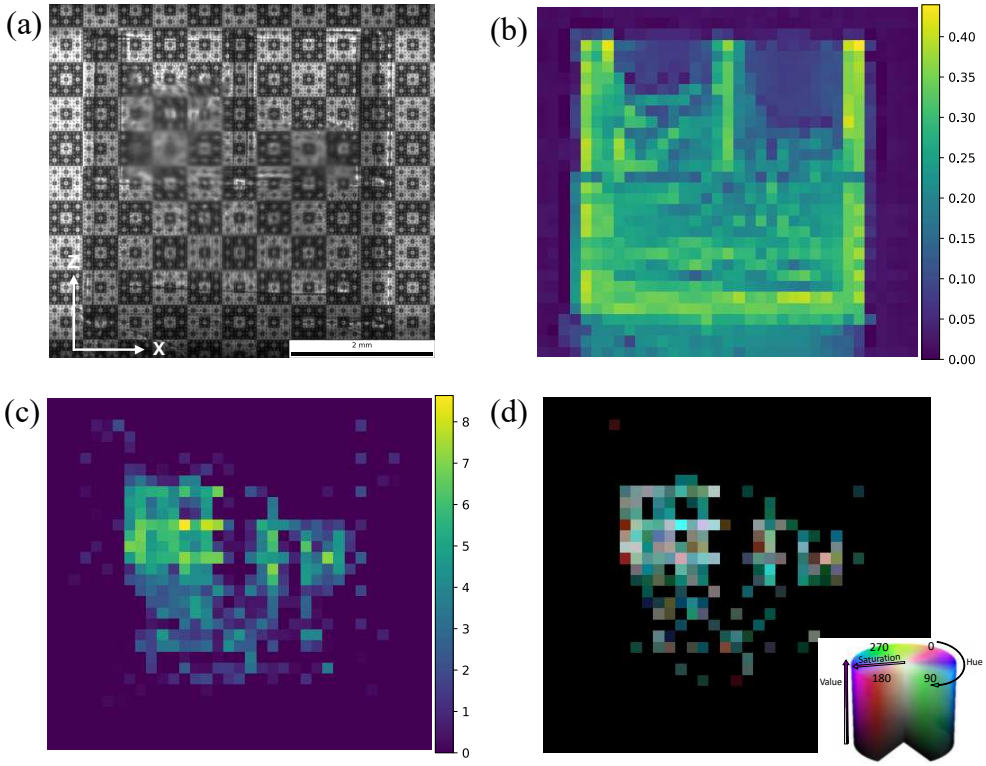

Figure 7.7: (a) Raw transmission image of the validation sample 1 with fractal array at $\alpha = 0°$, $\beta = 0°$. (b) Extracted absorption image, (c) mean scattering in arbitrary units and (d) main orientation signals.

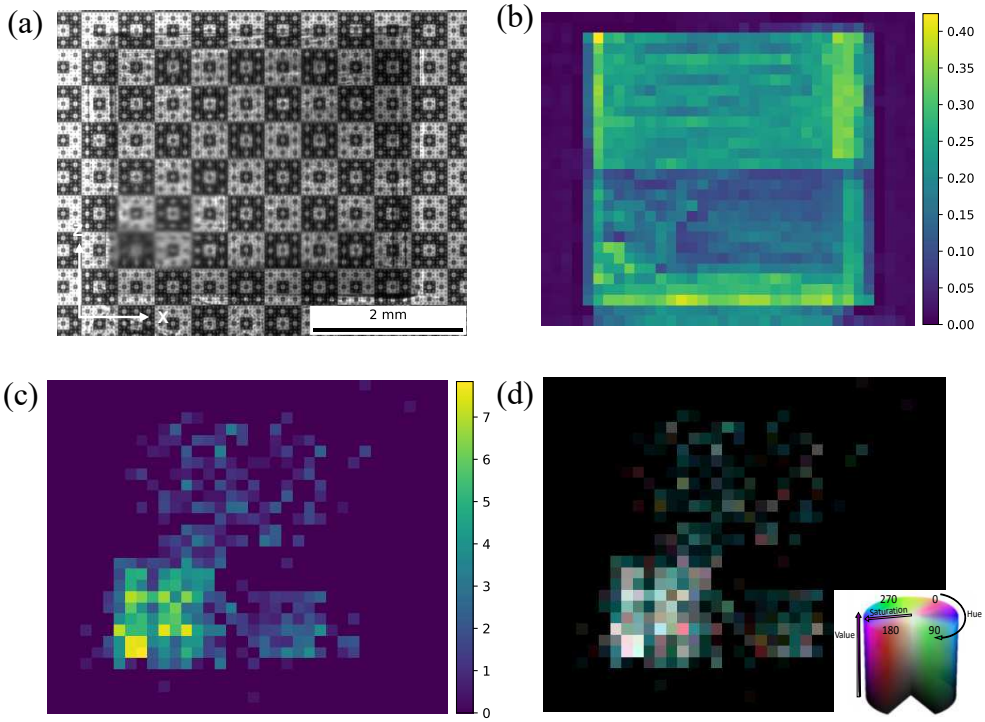

Figure 7.8: (a) Raw transmission image of the validation sample 2 with fractal array at $\alpha = 0°$, $\beta = 0°$. (b) Extracted absorption image, (c) mean scattering in arbitrary units and (d) main orientation signals.

stationary, to achieve a higher spatial resolution **[DeMarco2023]**. Images were acquired with a water-cooled sCMOS camera (Orca Flash 4.0, Hamamatsu) coupled with an X-ray microscope (Optique Peter). The optics were adjusted to have an effective pixel size of 3.82 µm. The detector was placed at a distance of 52 cm from the diffuser, while the diffuser-sample distance was 92.5 cm. The exposure time for each projection was 75 ms and the FOV was 1452×2048 pixels. The computation time per projection was 50 s.

Since the pattern created by the sandpaper is random, there is no periodic unit cells as for gratings, hence the analysis window can be of arbitrary size. We chose a square analysis window with size 6 pixels or 22.8 µm. This window is a good compromise between a high spatial resolution and a low noise level in the images. The computation time also plays a role in the decision of a proper analysis window. The optimal analysis window is chosen empirically, with the only limit that the size of the widow should be bigger than the speckle size. In the case of this validation sample, choosing a bigger analysis window will not affect the reconstructed orientations, but the final spatial resolution will be lower.

The results in Fig. 7.9d show that the main orientation signal matches with the expected orientation of the fibres (blue along the y-axis and purple at 45°), thus demonstrating the effectiveness of the proposed method for random reference patterns as well.

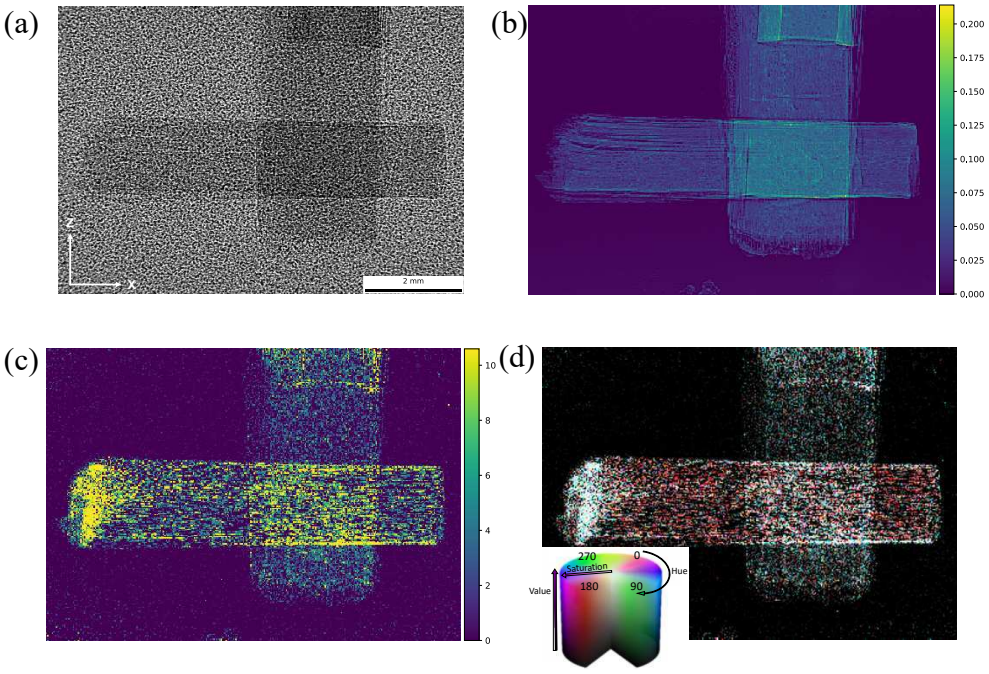

Figure 7.9: (a) Raw transmission image of a carbon fibre cross with speckles. (b) Extracted absorption image and (c) mean scattering signals. (d) Main orientation signals in green and red, contrast has been enhanced for visualisation purposes.

7.4.2 Tensor tomography reconstruction

Once the omnidirectional dark-field signal is extracted and Eq. 7.17 is known, it is sufficient to solve the linear system with CG. We validated our tensor tomography reconstruction for the circular gratings dataset, in order to compare our results with a previously established method validated only for circular gratings. However, the same analysis can be applied to datasets obtained with the other wavefront markers. The tomographic slices of sample 1 are shown in Fig. 7.10. Before reconstruction, all projections were aligned using a customized version of the alignment algorithm described in **[Liebi2015]**. Two axial slices are shown: one through the upper part of the validation sample, and one through the lower part. From the MS images, it can be seen that in each bundle, there exist clusters with varying local fibre densities rather than a consistent distribution of fibres. The fibre orientation signal images (Figs. 7.10c, 7.10f) show colour as an RGB representation of the local structure orientation. The reconstructed main orientations agree with the orientations of the fibres. However, within each bundle, there are local clusters with orientations that slightly deviate from the main fibre direction. This effect is caused by the fibres placed at the edges, that are bending along the wall, as verified by visual inspection and also by micro-CT measurements of the validation samples.

The same analysis has been performed on sample 2 (Fig. 7.11). The reconstructed main orientations line up with the expected fibre orientations. However, there are local clusters with orientations that stray from the main fibre direction owing to fibres placed at the edges, that are bending along the walls.

We applied our method also to the sample described in **[Kim2020]**. The only difference with the sample we already described is the orientation of the fibres, which in this case are placed along the three main axes. The fibre orientation signals are shown in Figs. 7.12c, 7.12f. Also in this case, the reconstructed main orientations agree with the orientations of the fibres. Local clusters of different orientations are also visible for this sample, as a result of fibres bending along the wall. The reconstructed orientations are comparable with those obtained with the previous method restricted to gratings **[Kim2020]**.

A 3D visualisation of the scattering tensor reconstruction of the validation samples is shown in Fig. 7.13. In this visualisation, each arrow's direction and colour represent the main orientation within its respective voxel. We have therefore validated that our method accurately reproduces structure orientations also in tomographic volumes and that the results, in the case of the circular grating array, are comparable with other reconstruction algorithms.

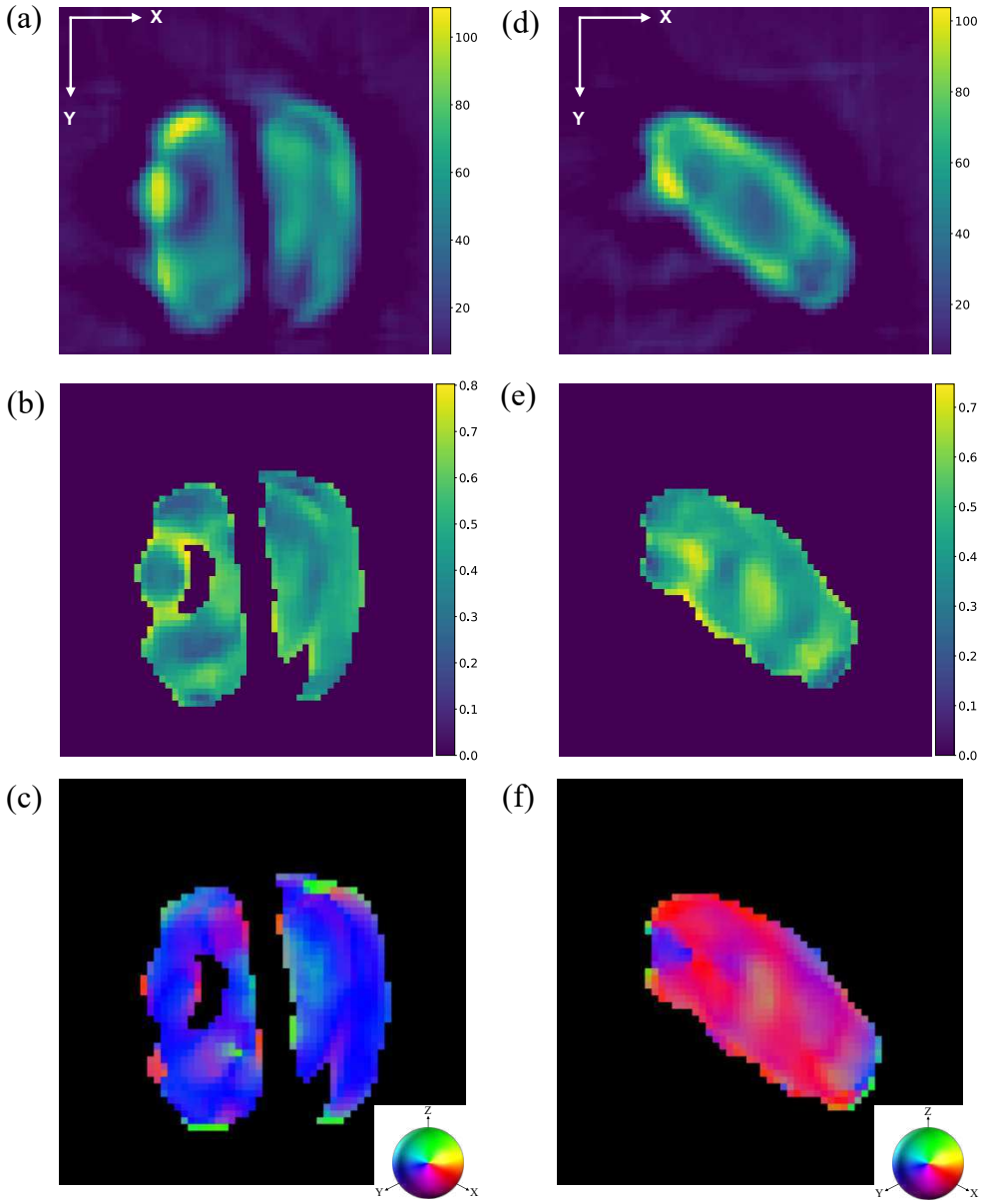

Figure 7.10: Axial slices through the upper (a-c) and the lower part (d-f) of the validation sample 1. (a,d) Mean scattering in arbitrary units and (b,e) scattering anisotropy signals in arbitrary units are shown. (c,f) Fibre orientation signals, where the colour is an RGB representation of the local structure orientation. The colour ball is symmetric with respect to the $x-y$, $x-z$, and $y-z$ planes.

7.5 CONCLUSIONS

In conclusion, this study introduces a general algorithm applicable to a wide range of X-ray imaging approaches that have access to the scattering signal, without the need for additional regularization. We have demonstrated its effectiveness for three different full-field dark-field imaging setups (gratings, fractal, and speckle). Then, we validated the results obtained with GI, comparing them with previous findings. The algorithm has enabled us to pave the way for tensor tomography using SBI, as well as using a fractal

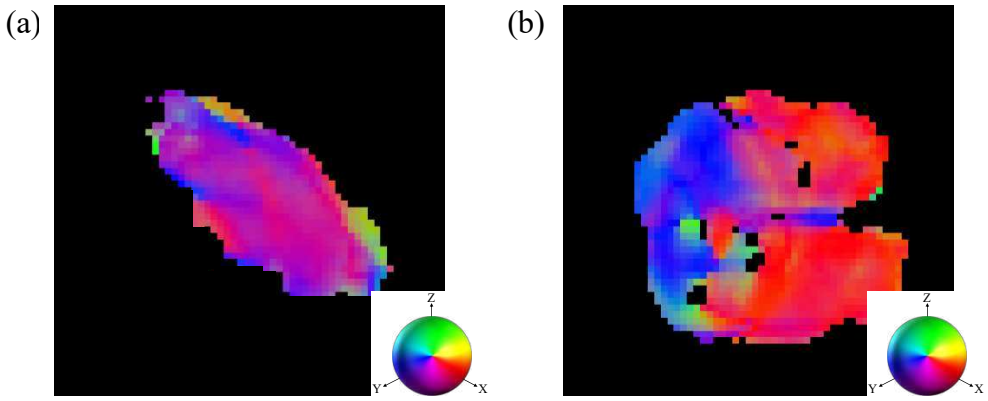

Figure 7.11: Axial slices through the upper (a) and the lower part (d) of the validation sample 2. Both figures show fibre orientation signals, where the colour is an RGB representation of the local structure orientation.

wavefront modulator. Our method allows for full reconstruction of tensor tomograms, with a simpler setup and simpler optics. Therefore, it has the potential to transition to laboratory setups, extending its reach to a wider user community. The main difference with previous works is the fact that we present a full-field method that can be applied to different wavefront modulators, also non-periodic. The scattering signal extraction and the tensor tomographic reconstruction are independent of the experimental geometry used in previous works. Moreover, we reconstruct the full tensor field, not only the scattering signal along predefined directions. Several disciplines can profit from this work, to mention only a few: medical physics to study the microstructural architectures of bones, and material physics to characterize fibre-reinforced materials.

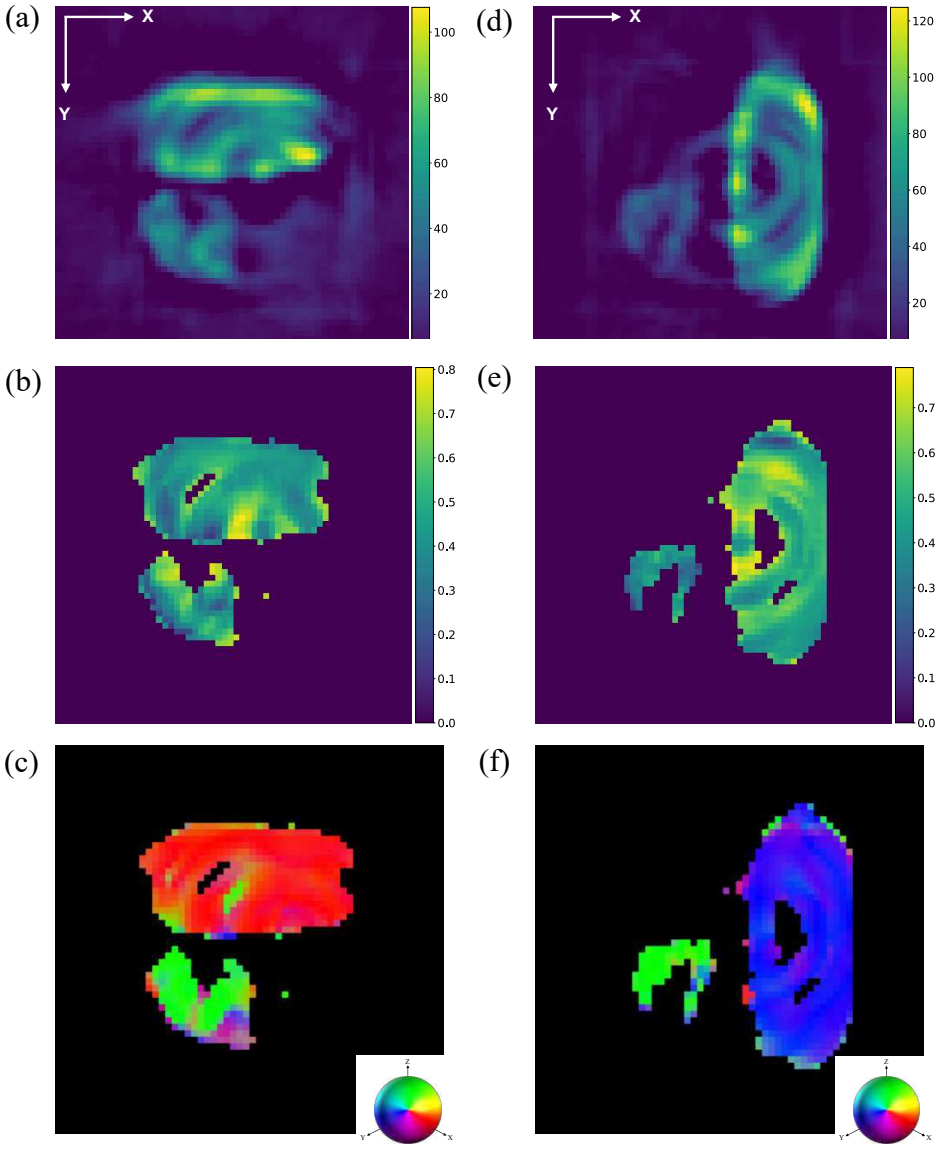

Figure 7.12: Axial slices through the upper (a-c) and the lower part (d-f) of the validation sample described in **[Kim2020]**. (a,d) Mean scattering in arbitrary units and (b,e) scattering anisotropy signals in arbitrary units are shown. (c,f) Fibre orientation signals, where the colour is an RGB representation of the local structure orientation.

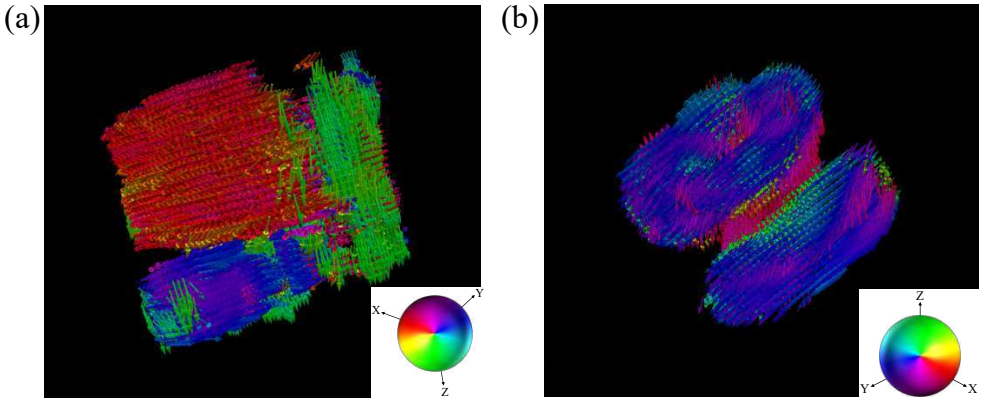

Figure 7.13: 3D visualisation of the reconstructed scattering tensor of (a) the validation sample described in **[Kim2020]** and (b) validation sample 1. In this representation, each arrow's orientation corresponds to the main direction in each voxel.

8 A ROBUST DARK-FIELD SIGNAL EXTRACTION FOR MODULATION-BASED X-RAY TENSOR TOMOGRAPHY

In this chapter, we present a method for the extraction of the directional dark-field signal tailored for data acquired with random diffusers that allowed us to perform the first reconstruction of speckle-based tensor tomography. We validate the effectiveness of the method for several carbon fibre composites, highlighting its potential for industrial applications. This chapter is a revised and expanded version of a paper accepted for publication on Applied Physics Letters: "Robust dark-field signal extraction for modulation-based X-ray tensor tomography" by Ginevra Lautizi, Vittorio Di Trapani, Alain Studer, Marie-Christine Zdora, Fabio De Marco, Jisoo Kim, Federica Marone, Marco Stampanoni and Pierre Thibault.

8.1 INTRODUCTION

Modulation-based imaging (MBI) exploits heterogeneous illumination patterns to locally encode the X-ray interaction with a sample. While a uniform illumination can normally reveal only the attenuating properties of the sample, a non-uniform X-ray illumination can be used to encode the otherwise invisible X-ray refraction and ultra-small-angle scattering effects in the sample **[Pfeiffer2008; Olivo2021]**. This concept is most commonly implemented with regular grid patterns, such as in (Talbot-)Lau interferometers **[David2002; Momose2003]**. Encoding and decoding of these signals can also be achieved with other types of illumination profile. In particular, speckle-based imaging (SBI) uses a diffuser, for instance one or more layers of sandpaper, to allow for extraction of the three complementary image signals: attenuation, refraction, and small-angle scattering, also known as dark-field signal **[Morgan2012; Berujon2012; Zanette2015; Zdora2018; Zhou2018; Zdora2021; DeMarco2023]**.

The X-ray dark-field signal is a manifestation of the small-angle scattering properties of a sample, which are caused by inhomogeneities in the local electron density at a scale smaller than the imaging system's resolution **[Pfeiffer2008]**. Samples with strongly oriented microstructural features often exhibit an anisotropic X-ray scattering profile. In these cases, the directionality of the scattering can also be extracted to reveal information about their orientation, e.g., of fibres in a composite material. This directional information is conventionally measured in small-angle X-ray scattering (SAXS) tomography

experiments **[Schaff2015; Liebi2015]**, and maps can be obtained by scanning a pencil beam on the sample **[Jensen2010]**. It is now known that MBI methods can also provide directional information through a careful analysis of the pattern distortions **[Wang2015; Kagias2016; Pavlov2021; Smith2022]**.

When measured for various orientations of the sample, two-dimensional directional scattering signals can be combined to tomographically reconstruct the local scattering tensor of the sample using X-ray tensor tomography (XTT) **[Malecki2014; Vogel2015; Schaff2015; Sharma2016; Sharma2017; Felsner2019; Kim2020]**. Compared to traditional X-ray microtomography, XTT enables the study of the microstructural organization in significantly larger volumes without the need for high spatial resolution of the imaging system **[Kagias2019; Kim2021; Kim2022]**. As a new microtomography modality, XTT has great potential for applications in different areas of research, such as the detection of wrinkling and fibre-waviness within fibre-reinforced polymers (FRPs) and the investigation of fibrous tissues in biological samples.

The fast full-field modality of MBI methods makes it an excellent contender for XTT applications **[Lautizi2024; Kim2021]**. While directional dark-field extraction methods have been developed for SBI, they tend to be slow **[Smith2022]** or otherwise lack robustness **[Wang2015; Pavlov2021]**.

In this chapter, we present a robust method for the extraction of the directional dark-field signal from data acquired with random diffusers. For a random diffuser, the signal extraction method described in Ref. **[Lautizi2024]** struggles when calculating the 2D scattering tensor in some regions for numerical instabilities caused by abrupt local variations in intensity. The main difference of our omnidirectional dark-field signal extraction method compared to earlier studies lies in the robustness and the versatility of our full-field method, which is applicable to various wavefront modulators, including non-periodic ones. We apply this approach to experimental measurements and demonstrate the first reconstruction of X-ray speckle-based tensor tomography.

8.2 MODEL

A full MBI-XTT dataset is made of multiple image acquisitions that encode complementary scattering information through diverse sample positioning. A schematic of our experiment is shown in Fig. 8.1.

Unlike conventional tomography, the dataset must contain multiple full tomographic scans (where the angle α is sampled over the full 360° range) taken at different tilts of the axis of rotation β. For each pair (α, β), multiple lateral displacements of the sample with respect to the patterned illumination are recorded, as is normally done with MBI methods.

The results presented in this letter were obtained from an experiment conducted at the SYRMEP beamline (Elettra Sincrotrone Trieste) using a filtered

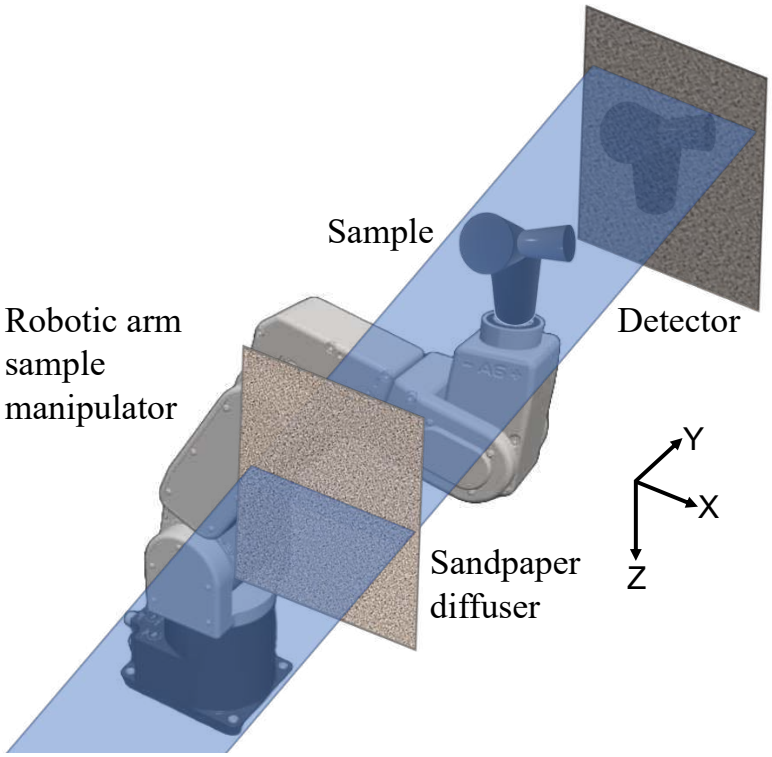

Figure 8.1: Schematic overview of the experimental setup. The X-ray beam is modulated by a diffuser mounted on a scanning stage upstream of the robotic arm, used as the sample manipulator. The detector system consists of a sCMOS camera with an X-ray microscope.

white beam with a mean energy of 37.6 keV. Using a filtered white beam, instead of a monochromatic beam, supports a successful translation to a laboratory-based setup.

To get lateral diversity, we employed the diffuser-stepping approach of SBI, which involves translating the diffuser to 20 different transverse positions while keeping the sample fixed **[DeMarco2023]**. The detector was a water-cooled sCMOS camera (Orca Flash 4.0, Hamamatsu) coupled with an X-ray microscope (Optique Peter), with an effective pixel size of 3.82 µm. The illuminated region of the sensor was 1452×2048 pixels, resulting in a field of view of $5.5 \times 7.8\,\mathrm{mm}^2$. We used three layers of P320 sandpaper as diffuser, having a speckle size of 6.3 pixels. In our experiment, the sample-detector distance was 52 cm, while the diffuser-sample distance was 92.5 cm. The exposure time for each projection was 75 ms. The sample manipulator was a Meca500 robotic arm (Mecademic Robotics, Montreal, Canada) with a repeatability of 5 µm and six degrees of freedom **[DiTrapani2024]**.

Extraction of the directional scattering information is done on pairs of images (with sample / without sample). The analysis is performed over a local window, which is translated to cover all the image. For each local window, the scattering signal can be modelled, in first approximation, as an anisotropic

Gaussian function. Therefore, for a single projection at a j-th diffuser position and for each local window, we can model the sample intensity pattern as

$$I_s^j(\mathrm{k}) = e^{-f(\mathrm{k})} I_0^j(\mathrm{k}), \tag{8.1}$$

where k is the Fourier transformed of the 2D pixel coordinates in each local window. $I_s^j(\mathrm{k})$ is the magnitude of the Fourier transform of the intensities with both the diffuser and the sample in the beam at the j-th diffuser position (sample image), and $I_0^j(\mathrm{k})$ the magnitude of the Fourier transform of the intensities with only the diffuser in the beam at the j-th diffuser position (reference image). $f(\mathrm{k})$ is a positive definite quadratic form that models the local attenuation and Gaussian scattering function $f(\mathrm{k}) = \mu + \frac{1}{2}(ak_x^2 + bk_y^2 + ck_xk_y)$.

With diverse speckle measurements, the trivial approach using $f(\mathrm{k}) = -\ln(I_s/I_0)$ is numerically unstable, assuming that the main source of instability is noise in the images. It is therefore necessary to combine information from all the measured frames obtained for multiple diffuser positions. Given $I_s^j(\mathrm{k})$ and $I_0^j(\mathrm{k})$, f can be found by solving the following non-linear least-squares problem:

$$\mathcal{L} = \sum_{j,\mathrm{k}} w_\mathrm{k}^j |I_s^j(\mathrm{k}) - e^{-f(\mathrm{k})} I_0^j(\mathrm{k})|^2 \tag{8.2}$$

The statistical weights w_k^j can be used to account for known uncertainties. Since I_s^j and I_0^j are discrete Fourier transforms of input data windows, these weights could be set proportional to the detector's modulation transfer function, if it is known.

Close to the optimal f, $\mathcal{L}$ can be linearized as follows. Let $I_s^j = e^{u_s^j}$ and $I_0^j = e^{u_0^j}$. It follows that

$$I_s^j(\boldsymbol{k}) - e^{-f(\boldsymbol{k})} I_0^j(\boldsymbol{k}) = e^{u_s^j} - e^{u_0^j - f} = e^{u_s^j}(1 - e^{u_0^j - u_s^j - f}). \tag{8.3}$$

Close to the solution, $u_0^j - u_s^j - f$ is expected to be small, so the exponential can be approximated to the first term of the Taylor series. We can rewrite $\mathcal{L}$ as

$$\mathcal{L} = \sum_{j,\boldsymbol{k}} w_{\boldsymbol{k}}^j |e^{u_s^j}|^2 |u_0^j - u_s^j - f|^2. \tag{8.4}$$

Labelling $w_{\boldsymbol{k}}^j |I_s^j(\mathrm{k})|^2$ with $W_{\boldsymbol{k}}$, it follows that

$$\mathcal{L} = \sum_{j,\mathrm{k}} \mathrm{W}_\mathrm{k}^j \left| f - \ln\left(\frac{I_0^j(\mathrm{k})}{I_s^j(\mathrm{k})}\right)\right|^2. \tag{8.5}$$

This is now a weighted linear least-squares problem of the form $\mathcal{L} = |\mathrm{A}x - b|^2$, which can be solved readily using existing routines. It is worth noting that if $I_s^j(\mathrm{k})$ is close to 0, the numerical stability is assured by the weight $W_\mathrm{k} \propto |I_s^j(\mathrm{k})|^2$.

We obtain the 2D scattering tensor for each local window from (8.5). The 2D scattering tensor can then be eigendecomposed to obtain eigenvalues and eigenvectors. The mean of the eigenvalues represents the mean scattering signal, the fractional anisotropy **[Basser1996]** describes how well-aligned the fibres are in each voxel, and the eigenvector with the shortest length is associated with the preferential local fibre orientation.

8.3 SOFTWARE ARCHITECTURE

The layout of the data acquired for this analysis is not optimal for our data analysis algorithm. Therefore, we had to rearrange the layout by manipulating memory. This is done with memory mapping (`mmap`) of all the files without consuming system memory. Indeed, the files are only virtually open because they are memory mapped. Regions of files are therefore accessed as needed, and the main overhead is the I/O time of the disk.

The original layout can be summarised as follows. The acquired data is saved in four `.his` files for each tilt angle and for each diffuser step, containing the dark images, the flat images, and the reference images. Moreover, each sample image file contains all the projections.

To access the images in a memory efficient way, we memory mapped all the files. We used the concept of "lazy computation" to open all the files at once, and treated the content like it is in the system memory, even if it is not. It is also possible to easily select a region of interest or a subset of projections, and work only with it.

Then, we use a class called `DataCollection` that represents a data collection (dark, flat, reference, sample images) for all the diffuser steps, but for a single tilt angle.

The images are normalised for flat and dark in the class `DataReduction` allowing also the optimisation of the diffuser positions, correcting eventual motor instabilities.

In the class `DataExtraction` we calculate the transmission for each projection using UMPA and we divide the sample image by this transmission in order to have an image where only the small-angle scattering signal is present.

The analysis code proceeds similarly to what was described in subsection 7.2.2. The main difference is that here we have different diffuser positions. In this case, the fit is calculated for each pair of sample-reference images and the weighted least-squares fit is implemented using the `lstsq` function of `numpy.linalg` on the model described in Eq. 8.5, where the weights are calculated as $|I_s^j(\mathbf{k})|^2$. This approach assures the numerical stability.

The algorithm was parallelized also for tilt angles, having a worker for each tilt angle. In addition, each tilt angle is processed with an async Python

function. The log output of the code is created using `structlog` for the sake of clarity.

8.4 EXPERIMENTAL DEMONSTRATION

To validate the method, we acquired SBI projections of four different samples fabricated with carbon fibre materials. In all cases, we used an analysis window of 6×6 pixels. The computation time per projection was 50 s.

The first test sample was made of two sheets of unidirectional carbon fibres, with a mean diameter between 5 µm and 10 µm, glued together at an angle of 90°. This sample was already analysed with our previous reconstruction method **[Lautizi2024]**. The result of the 2D scattering analysis is shown in Fig. 8.2. Figure 8.2a shows one of the 20 frames that form the complete dataset. The strong scattering in the sample leads to locally blurred areas. The extracted absorption and scattering strength are displayed in 8.2b–c. In the latter, we see that beyond the strong scattering by the sharp edges, a clear scattering signal is also recorded within the sample itself. These two images correspond to the conventional, non-directional analysis generally done with SBI. Fig. 8.2d shows the full scattering tensor parameters using an HSV colour map. The hue represents the 2D fibre orientation calculated using the 2D eigenvectors with the shortest lengths, the saturation illustrates the fractional anisotropy, and the value is the mean scattering intensity. Comparison with our previous approach **[Lautizi2024]** (Fig. 8.2e) clearly demonstrates that our new algorithm proposed here is significantly more stable, resulting in improved image quality with reduced noise.

The results of the 2D scattering analysis on a second test sample are shown in Fig. 8.3. This sample was made using four rods cut and glued in four different positions. Each rod was made by unidirectional carbon fibres oriented along the rod lengths. The main-orientation signal confirms that the fibres run along the long axis of the rods.

The third test sample (Fig. 8.4) was made of two sheets of unidirectional glass-fibre tape (15 µm diameter), glued together at an angle of 90°. Also for this sample, the main-orientation signal confirms that the fibres run along the long axis of the sample. In the regions where the fibres cross at 90° the low saturation of the colours indicates a low anisotropy value. Indeed, with our model, a single orientation is extracted for each local window.

The last sample consists of a sheet of interwoven carbon and kevlar fibres, damaged in one point. The results of the 2D scattering analysis on this sample are shown in Fig. 8.5. It is interesting to notice that, while the damage is not visible in the absorption image (Fig. 8.5b), it is clearly recognisable in the mean scattering image (Fig. 8.5c, arrow). From the HSV representation of the main orientations (Fig. 8.5d) it is possible to see that the damage propagated mainly along the vertical fibres and also to which extent. This

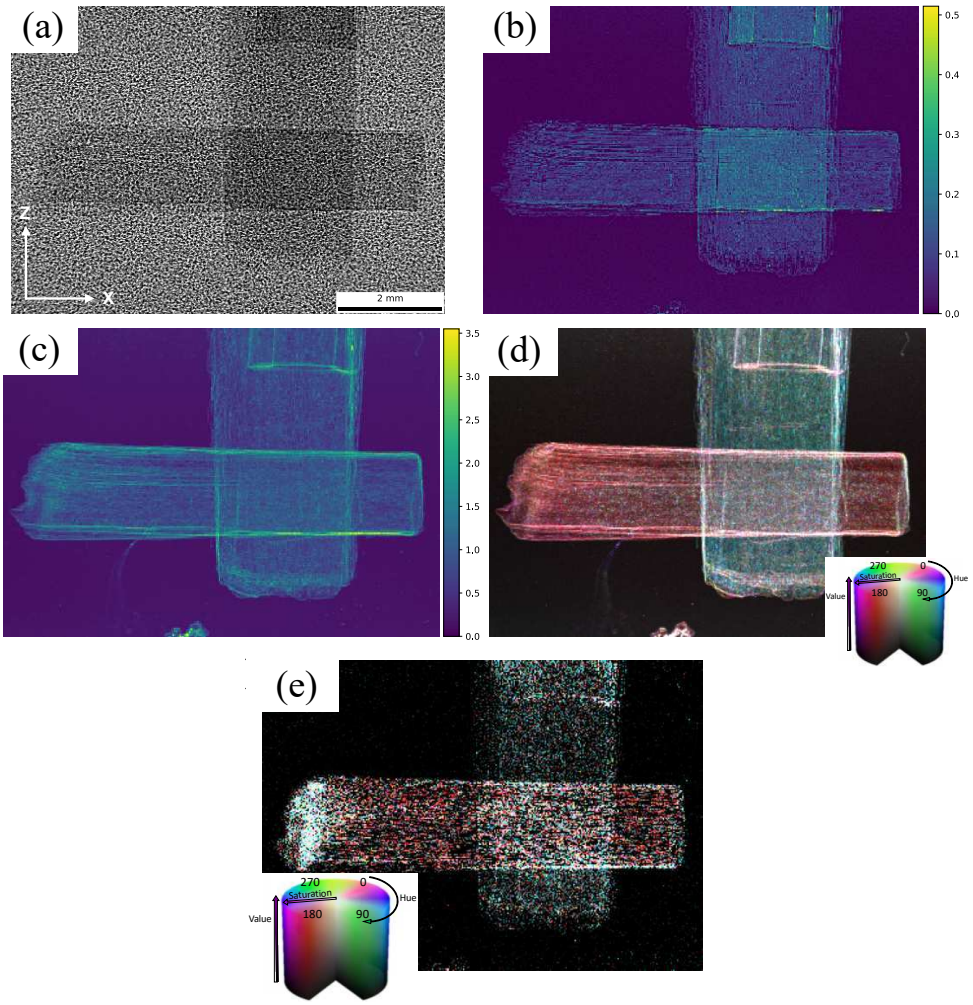

Figure 8.2: (a) Raw transmission image of a carbon fibre cross with speckles. (b) Extracted absorption image and (c) mean scattering signal in arbitrary units. (d) Main orientation signals (green and red). (e) Main orientation signals with the dark-field signal extraction method presented in **[Lautizi2024]**. Contrast has been enhanced for visualisation purposes by linear scaling.

non-invasive technique could be therefore used to quantify the severity and the extent of a damage which is neither visible from visual inspection of the surface nor by conventional X-ray computed tomography. A comparison of the damage extension with the Unified Modulated Pattern Analysis (UMPA) model is shown in Fig. 8.6c. A description of the UMPA model can be found in **[DeMarco2023; Zdora2017]**.

Following the demonstration of successful 2D orientation analysis, we show that our proposed algorithm enables X-ray speckle-based tensor tomography. For this demonstration, we performed XTT measurement of the carbon-fibre sample shown in Fig. 8.3. We used the stair-wise acquisition protocol described in Ref. **[Kim2020]** and **[Kim2021]**, varying the tilt angle β from 0° to 40°, with an angular step of 10°. For each angle β, we continuously rotated the sample over 360°, acquiring 360 projections with the setup shown in Fig. 8.1. This procedure was repeated for 20 different positions of the

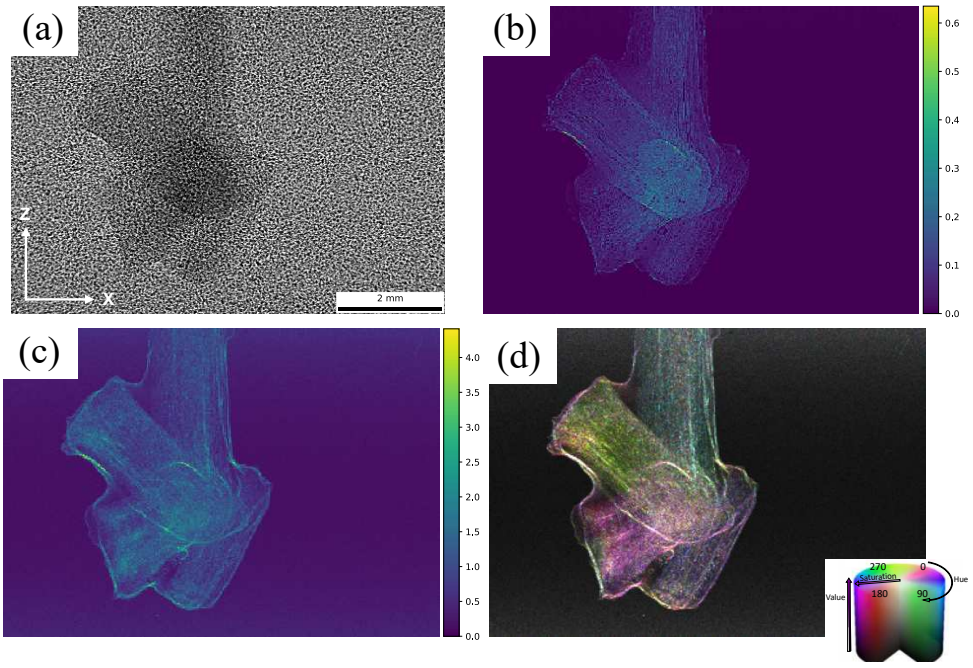

Figure 8.3: (a) Raw transmission image of four carbon-fibre rods with speckles. (b) Extracted absorption image and (c) mean scattering signal in arbitrary units. (d) Main orientation signals (green, yellow, pink, violet). Contrast has been enhanced for visualisation purposes by linear scaling.

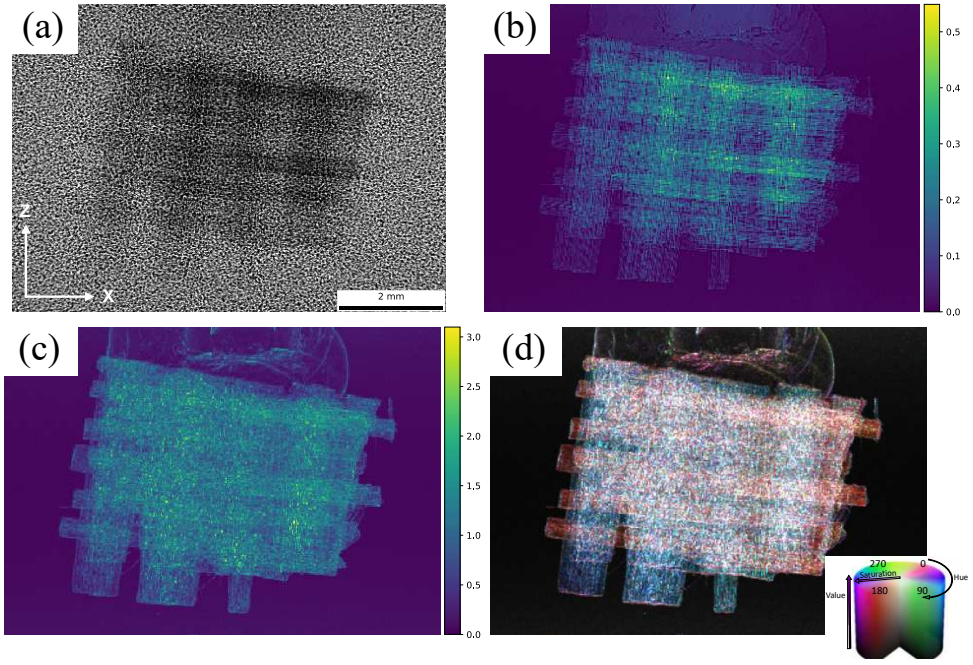

Figure 8.4: (a) Raw transmission image of two glued glass-fibre sheets with speckles. (b) Extracted absorption image and (c) mean scattering signal in arbitrary units. (d) Main orientation signals (cyan and red). Contrast has been enhanced for visualisation purposes by linear scaling.

diffuser. The omnidirectional dark-field signal was then extracted from all projections of the tomographic dataset, thus providing the 2D scattering tensor for each local window and for each projection. These results are

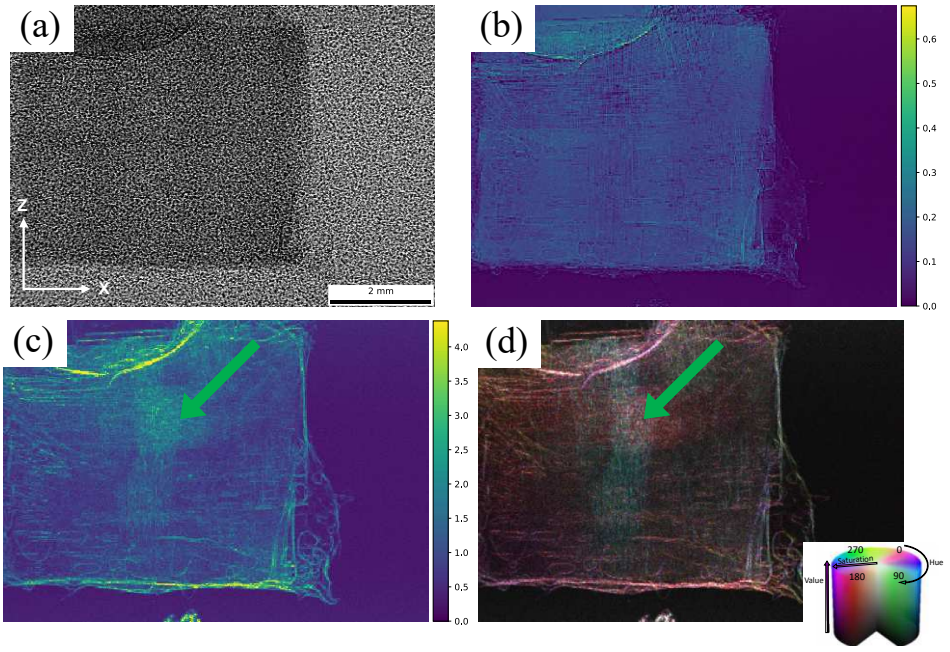

Figure 8.5: (a) Raw transmission image of a sheet of interwoven carbon and kevlar fibres with speckles. (b) Extracted absorption image and (c) mean scattering signal in arbitrary units. (d) Main orientation signals in green and red, contrast has been enhanced for visualisation purposes by linear scaling. The damage is indicated with an arrow.

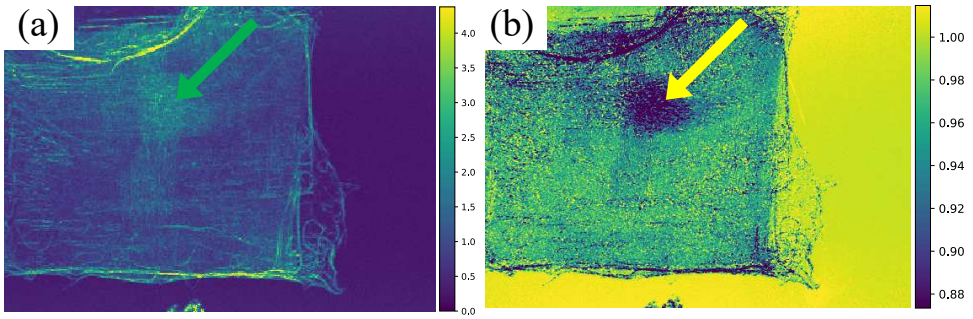

Figure 8.6: (a) Mean scattering signal in arbitrary units of a sheet of interwoven carbon and kevlar fibres. (b) Dark-field signal of the same sample extracted with UMPA model. The damage is indicated with an arrow.

combined to make the tensor sinogram to find the full scattering tensor field in 3D **[Lautizi2024]**. For this reconstruction, we used an analysis window of 6×6 pixels. The projections were aligned using a customised version of the alignment algorithm described in Ref. **[Liebi2015]**.

Tomographic slices of the tensor tomogram are displayed in Fig. 8.7. Three slices of the sample volume are shown: an axial slice (Fig. 8.7a), a coronal slice (Fig. 8.7b), and a sagittal slice (Fig. 8.7c). Since the local structure-orientation signal is prone to noise, in particular in background regions and at sharp edges, the tomographic volume was masked with a threshold-based mask that was both based on the average scattering and the absorption signals.

The glue used to fix the four parts of the sample contributed to the scattering signal and was therefore segmented out.

In the tomographic slices, the colour represents the local structure orientation of the fibres within each voxel, where the voxel size is given by the size of the analysis window. A 3D visualisation of the scattering tensor reconstruction of the sample is shown in Fig. 8.7d. Each arrow's direction and colour (RGB) represent the main orientation direction within a voxel.

As visible both in the tomographic slices and in the 3D visualisation, the four main orientations of the carbon fibre rods were extracted. At the edges, the colours are not perfectly uniform, which we attribute to damage to the rods during sample preparation and to unsegmented glue. We have therefore shown a successful tensor tomography reconstruction using speckle-based imaging.

8.5 CONCLUSIONS

In conclusion, we have presented the first demonstration of speckle-based tensor tomography. This achievement was made possible by developing a new method to optimally extract the X-ray directional dark-field signal for data acquired with a random diffuser. Formulating the problem with a weighted linear least-squares approach guaranteed the numerical stability needed for a successful reconstruction. We demonstrated the effectiveness of our approach for SBI projection scans of different samples and compared the results with previous findings on the same sample. The new algorithm proved to be more stable, resulting in less noisy dark-field images than our previous approach.

The proposed method, applicable to different data acquisition schemes, creates new opportunities for the applications of X-ray scattering tensor tomography using a non-periodic X-ray beam modulator. Our approach operates independently of the experimental geometries, reconstructing the full tensor field.

Thanks to its experimental simplicity, SBI has been demonstrated using laboratory setups **[Zanette2014; Zhou2015]**, hence speckle-based tensor tomography could also be performed using laboratory sources, thus reaching a broader community.

In the near future, we plan to modify the acquisition procedures testing a sample-scanning approach **[DeMarco2023]** rather than diffuser-stepping to increase the field of view, minimizing the acquisition time.

A current limitation of the model is that for each analysis window of a projection, a single orientation is extracted. Therefore, ongoing research is aimed at ensuring reliable reconstruction even in the case where multiple

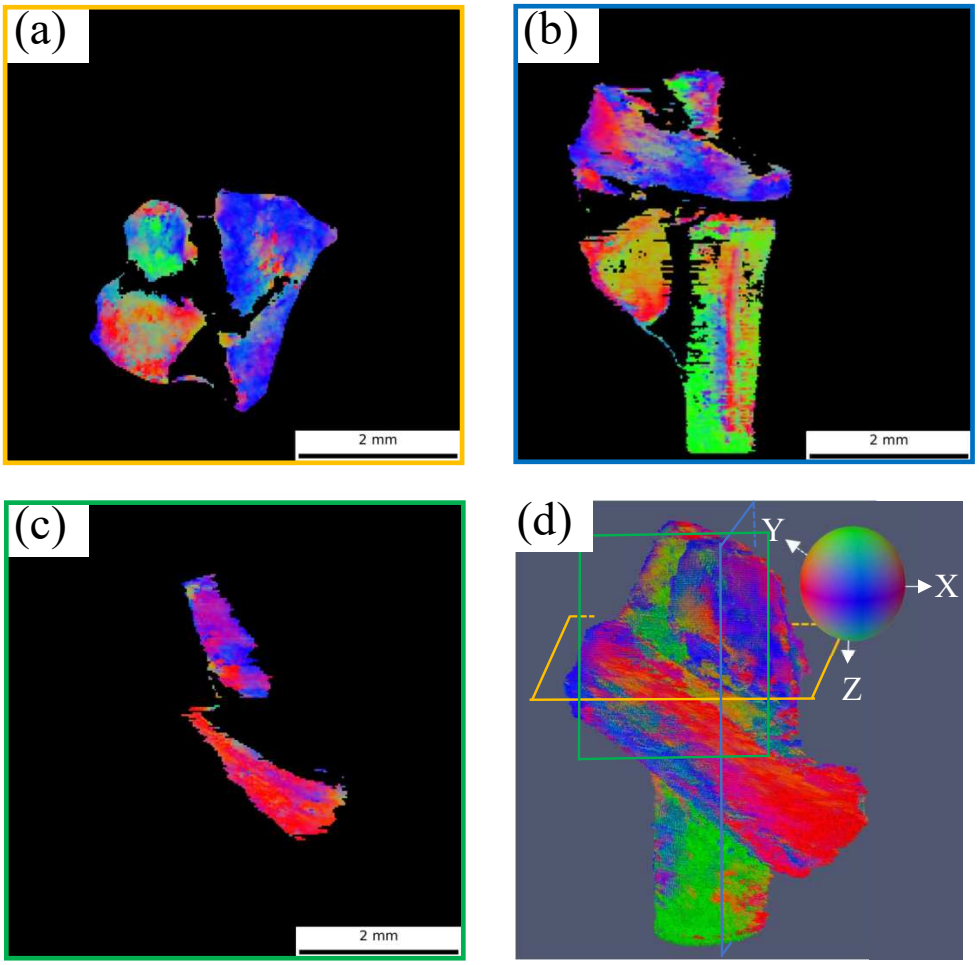

Figure 8.7: XTT image of a carbon fibre sample made using 4 unidirectional carbon fibres rods cut and glued in 4 different positions. (a) An axial slice, (b) a coronal slice and (c) a sagittal slice of the sample volume. The colour is an RGB representation of the local structure orientation. The colour ball is represented in (d) and it is symmetric with respect to the x - y, x - z, and y - z planes. (d) A 3D visualisation of the reconstructed scattering tensor. In this representation, each arrow's orientation corresponds to the main direction in each voxel. The colourful planes indicate the slices shown in the other panels.

scattering orientations overlap in a single analysis window, which could significantly enhance the versatility and robustness of this approach.

9 A NUMERICAL WAVE-OPTICS SIMULATION FOR SPECKLE-BASED IMAGING

In this chapter, we present a numerical wave-optics simulation model for speckle-based imaging (SBI). We validate the effectiveness of the simulation providing two examples: a SBI measurement of carbon fibre cross and an X-ray tensor tomography experiment on a cube containing three fibre bundles along three different orientations. The simulation is a versatile tool for investigating new experimental conditions for speckle-based imaging and tensor tomography experiments.

9.1 MODEL

9.1.1 Wave propagation model

The simulation model in this chapter is based on a wave-optical formulation, implemented primarily in Python and Cython, starting from the simple model explained in **[Zdora2015]**. The simulated experimental setup consists of an X-ray source, a diffuser, a sample, and a detector. The setup assumes a parallel beam originating from a distant source.

The wavefront propagation between components is calculated using the diffraction integral under the near-field Fresnel approximation. We consider a Cartesian coordinate system (x, y, z), with the positive z-axis being the optic axis. We then consider two parallel planes separated by vacuum, at $z = 0$ and $z = \Delta$, respectively, with $\Delta > 0$. An elementary plane-wave solutions to the Helmholtz equation can be written in the following form **[Paganin2006]**:

$$\psi(x, y, z) = \exp[i(k_x x + k_y y)] \exp\left[iz\sqrt{k^2 - k_x^2 - k_y^2}\right], \tag{9.1}$$

where (k_x, k_y, k_z) are the three components of the wave-vector $\boldsymbol{k}$ of the plane wave. The exponential factor is known as the "free space propagator". It follows **[Paganin2006]** that the propagated wave-field can be calculated as:

$$\begin{aligned}\psi_(x, y, z = \Delta) = \frac{1}{2\pi} \iint \hat{\psi}(k_x, k_y, z = 0) \exp\left[i\Delta\sqrt{k^2 - k_x^2 - k_y^2}\right] \\ \times \exp[i(k_x x + k_y y)]\, dk_x\, dk_y, \quad \Delta \geq 0.\end{aligned} \tag{9.2}$$

This expression is known as the angular-spectrum representation for the propagated wave-field. $\hat{\psi}(k_x, k_y, z = 0)$ is the Fourier transform of $\psi(x, y, z = 0)$ with respect to x and y.

The angular-spectrum representation for the propagated wave-field can be rewritten as:

$$\psi_\omega(x, y, z = \Delta) = D_\Delta \psi_\omega(x, y, z = 0), \quad \Delta \geq 0, \tag{9.3}$$

where D_Δ is known as the diffraction operator, and it is equal to

$$D_\Delta = \mathcal{F}^{-1} \left\{ \exp \left[i\Delta \sqrt{k^2 - k_x^2 - k_y^2} \right] \right\} \mathcal{F}. \tag{9.4}$$

Within the paraxial approximation, the diffraction operator becomes:

$$D_\Delta \approx \exp(ik\Delta) \mathcal{F}^{-1} \left\{ \exp \left[-i\Delta \frac{k_x^2 + k_y^2}{2k} \right] \right\} \mathcal{F}. \tag{9.5}$$

Therefore, recasting Eq. 9.3 in the form of a convolution integral and substituting the diffraction operator, Eq. 9.3 becomes:

$$\begin{aligned} \psi(x, y, z = \Delta) = -\frac{ik \exp(ik\Delta)}{2\pi\Delta} \exp \left[\frac{ik}{2\Delta} (x^2 + y^2) \right] \iint \psi(x', y', z = 0) \\ \times \exp \left[\frac{ik}{2\Delta} (x'^2 + y'^2) \right] \exp \left[-\frac{ik}{\Delta} (xx' + yy') \right] dx' dy' \end{aligned} \tag{9.6}$$

The wavefront after interaction with the diffuser is obtained by applying the projection approximation **[Born1999; Paganin2006; Meyer2021]** to compute the complex transmission function of the diffuser, which is then multiplied by the incident wavefront. The same procedure is performed for the sample and the resulting wavefront is recorded in the detector plane.

$$\hat{\psi}(x, y, z = \Delta) \approx \exp \left\{ -ik \int_{z=0}^{\Delta} [\delta(x, y, z) - i\beta(x, y, z)] \, dz \right\} \hat{\psi}(x, y, z = 0) \tag{9.7}$$

where δ and β represent the components of the refractive index ($n = 1 - \delta + i\beta$) distribution of the object, calculated for each material using the `xraylib` library. In this approximation, the object is treated as a projection of its complex refractive index along the thickness in the propagation direction, ignoring diffraction effects within the volume of the object. In this approximation, the object's complex transmission function is the exponential term on the right-hand side of Eq. 9.7. In the simulation, finite Fast Fourier Transforms (FFT) are used instead of the Fourier transform and its inverse operator.

9.1.2 Diffuser model

The simulated diffuser is made of one or more layers of sandpaper. Each sandpaper sheet includes a layer of randomly distributed silicon carbide (SiC) grains, a layer of glue, and a cellulose substrate.

The abrasive part of sandpaper is simulated by modelling the surface as a collection of SiC grains, which are represented as randomly oriented and randomly distributed cubes. Each SiC grain is modelled as a cube with a size that varies according to a Gaussian distribution, where the mean and the variance can be tuned. This distribution reflects the variability in grain size found in real sandpaper, where grains are not uniform, but have a range of sizes around the nominal value.

Once the grain sizes are established, each grain is randomly placed on the sandpaper surface. The individual grains are placed avoiding an excessive overlap of grains, which could otherwise result in a bigger grain size. The grains are also randomly oriented to simulate the manufacturing process of sandpaper. The 3D grains are then projected using the TIGRE library. The number of grains placed on the surface is proportional to the number of sandpaper layers.

After all grains are placed, the simulated abrasive surface is coupled with a uniform layer of glue, and a uniform layer of cellulose to mimic a real sandpaper diffuser.

9.1.3 Energy model

Speckle-based imaging experiments can be performed using different setup conditions. For instance, using a monochromatic beam at a synchrotron beamline. In this case, the X-ray beam has only one energy, which results in images that are almost artefact-free. However, most clinical and industrial setups use polychromatic beams with a spectrum of energies that may introduce artefacts, such as beam hardening. Simulating all these different conditions is essential in order to optimise imaging experiments.

Monochromatic Energy Model

The monochromatic energy model assumes that all photons in an X-ray beam share identical energy. This simplified model is particularly useful for applications requiring high precision in contrast and attenuation measurements, such as in synchrotron experiments. Monochromatic X-rays avoid the beam-hardening artefacts seen in polychromatic beams. However, this model is less common in conventional medical imaging, since it would require a specialized X-ray source producing a single-energy beam.

Polychromatic Energy Model

The polychromatic energy model is closer to what is found in standard X-ray tubes used in clinical and industrial contexts. In this case, photon of different energies interact differently with materials, resulting in an image subject to potential artefacts, such as beam hardening.

In simulating a polychromatic beam, different energy contributions are integrated according to their weights, which reflect how different energies are distributed along the X-ray spectrum. The weight for each energy is based on its relative contribution to the overall spectrum, for instance derived from a tungsten anode with a specific peak voltage (e.g., 80 kVp). The composite image is obtained by superimposing results from different wavelengths across the source spectrum

9.1.4 Simulating the images

The simulation is designed to be user-friendly, and it comes with a variety of features which can be tuned. For example, it allows for the selection of different beam types (monochromatic or polychromatic), setup configurations (parallel beam, cone beam), and source sizes (infinite or finite). Additionally, other parameters can be tuned, such as the energy, the propagation distances, the pixel size, the field of view, the sandpaper type, and the number of diffuser steps. A schematic overview of the simulated setup is shown in Fig. 9.1.

After the geometry and the parameters are chosen, the diffuser is generated. A defined number of SiC cubes are generated, according to the chosen distribution of grain sizes, and randomly placed and oriented. The projection approximation (Eq. 9.7) is then used to calculate the altered wave-field exiting the diffuser. Subsequently, the wave-field propagation equation (Eq. 9.3) is used to propagate the wave-field in vacuum from the diffuser plane to the sample plane.

At this stage, the 3D sample is generated or loaded. Since the dark-field signal is the result of spatially-unresolved random microstructures in the sample, the simulation process takes place in an artificially super-resolved space. The final images (reference and sample images) are then rebinned to the actual experimental field of view before the output is saved. In this way, the simulated microstructures become unresolvable in the final configuration, and their contribution to the dark-field signal can be studied. The 3D sample is then projected, using the TIGRE library, according to the selected projection angles and tilt angles. The following process is iterated for each projection.

The projection approximation is used again to calculate the altered wave-field exiting the sample. In addition, the wave-field propagation equation is used to propagate the wave-field in vacuum from the sample plane to the detector plane. If a cone-beam geometry is selected, and the propagation of a spherical

wave is required, the geometry of the divergent beam is converted into an equivalent parallel beam using the Fresnel scaling theorem **[Munro2019]**. To mimic a speckle-based experiment, different diffuser positions are simulated, and the diffuser is shifted to the chosen positions before the wave-field is propagated from the sample plane to the detector plane. The squared magnitude of the wave-field is then calculated, being the intensity of the detected image. The final images are then rebinned to the actual experimental field of view.

A detector point spread function of two pixels FWHM (full width at half maximum) is assumed. The simulated results are therefore smoothed with a Gaussian smoother with a standard deviation of $(2/2.355) \times \textit{pixel size}$. Additionally, to account for the extended focal spot size, it is possible to blur the images using a Gaussian smoother, where the full width at half maximum is scaled according to the divergent beam geometry. A Poisson noise can also be added to the intensities, given a mean number of photons per pixel.

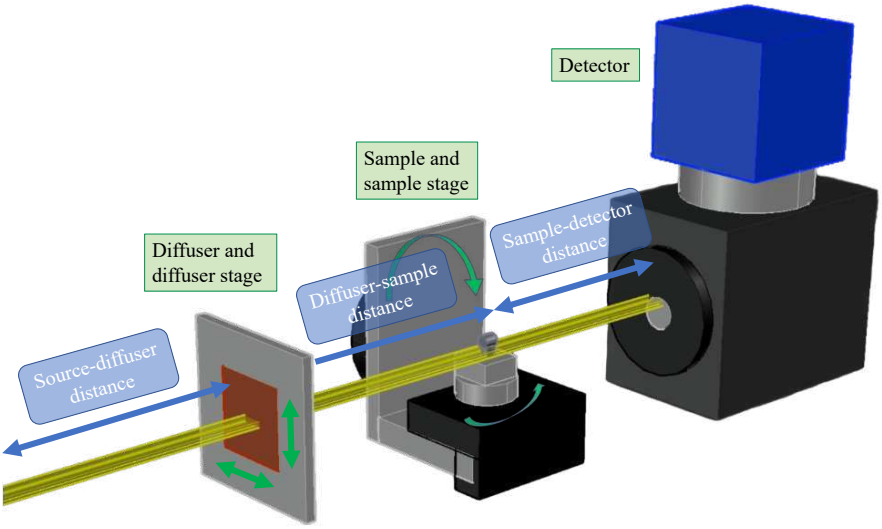

Figure 9.1: Schematic overview of the simulated setup. The X-ray beam can be monochromatic or polychromatic, in a parallel or cone-beam geometry. The beam is modulated by a diffuser that is shifted to match different diffuser positions. The sample is located downstream the diffuser, and it is rotated and tilted. The detector system has a definite point spread function.

9.2 SOFTWARE ARCHITECTURE

```
Input Data:
  - Load simulation parameters from YAML file
  |
  v
Preprocessing:
  - Calculate derived experimental parameters (SimulatePair)
```

```
  - Generate or load sandpaper (generate_sandpaper)
  |
  v
Simulation Process:
  - Interact beam with sandpaper (interact_beam_with_sandpaper)
      -> Use projection approximation to calculate wave-field
        exiting the diffuser
  - Propagate wave-field to sample plane
    (propagate_speckle_to_sample)
      -> Use wave-field propagation equation (free space)
  - Generate or load 3D sample model (generate_sinogram)
      -> Use TIGRE library for sinogram generation
  - Generate sample projections (generate_sample)
      -> Altered wave-field exiting the sample based on
        thickness profile and refractive indices
  |
  v
Ground Truth Calculation:
  - Propagate without pattern (propagate_without_pattern)
      -> Use analytical formulae to calculate transmission and
        differential-phase signals
  |
  v
Final Image Calculation:
  - Define diffuser or sample stepping positions
    (define_positions)
      -> Different positions for the diffuser or sample
  - Calculate final intensities (interact_and_propagate)
      -> Squared magnitudes of wave-field at detector plane
  - Apply Gaussian smoothing (Gaussian smoother)
      -> Account for PSF of detector and source size
  - Rebin images (rebin)
      -> Apply binning factor to make microstructures unresolvable
  |
  v
Output Data:
  - Save or return the processed reference and sample images
```

The simulation is implemented primarily in Python and Cython, using an object-oriented approach, and it provides a `yaml` file for the choice of the simulation parameters.

In the `yaml` file different parameters can be tuned, for instance the energy, the propagation distances, the pixel size, the field of view, the sandpaper type, and the number of diffuser steps. Also the type of generated sample and its characteristics can be selected. Moreover, some flags allow introducing Poisson noise in the images, or simulating a finite source size. The number of tilts and equispaced projections can also be selected in this user-friendly file.

The whole imaging process is contained in a class called `SimulatePair`. Firstly, the experimental parameters that are derived from the ones already defined in the `yaml` file are calculated. For instance, the source size and the magnification of the system, among the other variables, are calculated in this stage. The following step is generating the sandpaper. This is done in the function `generate_sandpaper` which generates sandpaper as an array of SiC cubes, randomly tilted and oriented. A layer of cellulose acts as backing, together with a layer of glue. The sandpaper can also be loaded from a saved file if it has to be reused in a different simulated experiment. The projection approximation (Eq. 9.7) is then used to calculate the altered wave-field exiting the diffuser in the function `interact_beam_with_sandpaper`, starting from the calculated thickness profile, the given complex refractive indices, and the wavelength of the system. The wave-field exiting the sandpaper is then propagated in free space up to the sample plane using the wave-field propagation equation (Eq. 9.3) in the function `propagate_speckle_to_sample`. A 3D model of the sample is generated or loaded from a saved file in `generate_sinogram`. Given the rotation angles and tilt angles, the function calculates the sinogram containing all the projections obtained using TIGRE library. A given projection is then loaded in `generate_sample` and converted to the altered wave-field exiting the sample, starting from the calculated thickness profile of the projection image, the given complex refractive indices, and the wavelength of the system. The ground truth for the transmission signal and the differential-phase signals is calculated in `propagate_without_pattern` by propagating the wave-field in free space and using the analytical formulae. Different positions for the diffuser stepping or the sample stepping approach **[DeMarco2023]** are defined in the function `define_positions`. The final images intensities are calculated as the squared magnitudes of the wave-field that reached the detector plane in the function `interact_and_propagate`, where either the sample (sample stepping) or the reference (diffuser stepping) wave-fields are shifted of the amount specified by the positions. To the obtained reference and sample images, a Gaussian smoother is applied that takes into account the PSF of the detector and, if it is the case, the finite size of the source. Finally, in the function `rebin`, the reference and sample images are rebinned of the selected binning factor so that the simulated microstructures become unresolvable in the final configuration, and their contribution to the dark-field signal can be studied.

The class `SimulatePair` is then used in the appropriate function, depending on whether a monochromatic or polychromatic model is chosen. Excluding the generation of the sandpaper and the generation of the sample projections, the remaining process is iterated for all the projections and tilts.

The Cython code is used to speed up processes such as the generation of the samples and the sandpaper. Also the generation of the sample's projections using TIGRE and the generation of the diffuser/sample positions given the step size are contained in the Cython code. We believe that a detailed description of the numerous functions of the simulation is not suitable in this context. The interested reader is referred to the open access code.

9.3 SIMULATION OF A SPECKLE-BASED IMAGING MEASUREMENT

9.3.1 Simulation of a carbon fibre cross

The first example of application of the simulation is a speckle-based imaging measurement of a carbon fibre cross, to extract the 2D orientations of the fibres.

To represent carbon fibres in a bundle, we used Poisson disc sampling to pack discs. This method is optimal for producing distributions of points with a minimum distance constraint. With the Poisson disc sampling method, no two points, which represent the centres of the fibres, are too close to each other. Therefore, it is possible to mimic the random yet non-overlapping nature of the fibres in a bundle.

Firstly, the simulation space is defined in two dimensions, width and height. This the field-of-view (FOV) if only one bundle will be simulated, or part of the FOV if more than one bundle is present. Then, the sampling of the points is controlled by parameters such as the minimum allowable distance between points, which depends also on the fibre radius, and the number of candidate points generated around each reference point before it is rejected as being too close to others. The simulation space is divided into cells, where each cell can host a point, and therefore a fibre.

A random point is selected to initiate the process. Then, the algorithm tries to generate more points around this first point by randomly sampling within an annular region, defined by the minimum distance and twice that distance. In this way, every new point is far enough from the previously accepted points. If a good point is found, it is added to the list of samples and it is labelled as active. The algorithm will then try to create more points around the active one. The process continues until no more valid points can be generated around any of the active points, resulting in a set of points that will be the fibre centres in the bundle.

The next step is to grow the fibre bundle in a 3D simulation space. The radii of both the fibre bundle and the individual fibres are specified, with corresponding diameters calculated. A circular mask is applied to the domain to define the bundle's boundaries, ensuring that fibres are placed only within this circular region. Each fibre is represented as a small circle, arranged based on the previously generated Poisson disc sample points. The bundle is built layer by layer through the depth of the simulated space, so that the orientation of the fibres is continuous. Although not explicitly applied in this example, it is possible to twist the bundle by rotating each slice by a small angle, cumulatively adding up to a specified twist angle. This spinning step models the twisting of actual fibres in a yarn.

The final output consists of two arrays: one representing the fibre-filled bundle (epoxy resin) and another representing the unfilled regions (carbon).

An example is shown in Fig. 9.2. The 3D sample is then projected, using the TIGRE library, according to the selected projection angles and tilt angles. The projection approximation with the correct refractive indices (Eq. 9.7) is then used to calculate the altered wave-field exiting the sample plane.

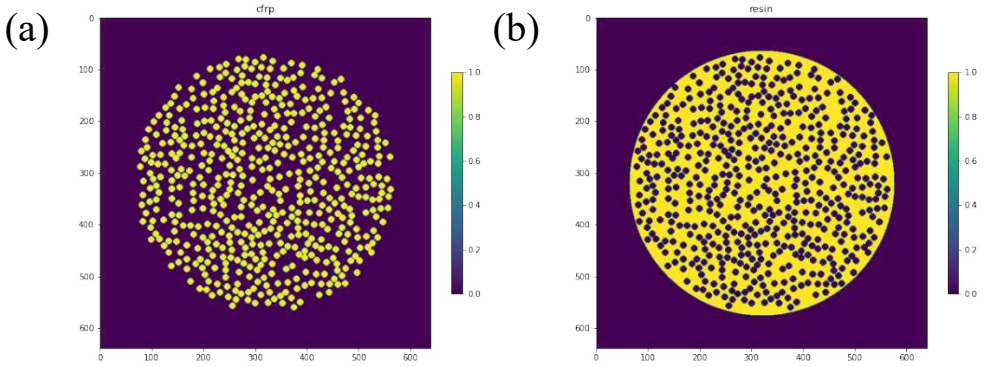

Figure 9.2: An example of an axial slice of the 3D volume of a carbon fibre bundle. (a) The single carbon fibres, placed in the bundle using Poisson disc sampling. (b) The inverse mask, representing the epoxy resin.

9.3.2 Parameters of the simulation

For this simulation, we used a parallel, monochromatic beam with an energy of 30 keV. The diffuser-sample distance is 0.25 m, and the sample-detector distance is 1.5 m. The diffuser was realised with cube SiC grains with average size of 25.8 µm. We generated 25 different diffuser positions. A schematic overview of a general simulated setup is shown in Fig. 9.1.

The sample consists of 3 bundles of 2000 fibres each. The number of candidate points generated around each reference point before it is rejected as being too close to others is 500. Each bundle has a diameter of 520 pixels. In the simulation space, the pixel size is 1 µm. The 3D simulated space for each bundle has a size of 650 pixels. This allows for empty spaces between the individual bundles. Each fibre has a diameter of 6.5 pixels. The FOV is 3000×3000 pixels. Two bundles are placed vertically and one bundle is placed horizontally to cross the other two bundles. The reference and sample images have been rebinned of a factor 12, so that the resulting FOV is 250×250 pixels and the effective pixel size is 12 µm.

9.3.3 Analysis of the results

Fig. 9.3a shows an example of an axial slice of the 3D volume of one of the three carbon fibre bundles. A projection of the 3D sample at rotation angle $\alpha = 0°$ and tilt angle $\beta = 0°$ is shown in Fig. 9.3b. For this example, we were mainly interested in a fast extraction of the omnidirectional dark-field signal, so only one projection was generated.

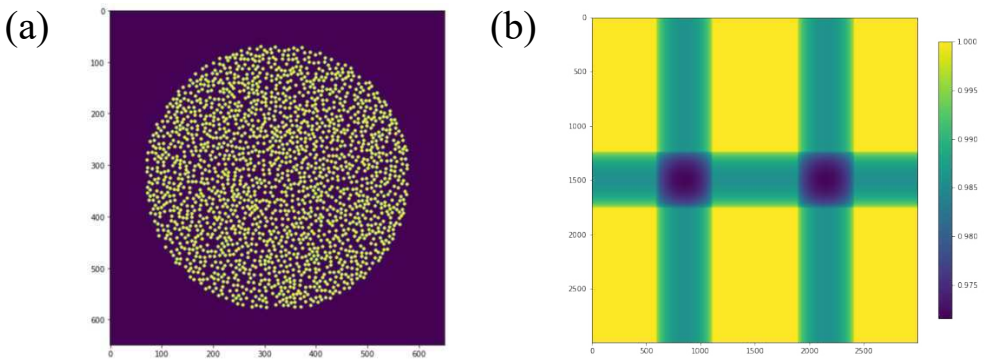

Figure 9.3: The simulated sample. (a) An example of an axial slice of the 3D volume of one of the three carbon fibre bundles in the simulated sample. (b) A projection of the 3D sample at rotation angle $\alpha = 0°$ and tilt angle $\beta = 0°$.

In Fig. 9.4a the diffuser thickness map is shown, before the binning procedure. The diffuser was realised with cube SiC grains with. The average grain size of 25.8 µm corresponds to a P600 sandpaper. Three layers were generated. The visibility of the reference pattern is determined as the ratio of the standard deviation to the mean intensity value of the reference image. The visibility map is then computed using a Gaussian filter, with a kernel size of 5 pixels. The visibility map shown in Fig. 9.4b is not homogeneous all over the FOV, and its mean value is 52.38%.

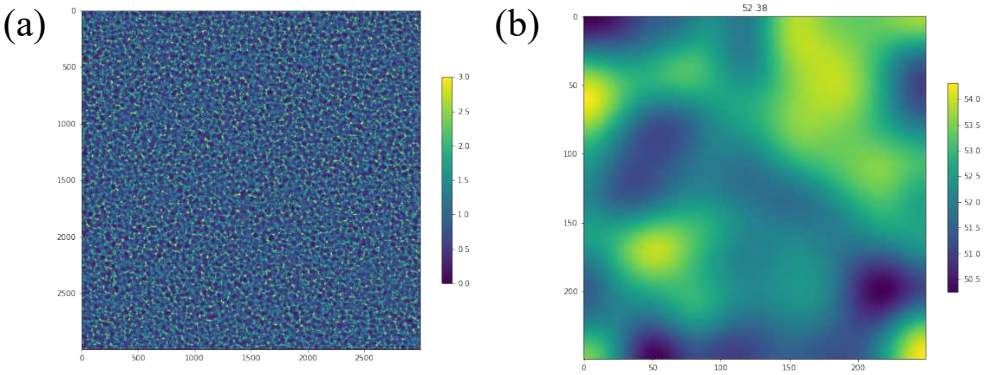

Figure 9.4: (a) The diffuser thickness map before the binning procedure. (b) The visibility analysis of a reference image.

We used UMPA algorithm to process the sets of 25 sample frames captured at identical angles but different modulator positions, along with the 25 reference frames taken at corresponding modulator positions. The transmission, dark-field, and refraction angle signals for each projection in both the vertical and horizontal directions were generated by this procedure. The result of this analysis may be seen in Fig. 9.5.

The horizontal profiles through the differential-phase signal in the horizontal direction are then compared with the corresponding profiles obtained on the ground truth of the differential-phase signals. The latter quantities are calculated as follows:

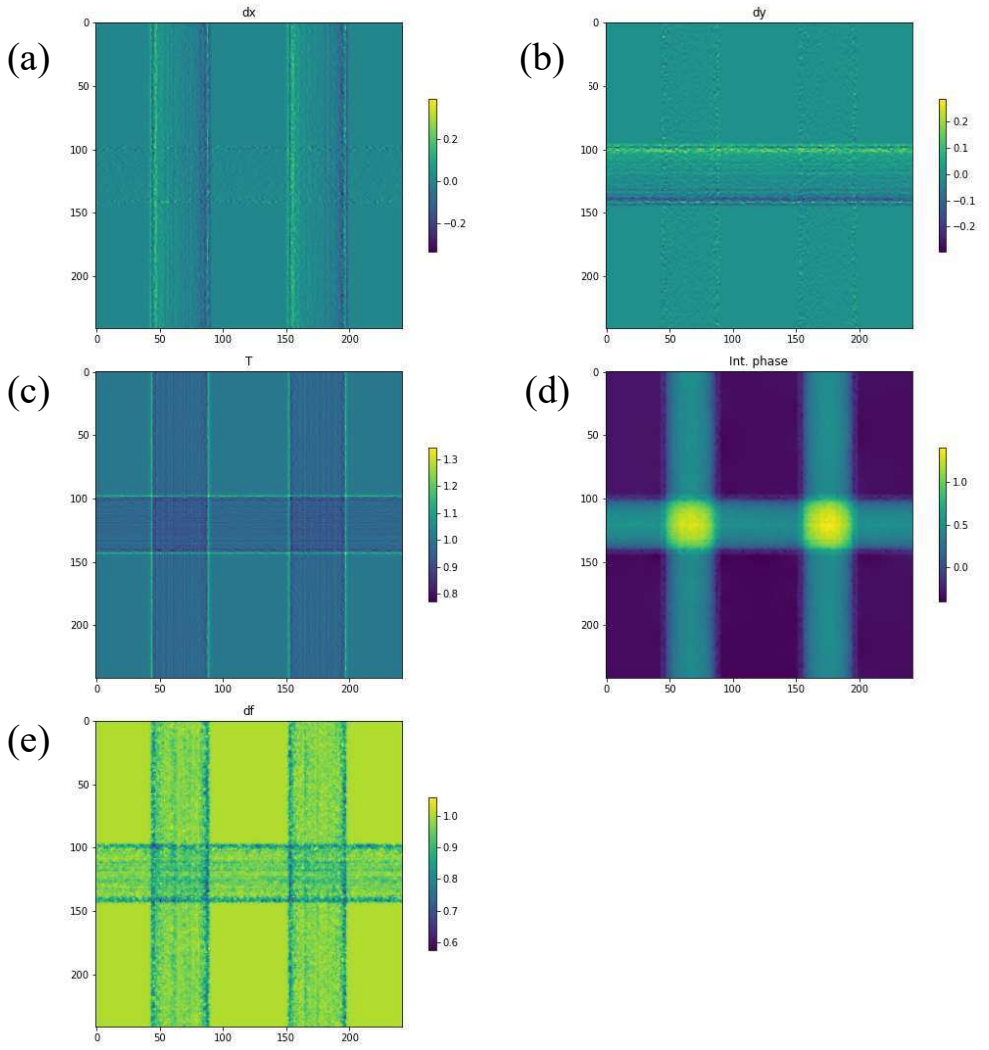

Figure 9.5: One projection of the simulated sample, obtained with SBI using UMPA algorithm. (a) The differential-phase signal in the horizontal and (b) vertical direction, reported in pixels. (c) The transmission, (d) the integrated phase, and (e) the dark-field signals.

$$\begin{cases} dx = -\frac{g_x \cdot d \cdot \lambda}{2\pi \cdot p^2} \\ dy = -\frac{g_y \cdot d \cdot \lambda}{2\pi \cdot p^2}, \end{cases} \tag{9.8}$$

where g_x and g_y are the gradients of the phase angle, d is the distance from the sample to the detector, λ is the wavelength, and p is the pixel size.

After having verified the correctness of the images analysed with UMPA, we checked the directionality of the fibres in the simulated bundles. Firstly, we calculated the magnitude, directionality, and orientation of the bundles, using the algorithm described in Ref. **[Smith2022]** (UMPA-DDF). A multi-resolution approach is used, with earlier steps in the process are the results of a run for a limited number of pixels. The results are reported in Fig. 9.7. We used a window size of 11×11 pixels and an UMPA step size in the final iteration of 5 pixels. In Fig. 9.7a-c, we show a composite HSV image of the extracted

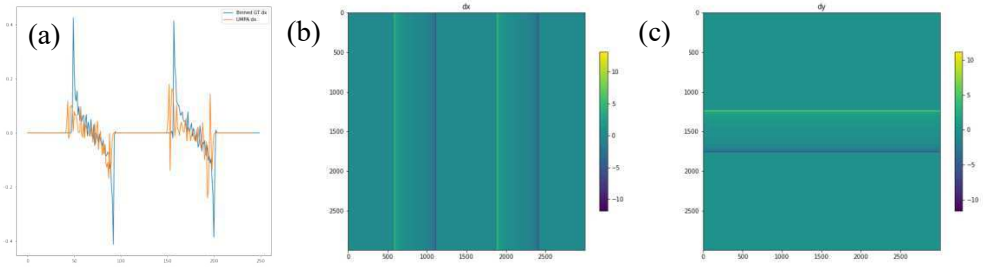

Figure 9.6: (a) A comparison of the horizontal profiles through the differential-phase signal in the horizontal direction of the analysed image and the ground truth image. The ground truth of the differential-phase signal in the horizontal (b) and vertical (c) direction, respectively.

directional dark-field signal in the three steps of UMPA-DDF. The magnitude of the directional dark-field signal (Fig. 9.7g), the directionality (Fig. 9.7h) and the orientation of the scattering (Fig. 9.7i) represents the hue, the saturation, and the value, respectively. In Fig. 9.7d-f the extracted transmission signals for the three steps. The main-orientation signal in the composite HSV image confirms that the fibres run along the long axis of the rods. The HSV colour map is identical to the one reported in Ref. **[Smith2022]**.

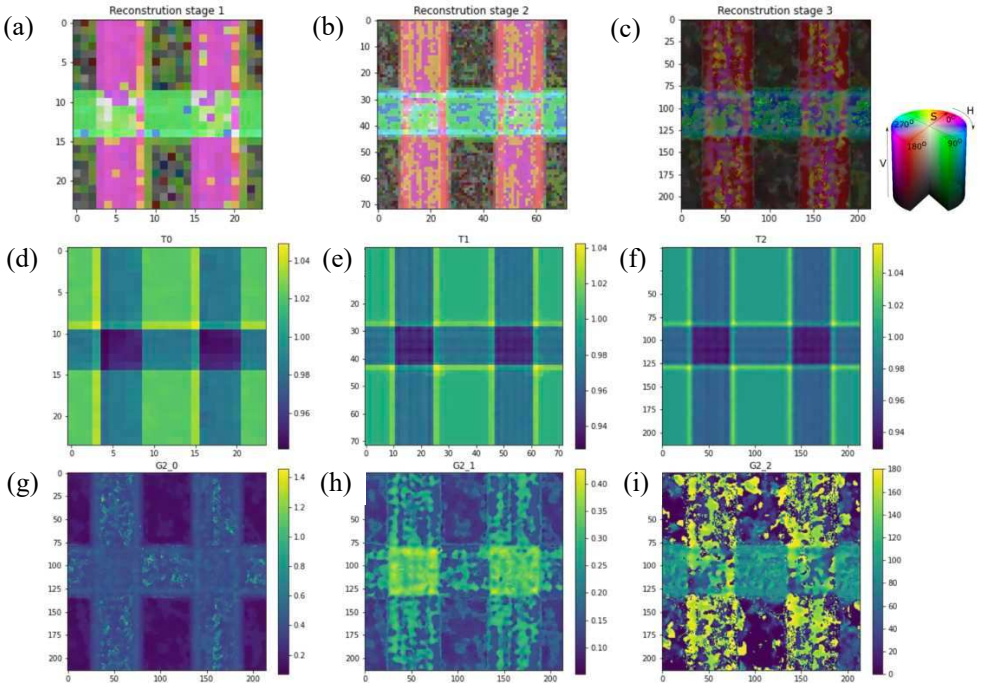

Figure 9.7: Directional analysis on one projection of the simulated sample, obtained with SBI using UMPA-DDF algorithm. (a-c) A composite HSV image of the extracted directional dark-field signal in the three steps of UMPA-DDF. (d-f) the extracted transmission signals for the three steps. (g) The magnitude of the directional dark-field signal in pixel units, (h) the directionality in arbitrary units (i) and the orientation of the scattering in degrees.

Moreover, the SBI images were analysed with the reconstruction method presented in Ref. **[Lautizi2024]** and in chapters 7 and 8. We used as the

analysis unit cell, i.e. the resulting spatial resolution, a square with size of 5 pixels or 60 µm, translated of 3 pixels to cover the whole FOV.

The results in Fig. 9.8d show that the main orientation signal matches with the expected orientation of the fibres (cyan along the vertical axis and red at 90°), thus demonstrating the effectiveness of the proposed method for a simulated dataset. It is worth noticing that here the HSV colour map is rotated of 90° with respect to the one presented in Fig. 9.7, so the colours appear switched. Also in this case, the main-orientation signal in the composite HSV image confirms that the fibres run along the long axis of the rods. In addition, the reconstruction of the omnidirectional dark-field signal was significantly faster: 2 s, compared to 12 min of UMPA-DDF.

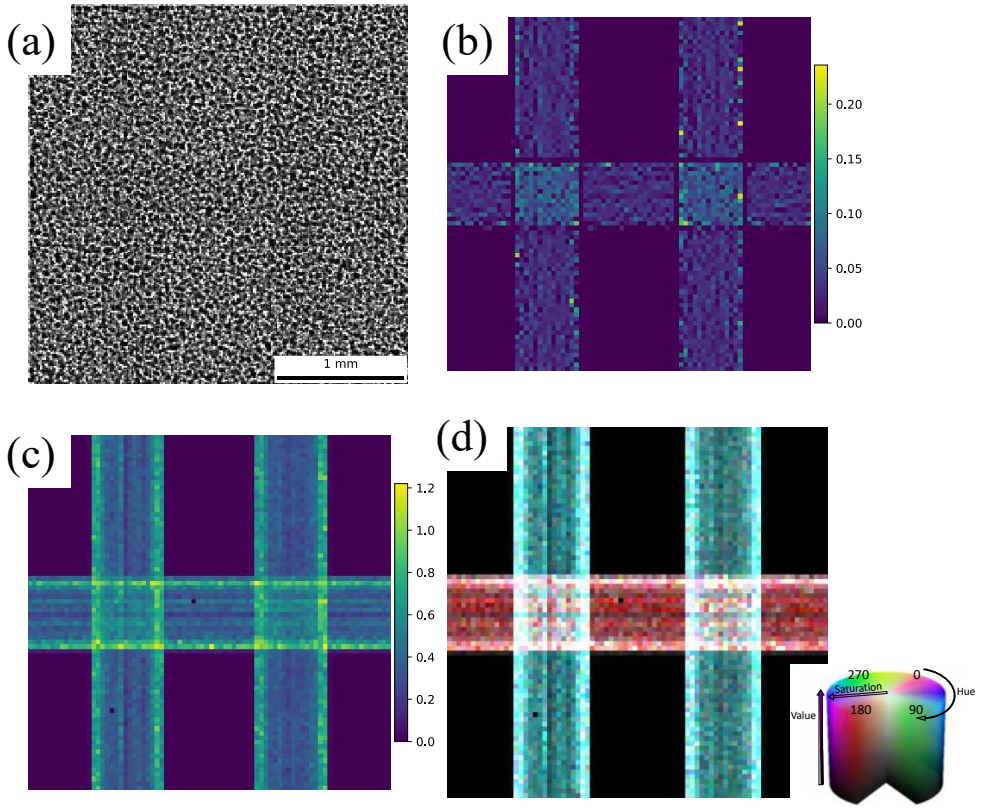

Figure 9.8: (a) Raw transmission image of a simulated carbon fibre cross with speckles at $\alpha = 0°$, $\beta = 0°$. (b) Extracted absorption image and (c) mean scattering signals in arbitrary units. (d) Main orientation signals in cyan and red, contrast has been enhanced for visualisation purposes.

9.4 SIMULATION OF AN X-RAY TENSOR TOMOGRAPHY EXPERIMENT

The last example of application of the simulation is an X-ray tensor tomography experiment, where the sample consists of three different carbon fibre bundles displaced along the three main axes, to extract the 2D and 3D orientations of the fibres.

9.4.1 Parameters of the simulation

For this simulation, we used a parallel, monochromatic beam with an energy of 20 keV. The diffuser-sample distance is 0.25 m, and the sample-detector distance is 0.1 m. The diffuser was realised with cube SiC grains with a mean size of 30 µm and a variance of the grain size distribution of 3 µm. We generated 6 layers of sandpaper and 20 different diffuser positions.

The sample consists of 3 bundles of 2000 fibres each. Each bundle has a diameter of 348 pixels. In the simulation space, the pixel size is 1 µm. Each fibre has a diameter of 5 pixels. The FOV is 1500×1500 pixels. Two bundles are placed vertically, and one bundle is placed horizontally to cross the other two bundles. The reference and sample images have been rebinned of a factor 6, so that the resulting FOV is 250×250 pixels and the effective pixel size is 6 µm.

For each tilt angle β, we acquired 360 projections with a continuous rotation of the sample over $\alpha \in [0°, 360°]$, while $\beta \in [0°, 20°]$ with an angular step of 5°. A schematic overview of a general simulated setup is shown in Fig. 9.1.

9.4.2 Analysis of the results

The sample consists of 3 bundles of 2000 carbon fibres each, placed in a cube along three different orientation. The fibres are placed using the Poisson disc sampling, as previously described. In Fig. 9.9 a 3D visualisation of the sample is presented, from two different point of views. Each bundle occupies a different corner of the cube. The first bundle is placed in the back-left corner and is oriented along the z-axis, with the fibres aligned accordingly along the main axis of the cylindrical bundle. The second bundle is located in the top-left corner, aligned along the x-axis. The third bundle is positioned in the bottom-right corner of the cube, aligned along the y-axis. The rest of the cube is empty, without any overlap between the three bundles.

In Fig. 9.10a a reference image is shown. The visibility of the reference pattern is determined as the ratio of the standard deviation to the mean intensity value of the reference image. The visibility map is then computed using a

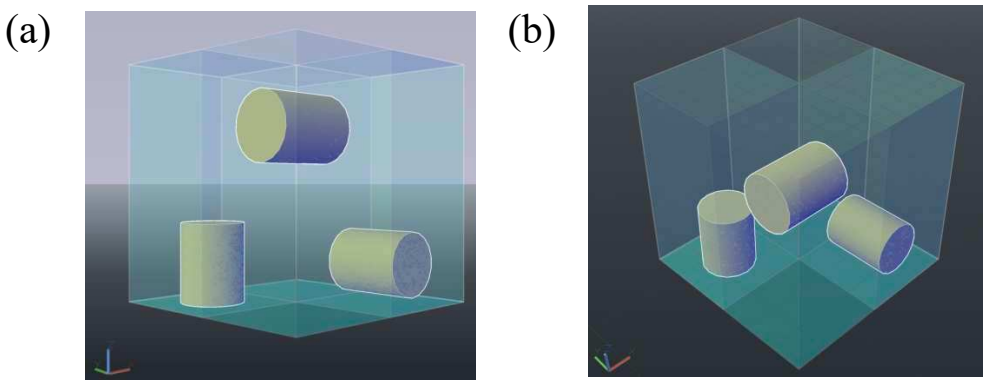

Figure 9.9: A 3D visualisation of the simulated XTT sample, viewed (a) from the side and (b) from the top.

Gaussian filter, with a kernel size of 5 pixels. The visibility map shown in Fig. 9.10b is not homogeneous all over the FOV, and its mean value is 52.36%.

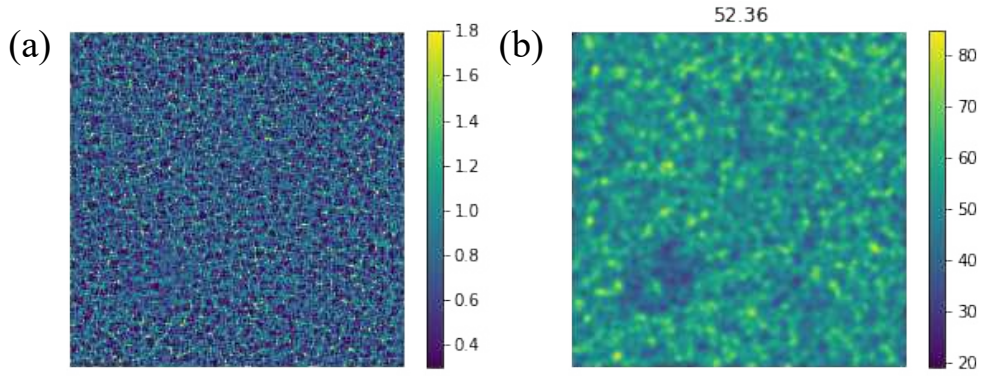

Figure 9.10: (a) A reference image of the XTT dataset and (b) the corresponding visibility analysis.

We used UMPA algorithm to process the sets of 20 sample and reference frames captured at identical angles but different modulator positions. We used a window size of 5×5 pixels and a step size of 3 pixels. Some transmission images obtained with UMPA for different rotation angles are shown in Fig. 9.11. This representation clarifies the positions of the bundles inside the cube.

The SBI images were analysed with the reconstruction method presented in Ref. **[Lautizi2024]** and in chapters 7 and 8. We used as the analysis unit cell, i.e. the resulting spatial resolution, a square with size of 6 pixels or 36 µm, translated of 6 pixels to cover the whole FOV. The results in Fig. 9.12d show that the main orientation signal matches with the expected orientation of the fibres (cyan along the vertical axis and red at 90°). In the bundle oriented along the beam direction (bottom-left in Fig. 9.12d) the fibres are mainly oriented perpendicularly to the plan of the image. This information is reproduced by a high mean scattering (Fig. 9.12c), but low fractional anisotropy, indicated by the low saturation in Fig. 9.12d (colour tending to white).

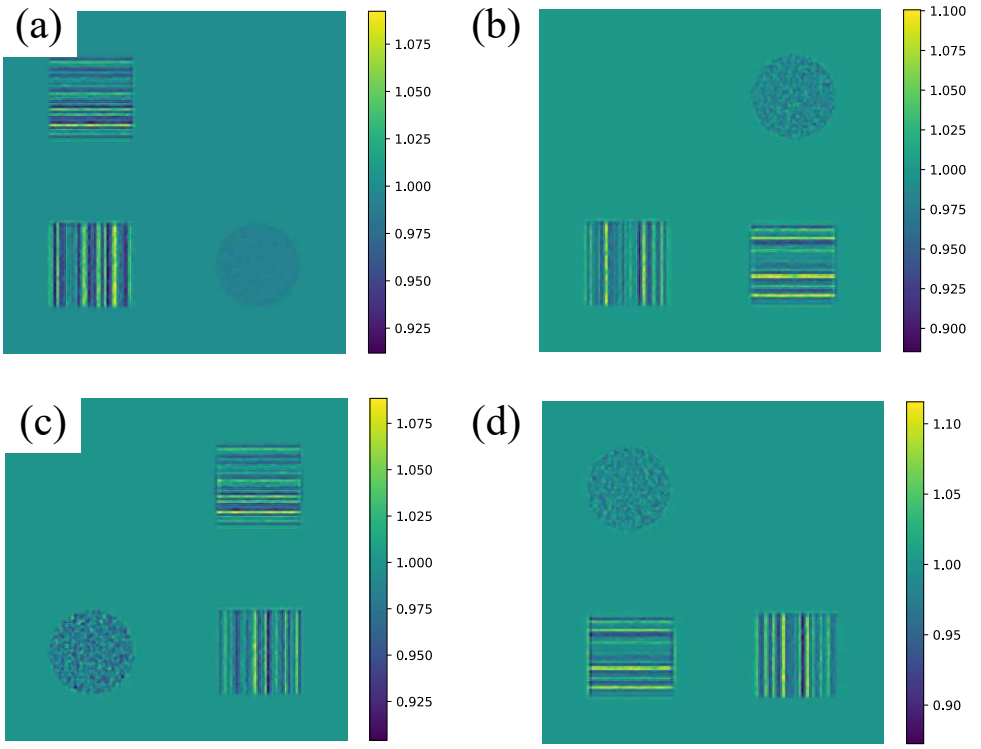

Figure 9.11: Four transmission images obtained with UMPA for different rotation angles: (a) $\alpha = 0°$, (b) $\alpha = 90°$, (c) $\alpha = 180°$, and (d) $\alpha = 270°$.

Following the demonstration of successful 2D orientation analysis, we show that our reconstruction method enables X-ray speckle-based tensor tomography for a simulated dataset. Two axial slices of the tensor tomogram are shown: one through the upper part (Fig. 9.13) of the cube, and one through the lower part (Fig. 9.14). Since the local structure-orientation signal is prone to noise, in particular in background regions and at sharp edges, the tomographic volume was masked with a threshold-based mask that was based on the average scattering. In the tomographic slices, the colour represents the local structure orientation of the fibres within each voxel, where the voxel size is given by the size of the analysis window. As expected, the bundle in the upper part of the cube is oriented horizontally along the x-axis, and it is therefore reconstructed with red colour in the main orientation signal (Fig. 9.13b). In the bottom part of the cube, the bundles are oriented vertically along the z-axis, reconstructed with green colour in the main orientation signal and along the y-axis, reconstructed with blue colour (Fig. 9.14b). When the tensor tomogram is reconstructed, a sphere mask is applied. This explains the shape of the bundles in the axial slices, cut at the edges by the sphere mask.

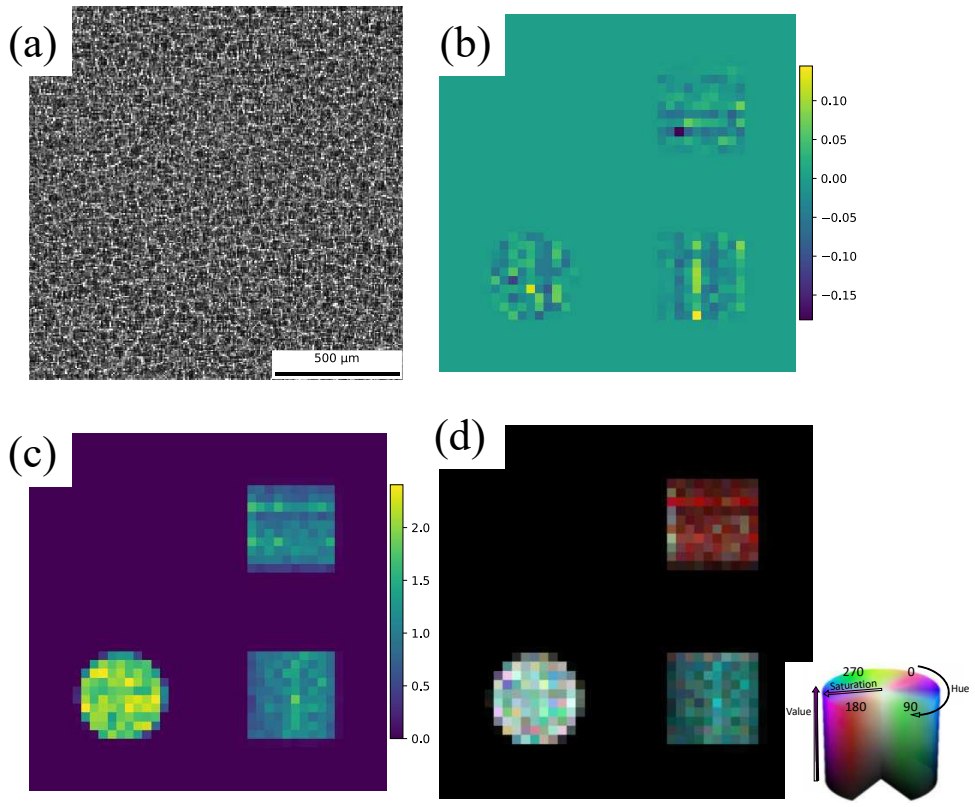

Figure 9.12: a) Raw transmission image of a simulated cube with speckles at $\alpha = 180°$, $\beta = 0°$. (b) Extracted absorption image and (c) mean scattering signals in arbitrary units. (d) Main orientation signals in cyan and red.

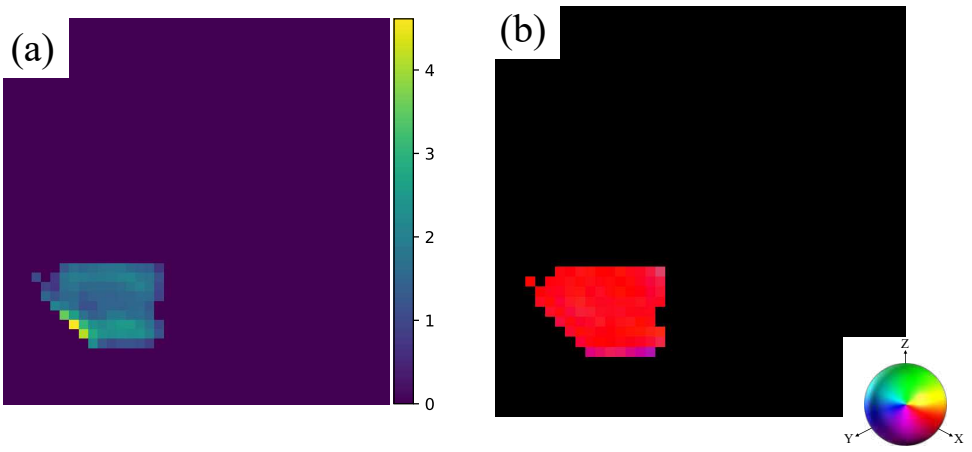

Figure 9.13: An axial slice through the upper part of the simulated cube. (a) The mean scattering signal in arbitrary units. (b) The main orientation signal. The colour is an RGB representation of the local structure orientation.

9.5 CONCLUSIONS

In this chapter, we presented a numerical wave-optics simulation model for speckle-based imaging. Speckle-based imaging experiments can be performed

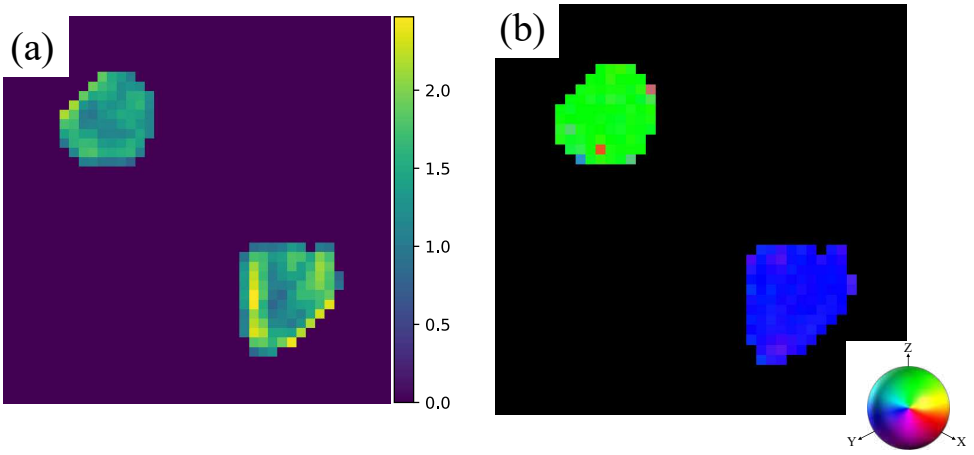

Figure 9.14: An axial slice through the bottom part of the simulated cube. (a) The mean scattering signal in arbitrary units. (b) The main orientation signal. The colour is an RGB representation of the local structure orientation.

using different setup conditions, and so does the simulation, where key parameters such as the beam type, the geometry, the sandpaper type and the diffuser steps can be tuned.

We provided some example, including the simulation of a SBI measurement of carbon fibre cross, which we successfully analysed using UMPA and our omnidirectional dark-field signal extraction model. Finally, we simulated an X-ray tensor tomography experiment, and we managed to correctly reconstruct the main orientation of the sub-resolution microstructures. In chapter 10 another simulation of an X-ray tensor tomography experiment is presented as a comparison with the real dataset.

In conclusion, the presented simulation provides a powerful and versatile tool for exploring new configurations, and optimising experimental designs, particularly for applications in speckle-based imaging and tensor tomography. In the future, it would be interesting to test different configurations, such as a laboratory setup, and compare the simulated results with experimental data.

10 APPLICATIONS OF MODULATION-BASED X-RAY TENSOR TOMOGRAPHY

This chapter presents three main applications of the X-ray tensor tomography model described in this thesis: an industrial application on carbon-fibre composites, a medical application on human middle ear ossicles, and a cultural heritage application on a fossil tooth and a fossil femur. The first section of this chapter (10.1) was done in collaboration with Yeajin Lee, Mark Mavrogordato, Ian Sinclair and Richard Boardman of Southampton University, who provided the carbon-fibre composites. The second section (10.2) was done in collaboration with Margaux Pauline Schmeltz of Paul Scherrer Institut and Lukas Anschuetz of Inselspital Bern, who provided the human middle ear ossicles. The third section (10.3) was done in collaboration with Simone Anna Maria Lemmers of Elettra Sincrotrone Trieste, who provided the cultural heritage samples.

10.1 INDUSTRIAL APPLICATION: CARBON–FIBRE COMPOSITES

10.1.1 Motivation

Composites are a critical part of future lightweighting strategies, with great relevance to green/sustainable engineering, particularly in transport systems (e.g., aircraft, buses, cars), but also energy (e.g. wind turbine blades, hydrogen gas containment). As structural materials, they are distinctive in having high levels of heterogeneity and anisotropy, intrinsic to their design and manufacturing. Important aspects of performance are coupled across several length-scales, and closely linked to fibre orientation. For example, macroscopic ply delaminations (cm scales), mesoscopic matrix cracking (0.1 mm) and microscopic single fibre breaks (sub-10 µm): they can all influence each another, and occur in concert during the aerospace critical "compression after impact" assessment. Tensor tomography, with associated ability to extract sub-voxel orientation information, may offer unique opportunity to address real engineering concerns by being able to see structure and behaviour with sufficient simultaneous field of view to address the length scales of real manufacturing and mechanical interest.

10.1.2 Sample preparation

We have prepared two aerospace-type unidirectional carbon-epoxy materials. The first sample, that from now on we will refer to it as the "T-shape" sample, was made of two cylinders of well aligned (99+% of fibres falling within a few degrees) plies, made combining different plies whose thickness was around a few hundreds µm. The two cylinders were extracted from the stacked plies using a lathe and a diamond saw in order to obtain two equilateral cylinders with a diameter of 3 mm. The second sample, from now on the "notch" sample, was manufactured utilising well aligned plies layup with a $[90/0/90]$ stacking sequence. The individual carbon fibres have a mean diameter between 5 µm and 10 µm.

10.1.3 Experimental setup and data acquisition

X-ray tensor tomography with a sandpaper modulator was performed at the ID19-ESRF beamline. An outline of the experimental setup is shown in Fig. 10.1. We used the U13 undulator in combination with 2.8 mm of aluminium to obtain a mean energy of 26.5 keV. As a wavefront modulator, we used a diffuser made of 6 sheets of *P*180 grit silicon-carbide sandpaper. As a detector, we used a PCO.edge sCMOS detector coupled to a Gadox scintillator and a magnifying objective. The pixel size in the sample plane was 6.5 µm. The sample-diffuser distance was 0.89 m, while the sample-detector distance was 0.88 m. The total FOV was 1650×1570 pixel or $10.7\,\text{mm} \times 10.2\,\text{mm}$.

To acquire the images, we followed the stair-wise acquisition protocol described in **[Kim2020; Kim2021]**. For each tilt angle β, we acquired 400 projections with a continuous rotation of the sample over $\alpha \in [0°, 360°]$, while $\beta \in [0°, 45°]$ with an angular step of 15°. The exposure time for each projection was 100 ms.

To characterise the performance of the modulator we used, we calculated its visibility and mean speckle size. In Fig. 10.2a a flat-corrected reference image is shown, together with its visibility analysis. The visibility is determined as the ratio of the standard deviation to the mean intensity value of the reference image. The visibility map is then computed using a Gaussian filter, with a kernel size of 5 pixels. The visibility map shown in Fig. 10.2b is not homogeneous all over the FOV, and its mean value is 17%.

In Fig. 10.3 the mean speckle size of the modulator, which is determined by calculating the full width at half maximum (FWHM) of the radial profile from the 2D auto-correlation function of a reference image. The speckle size is 6.5 pixel or 42.2 µm.

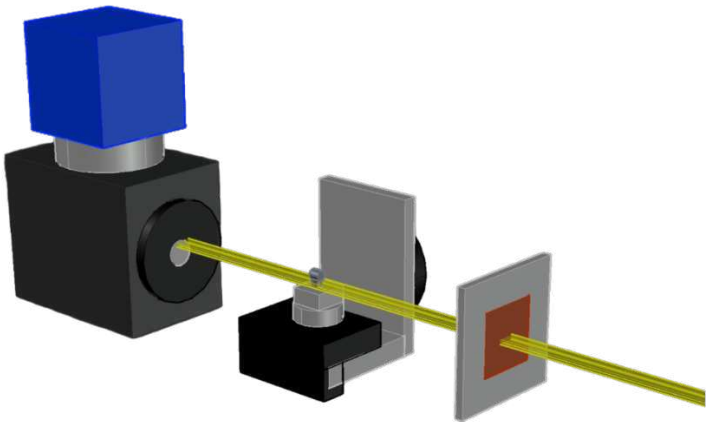

Figure 10.1: Schematic overview of the experimental setup. The X-ray beam is modulated by a diffuser mounted on a scanning stage upstream of the tilt and rotation stages. The rotation motor revolves α degrees and the rotation axis can be tilted β degrees. The detector system consists of a sCMOS camera with an X-ray microscope.

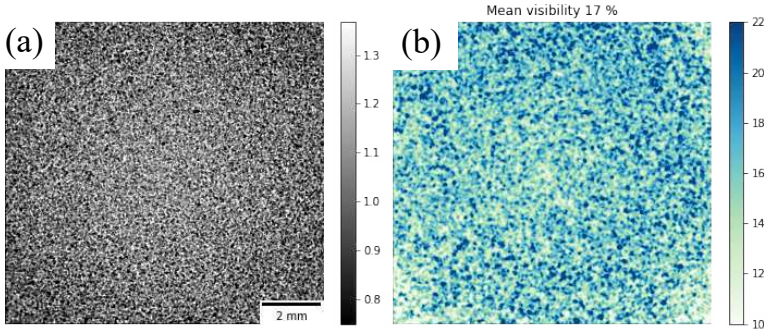

Figure 10.2: A flat-corrected reference image (a) and (b) its visibility analysis.

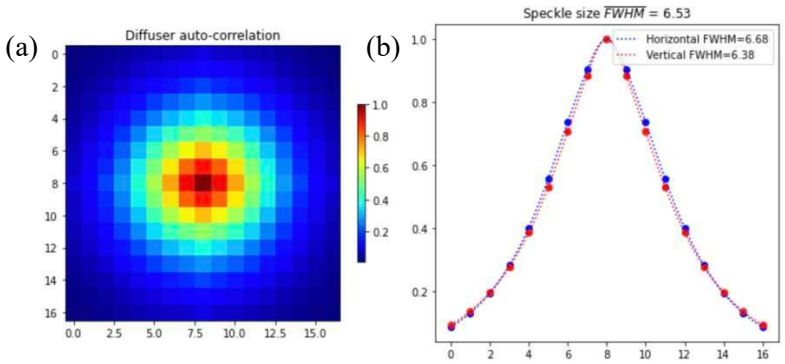

Figure 10.3: A 3D representation of the speckle size auto-correlation function in (a) and its radial profile in (b).

10.1.4 Analysis of the results

The acquired projections were analysed with the reconstruction method presented in Ref. **[Lautizi2024]** and in chapters 7 and 8. For the T-shape

sample, we used as the analysis unit cell, i.e. the resulting spatial resolution, a square with size of 20 pixels or 130 µm. We chose this analysis window for a fast reconstruction of a validation sample that has well-aligned fibre bundles.

Fig. 10.4a shows a raw transmission image of the validation sample obtained with the sandpaper modulator. In the region where the sample is present, a blurring is visible, caused by strong scattering from the sample. The extracted absorption image is presented in Fig. 10.4b. The mean scattering (Fig.10.4c) is calculated as the mean of the eigenvalues of the scattering tensor. The main orientation (Fig.10.4d) is represented using the 2D eigenvectors with the shortest lengths with HSV colour scheme, where the hue (colour shade) indicates fibre orientation projected onto the detector plane, the saturation represents the fractional anisotropy, and the value (brightness) reflects the mean scattering intensity.

Both in the top and in the bottom part of the sample, the main orientation of the fibres is clearly recognisable. In the top part, fibres are primarily oriented horizontally, while in the bottom part they are oriented vertically. The mean scattering is enhanced at the edges of the sample and in the delamination damage caused by the use of the lathe. This effect is partially due to the strong scatter at sharp interfaces, but also by the fact that the refraction signal is not modelled in this approximation, and therefore it is considered by the model as a scattering signal.

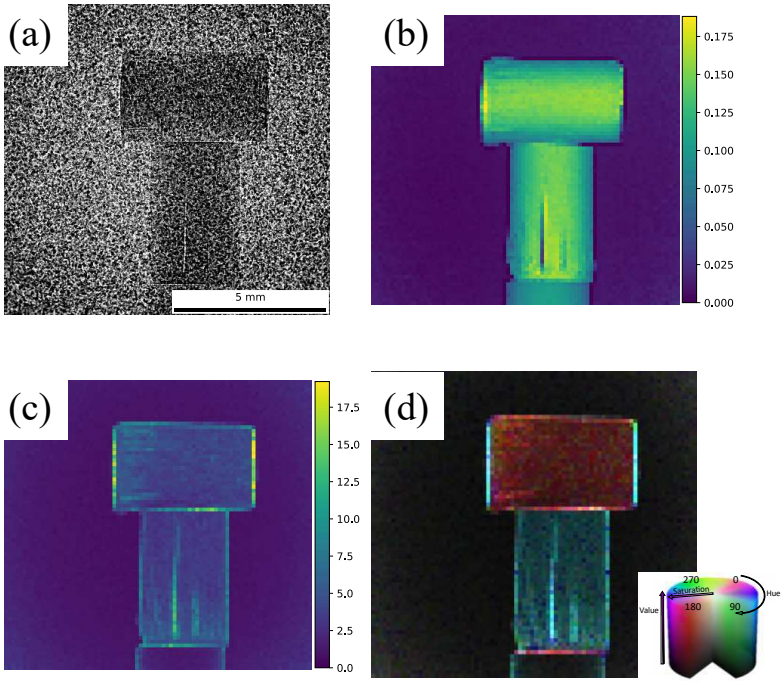

Figure 10.4: (a) An example of one of the projections of the T-shape sample with a sandpaper modulator at $\alpha = 0°$, $\beta = 0°$. (b) Extracted absorption image, (c) mean scattering in arbitrary units and (d) main orientation signals. Each pixel corresponds to one unit cell.

In Fig. 10.5 the results of the 2D omnidirectional signal extraction are shown for the notch sample at $\alpha = 90°$. For this sample we used as the analysis unit

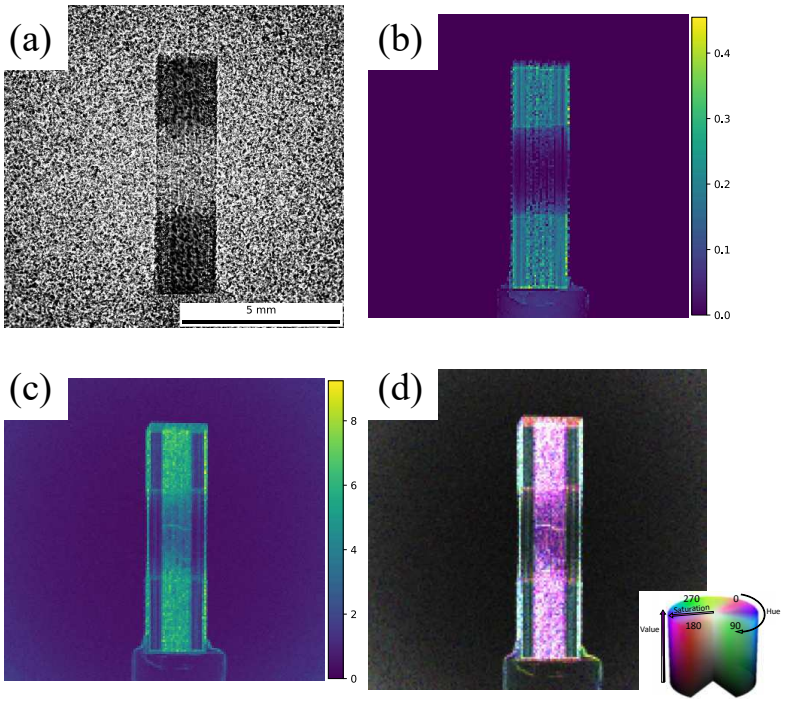

Figure 10.5: (a) An example of one of the projections of the notch sample with a sandpaper modulator at $\alpha = 90°$, $\beta = 0°$. (b) Extracted absorption image, (c) mean scattering in arbitrary units and (d) main orientation signals. Each pixel corresponds to one unit cell.

cell a square with size of 10 pixels translated of 5 pixels, with a resulting spatial resolution of 32.5 µm. This window is a good compromise between a high spatial resolution and a low noise level in the images. The computation time also plays a role in the decision of a proper analysis window. In the notch sample imaged at $\alpha = 90°$, the fibres are oriented vertically in the lateral slabs and perpendicularly to the page in the central slab. The notch (curved indentation located at both sides of the sample) is visible as a slightly absorbing region in Fig. 10.5b and also as a region with less intense mean scattering in Fig. 10.5c.

For both samples, the 2D scattering tensor for each local window and projection was obtained by extracting the omnidirectional dark-field signal from each projection of the tomographic dataset. The tensor sinogram, described in chapter 7, was created by combining these results to determine the entire 3D scattering tensor field. A modified version of the alignment procedure from **[Liebi2015]** was used to align the projections. Since the local structure-orientation signal is sensitive to noise, especially in background areas and at sharp edges, a threshold-based mask based on attenuation was applied to the tomographic volumes to exclude background regions.

In Figs. 10.6,10.7,10.8 three slices (coronal, sagittal, and axial respectively) through the reconstructed volume of the T-shape sample are shown. As it was visible also from the results of the 2D omnidirectional signal extraction, the main-orientation signal confirms that the fibres run along the long axis of the rods. In the top part, fibres are primarily oriented horizontally (red, x

axis), while in the bottom part they are oriented vertically (green, z axis). It is interesting to notice that in the mean scattering image, the regions with higher scattering are the result of the delamination damage occurred during the lathe cut. In Fig. 10.8d it is visible how the damaged region has a different orientation with respect to the rest of the cylinder. The sample holder was a homogeneous plastic cylinder, therefore it exhibits random orientations and a low mean scattering signal.

In Figs. 10.9,10.10,10.11 three slices (coronal, sagittal, and axial respectively) through the reconstructed volume of the notch sample are shown. As it was visible also from the results of the 2D omnidirectional signal extraction, the main-orientation signal confirms that the fibre's orientation differ, and it is attributable to the presence of three main slabs with a $[90/0/90]$ stacking sequence. In the two lateral slabs, the fibres are oriented vertically (green, z axis), while in the central region the fibres run horizontally (red, x axis). In the mean scattering images, the regions with higher scattering are the edges, as previously mentioned, and the central region. The two long surfaces of the notch sample exhibit a horizontal orientation. This effect was not visible in the 2D projection, and it is due to the conformation of the surface, consisting of horizontal grooves. Also in this case, the sample holder exhibits random orientations and a low mean scattering signal.

A 3D visualisation of the reconstructed scattering tensor of the two carbon-fibre composites is shown in Fig. 10.12. In this representation, each arrow's orientation corresponds to the main direction in each voxel. The colour ball is symmetric with respect to the $x-y$, $x-z$, and $y-z$ planes. This visualisation is mainly of the surface orientation, therefore more subjected to contributes from the refraction signal and noise.

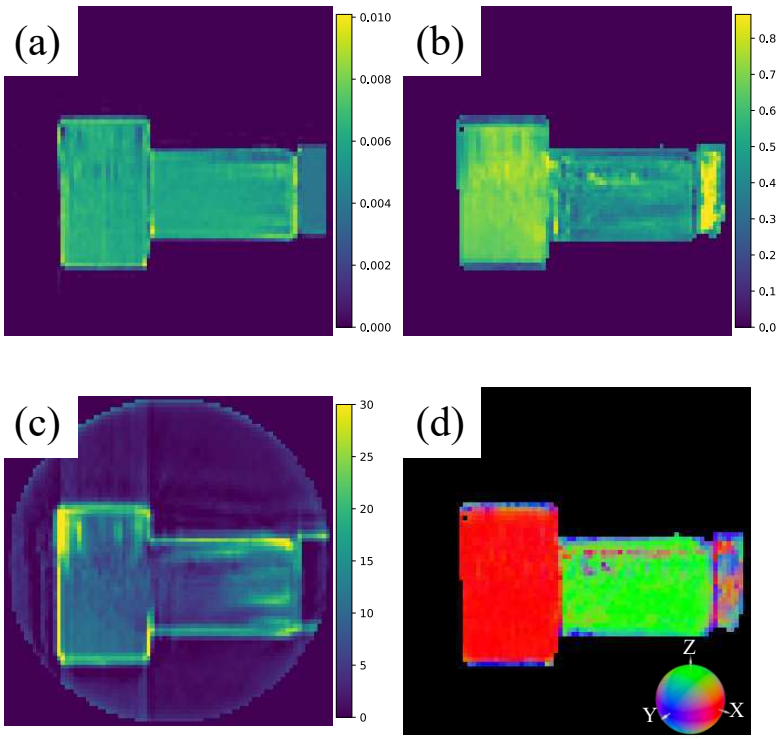

Figure 10.6: A coronal slice through the tomographic volume of the T-shape sample. (a) Extracted absorption, (b) scattering anisotropy in arbitrary units and (c) mean scattering signals in arbitrary units are shown. (d) Orientation signals, where the colour is an RGB representation of the local structure orientation. The colour ball is symmetric with respect to the $x-y$, $x-z$, and $y-z$ planes.

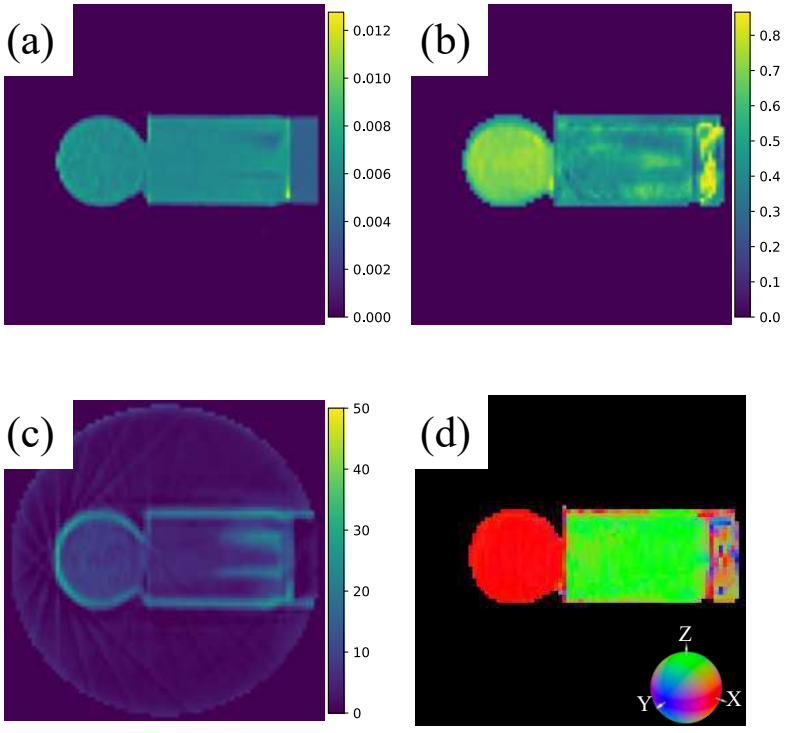

Figure 10.7: A sagittal slice through the tomographic volume of the T-shape sample. (a) Extracted absorption, (b) scattering anisotropy in arbitrary units and (c) mean scattering signals in arbitrary units are shown. (d) Orientation signals, where the colour is an RGB representation of the local structure orientation.

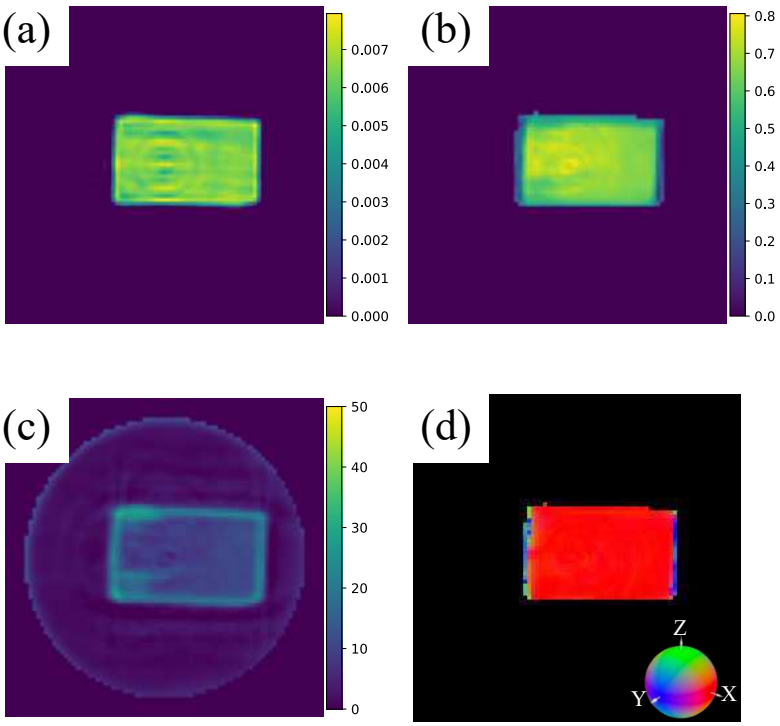

Figure 10.8: An axial slice through the upper part of the tomographic volume of the T-shape sample. (a) Extracted absorption, (b) scattering anisotropy in arbitrary units and (c) mean scattering signals in arbitrary units are shown. (d) Orientation signals, where the colour is an RGB representation of the local structure orientation.

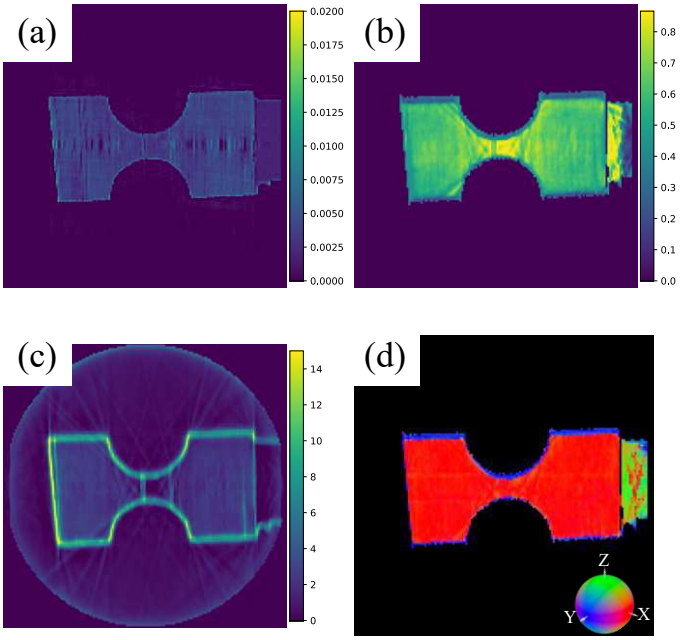

Figure 10.9: A coronal slice through the tomographic volume of the notch sample. (a) Extracted absorption, (b) scattering anisotropy in arbitrary units and (c) mean scattering signals in arbitrary units are shown. (d) Orientation signals, where the colour is an RGB representation of the local structure orientation.

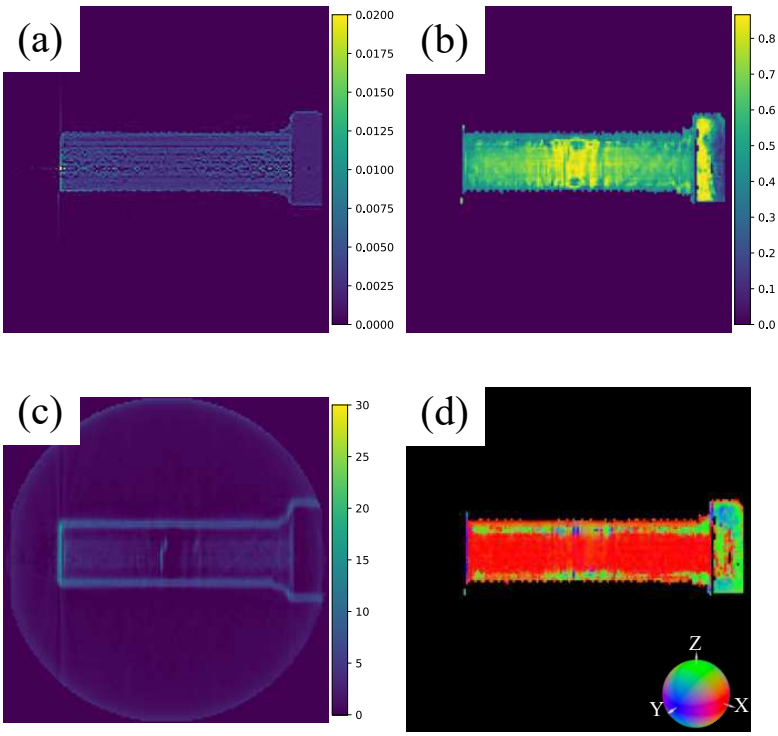

Figure 10.10: A sagittal slice through the tomographic volume of the notch sample. (a) Extracted absorption, (b) scattering anisotropy in arbitrary units and (c) mean scattering signals in arbitrary units are shown. (d) Orientation signals, where the colour is an RGB representation of the local structure orientation.

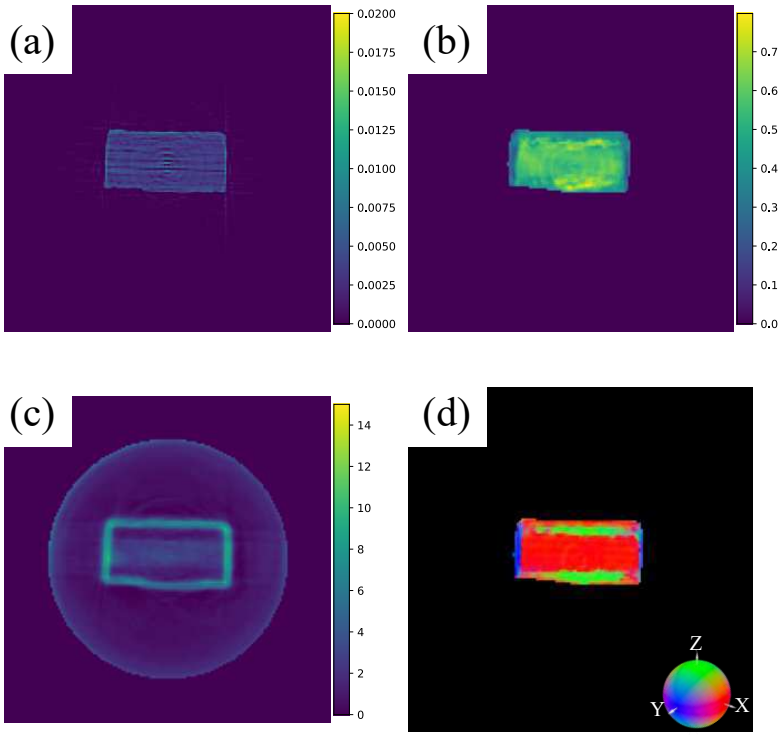

Figure 10.11: An axial slice through the tomographic volume of the notch sample. (a) Extracted absorption, (b) scattering anisotropy in arbitrary units and (c) mean scattering signals in arbitrary units are shown. (d) Orientation signals, where the colour is an RGB representation of the local structure orientation.

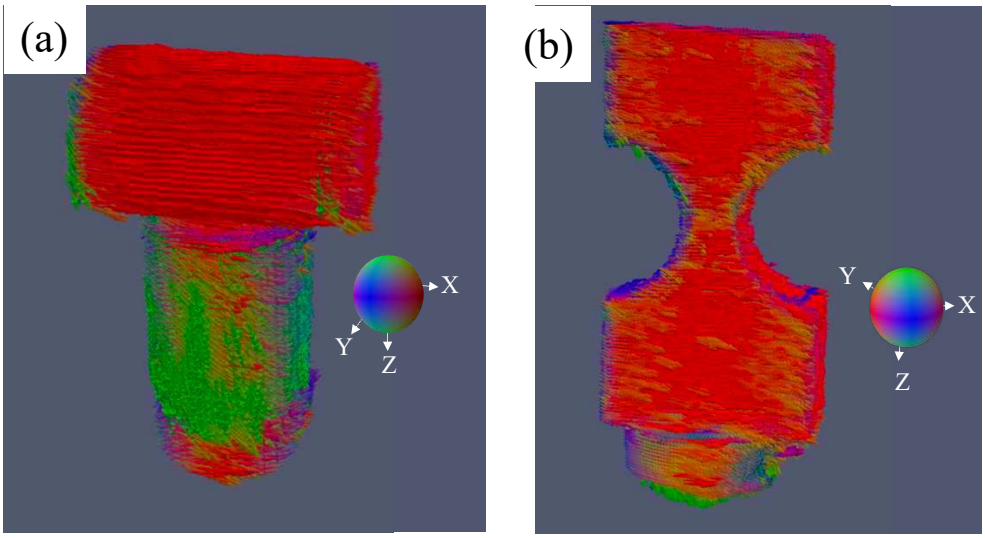

Figure 10.12: A 3D visualisation of the reconstructed scattering tensor of the T-shape (a) and notch (b) samples. In this representation, each arrow's orientation corresponds to the main direction in each voxel. The colour is an RGB representation of the local structure orientation. The colour ball is symmetric with respect to the $x-y$, $x-z$, and $y-z$ planes.

10.1.5 Simulated dataset

A numerical wave-optics simulation of an X-ray tensor tomography using a random modulator has been carried out using a simulated sample that mimics the T-shape sample described in this section. For a more detailed description of the simulation process, the reader is referred to chapter 9.

The sample consists of 2 bundles of 2000 carbon fibres each, filled with epoxy resin, superimposed forming a T-shape. The fibres are placed using the Poisson disc sampling, as described in chapter 9. Each bundle has a diameter of 1000 pixels (Fig. 10.13). In the simulation space, the pixel size is 3 µm, so each bundle has a diameter of 3 mm, matching the real T-shape sample. Each fibre has a diameter of 4 pixels. The FOV is 2500×2500 pixels. The reference and sample images have been rebinned of a factor 3, so that the resulting FOV is 833×833 pixels and the effective pixel size is 9 µm. The diffuser was realised with cube SiC grains with a mean size of 80 µm and a variance of the grain size distribution of 3 µm. It corresponds to a *P*180 grit silicon-carbide sandpaper. We generated 6 layers of sandpaper and 20 different diffuser positions. The distances, the energy, and the acquisition geometry have been simulated to match exactly the experimental parameters.

In Fig. 10.14a a reference image is shown. The visibility of the reference pattern is shown in Fig. 10.14b. It is not homogeneous all over the FOV, and its mean value is 23.71%, slightly higher compared to the corresponding experimental dataset.

We used UMPA algorithm to process the sets of 20 sample frames captured at identical angles (tilt angle $\beta = 0°$ and rotation angle $\alpha = 0°$) but different

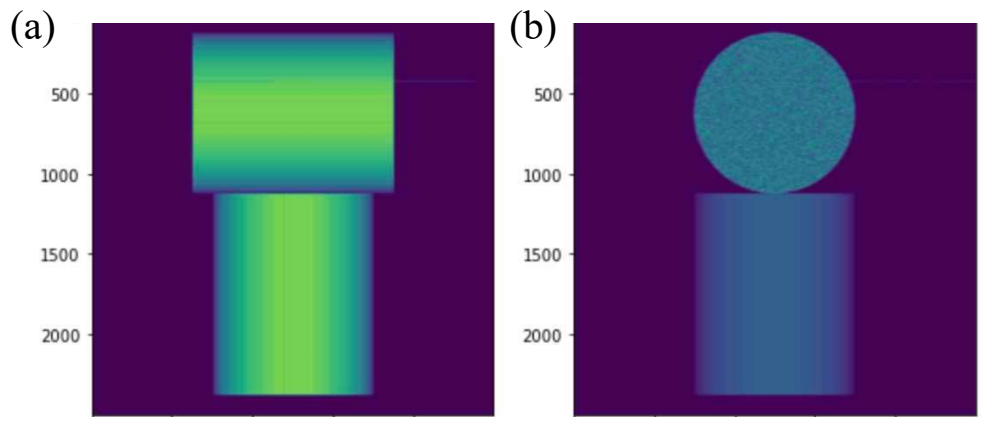

Figure 10.13: The simulated sample. Two projections of the 3D sample at tilt angle $\beta = 0°$ and rotation angle (a) $\alpha = 0°$ and (b) $\alpha = 90°$.

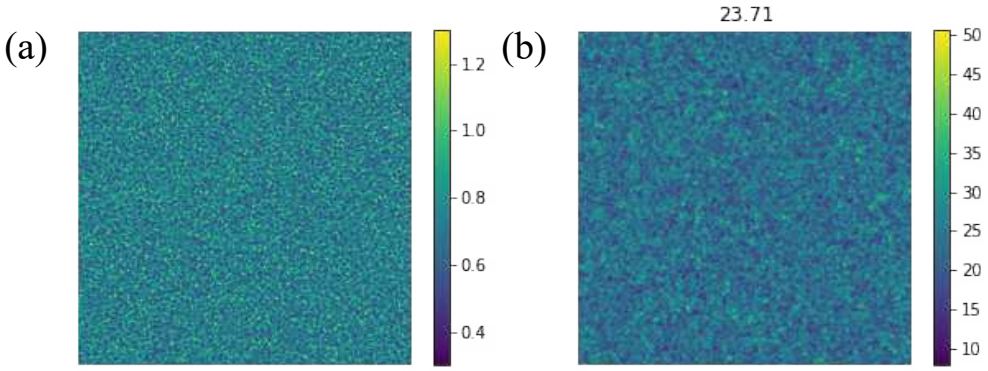

Figure 10.14: (a) A reference image of the XTT simulated dataset and (b) the corresponding visibility analysis.

modulator positions, along with the 20 reference frames taken at corresponding modulator positions. The transmission, dark-field, and refraction angle signals for each projection in both the vertical and horizontal directions were generated by this procedure. The result of this analysis may be seen in Fig. 10.15.

After having verified the correctness of the images analysed with UMPA, we checked the directionality of the fibres in the simulated bundles. The SBI images were analysed with the reconstruction method presented in Ref. **[Lautizi2024]** and in chapters 7 and 8. We used as the analysis unit cell, i.e. the resulting spatial resolution, a square with size of 15 pixels or 135 µm. We chose this analysis window to compare the results with the experimental dataset, where the resulting spatial resolution was 130 µm. The results in Fig. 10.16d show that the main orientation signal matches with the expected orientation of the fibres (cyan along the vertical axis and red at 90°), thus demonstrating the effectiveness of the proposed method for a simulated dataset that mimics an experimental case. The main-orientation signal in the composite HSV image confirms that the fibres run along the long axis of the rods.

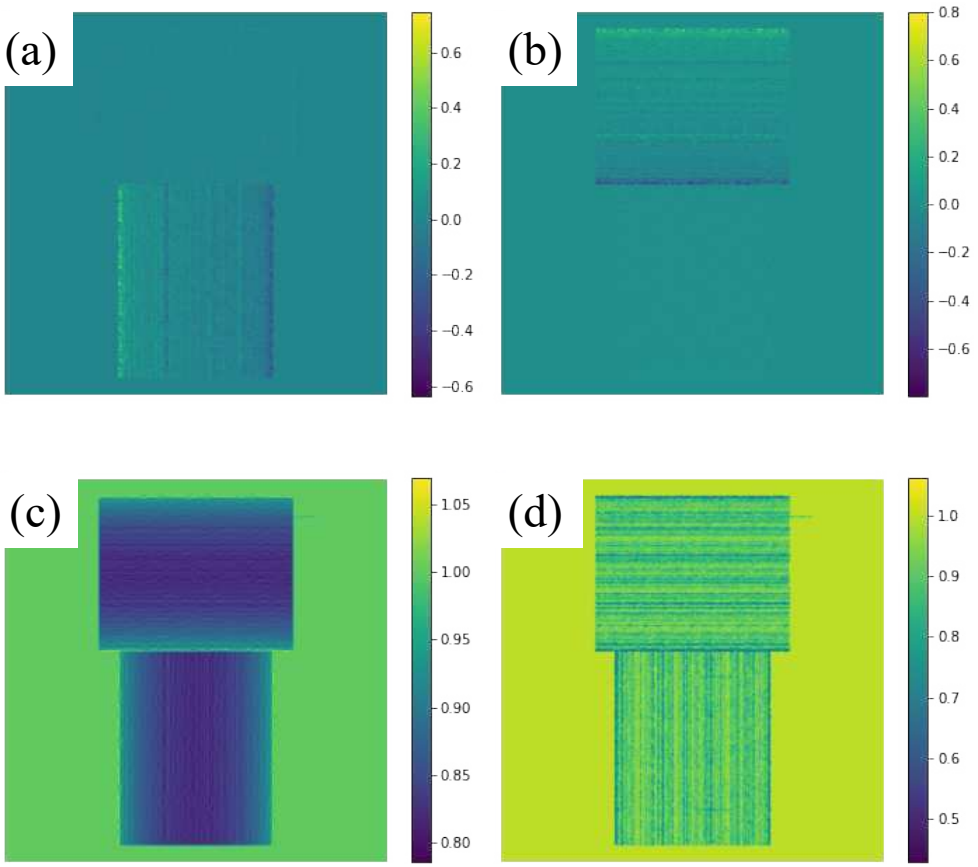

Figure 10.15: One projection of the simulated sample, obtained with SBI using UMPA algorithm. (a) The differential-phase signal in the horizontal and (b) vertical direction, reported in pixels. (c) The transmission, and (d) the dark-field signals.

Once the omnidirectional dark-field signal is extracted for all the projections of the simulated dataset, it is sufficient to solve the linear system with CG, as described in chapter 7. In Figs. 10.17,10.18,10.19 three slices (coronal, sagittal, and axial respectively) through the reconstructed volume of the simulated T-shape sample are shown. A threshold-based mask based on attenuation was applied to the tomographic volumes to exclude background regions. The main-orientation signal confirms that the fibres run along the long axis of the rods. As expected, the bundle in the upper part of the cube is oriented horizontally along the x-axis, and it is therefore reconstructed with red colour in the main orientation signal. In the bottom part of the cube, the bundles are oriented vertically along the z-axis, reconstructed with green colour in the main orientation signal. The reconstructed main-orientation signal agree with the expected orientations and with the experimental results (Figs. 10.6,10.7,10.8). The presented results are, to our knowledge, the first simulated X-ray tensor tomography experiment.

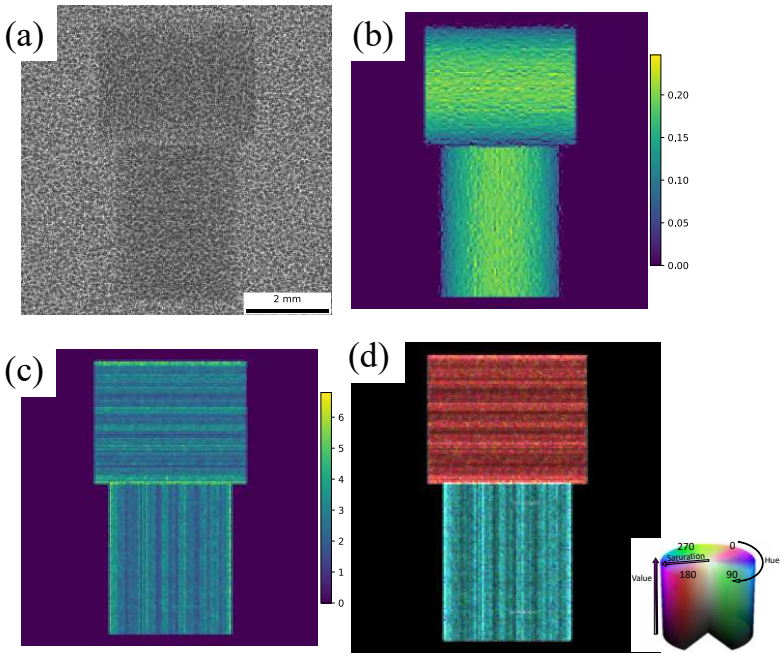

Figure 10.16: (a) Raw transmission image of a simulated carbon fibre cross with speckles at $\alpha = 0°$, $\beta = 0°$. (b) Extracted absorption image and (c) mean scattering signals in arbitrary units. (d) Main orientation signals in cyan and red, contrast has been enhanced for visualisation purposes.

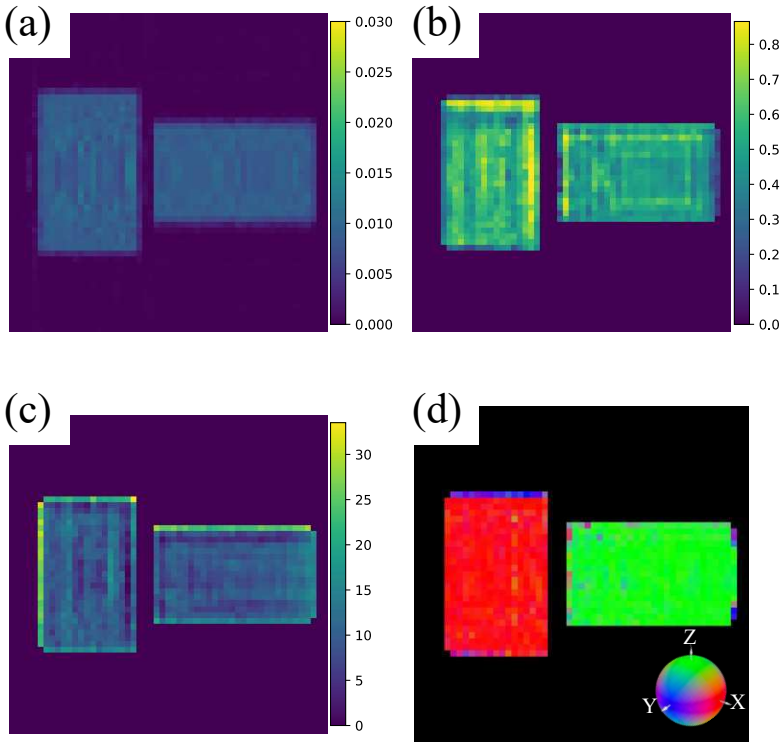

Figure 10.17: A coronal slice through the upper part of the tomographic volume of the simulated T-shape sample.(a) Extracted absorption, (b) scattering anisotropy in arbitrary units and (c) mean scattering signals in arbitrary units are shown. (d) Orientation signals, where the colour is an RGB representation of the local structure orientation.

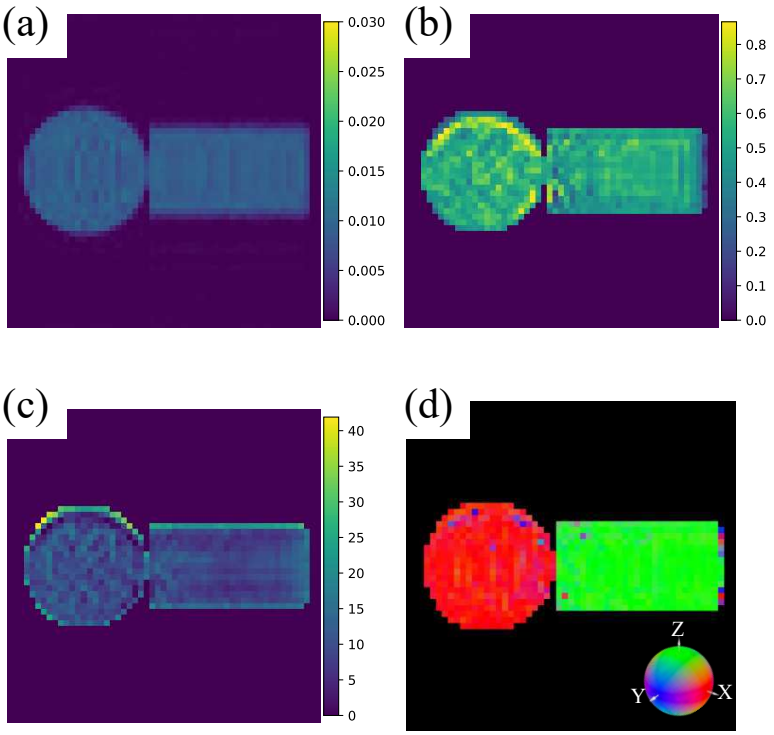

Figure 10.18: A sagittal slice through the upper part of the tomographic volume of the simulated T-shape sample. (a) Extracted absorption, (b) scattering anisotropy in arbitrary units and (c) mean scattering signals in arbitrary units are shown. (d) Orientation signals, where the colour is an RGB representation of the local structure orientation.

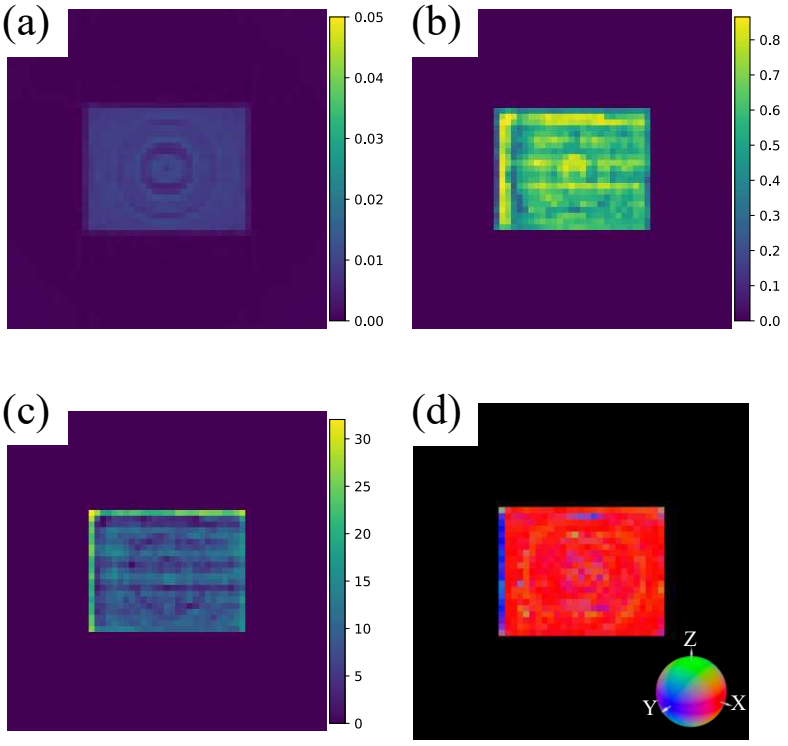

Figure 10.19: An axial slice through the upper part of the tomographic volume of the simulated T-shape sample. (a) Extracted absorption, (b) scattering anisotropy in arbitrary units and (c) mean scattering signals in arbitrary units are shown. (d) Orientation signals, where the colour is an RGB representation of the local structure orientation.

10.1.6 Conclusions

In conclusion, we validated our algorithm using a sandpaper modulator at a fourth-generation synchrotron on carbon-fibre composites interesting for industrial applications. X-ray tensor tomography allowed us to retrieve the main orientations of carbon fibres in various aerospace-type unidirectional carbon-epoxy materials. Moreover, we applied a numerical wave-optics simulation to simulate for the first time an X-ray tensor tomography dataset obtained with a random modulator and sample that mimics a real sample used in the measurements.

Applying these findings could be valuable to enhance our comprehension of carbon-epoxy materials. In the future, it would be interesting to apply this method to samples that have undergone low velocity impact testing, exhibiting various cracks and delaminations. Another interesting samples would be composites made of recycled carbon fibre, where orientation mapping is a key finding since the fibres have been re-oriented.

10.2 MEDICAL APPLICATION: HUMAN MIDDLE EAR OSSICLES

10.2.1 Motivation

The ossicles are the smallest bones in the human body, responsible for transmitting sound from the tympanic membrane to the inner ear structures (Fig. 10.20). Their micro- and nano-scale arrangement is, to date, largely unknown, and further knowledge is needed to better understand their biomechanical properties, and subsequently ossicle-related hearing loss.

In the event of acute infections, chronic inflammation, congenital anomalies, or trauma, the ossicles can be damaged, and an ossiculoplasty (ossicular chain reconstruction) is needed to restore hearing function. Today, the use of autogenous ossicles (patient's own ossicles) is considered as the main surgical technique, as the alternatively used titanium prosthesis may lead to foreign-body reaction, a hole in the tympanic membrane, or inflammation. Therefore, studying the arrangement of the collagen network in the ossicles is fundamental for a deeper understanding of their specific biomechanical properties for the optimisation of sculpting procedures employed during middle-ear reconstructive surgery.

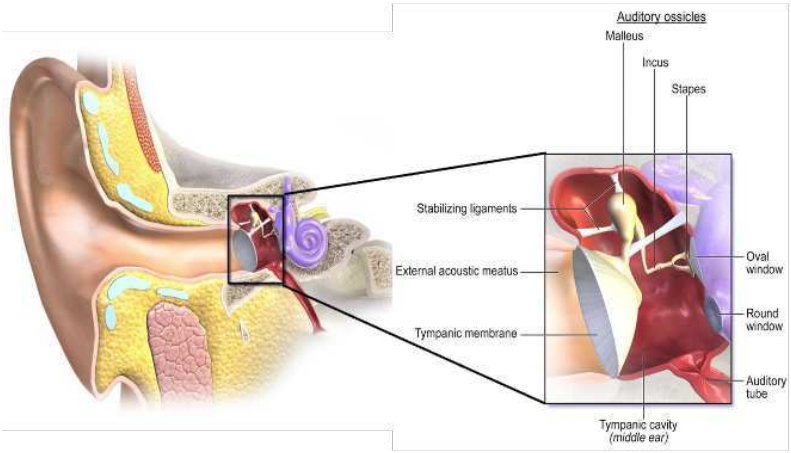

Figure 10.20: A model of the middle-ear auditory ossicles. Image courtesy of Margaux Pauline Schmeltz.

10.2.2 Sample preparation

Three ossicles — malleus, incus, and stapes — from the same ossicular chain were dissected from a Thiel-fixed human temporal bone of an anonymous donor. Similar samples have already been studied at TOMCAT beamline with full-field microtomography **[Anschuetz2019]**. In Fig. 10.21 a maximum intensity projection and an absorption 3D reconstruction of an incus obtained at TOMCAT beamline with high-resolution microtomography. In Fig. 10.22

a maximum intensity projection and a 3D visualisation with segmentation, showing the tympanic membrane and the ossicular chain **[Schmeltz2024]**.

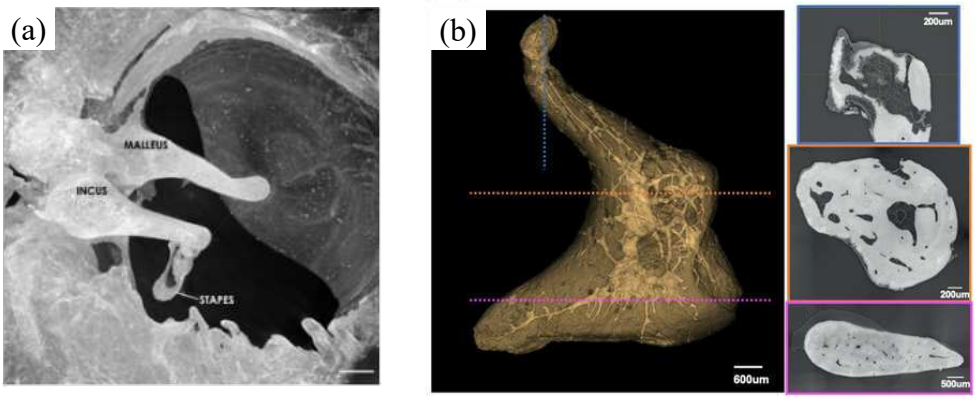

Figure 10.21: (a) A maximum intensity projection obtained at TOMCAT beamline with conventional propagation-based phase contrast. Image adapted from **[Schmeltz2024]**. (b) An absorption 3D reconstruction of an incus obtained with high-resolution microtomography at TOMCAT beamline. Images courtesy of Margaux Pauline Schmeltz.

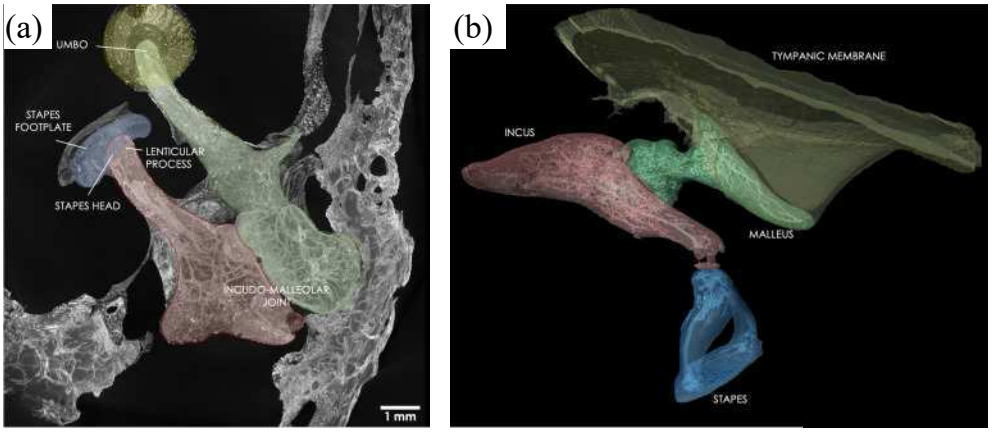

Figure 10.22: (a) A maximum intensity projection and (b) 3D visualisation with segmentation, showing the tympanic membrane and the ossicular chain. Images adapted from **[Schmeltz2024]**.

10.2.3 Experimental setup and data acquisition

In this work, full-field XTT using this novel algorithm is applied to investigate the main 3D orientation and anisotropy of microstructures within human auditory ossicles. To perform this study, we used a π-shifting circular grating array **[Kagias2016; Kagias2019]** with a unit cell period $P = 49.5\,\mu m$ and a fine grating period $g = 1.46\,\mu m$. We employed the in-house developed CMOS-based fast-acquisition GigaFRoST detector **[Mokso2017]** combined with a high-numerical-aperture tandem 1:1 microscope optic, resulting in an effective pixel size of 11 µm. The detector was located 49.5 cm downstream of the grating array, and the grating-sample distance was 46.3 cm. The exposure

time for each projection was 12 ms, and the field of view (FOV) was 460×1008 pixels. An outline of the experimental setup is shown in Fig. 10.23.

The projection images were acquired at the TOMCAT beamline (Swiss Light Source, Paul Scherrer Institut) following the stair-wise acquisition protocol described in **[Kim2020; Kim2021]**, using a monochromatic X-ray beam of 17 keV. For each tilt angle β, we acquired 1000 projections with a continuous rotation of the sample over $\alpha \in [0°, 360°]$, while $\beta \in [0°, 44°]$ with an angular step of 4°. For the incus and the malleus, two FOVs were necessary to cover the sample. The projections were then stitched after the analysis.

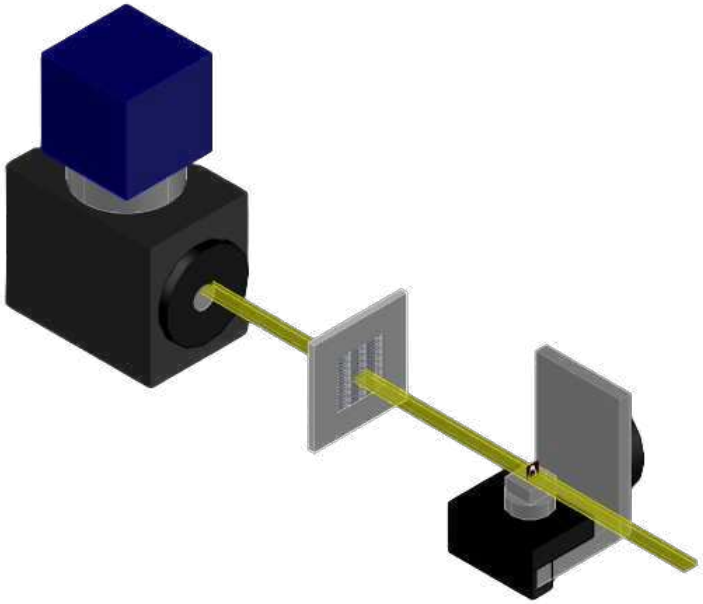

Figure 10.23: Schematic overview of the experimental setup. The X-ray beam is modulated by a circular grating array mounted on a scanning stage downstream of the tilt and rotation stages. The detector system consists of a sCMOS camera with an X-ray microscope.

10.2.4 Analysis of the results

The acquired projections were analysed with the reconstruction method presented in Ref. **[Lautizi2024]** and in chapter 7. The analysis unit cell, i.e. the resulting spatial resolution, is a square whose size corresponds to the diameter of a single circular grating: 9 pixels or 99 µm. In Fig. 10.24 an example of one of the projections for the stapes is visible. In Fig. 10.24a we show a projection with the sample and the modulator (a sample image) at $\alpha = 0°$ and $\beta = 0°$, while in Fig. 10.24b we show a projection with only the modulator (a reference image). Both images are necessary to extract the omnidirectional dark-field signal. In Fig. 10.24c a zoomed region where the circular grating structure is visible. The red squares represent four example analysis windows.

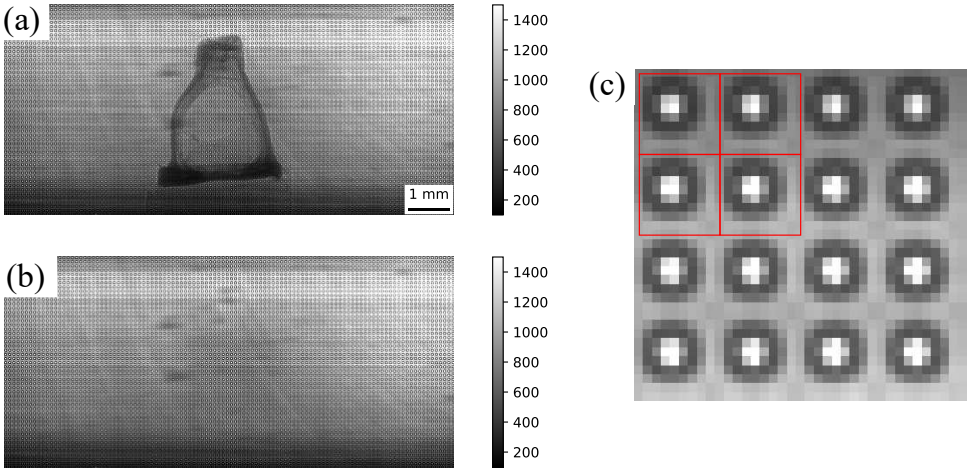

Figure 10.24: An example of one of the projections for the stapes. (a) A projection with the sample and the modulator (a sample image) at $\alpha = 0°$ and $\beta = 0°$. (b) A projection with only the modulator (a reference image). (c) A zoomed region where the circular grating structure is visible.

Fig. 10.25a displays the raw transmission imagine of the stapes sample. The image displays the gratings' circular fringes, which are blurred as a result of the sample's scattering. Fig. 10.25b displays the extracted absorption image, whereas Fig. 10.25c represents the mean scattering, which is determined by taking the mean of the scattering tensor's eigenvalues as explained in chapter 7. The HSV representation of the 2D eigenvectors with the shortest lengths is the main orientation (Fig. 10.25d), where the mean scattering intensity is the brightness, the fractional anisotropy is the saturation, and the hue (colour shade) is the fibre orientation projected onto the detector plane. The dark-field signal extracted from the stapes is not as intense as for a carbon-fibre sample. However, it is possible to extract the main orientations, especially in the stapes footplate.

For the two other ossicles, one FOV was not sufficient to cover the full sample, so two FOVs were acquired and then, after the analysis, the resulting images were blended along the vertical axis by weighting the overlap with a linear ramp. In Figs. 10.26 and 10.27 the results of the 2D omnidirectional signal extraction are shown for the incus and the malleus, respectively.

The 2D scattering tensor for each local window and projection was then obtained by extracting the omnidirectional dark-field signal from each projection of the tomographic dataset. The tensor sinogram described in chapter 7 is created by combining the results above to determine the whole 3D scattering tensor field. A modified version of the alignment procedure described in **[Liebi2015]** was used to align the projections. The local structure-orientation signal is susceptible to noise, especially in background areas and at sharp edges, thus a threshold-based mask based on average scattering was applied to the tomographic volumes.

In Fig. 10.28 an axial slice through the reconstructed volume of the stapes is shown, the slice is indicated by the shaded region in Fig. 10.28d and it is

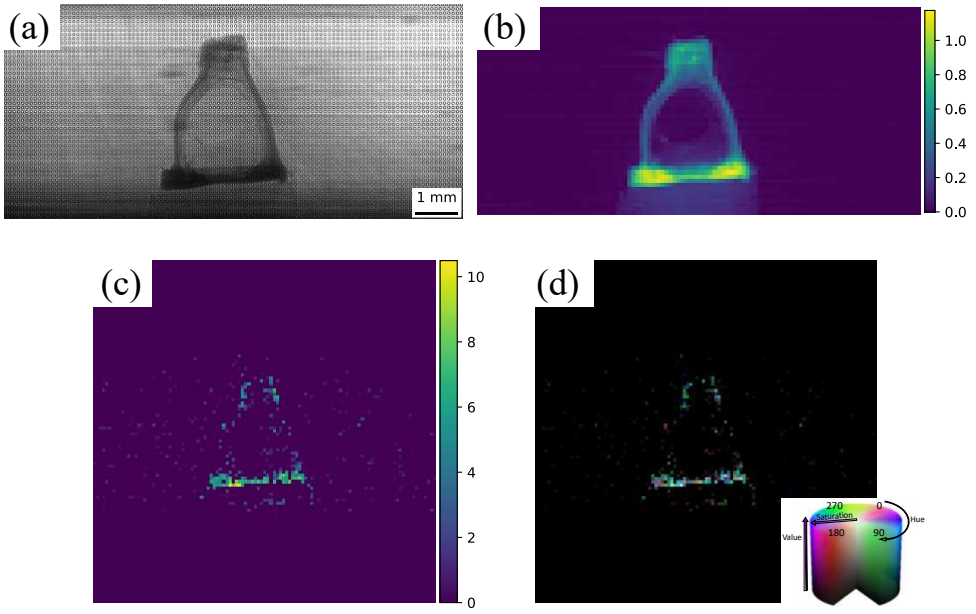

Figure 10.25: (a) Raw transmission image of the stapes with a grating array at $\alpha = 0°$, $\beta = 0°$. (b) Extracted absorption image, (c) mean scattering in arbitrary units and (d) main orientation signals. Each pixel corresponds to one unit cell.

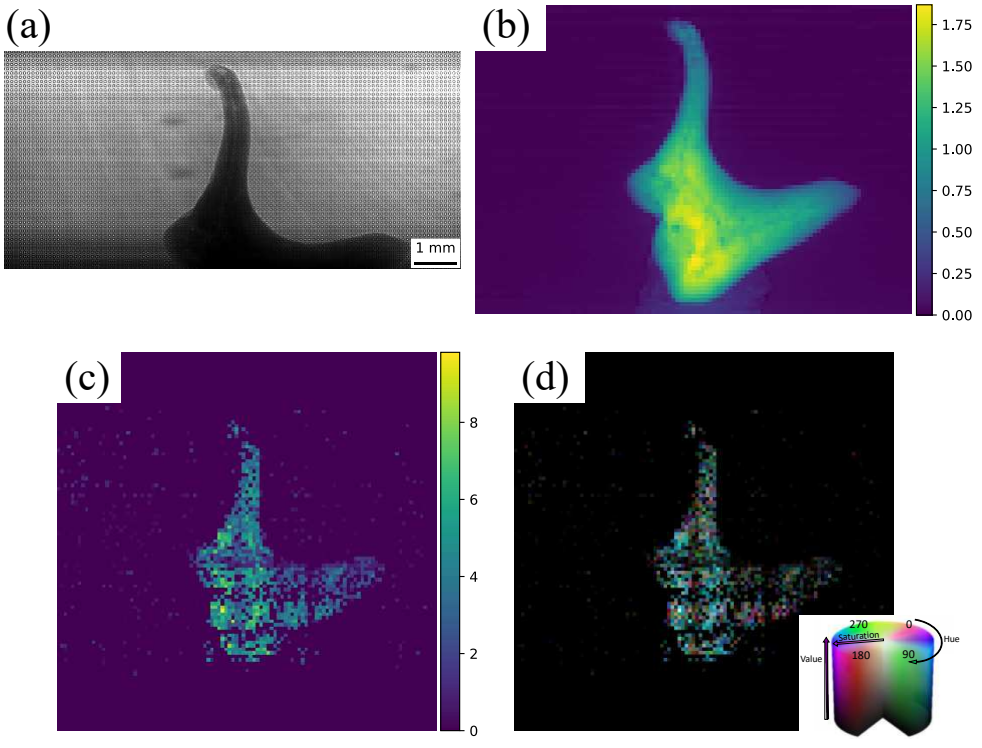

Figure 10.26: (a) Raw transmission image of the incus with a grating array at $\alpha = 0°$, $\beta = 0°$ for the upper FOV. (b) Extracted absorption image, (c) mean scattering in arbitrary units and (d) main orientation signals after the stitching of the two FOVs. Each pixel corresponds to one unit cell.

located in the stapes footplate. In this region, the collagen bundles are mainly

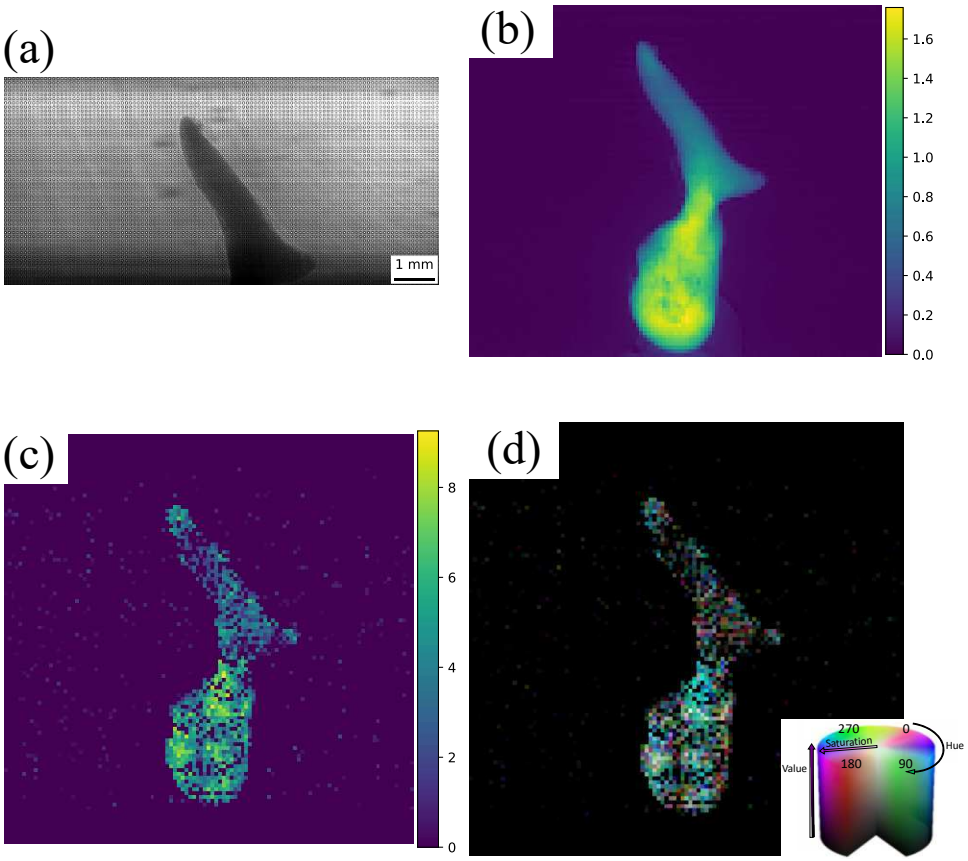

Figure 10.27: (a) Raw transmission image of the malleus with a grating array at $\alpha = 0°$, $\beta = 0°$ for the upper FOV. (b) Extracted absorption image, (c) mean scattering in arbitrary units and (d) main orientation signals after the stitching of the two FOVs. Each pixel corresponds to one unit cell.

oriented vertically, as in this configuration the stapes can bear load in the footstep.

In Fig. 10.29 an axial slice through the reconstructed volume of the incus is shown, the slice is indicated by the shaded region in Fig. 10.29d, and it is located in the incus body and short crus. The collagen fibrils have a higher orientation order in the body of the incus, as visible in the scattering anisotropy image (Fig. 10.29a). In this region, the collagen bundles are mainly oriented vertically. The upper part of the incus, known as the lenticular process, is also interesting to study since bone formation occurs in this region. In contrast with the long process, where the scattering anisotropy is higher, maybe due to the inner vascular network, the lenticular process has a lower scattering anisotropy. A study of the 3D orientations and the anisotropy at the nano-scale of the mineralised collagen in the lenticular process of a similar sample has been conducted with SAS-TT, and the results can be found in Ref. **[Appel2024; Schmeltz2024b]**.

Finally, in Fig. 10.30 an axial slice through the reconstructed volume of the malleus is shown, the slice is indicated by the shaded region in Fig. 10.30d,

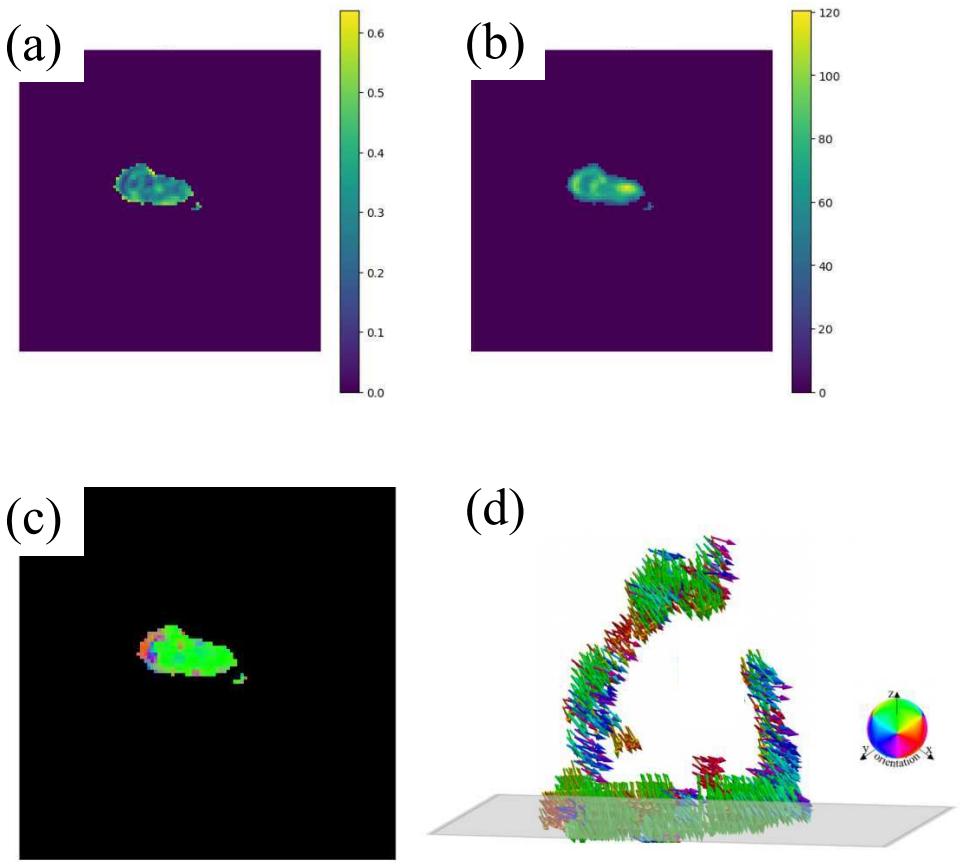

Figure 10.28: An axial slice through the tomographic volume of the stapes. (a) Scattering anisotropy in arbitrary units and (b) mean scattering signals in arbitrary units are shown. (c) Orientation signals, where the colour is an RGB representation of the local structure orientation. (d) 3D visualisation of the reconstructed scattering tensor of the stapes. In this representation, each arrow's orientation corresponds to the main direction in each voxel. The colour ball is symmetric with respect to the $x-y$, $x-z$, and $y-z$ planes, and it is used also for figure (c).

and it is located in the malleus neck and lateral process. In this region, collagen fibrils are mainly oriented along the neck of the malleus.

10.2.5 Conclusions

In conclusion, our algorithm delivered 3D information without requiring time-consuming sample preparation and slicing processes and overcoming the common risk of structural deformation associated with histology, the traditional technique to study the sub-micron structure of auditory ossicles **[Hamberger1964]**. It allowed us to retrieve the main orientations of mineralised collagen fibrils.

Applying these findings could be valuable to enhance our comprehension of sound transmission within the human middle ear and can offer valuable insights into the bone remodelling process within the auditory ossicles,

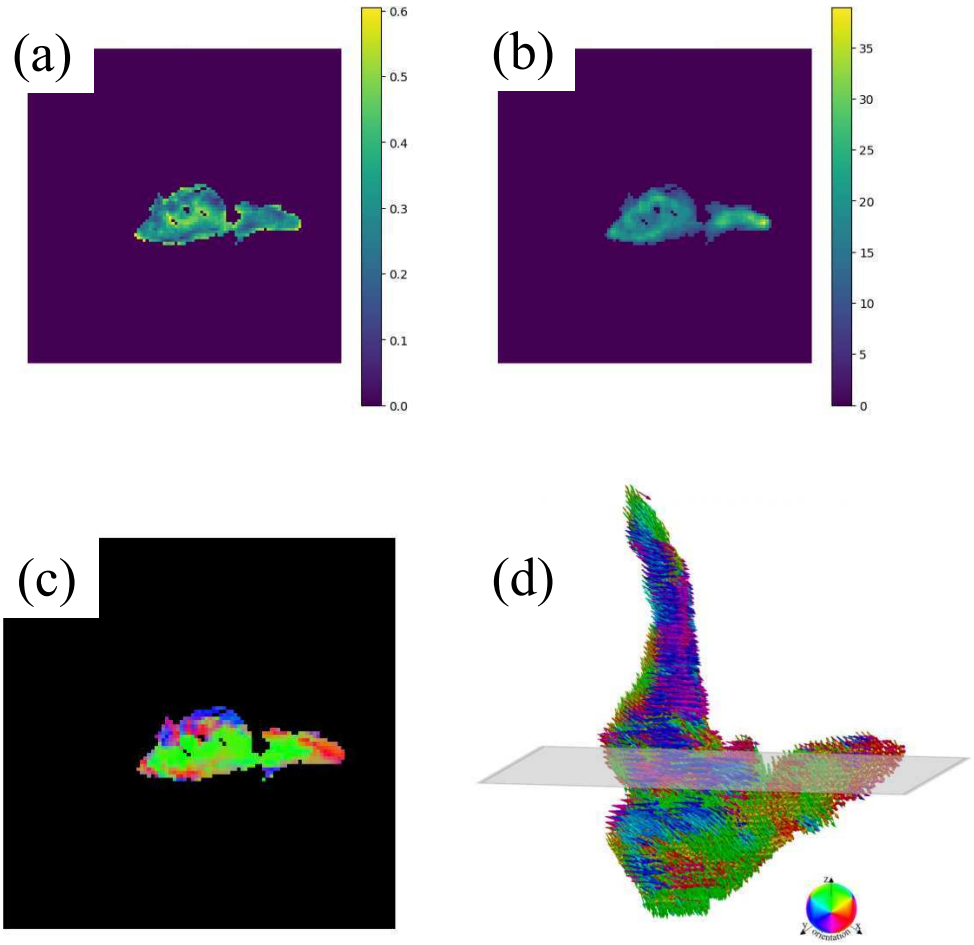

Figure 10.29: An axial slice through the tomographic volume of the incus. (a) Scattering anisotropy in arbitrary units and (b) mean scattering signals in arbitrary units are shown. (c) Orientation signals, where the colour is an RGB representation of the local structure orientation. (d) 3D visualisation of the reconstructed scattering tensor of the stapes. In this representation, each arrow's orientation corresponds to the main direction in each voxel.

particularly at sites where new bone formation occurs. This will be important information for the further development and optimisation of middle-ear surgery with potential wide-ranging benefits for patients with conductive hearing loss.

In the future, it would be interesting to compare the results with techniques that have higher spatial resolution, such as speckle-based tensor tomography or SAS-TT. In these samples, the mineralised collagen fibrils exhibit many orientations on a small scale, and forcing the final resolution to 99 µm might be a limitation for these kinds of samples.

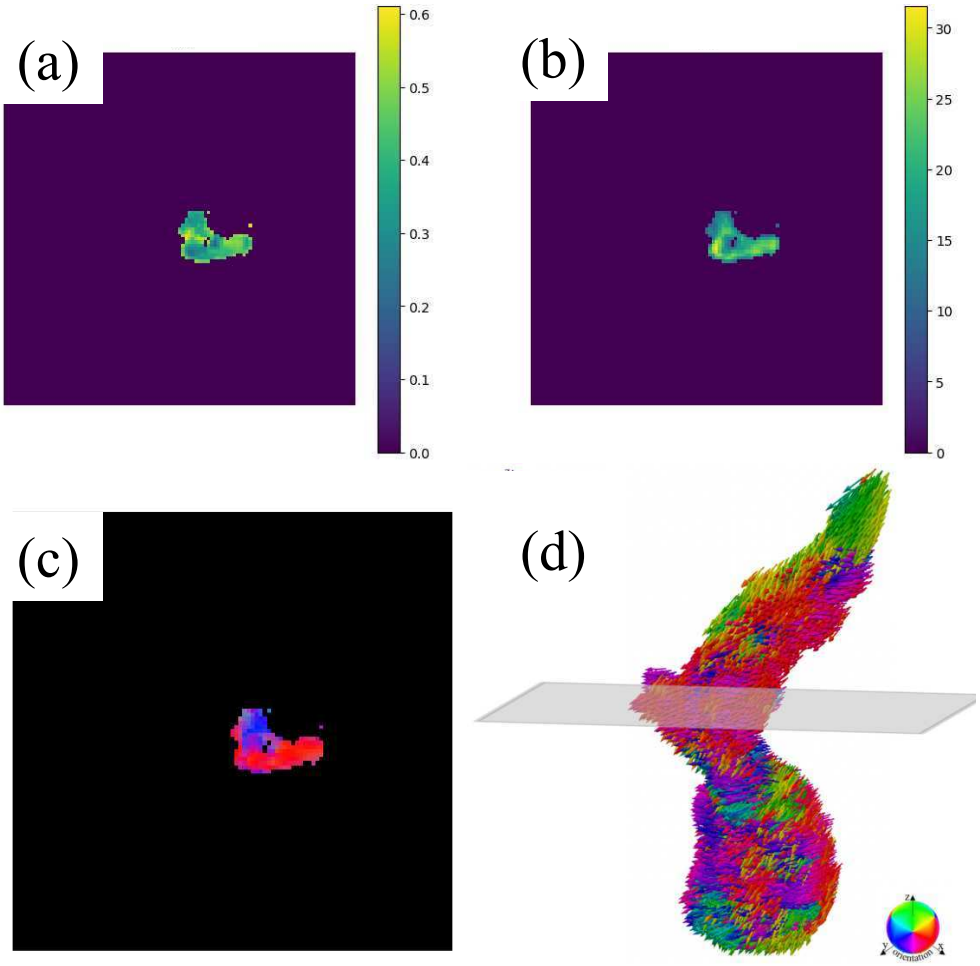

Figure 10.30: An axial slice through the tomographic volume of the malleus. (a) Scattering anisotropy in arbitrary units and (b) mean scattering signals in arbitrary units are shown. (c) Orientation signals, where the colour is an RGB representation of the local structure orientation. (d) 3D visualisation of the reconstructed scattering tensor of the stapes. In this representation, each arrow's orientation corresponds to the main direction in each voxel.

10.3 CULTURAL HERITAGE APPLICATION

This section is a revised version of a paper submitted to JINST: "X-ray scattering tensor tomography with a random wavefront modulator to study 3D microstructures in archaeological skeletal remains" by Ginevra Lautizi, Simone A. M. Lemmers, Vittorio Di Trapani, Margaux Schmeltz, Alain Studer, Marie-Christine Zdora, Ludovic Broche, Federica Marone, Marco Stampanoni and Pierre Thibault.

10.3.1 Motivation

In biological samples such as bones and teeth, the scattering signal can provide valuable insights into the microstructural arrangement of components like collagen fibres or dentinal tubules, with a centimetre-scale field of view. In this section, we present a tensor tomography experiment conducted at the ID19-ESRF beamline in Grenoble, where we experimentally investigated two fragments from different tissue types - cortical bone and a root dentine - commonly analysed in archaeological and palaeoanthropological research.

In the archaeological tooth sample, dentine tubules - microscopic, hollow channels extending from the pulp chamber to the outer dentine surface - were of particular interest. Filled with fluid and containing extensions of odontoblast cells, these tubules are more densely packed and wider near the pulp, gradually becoming sparser and narrower towards the enamel-dentine junction. Their directional organization plays a key role in the mechanical properties of the dentine, influencing its response to stress and wear. Their orientation offers insights into functional adaptations, such as how teeth evolved to accommodate different diets or chewing forces, and may also indicate stress or developmental disruptions during growth **[Nanci2017; Dean2017]**.

Similarly, in the archaeological bone sample, the focus was on the orientation of collagen fibres within the bone matrix, which is crucial for the bone's strength and flexibility. Collagen fibres in bone can exhibit two patterns: disorganized in woven bone, or highly organized in lamellar bone. Woven bone, typically found in newly forming or healing bone, has randomly arranged collagen fibres, providing quick but temporary strength. In contrast, lamellar bone has a more orderly structure, with parallel fibres arranged in layers within osteons, offering greater durability and mechanical stability. The alignment of these fibres plays a critical role in the bone's ability to withstand forces and distribute stress, influencing its overall structure and function during growth, repair, and regular activity.

By examining these two samples, this study aims to give a first insight into whether tensor tomography can resolve the orientation of fibres in these tissues, potentially advancing methodologies for studying archaeological human remains.

10.3.2 Experimental setup and data acquisition

X-ray tensor tomography with a sandpaper modulator was performed at the ID19-ESRF beamline. We used the U13 undulator (bandwidth = 1%) in combination with 2.8 mm of aluminium filter to obtain a mean energy of 26.5 keV. As a wavefront modulator, we used a diffuser made of 6 sheets of *P*180 grit silicon-carbide sandpaper. As a detector, we used a PCO.edge sCMOS detector coupled to a LuAG:Ce scintillator and a coupled objective, featuring a pixel size of 6.5 µm. The diffuser-sample distance was 0.89 m, while the sample-detector distance was 0.88 m. The total FOV was 1650×1570 pixel or 10.7 mm $\times$ 10.2 mm.

To acquire the images, we followed the stair-wise acquisition protocol described in **[Kim2020; Kim2021]**. For each tilt angle β, we acquired 400 projections with a continuous rotation of the sample over 360°, while β ranged from 0° to 45° with an angular step of 15°. The exposure time for each projection was 100 ms. The reader is referred to section 10.1 for a detailed description and characterisation of the experimental setup.

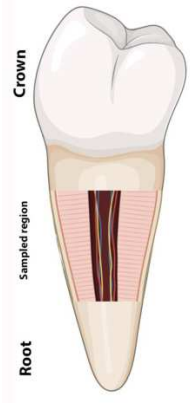

Figure 10.31: An outline of the sampled region of the analysed permanent premolar.

10.3.3 Sample preparation

The samples used in this study were remnants of histological sections prepared for Ref. **[Lemmers2020]**, originating from a historical cemetery. These fragments were control samples for a project focused on examining bioerosion and the preservation state of skeletal remains after heat exposure. All skeletal remains are from adult individuals, although no additional life history data was available. The selected bone sample concerns a femur anterior midshaft cortical bone fragment. The dental sample concerns a root fragment of a permanent premolar. Both fragments, despite being archaeological in origin, were in a good preservation state with minimal signs of microbial damage.

10.3.4 Analysis of the results

The acquired projections were analysed with the reconstruction method presented in Ref. **[Lautizi2024; Lautizi2024b]**. For both archaeological samples, we used as analysis window a 10×10 pixels square translated by 5 pixels, with a resulting spatial resolution of 32.5 µm. This window is a good compromise between a high spatial resolution and a low noise level in the reconstructed images. The computation time also plays a role in the decision of a proper analysis window.

For each analysis window, the 2D scattering tensor is calculated **[Lautizi2024; Lautizi2024b]** and eigendecomposed. Given the eigenvalues of the scattering tensor for each voxel, the following quantities can be derived. The mean of the eigenvalues represents the mean scattering within a defined window. The fractional anisotropy (FA) **[Basser1996]** indicates the degree of fibre alignment within the window. Regions with a high volume fraction of well-aligned fibres will display elevated FA values. The eigenvector corresponding to the smallest eigenvalue signifies the preferential local fibre orientation. We will show the above-mentioned quantities, as indicators for assessing the level of fibre scattering, alignment, and orientation.

For both samples, the omnidirectional dark-field signal was extracted from each projection of the tomographic dataset. The tensor sinogram was created by combining these results to determine the entire 3D scattering tensor field. A modified version of the alignment procedure from **[Liebi2015]** was used to align the projections. Since the local structure-orientation signal is sensitive to noise, especially in background areas and at sharp edges, a threshold-based mask based on attenuation was applied to the tomographic volumes of fractional anisotropy signal and orientation signal to exclude background regions.

Root dentine

Figure 10.32a shows a raw transmission image of the tooth sample obtained with the sandpaper modulator. The tooth fragment, a mid-section of the root (figure 10.31), is manually rotated by 90° and then placed on a holder. The extracted absorption image is presented in figure 10.32b. The mean scattering is shown in figure 10.32c. The main orientation (figure 10.32d) is represented using the eigenvectors of the 2D scattering tensor with the shortest length using an HSV colour scheme, where the hue (colour shade) indicates fibre orientation projected onto the detector plane, the saturation represents the fractional anisotropy, and the value (brightness) reflects the mean scattering intensity.

We hypothesize that the scattering signal primarily originates from the dentinal tubules. As the tubules move toward the outer regions of the tooth, their density decreases. This explains why there is an enhancement in the central area of the sample in the mean scattering signal (figure 10.32c). It

is important to highlight that these tubular structures are not resolved and remain invisible in the absorption signal (figure 10.32a).

In figure 10.33 two tomographic slices (sagittal, and coronal respectively) through the tooth sample are shown. Although dentine tubules are not directly visible in the absorption signal, they generate scattering signals that provide insights into the local microstructure. The main-orientation signal confirms the expected orientation of the dentinal tubules, which run from the dentine enamel junction to the dentine pulp border. Secondary dentine might be responsible for the changing orientation towards the centre (pulp chamber). In figure 10.33 the reconstructed tubules are aligned along the central axis of the tooth (red, x axis) in the central region and fan out toward the surface in the peripheral area (green, z axis, and blue, y axis). Despite the archaeological origin of the tooth sample, the general strong directionality of fibres is visible in the acquired data.

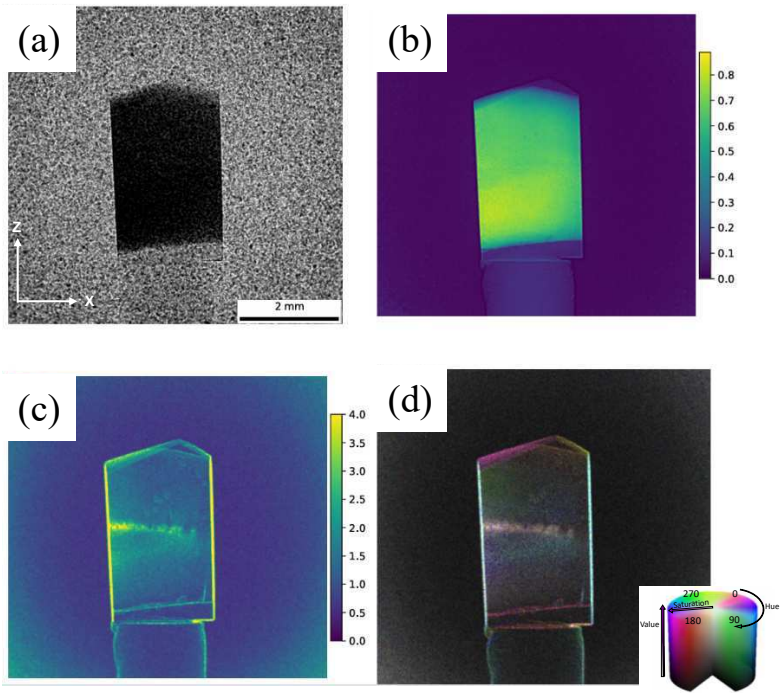

Figure 10.32: (a) An example of one of the projections of the tooth sample with a sandpaper modulator at $\alpha = 0°$, $\beta = 0°$. (b) Extracted absorption image, (c) mean scattering in arbitrary units and (d) main orientation signals. Each pixel corresponds to a unique region of the input image covered by overlapping windows (5×5 pixels).

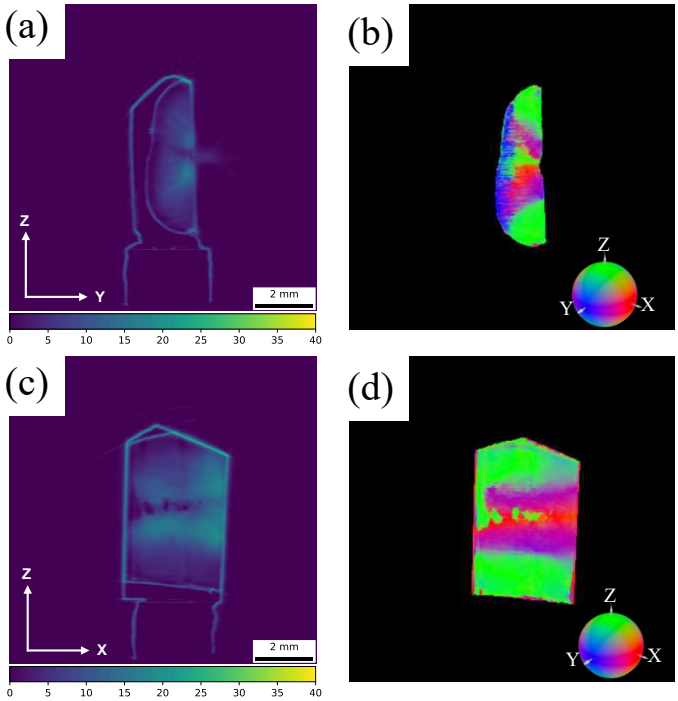

Figure 10.33: Two slices through the tomographic volume of the tooth fragment. A sagittal slice of the tooth: (a) mean scattering signals in arbitrary units, (b) main orientation signals, where the colour is an RGB representation of the local structure orientation. The colour ball is symmetric with respect to the $x - y$, $x - z$, and $y - z$ planes. A coronal slice of the tooth: (c) mean scattering signals in arbitrary units, (d) main orientation signals.

10.3.5 Cortical bone

Figure 10.34a shows a raw transmission image of the femur sample obtained with the sandpaper modulator. The extracted absorption image is presented in figure 10.34b. The mean scattering (figure 10.34c) is calculated as the mean of the eigenvalues of the scattering tensor. From the main orientation signal of this projection (figure 10.34d), it is visible how the main orientation is along the main axis of the sample (cyan colour), as expected from a femur fragment.

In figure 10.35, a coronal slice through the reconstructed volume of the femur fragment is shown. The interpretation of the extracted orientations (figure 10.35d) in this sample is not obvious. In these preliminary results, we were able to measure a signal and therefore an information about the sample. Due to the complex and hierarchical nature of bone and possible bone remodelling occurring in the measured specimen, it is not clear yet where this signal is originating from. For such complex materials, a more systematic approach with better known bone samples and validation is necessary to first understand the origin of the signal and possibly moving to more complex cases. However, from the scattering anisotropy signal (figure 10.35b) and especially from the mean scattering signal (figure 10.35c) it is possible to identify the cement lines (white arrow), interfaces between the osteons and the bone matrix, as vertical lines with a stronger scattering signal compared to the rest of the bone.

10.3.6 Conclusions

In conclusion, tensor tomography has the potential to generate detailed 3D reconstructions of microstructural features in biological tissues, such as dentinal tubules in teeth, but also demonstrates its limitations.

In the dental sample, we reconstructed the orientation and the distribution of dentinal tubules, key determinants of dentine's mechanical properties. These tubules differ in size, density, and arrangement between species and can be influenced by physiological or environmental stress. By analysing the directional characteristics of dentine's anisotropic structure, tensor tomography could contribute to the understanding of differences in the feeding behaviours of different species. For example, a change in dentine structure could indicate adaptation to tougher diets, which could be compared between different hominin species or across periods. The method could also have clinical dentistry applications. As highlighted by Zaslansky et al. **[Zaslansky2010]**, understanding the 3D structure and orientation of dentine tubules could enhance restorative procedures and improve simulations of teeth's mechanical properties, as well as for palaeopathology and oral health.

In addition, the first attempt of tensor tomography with cortical bone is presented. The interpretation of the extracted orientations in this sample

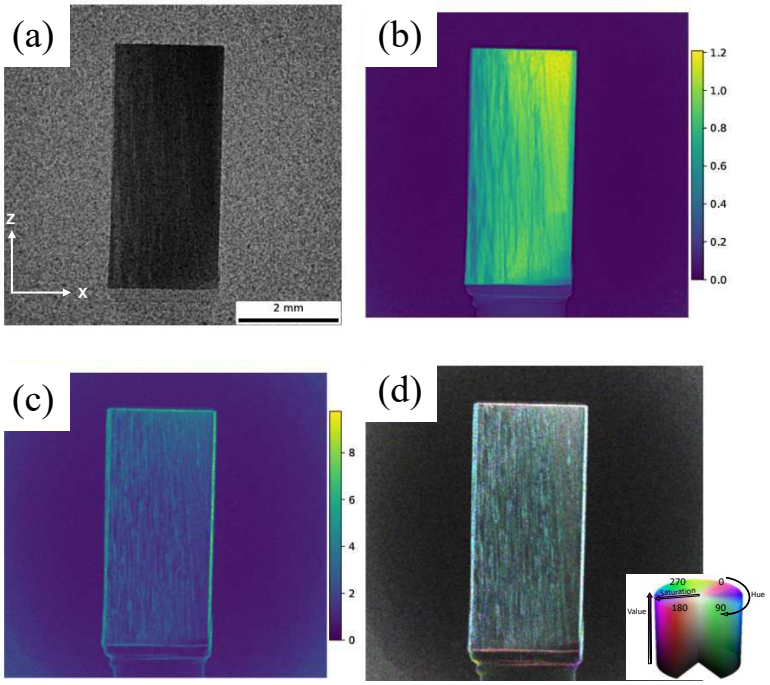

Figure 10.34: (a) An example of one of the projections of the femur sample with a sandpaper modulator at $\alpha = 0°$, $\beta = 0°$. (b) Extracted absorption image, (c) mean scattering in arbitrary units and (d) main orientation signals.

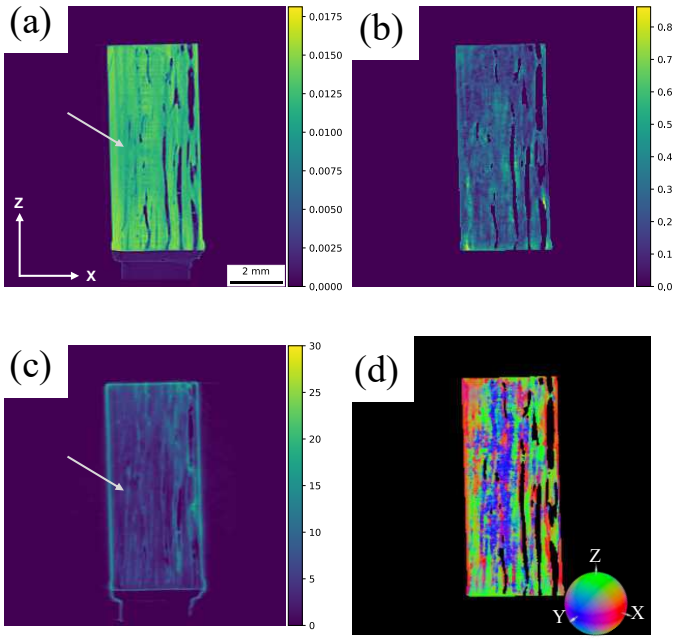

Figure 10.35: A coronal slice through the tomographic volume of the femur fragment. (a) Extracted absorption, (b) scattering anisotropy in arbitrary units and (c) mean scattering signals in arbitrary units are shown. (d) Orientation signals, where the colour is an RGB representation of the local structure orientation. The white arrow indicates one cement line.

presented challenges due to its complex microstructure **[Stockhausen2021]**. The imaged bone fragment, derived from an adult individual, consisted of remodelled lamellar bone with high osteon density and lacked woven bone. Due to the changes and layering of the orientation along the axis of the bone and the nanoscale sizes of the collagen fibres, a more systematic approach with better known bone samples and validation is necessary to first understand the origin of the signal in order to visualize features of relevance.

Overall, this study illustrates some potentials and limitations of tensor tomography for analysing the microstructural organization of archaeological human tissues. Further advancements, such as increased resolution and a reliable reconstruction of multiple overlapping scattering orientations within a single analysis window, could significantly enhance the versatility and robustness of tensor tomography. These developments would make the method even more valuable for both archaeological research and clinical applications.

11 THE OPTIMATO (OPTIMAL IMAGING AND TOMOGRAPHY) LABORATORY

During this PhD project, the development of the OPTIMATO laboratory was significantly contributed to, including the execution of routine testing during its construction. This chapter provides a detailed description of the new laboratory, the study for the optimisation of the acquisition settings, and some speckle-based imaging reconstructions with UMPA, led by Dr. Vittorio Di Trapani. In addition, the first results in the laboratory of the proposed omnidirectional dark-field signal extraction method are presented. The sections 11.2 and 11.3 of this chapter are a revised version of a paper published in Journal of Instrumentation: "Speckle-based imaging (SBI) applications with spectral photon counting detectors at the newly established OPTIMATO (OPTimal IMAging and TOmography) laboratory" by Vittorio Di Trapani, Sara Savatović, Fabio De Marco, Ginevra Lautizi, Marco Margini, and Pierre Thibault.

11.1 EXPERIMENTAL SETUP

The OPTIMATO (OPTimal IMAging and TOmography) laboratory (Fig. 11.1) is hosted at Elettra Sincrotrone, Trieste. X-rays are generated by a microfocal, high-brilliance liquid-metal-jet source (MetalJet D2+, Excillum, Sweden), having a maximum voltage of 160 kV, a power of 250 W, and adjustable focal spot sizes ($\geq$ 15 µm). This source can emit photons on two opposite sides, enabling two semi-independent imaging branches. The experimental setup is housed in a 7 m $\times$ 2.5 m lead-shielded hutch. The first branch, which we will refer to as the "long branch" uses two optical tables (2 m $\times$ 0.8 m each) for a maximum source-detector distance of 4 m. The second branch or "short branch" uses a single table, allowing a maximum source-detector distance of 2 m.

The short branch, currently under development and not used for this work, is for high-resolution imaging with resolutions between $0.65 - 3.3$ µm, achieved using an X-ray microscope coupled with an sCMOS camera. In the short branch, the propagation distance is up to 2 m. This setup includes an X-ray microscope (Optique Peter, France) with an sCMOS PCO edge 5.5 camera (PCO AG, Germany), featuring a pixel size of 6.5 µm and an active area of 2560 $\times$ 2160 pixels. The microscope has scintillator holders and objectives with 2$\times$, 4$\times$, and 10$\times$ magnifications. For high resolution, the system includes precise translation and rotation stages, allowing CT scans with

nanometric precision ($SLC - 1730$ Linear Piezo Stage, SmarAct, Germany) and high-resolution rotation (air-bearing direct-drive rotary stage, Aerotech Inc., USA).

The long branch is dedicated to modulation-based imaging applications and micro-CT (Fig. 11.2). In the long branch, the propagation distance is up to 4 m. This branch features two detectors: the LAMBDA 350k (X-Spectrum, Germany), an X-ray photon counting detector (XPCD) with 3×2 Medipix3 chips and a 1 mm thick CdTe sensor, with an active area of 28 mm $\times$ 42 mm and a pixel pitch of 55 µm. The Medipix3 chip operates in single-pixel mode or charge-summing mode, the latter overcoming charge-sharing issues for optimal resolution. The second detector in the OPTIMATO laboratory is a flat-panel detector (FPD): a Varex Imaging 1512 CMOS camera with a 200 µm CsI scintillator, an area of 145 mm $\times$ 115 mm, and a pixel pitch of 74.8 µm. Samples can be mounted on a Meca500 robotic arm (Mecademic Robotics, Canada) with 5 µm repeatability and six degrees of freedom, capable of translations and tomographic acquisitions, making it ideal for CT setups. Wavefront modulators like sandpaper or gratings can be mounted on motorized translation stages for horizontal and vertical motion. The spatial resolution in this branch is limited by the source size.

All instrumentation is connected to a control computer via Ethernet. An in-house developed Python-based software (`labcontrol`) manages the detectors, motors, and source, allowing complex acquisitions through scripts. The software also collects metadata (source voltage, current, detector settings, motor positions) stored in `.h5` files along with the frames. A live viewer based on the Python `napari` library monitors the frames during alignment and acquisition. Files are organized by investigation (global topic), experiment (specific sample), and acquisition (e.g., CT scan, planar acquisition, modulation-based imaging acquisition). For a more detailed description of the laboratory, the interested reader is referred to Ref. **[DiTrapani2024]**.

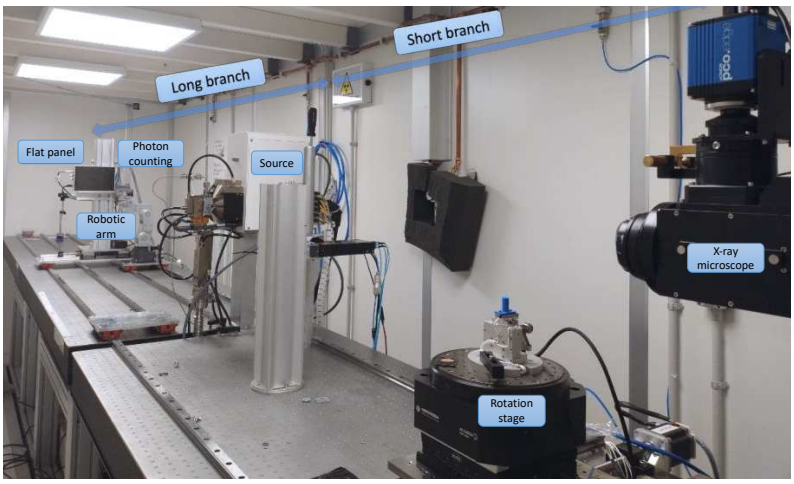

Figure 11.1: Image of the OPTIMATO laboratory setup showing the main components in the two branches.

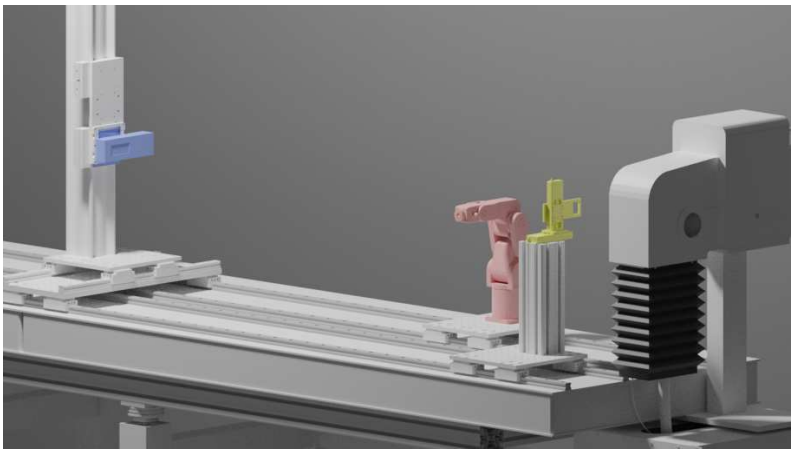

Figure 11.2: Render of the long branch. In yellow the diffuser holder, in pink the robotic arm, in blue the photon counting detector. Image courtesy of Fabio De Marco.

11.2 SPECKLE VISIBILITY

A key application for this type of laboratory is speckle-based imaging (SBI). In SBI, the visibility of the speckles increases with both transverse and temporal coherence at the diffuser plane, and it is crucial for retrieving differential-phase and dark-field signals. Transverse coherence improves with greater source-diffuser distances and smaller source sizes, while temporal coherence is enhanced by the monochromaticity of the X-ray beam. These factors explain why SBI is particularly well-suited for synchrotron facilities, which offer long propagation distances, monochromatic radiation, parallel-beam geometry, and high fluence rates.

When adapting SBI from synchrotron to laboratory sources, several limitations arise. Temporal coherence is constrained by the polychromatic nature of the X-ray beam, and transverse coherence is restricted by the finite source size and shorter propagation distances achievable in a laboratory setting. Unlike synchrotron sources, where X-ray wavefronts can be approximated as plane waves, laboratory setups typically use a cone-beam geometry. In this case, propagation effects are described by spherical waves, and the effective propagation distance (z_{eff}), needed to achieve results comparable with a parallel beam, is determined by the Fresnel scaling theorem **[Paganin2006]**:

$$z_{\text{eff}} = z/M, \tag{11.1}$$

where M is the geometrical magnification and z is the sample-detector distance. Therefore, for a cone-beam geometry, larger distances are required.

Optimization of acquisition settings, such as the effective propagation distance and the selection of an appropriate detection system, is crucial in overcoming the limitations of a laboratory-based SBI setup. The cone-beam geometry requires careful consideration of the source-detector and source-diffuser distances. According to the Fresnel scaling theorem, the effective

propagation distance is given by the ratio of the sample-detector distance (z) to the magnification factor (M), i.e., $z_{\text{eff}} = z/M$. For the long branch setup at the OPTIMATO laboratory, the maximum z_{eff}, and thus the visibility enhancement from propagation effects, is limited by this magnification. Plots illustrating the effective propagation distances achievable under various conditions at the OPTIMATO laboratory are provided in Fig. 11.3. It is visible how, for a given source-detector distance, the maximum effective propagation distance is obtained for magnification $M = 2$. Therefore, for a propagation distance in the long branch of to 2 m, the maximum effective propagation distance is $z_{\text{eff}} = 1$ m.

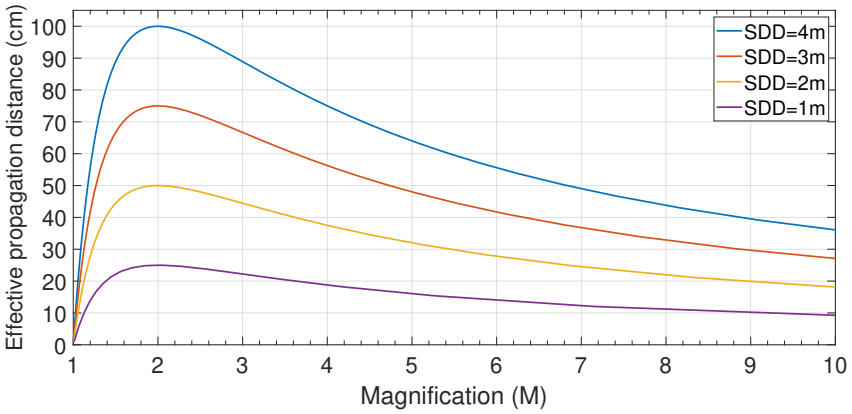

Figure 11.3: Effective propagation distance as a function of the magnification for different source-detector distances. Reprinted with permission from **[DiTrapani2024]**.

Once the effective propagation distance has been optimised, the selection of an appropriate detection system is fundamental in the optimisation of a laboratory-based SBI setup. To improve speckle visibility, a detector with a high spatial resolution is desirable. The spatial resolution of a detection system is typically characterized by the point spread function (PSF) **[Cunningham2000]**. In cone-beam X-ray setups, the system's PSF_{sys} is influenced by the detector's PSF_{det}, the magnification (M), and the source size (D), as expressed by the following equation **[DiTrapani2024]**:

$$PSF_{\text{sys}} = \sqrt{\left(\frac{PSF_{\text{det}}}{M}\right)^2 + \left(\frac{M-1}{M}\right)^2 \cdot D^2}. \tag{11.2}$$

Eq. 11.2 indicates that increasing M can enhance spatial resolution up to the limit set by the source size ($PSF_{\text{sys}} \geq D$). However, the effective propagation distance decreased for $M > 2$ as seen in Fig. 11.3. Thus, to maximise speckle visibility, an inherently higher spatial resolution detector, with a small PSF_{det}, is desirable.

We compared the PSF_{sys} and the speckle visibility in the OPTIMATO laboratory for two detectors: the LAMBDA (XPC) and the Varex (FPD), as described in section 11.1.

We used the slanted edge method **[Samei1998]** to calculate the full-width at half maximum (FWHM) of the presampling PSFs. It was determined to be (130 ± 3)µm for the FPD and (49 ± 3)µm for the XPCD. Fig. 11.4a illustrates the spatial resolutions achievable with the XPCD and FPD as a function of magnification. The XPCD provides superior spatial resolution, particularly near $M = 2$, where effective propagation distance is maximized, enhancing propagation effects.

We conducted speckle visibility measurements for both detectors, varying the source-diffuser distance, and keeping the source-detector distance fixed at 150 cm. Four layers of $P120$ sandpaper were used as the diffuser. Visibility was calculated as the ratio of the standard deviation (σ) to the mean (μ) of the speckle pattern. Figure 11.4b shows the measured speckle visibility as a function of magnification. The results reveal that the XPCD outperforms the FPD. Additionally, the highest visibility for both detectors was observed at $M = 2$, corresponding to the maximum z_{eff}, as seen in Fig. 11.3.

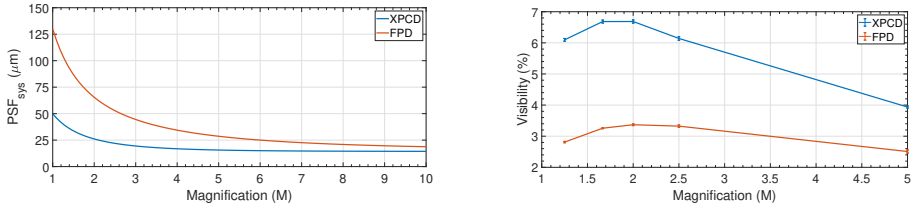

(a) (b)

Figure 11.4: (a) PSF_{sys} as a function of the magnification for the XPCD and FPD available in the long branch, and a source size of $D = 20$ µm. (b) Visibility as a function of the magnification obtained with the FPD and the XPCD placed at 150 cm from the source. Reprinted with permission from **[DiTrapani2024]**.

11.3 THE FIRST SBI IMAGES

After finding the parameters for an optimised speckle visibility and spatial resolution, two SBI scans were conducted, both for the XPCD and the FPD. Four layers of $P120$ sandpaper were used as the diffuser. The source-detector distance was set at 150 cm, the source-diffuser distance was 75 cm, and the magnification was $M = 2$. The sample, consisting of a water-filled pipette tip, a beetle attached to a pipette tip, and a wooden toothpick, was placed 80 cm from the source. For the XPCD, dead pixels and artefacts from CdTe charge trapping, which could interfere with the speckle tracking algorithm, were filtered using the method in **[DiTrapani2021]**. With both detectors, an equivalent exposure time per projection of 60 s was used, ensuring a visible speckle pattern over the Poissonian noise. Multiple images were taken and averaged for each projection to improve photon statistics. In addition, 20 diffuser positions were captured.

The images were then processed using the new version of UMPA **[DeMarco2023]**. This processing produced the transmission (T), dark-field (df), and horizontal differential-phase (dx) signals. The results of the analysis are shown in Fig. 11.5.

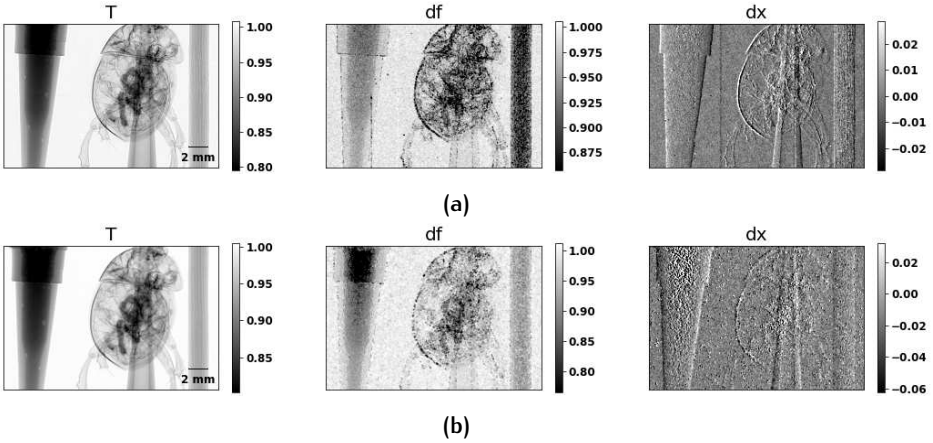

Figure 11.5: Transmission (T), dark-field (df), and horizontal differential-phase (dx) images reconstructed with UMPA from SBI datasets acquired with (a) XPCD, (b) FPD. Reprinted with permission from **[DiTrapani2024]**.

From a visual inspection of the dark-field and differential phase images in Fig. 11.5, it is clear how the XPCD clearly distinguishes sample features from the background, while the FPD images is more subject to noise, leading to lower-quality UMPA reconstructions. This result is largely due to the higher speckle visibility provided by the XPCD. The results suggest that the visibility of about 3% achieved by the FPD is insufficient for reliable SBI reconstructions using UMPA. It is worth noting that while the FPD may not be ideal for SBI with sandpaper diffusers, it might still be possible to use it for SBI with custom diffusers made of more absorbent materials. It is also important to recognize that FPDs, with their large detection areas, are valuable for propagation-based imaging and conventional micro-CT of large samples.

The XPCD in the long branch also supports spectral imaging applications. In Fig. 11.6 a spectral decomposition is shown, using three materials on the same sample used in the SBI scans (Fig. 11.5). For this spectral acquisition, three absorption images were taken at different energy thresholds (13 keV, 23 keV, and 26 keV). The three thresholds divided the spectrum into three energy ranges with an equal photon count. The total exposure time for each projection was 60 s. Material decomposition was performed using the minimum residual spectral decomposition algorithm presented in **[DiTrapani2022]**. Three material bases were used: $CaCO_3$, water, and carbon. The results in Fig. 11.6 demonstrate the system's ability to differentiate between water and plastic pipettes and accurately identify $CaCO_3$ in the beetle's carapace. If combined with phase, dark-field, and transmission signals, this spectral decomposition significantly enhances the diagnostic potential of the setup.

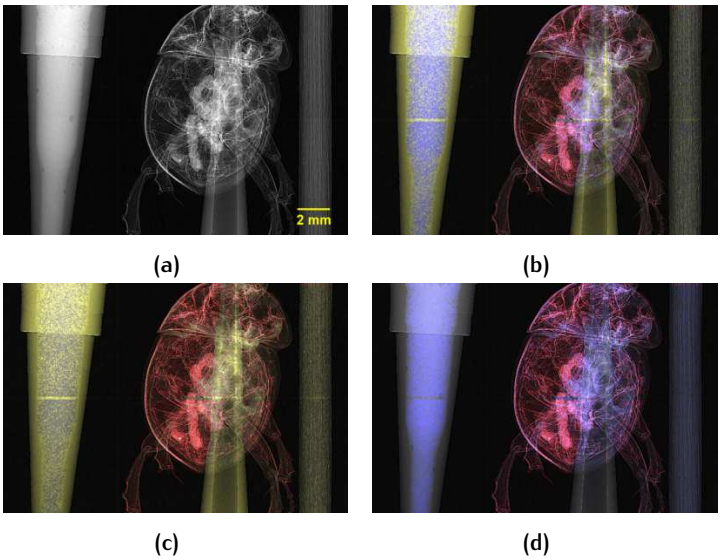

Figure 11.6: Spectral imaging applications on a validation sample. (a) Absorption radiography. Overlay of the absorption radiography with the decomposed bases: (b) $CaCO_3$ (red), water (blue), and carbon (yellow). (c) $CaCO_3$ and carbon. (d) $CaCO_3$ and water. Reprinted with permission from **[DiTrapani2024]**.

11.4 OMNIDIRECTIONAL DARK-FIELD SIGNAL EXTRACTION

SBI images were acquired in the long branch of the OPTIMATO laboratory (Fig. 11.7a). For this application, the test sample was built placing in sequence four samples already scanned at synchrotron, three carbon fibre composites and a fossil tooth: the "T-shape" sample and the "notch" sample described in section 10.1, the carbon fibre cross described in section 7.4.1, and the fossil tooth described in section 10.3. An image of the four samples is shown in Fig. 11.7b.

We used the optimised parameters with which we scanned the first SBI images in section 11.3. We used four layers of *P*120 sandpaper as a diffuser, and the LAMBDA 350k (XPCD) as a detector. This detector has an active area of 28 mm $\times$ 42 mm, with a pixel pitch of 55 µm. The source-detector distance was set at 150 cm, the source-diffuser distance was 75 cm, and the magnification was $M = 2$. The sample-diffuser distance was 8 cm. We used a tube voltage of 60 kV, and additionally filtered the beam with 1.08 mm of aluminium. The images were taken with a detector's energy thresholds of 13 keV. The exposure time for each projection was 3 s. Multiple images (10) were taken and averaged for each projection to improve photon statistics. SBI scans were performed using the diffuser-stepping method, where the diffuser is laterally translated (40 different positions), while the sample remains stationary, to achieve a higher spatial resolution **[DeMarco2023]**.

The images were then processed using the new version of UMPA **[DeMarco2023]**. This processing produced the transmission (T), dark-field (df), and horizontal and vertical differential-phase (dx, dy) signals. The results of the analysis are shown in Fig. 11.8.

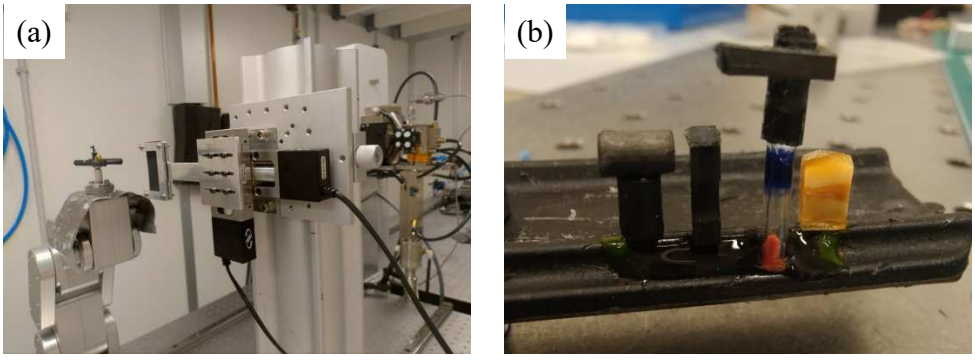

Figure 11.7: (a) An image of the experimental setup showing the sample with the sample holder and the diffuser with its motors. (b) An image of the validation sample, obtained placing in sequence three carbon fibre composites and a fossil tooth.

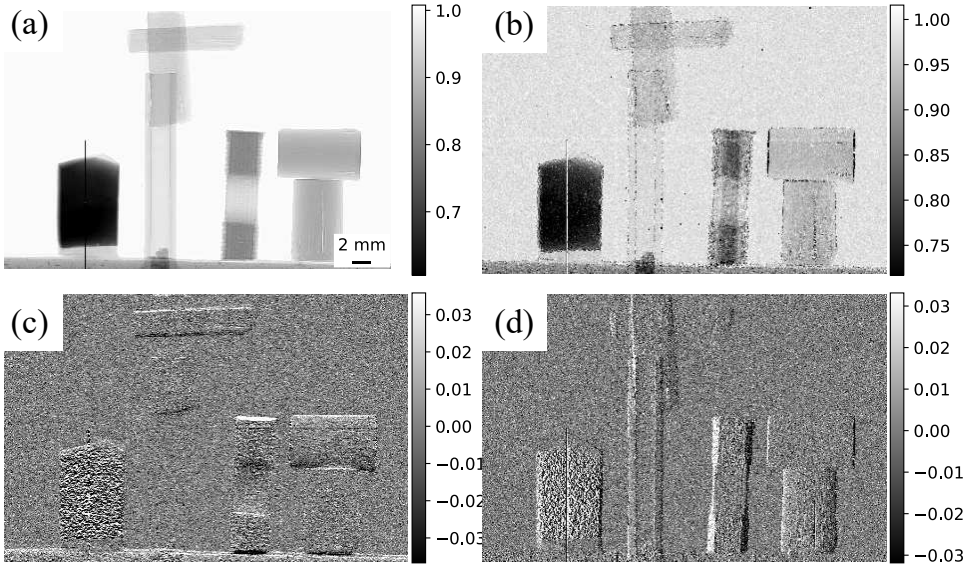

Figure 11.8: Results of the UMPA analysis on the validation sample made for the omnidirectional dark-field signal extraction. (a) Transmission, (b) dark-field, (c) horizontal and (d) vertical differential-phase images reconstructed with UMPA from SBI datasets acquired with the XPCD.

From a visual inspection of Fig. 11.8, a column of dead pixels and several dead pixels are visible in the reconstructed images, particularly in the dark-field image. The tooth is too dense and thick for this setup, therefore it suffers from beam starvation. The vertical and horizontal features of the carbon fibre cross and the T-shape sample are correctly reconstructed in the horizontal and vertical differential-phase images.

The SBI images were then analysed with the algorithm described in chapter 8 to extract the omnidirectional dark-field signal. Since the pattern created by the sandpaper is random, there is no periodic unit cells, hence the analysis window can be of arbitrary size. We chose a square analysis window with size 5 pixels, or 275 µm, and we translated the window with a step size of 1 pixel in order to cover all the image.

In Fig. 11.9 the results of the omnidirectional dark-field signal extraction method are shown. In Fig. 11.9a, a raw transmission image is visible. The near-field speckles are visible, and their blurring due to strong scattering from the sample can be observed, even if not intense. The extracted absorption image is shown in Fig. 11.9b, while the mean scattering is shown in Fig. 11.9c. The pixels at the border of the chips, bigger than the others, are clearly visible in the mean scattering image since in these pixels the visibility of the speckles is lower and therefore the dark-field signal extraction method struggles. The main orientation (Fig. 11.9d) is the HSV representation of the 2D eigenvectors with the shortest lengths, where the hue (colour shade) is the fibre orientation projected onto the detector plane, the saturation is the fractional anisotropy, and the value (brightness) is the mean scattering intensity. The results in Fig. 11.9d show that the main orientation signal matches with the expected orientation of the fibres (cyan along the vertical axis and red along the vertical axis), thus demonstrating the effectiveness of the proposed method for random reference patterns as well. Since the tooth was subject to photon starvation, it was not possible to obtain relevant orientations. In the near future, we plan to optimise the choice of the diffuser, for an enhanced visibility, resulting in a stronger dark-field signal.

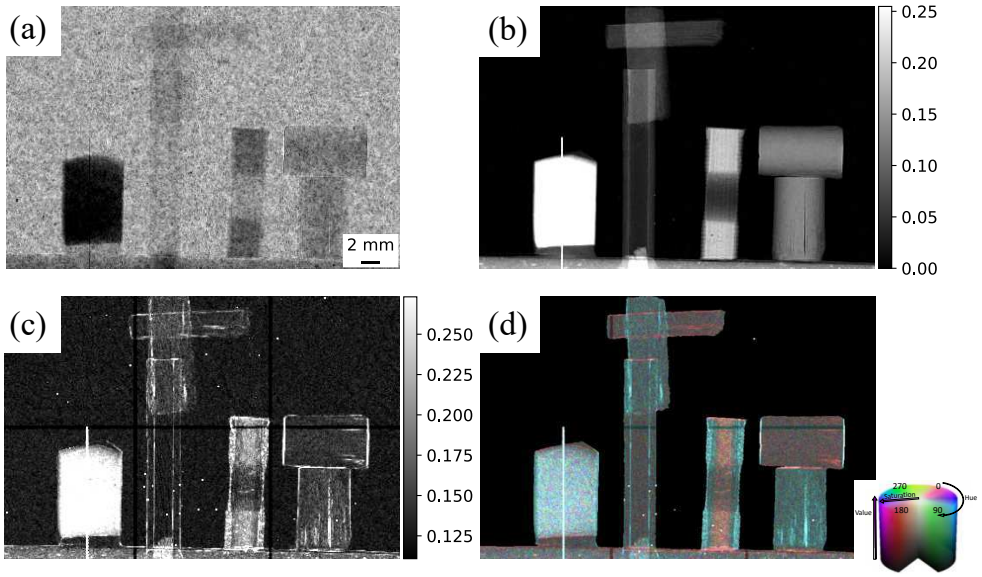

Figure 11.9: Results of the omnidirectional dark-field signal extraction on the validation sample made. (a) Raw transmission image. (b) Extracted absorption image and (c) mean scattering signals. (d) Main orientation signals in green and red, contrast has been enhanced for visualization purposes.

11.5 CONCLUSIONS

In this chapter, a newly developed X-ray setup at the Elettra synchrotron was presented. This versatile setup is designed for various imaging applications,

including absorption radiography, micro-CT, propagation-based imaging, X-ray modulation-based techniques like SBI, and spectral imaging.

Initial SBI tests in the long branch showed that XPCDs offer superior image quality compared to traditional FPDs, especially for differential-phase and dark-field images, due to their higher speckle visibility. This makes XPCDs crucial for adapting SBI from synchrotron sources to compact X-ray laboratories. Additionally, their spectral capabilities broaden the range of potential applications.

Moreover, the omnidirectional dark-field signal extraction analysis confirmed the effectiveness of the proposed method, accurately identifying the orientation of fibres in the sample, even with a random wavefront marker and a laboratory source. However, issues like dead pixels and low visibility have to be tackled in the near future.

Future work will aim to optimize the diffuser to enhance visibility and strengthen the dark-field signal, thereby improving the quality of the reconstructed images. Future developments include the acquisition of a full tensor tomography dataset to test the algorithm described in chapter 7 also with a laboratory source. In addition, the development of the short branch, enabling resolutions between $0.65 - 1\,\mu m$, will create, together with the long branch, a multimodal and multi-resolution X-ray facility for the scientific community.

12 SUMMARY, CONCLUSIONS, AND OUTLOOK

The main focus of this thesis was on the development and application of advanced X-ray imaging techniques: modulation-based dark-field imaging and X-ray scattering tensor tomography. In this thesis, all stages of the research process were conducted by the author. This includes the proposal writing for the synchrotron facilities, experimental design and execution, development of new algorithms, data collection and analysis, and the writing of research papers associated with this work, unless otherwise explicitly stated in the respective chapters or sections of the thesis.

In this chapter, the main conclusions of each chapter contained in this thesis are presented, along with the directions of future research studies.

12.1 SPECKLE-BASED DARK-FIELD DAMAGE DETECTION IN CFRP

With this study, we have demonstrated that by using dark-field radiography, it is possible to effectively visualise barely visible impact damage in carbon-fibre reinforced polymers. We examined two samples: one primarily affected by matrix-cracking damage, and the other characterised by delamination damage. In both cases, traditional transmission radiographs revealed little to no damage apart from the impact point, while dark-field radiographs clearly highlighted the damage. This study was the first demonstration of speckle-based dark-field imaging applied to detect barely visible impact damage. In addition, we were able to extend the field of view by using the UMPA algorithm, which combines multiple frames from different sample positions.

At present, a limitation of the method lies in the artefacts caused by variations in the X-ray beam's intensity across the various frames used to produce the final images. These artefacts cannot be corrected using intensity corrections, as the beam's location on the detector also fluctuates. These artefacts hinder a straightforward segmentation and have to be addressed in the future.

In the future, this approach has the potential to become a standard method for rapid non-destructive testing in laboratory settings. Additional samples, with different damage extensions, will also be investigated in the laboratory.

12.2 A MULTIMODAL X-RAY TOMOGRAPHY STUDY FOR THE EVALUATION OF THE MICROSTRUCTURAL CHANGES IN BIOLOGICAL TISSUES

We demonstrated the application of a combined propagation-based imaging and modulation-based imaging study to perform virtual histology on both ovarian and hepatic tissues. By exploiting phase tomograms, we were able to extract detailed structural information, enabling further analysis of various functional parts of the organs, such as follicles in the ovary and lipidic aggregates in the liver. This approach allowed a deeper understanding of the microvasculature and tissue architecture, revealing the effects of clinical cryopreservation on ovarian tissues and improving the understanding of hepatic tissue structure, particularly in relation to steatosis diagnosis.

These measurements were originally designed for a dark-field analysis of the microstructural changes in ovarian tissue and the sub-micrometer lipidic aggregates in hepatic tissue. However, the dark-field signal was severely affected by beam instabilities. Additionally, the sample preparation was not optimal, as this was also a test experiment for the collaborators. Moreover, a phase gradient is still present in the reconstructed liver volumes. Further analysis is required to address these artefacts, which are likely caused by edge-enhancement effects that are not accounted for in UMPA.

Future work could include revisiting dark-field analysis of sub-micrometer lipidic aggregates in hepatic tissues using different samples and improved resolution to minimise beam instabilities. We believe this method could significantly advance the study of microanatomy and tissue changes during maturation or clinical procedures.

12.3 A UNIVERSAL RECONSTRUCTION METHOD FOR X-RAY SCATTERING TENSOR TOMOGRAPHY BASED ON WAVEFRONT MODULATION

To overcome the limitations of previous omnidirectional dark-field extraction methods, we presented a general algorithm applicable to a wide range of X-ray imaging approaches that have access to the scattering signal, without the need for additional regularisation. We demonstrated its effectiveness for three different full-field dark-field imaging setups: a circular phase-grating array, a fractal wavefront modulator, and a sandpaper diffuser. We validated the results using grating interferometry by comparing them with previous studies. The presented algorithm lays the groundwork for tensor tomography using speckle-based imaging, enabling the complete reconstruction of tensor tomograms with a simpler setup and optics. This simplicity enhances the potential for its adoption in laboratory environments, making it accessible to a broader user community. The main distinction from earlier methods

is that our approach offers a full-field technique applicable to a variety of wavefront modulators, including non-periodic ones. Unlike previous works, our method extracts the scattering signal and reconstructs the full tensor field, not just the scattering along predefined directions.

Different full-field dark-field imaging setups (gratings, fractal, and speckle) have been tested. While the fractal modulator showed low visibility of the pattern, requiring optimization of both the setup and the modulator itself, the grating array and the random modulator both enabled successful reconstructions. Both setups have their respective strengths and limitations. The random modulator offers greater flexibility, allowing for the tuning of distances and spatial resolution, while the grating array provides higher visibility and enables single-shot acquisitions. The choice of modulator depends on the sample type. For industrial samples, where high spatial resolution is not required and fast acquisition is preferred, the grating array is more effective. On the other hand, for complex samples where resolving small structures is critical, and setup flexibility is advantageous, the random modulator is preferred. Further research is needed to enhance the quality of the random modulator to achieve higher visibility, particularly when using laboratory sources.

At present, a limitation of the reconstruction method arises when multiple scattering orientations overlap within a single analysis window, resulting in a mixed orientation that hinders accurate reconstruction. Further research is needed to develop a model that accounts for multiple scatterers.

Nevertheless, the proposed innovative method can benefit multiple fields, including medical physics for studying bone microstructures and material physics for characterising fibre-reinforced materials. In the future, our approach could potentially become a standard method for rapid non-destructive testing in laboratory settings.

12.4 A ROBUST DARK-FIELD SIGNAL EXTRACTION FOR MODULATION-BASED X-RAY TENSOR TOMOGRAPHY

After paving the way with our versatile reconstruction method, we introduced the first demonstration of speckle-based tensor tomography, achieved by developing a novel method to efficiently extract the X-ray directional dark-field signal from data obtained using a random diffuser. Formulating the problem using a weighted linear least-squares approach ensured the numerical stability necessary for accurate reconstructions. The effectiveness of this method was validated through speckle-based imaging projection scans on various samples, with results compared to prior studies on the same sample. Our new algorithm showed improved stability, producing dark-field images with significantly less noise than our previous approach.

The proposed method, adaptable to various data acquisition schemes, opens up new possibilities for applying X-ray scattering tensor tomography with a non-periodic X-ray beam modulator. Our approach reconstructs the full tensor field independently of the experimental setup.

Given the experimental simplicity of speckle-based imaging, which has already been demonstrated in laboratory environments, speckle-based tensor tomography can also be implemented using laboratory sources, making it accessible to a wider user community. In the near future, we plan to adjust the acquisition process by exploring a sample-stepping approach, rather than diffuser-stepping, to expand the field of view and reduce acquisition time. Moreover, a current limitation of the model is that only a single orientation is extracted for each analysis window of a projection. Ongoing research is focused on improving reconstruction reliability when multiple scattering orientations overlap within a single analysis window, which could greatly enhance the method's versatility and robustness.

12.5 A NUMERICAL WAVE-OPTICS SIMULATION MODEL FOR SPECKLE-BASED IMAGING

After validating modulation-based X-ray tensor tomography, we introduced a numerical wave-optics simulation model tailored for speckle-based imaging. Just as speckle-based imaging experiments can be conducted under various setup conditions, the simulation allows setup parameters, such as beam type, geometry, sandpaper type, and diffuser steps, to be adjusted. We provided several examples, including the simulation of a speckle-based imaging measurement on a carbon fibre cross, which we successfully analysed using the UMPA algorithm and our omnidirectional dark-field signal extraction model. Additionally, we simulated a small-angle scattering experiment and an X-ray tensor tomography experiment, successfully reconstructing the main orientation of sub-resolution microstructures.

A current limitation of the simulation is the speed of the sinogram generation process. The projections are calculated using the TIGRE library, which also allows for easy implementation of cone-beam geometry. It would be interesting to try generating projections using the ASTRA toolbox, after correctly defining the geometry, and compare the computational speed of the two methods.

In the future, this simulation will serve as a powerful and flexible tool for investigating new configurations and optimising experimental setups, especially for modulation-based imaging and tensor tomography applications. Future work could involve testing different configurations, such as laboratory setups, and comparing the simulated outcomes with experimental data acquired in the laboratory.

12.6 APPLICATIONS OF MODULATION-BASED X-RAY TENSOR TOMOGRAPHY

We validated our reconstruction algorithm for modulation-based X-ray tensor tomography using a sandpaper modulator at a fourth-generation synchrotron. Using our reconstruction algorithm, we were able to determine the main orientations of carbon fibres in aerospace-grade unidirectional carbon-epoxy composites, with have a great relevance to sustainable engineering.

In the future, it would be interesting to apply this method to materials subjected to low-velocity impact testing, which display cracks and delamination, as well as to composites made from recycled carbon fibres, where re-oriented fibres could be mapped for better characterisation.

In another application, we showed how our algorithm successfully delivered 3D main orientations of mineralised collagen fibrils in the auditory ossicles, offering insights into bone remodelling and potential improvements in understanding sound transmission in the middle ear. This could lead to advancements in middle-ear surgery and benefit patients with conductive hearing loss.

In a future research, we could compare these results with higher-resolution techniques like speckle-based tensor tomography or scanning small-angle scattering, especially since the complex orientations of collagen fibrils at the sub-micron scale might be better captured with higher resolution methods.

Finally, we provided a detailed 3D reconstructions of key microstructural features in cultural heritage samples, such as fossilised teeth and bones. In the case of a fossil tooth, our technique could reveal the orientation and distribution of dentinal tubules, which are crucial for understanding the dentine's mechanical properties. Differences in the arrangement of these tubules may reflect dietary adaptations, offering insights into the dietary behaviours of ancient species and primates. In the future, our method could be exploited in both palaeontological studies and potential clinical applications.

For fossil bones, such as the femur fragment studied in this thesis, tensor tomography could also extract a signal and therefore an information about the sample. Given the variations in orientation along the bone axis and the nanoscale size of collagen fibres, a more systematic approach using well-characterized bone samples and proper validation is required to understand the origin of the signal and accurately visualise relevant features.

12.7 THE OPTIMATO LABORATORY

In the last chapter of this thesis, we introduced a newly developed X-ray laboratory setup, designed for a wide range of imaging applications, such

as micro-CT, propagation-based imaging, X-ray modulation techniques like speckle-based imaging, and spectral imaging. Initial tests with speckle-based imaging in the long branch demonstrated that X-ray photon-counting detectors provide better image quality than traditional flat-panel detectors, making photon-counting detectors necessary to adapt speckle-based imaging from synchrotron sources to compact X-ray laboratories. After validation at the synchrotron and simulations, we validated our omnidirectional dark-field signal extraction method also in the laboratory, successfully determining the orientation of fibres in the sample.

A full tensor tomography dataset has not yet been acquired due to mechanical issues with the manipulator and the source. The sandpaper diffuser may not be an ideal modulator for a laboratory source, as it results in low visibility, requiring longer acquisition times. To enable efficient tensor tomography acquisition in a laboratory setup, a different random diffuser with higher visibility would be necessary.

In the future, challenges like dead pixels and low visibility need to be addressed. Future efforts will focus on optimising the diffuser to improve visibility and enhance the dark-field signal, which will lead to better image reconstruction. A longer propagation distance would also help in a resulting higher visibility. In addition, we plan to acquire a complete tensor tomography dataset to test our tensor tomography algorithm with a laboratory source. Finally, the development of a short branch with higher resolutions will complement the long branch, creating a multimodal, multi-resolution X-ray facility for the scientific community.

12.8 FINAL REMARKS

This thesis work has advanced the field of X-ray imaging by developing and applying innovative techniques, such as modulation-based directional dark-field imaging and X-ray scattering tensor tomography. These methods have been demonstrated across a variety of applications, including damage detection in carbon-fibre reinforced polymers, virtual histology of biological tissues, and orientation mapping of fibres in both composite materials and biological structures.

The introduction of a universal reconstruction algorithm, adaptable to different imaging setups and applicable in laboratory environments, marks a significant step toward making these advanced techniques accessible to a broader community of researchers.

Future research will aim to address current limitations, such as improving the signal extraction of overlapping scattering orientations and enhancing the visibility in laboratory setups. Optimising acquisition processes and extending these techniques to study materials under different conditions,

such as recycled composites and impacted samples, will further expand the scope and utility of this work.

The establishment of the OPTIMATO laboratory also promises to create a versatile platform for multimodal, multi-resolution X-ray imaging, supporting a wide range of scientific investigations in the years to come.

Together, these developments contribute significantly to the future of X-ray imaging, promising further applications in both materials science and medical research.

ACKNOWLEDGEMENTS

When I was a curious Physics student reading theses, the starting chapter for me was the Acknowledgements section. I believe that most of our achievements can be traced to interesting talks and clever guidance. Even though the press and social media tend to prioritise the story of a single researcher, self-taught and with a self-built nuclear reactor in the basement, I strongly believe that no researcher will go anywhere without an inspiring mentor, frequent exchanges with other minds, a supporting network of friends and family.

To Professor Pierre Thibault: thank you for giving me the opportunity to work on this exciting project. Thank you for your patience for all the last-minute ideas and workshops and for the financial support for schools, conferences, and the Switzerland experience. You gave me the freedom to enjoy every learning experience, and I really appreciated it.

To Professor Marco Stampanoni: thank you for welcoming me to PSI for five months. It was an invaluable learning experience, both for my research and my personal life. Thank you for the exclusive TOMCAT Swiss knife that I am often using and for your kind words.

To Alain Studer and Federica Marone, it is really difficult to express my gratitude in few words. You made my period in Switzerland one of the happiest parts of my PhD. Your constant support and kindness really made the difference to me.

To Marie-Christine Zdora, thank you for you kindness, your knowledge, for proofreading my bad writing and for saving me multiple times from sunburn. I am really grateful for having found a heart-warming person that I really get along with and that I am happy to call my friend.

Thanks to Yeajin Lee, Mark Mavrogordato, Ian Sinclair and Richard Boardman of Southampton University for proving the carbon-fibre composites, to Lukas Anschuetz of Inselspital Bern for providing the human middle ear ossicles. My gratitude goes also to Lorella Pascolo and Giuseppe Ricci from IRCCS Burlo Garofalo for providing the ovarian and hepatic tissue and to Simone Lemmers of Elettra Sincrotrone Trieste for providing the cultural heritage samples and discussing with me the results.

To the beamline scientists I had the pleasure to work with, expecially Ludovic Broche from ESRF-ID19 who patently stayed by my side when I was anxious and discouraged. To Christian Schlepuetz and Philipp Zuppiger from SLS-TOMCAT for assistance during the beamtimes. To Giuliana Tromba, Adriano Contillo and Elena Longo for assistance in using the SYRMEP beamline. To Elettra Sincrotrone Trieste and to the Department of Physics for hosting me

for eight years now and to all the Elettra staff that helped me during my PhD project. No, you are not quite rid of me yet!

In the preparation of this thesis, I used ChatGPT, an AI-based language model developed by OpenAI, to assist with rephrasing and improving the clarity of certain sections. All content was generated based on my original research and ideas, and the final revisions and approvals were made by me.

To my loved PhD mates: Vittorio, Fabio Sara, Marco, Bo, Ronan, Michèle, Mattia. I will miss our strolls after lunch with unexpected close encounters with snakes (don't worry, I never saw one! cit.), giant bugs and poor future samples. Thank you for having made my PhD a joyful experience with the time spent together. Thanks, Fabio, for your patient support during the first year, it has been invaluable to me. Thanks also to Francesca, Luca and Martina for the company and the delicious dinners you prepared.

My gratitude goes to Ralf Menk and Fulvia Arfelli, that I now consider part of my family. Thank you for guiding me since I was an undergraduate student. For all the parties, but also for the serious talks.

To TOMCAT group, thanks for welcoming me so warmly, for all the pizza Tuesdays and the drinks. To TOMCAT students: Stefano, Alex, Simon, Alexandra, Caori, Alehandra, Cristina. Thanks for your friendship and the dangerous Swiss experiences you convinced me to do. Sometimes we just need someone to push us beyond our limits. I will forever cherish the memories we made together, and the sledge will forever be in my "never-more" list.

To Jisoo, your knowledge and experience made the difference in my project. Thank you for answering all my "this is the last" emails. To Margaux, thanks for the beamtimes together and for all the fun we had at the conferences. I wish you all the best for your Italian future, and I hope we can meet again.

To the cookie meeting journal club and to Abe, thanks for all the thought-provoking presentations on novel and inspiring topics. To Manuel Guizar Sicairos for the fruitful meetings and for keeping me involved in your imaging group meetings even if I am not in Switzerland anymore.

To the Trieste micro-CT meeting group: Paola, Luca, Renata, Luigi, Giulia, and Andrew. Thank you for the fruitful discussions. To Melissa Amati, thank you for our discussions and for being my organised light of wisdom even in the darkest moments.

To Alberto Morgante and Enrico Morgante for giving me the opportunity to teach at the University. It was a pleasure to be surrounded by young and curious minds.

To all the people I was lucky to meet at the international conferences and schools: Federica, Till, Francesca, Martina, Matteo, Wannes, Matias and many others. It was a pleasure discussing with you about this project and having fun at the conferences.

My gratitude goes also to the people who helped me to realise the workshop "Beyond bones": the French Embassy in Italy, Institut Français, the ERC project, the Department of Physics of the University of Trieste, and Collegio Universitario Luciano Fonda. Thanks also to the speakers who made the event a success: Vincent Fernandez, Federico Bernardini, Amélie Beaudet, Enrico Greco and Jeremy Martin. It was a pleasure having you in Trieste.

To Riccardo Mincigrucci: thank you for giving me the opportunity to work on your interesting project, I am looking forward to work with you. Thank you also for waiting for me to finish this thesis.

To my friends, some still in Trieste or in Rome, but most spread throughout Europe and beyond. Even if far apart, I cherish every moment of your company and endless calls.

To Ivan, always by my side. We have been through a lot together, and I am grateful to feel at home with you. With your smile and enthusiasm, you make my life brighter. Finally, to my mum, dad and sister, every day I am far from you is difficult, but it is balanced by the immense support you give me. You are my biggest fans, and I will be forever grateful for all the efforts you made to let me find my way. Thank you for answering all the "lamb" calls and for being such an important part of my life.

BIBLIOGRAPHY

[Nielsen2011] Jens Als-Nielsen and Des McMorrow. *Elements of Modern X-ray Physics*. Hoboken, NJ: John Wiley & Sons, 2011. ISBN: 9780470973950.

[Anschuetz2019] Lukas Anschuetz et al. "Synchrotron radiation imaging revealing the sub-micron structure of the auditory ossicles". In: *Hearing Research* 383 (2019), p. 107806.

[Appel2024] Christian Appel et al. "Fast Small-Angle X-ray Scattering Tensor Tomography: An Outlook into Future Applications in Life Sciences". In: (2024).

[Aronson1999] R. Aronson and N. Corngold. "Photon diffusion coefficient in an absorbing medium". In: *J Opt Soc Am A Opt Image Sci Vis* 16 (1999), pp. 1066–1071.

[Basser1996] P. J. Basser and C. Pierpaoli. "Microstructural and physiological features of tissues elucidated by quantitative-diffusion-tensor MRI". In: *Journal of Magnetic Resonance B* 111 (1996), pp. 209–219.

[Bech2010] M Bech et al. "Quantitative x-ray dark-field computed tomography". In: *Physics in Medicine and Biology* 55.18 (2010), p. 5529.

[Berujon2012] S. Berujon, H. Wang, and K. Sawhney. "X-ray multimodal imaging using a random-phase object". In: *Physical Review A* 86 (2012), p. 063813.

[Berujon2017] Sebastien Berujon and Eric Ziegler. "Near-field speckle-scanning-based x-ray tomography". In: *Phys. Rev. A* 95 (6 2017), p. 063822.

[Boccaccio2012] Antonio Boccaccio et al. "Nanoscale characterization of the biomechanical hardening of bovine zona pellucida". In: *Journal of the Royal Society, Interface / the Royal Society* 9 (2012), pp. 2871–82.

[Born1999] M. Born, E. Wolf, and A.B. Bhatia. *Principles of Optics: Electromagnetic Theory of Propagation, Interference and Diffraction of Light*. Cambridge University Press, 1999. ISBN: 9780521642224.

[Bouvet2012] C Bouvet, S Rivallant, and J.J. Barrau. "Low velocity impact modeling in composite laminates capturing permanent indentation". In: *Composites Science and Technology* 72.16 (2012), pp. 1977–1988.

[Bull2014] D. J. Bull et al. "The influence of toughening-particles in CFRPs on low velocity impact damage resistance performance". In: *Composites Part A: Applied Science and Manufacturing* 58 (2014), pp. 47–55.

[Pipes1982] R. Byron P., R. L. McCullough, and D. G. Taggart. "Behavior of discontinuous fiber composites: Fiber orientation". In: *Polymer Composites* 3 (1982), pp. 34–39.

[Chen2022] Jian Chen, Zhenyang Yu, and Haoran Jin. "Nondestructive testing and evaluation techniques of defects in fiber-reinforced polymer composites: A review". In: *Frontiers in Materials* 9.October (2022), pp. 1–29.

[Dragonfly2022] Canada Comet Technologies Canada Inc. Montreal. *Dragonfly 2022.2 [Computer software]*. Software available at https://www.theobjects.com/dragonfly.

[Cunningham2000] Ian A. Cunningham. *Applied Linear-Systems Theory*. Ed. by Jacob Beutel, Harold L. Kundel, and Richard L. Van Metter. Vol. 1. SPIE Optical Engineering Press, 2000, pp. 79–160. ISBN: 0819436216.

[David2002] C. David et al. "Differential x-ray phase contrast imaging using a shearing interferometer". In: *Applied Physics Letters* 81.17 (2002), pp. 3287–3289.

[DeMarco2023] Fabio De Marco et al. "High-speed processing of X-ray wavefront marking data with the Unified Modulated Pattern Analysis (UMPA) model". In: *Optics Express* 31 (2023), pp. 635–650.

[Dean2017] Christopher Dean. "How the microstructure of dentine can contribute to reconstructing developing dentitions and the lives of hominoids and hominins". In: *Comptes Rendus Palevol* 16.5 (2017), pp. 557–571.

[Deans1983] S. R. Deans. *The Radon transform and some of its applications*. Dover publications Inc., 1983.

[DiTrapani2022] V. Di Trapani, L. Brombal, and F. Brun. "Multi-material spectral photon-counting micro-CT with minimum residual decomposition and self-supervised deep denoising". In: *Opt. Exp.* 30.24 (2022), p. 42995.

[DiTrapani2021] Vittorio Di Trapani and Francesco Brun. "Pre- and post-reconstruction digital image processing solutions for computed tomography with spectral photon counting detectors". In: *NIM(A)* 1010 (2021), p. 165510.

[DiTrapani2024] Vittorio Di Trapani et al. "Speckle-based imaging (SBI) applications with spectral photon counting detectors at the newly established OPTIMATO (OPTimal IMAging and TOmography) laboratory". In: *Journal of Instrumentation (JINST)* 19 (2024), p. C01018.

[Endrizzi2015] M. Endrizzi et al. "Edge-illumination X-ray dark-field imaging for visualising defects in composite structures". In: *Composite Structures* (2015).

[ESRF] ESRF. *Synchrotron sources*. 2020. URL: **https://www.esrf.eu/**.

[Excillum] Excillum. *MetalJet D2+ 70 kV X-ray Source*. 2023. URL: **https://www.excillum.com/products/metaljet/**.

[Felsner2019] Lina Felsner et al. "A 3-D Projection Model for X-ray Dark-field Imaging". In: *Scientific Reports* 9 (2019), p. 9216.

[Fratzl2008] P. Fratzl. *Collagen: Structure and Mechanics, an Introduction*. Springer US, 2008.

[Gao2019] Z. Gao et al. "High-speed tensor tomography: iterative reconstruction tensor tomography (IRTT) algorithm". In: *Acta Crystallographica Section A* 75 (2019), pp. 223–238.

[Garcea2018] S C Garcea, Y Wang, and P J Withers. *X-ray computed tomography of polymer composites*. 2018.

[Gianoncelli2023] Alessandra Gianoncelli et al. "Morphological and Chemical Investigation of Ovarian Structures in a Bovine Model by Contrast-Enhanced X-ray Imaging and Microscopy". In: *International Journal of Molecular Sciences* 24.4 (2023).

[Goodman2005] J.W. Goodman. *Introduction to Fourier Optics*. McGraw-Hill physical and quantum electronics series. W. H. Freeman, 2005. ISBN: 9780974707723.

[Graetz2021] Jonas Graetz. "Simulation study towards quantitative X-ray and neutron tensor tomography regarding the validity of linear approximations of dark-field anisotropy". In: *Scientific Reports* 11 (2021), p. 18477.

[Hamberger1964] C.-A. Hamberger and Jan Wersall. "Vascular Supply of the Tympanic Membrane and the Ossicular Chain". In: *Acta Oto-Laryngologica* 57.sup188 (1964), pp. 308–318.

[Helfen2007] Lukas Helfen et al. "Synchrotron-radiation computed laminography for high-resolution three-dimensional imaging of flat devices". In: *Physica Status Solidi (A) Applications and Materials Science* 204.8 (2007), pp. 2760–2765.

[Hlushchuk2018] Ruslan Hlushchuk et al. "Cutting-edge microangio-CT: New dimensions in vascular imaging and kidney morphometry". In: *American Journal of Physiology - Renal Physiology* 314 (2017), ajprenal.00099.2017.

[Hounsfield1973] G. N. Hounsfield. "Computerized transverse axial scanning (tomography): Part 1. Description of system". In: *British Journal of Radiology* 46.552 (1973), pp. 1016–1022.

[Huang2009] Xiaosong Huang. "Fabrication and properties of carbon fibers". In: *Materials* 2.4 (2009), pp. 2369–2403.

[Jensen2010] Torben H Jensen et al. "Directional x-ray dark-field imaging". In: *Physics in Medicine and Biology* 55 (2010), p. 3317.

[Kagias2016] M. Kagias et al. "2D-Omnidirectional Hard-X-Ray Scattering Sensitivity in a Single Shot". In: *Physical Review Letters* 116 (2016), p. 093902.

[Kagias2019] M. Kagias et al. "Diffractive small angle X-ray scattering imaging for anisotropic structures". In: *Nature Communications* 10 (2019), p. 5130.

[Kagias2021] Matias Kagias et al. "Simultaneous Reciprocal and Real Space X-Ray Imaging of Time-Evolving Systems". In: *Phys. Rev. Appl.* 15 (4 2021), p. 044038.

[Kak1988] A. C. Kak and Malcolm Slaney. *Principles of Computerized Tomographic Imaging*. IEEE Press, 1988.

[Kim2021] J. Kim et al. "Fast acquisition protocol for X-ray scattering tensor tomography". In: *Scientific reports* 11 (2021), p. 23046.

[Kim2022] J. Kim et al. "Tomographic Reconstruction of the Small-Angle X-Ray Scattering Tensor with Filtered Back Projection". In: *Physical Review Applied* 18 (2022), pp. 014043–.

[Kim2020] J. Kim et al. "X-ray scattering tensor tomography with circular gratings". In: *Applied Physics Letters* 116 (2020), p. 134102.

[Kim2022b] Jisoo Kim et al. "Macroscopic mapping of microscale fibers in freeform injection molded fiber-reinforced composites using X-ray scattering tensor tomography". In: *Composites Part B: Engineering* 233 (2022), p. 109634.

[Kormanikova2015] Eva Kormanikova. "Mixed-Mode Delamination Failure Model of Sandwich Plate". In: *Boundary Field Problems and Computer Simulation* 54 (2015), p. 10.

[Lautizi2024b] Ginevra Lautizi et al. *Robust dark-field signal extraction for modulation-based X-ray tensor tomography*. 2024. arXiv: **2411.18482 [physics.app-ph]**.

[Lautizi2024] Ginevra Lautizi et al. "Universal reconstruction method for x-ray scattering tensor tomography based on wavefront modulation". In: *Phys. Rev. Appl.* 22 (2 2024), p. 024031.

[Lemmers2020] Simone A. M. Lemmers et al. "Burned Fleshed or Dry? The Potential of Bioerosion to Determine the Pre-Burning Condition of Human Remains". In: *Journal of Archaeological Method and Theory* 27.4 (2020), pp. 972–991.

[Liebi2015] M. Liebi et al. "Nanostructure surveys of macroscopic specimens by small-angle scattering tensor tomography". In: *Nature* 527 (2015), pp. 349–352.

[Liebi2021] Marianne Liebi et al. "3D nanoscale analysis of bone healing around degrading Mg implants evaluated by X-ray scattering tensor tomography". In: *Acta Biomaterialia* 134 (2021), pp. 804–817.

[Liebi2018] Marianne Liebi et al. "Small-angle X-ray scattering tensor tomography: model of the three-dimensional reciprocal-space map, reconstruction algorithm and angular sampling requirements". In: *Acta Crystallographica Section A* 74 (2018), pp. 12–24.

[Lynch2011] S. K Lynch et al. "Interpretation of dark-field contrast and particle-size selectivity in grating interferometers". In: *Applied Optics* 50 (2011), pp. 4310–4319.

[Magnin2023] Clara Magnin et al. "Dark-field and directional dark-field on low-coherence x ray sources with random mask modulations: validation with SAXS anisotropy measurements". In: *Opt. Lett.* 48.22 (2023), pp. 5839–5842.

[Malecki2014] A. Malecki et al. "X-ray tensor tomography". In: *Europhysics Letters* 105 (2014), p. 38002.

[Meyer2021] Sebastian Meyer et al. "Quantitative analysis of speckle-based X-ray dark-field imaging using numerical wave-optics simulations". In: *Scientific Reports* 11.1 (2021), p. 16113.

[Moffat2010] A. J. Moffat et al. "In situ synchrotron computed laminography of damage in carbon fibre-epoxy [90/0]s laminates". In: *Scripta Materialia* 62.2 (2010), pp. 97–100.

[Mokso2017] R. Mokso et al. "GigaFRoST: The gigabit fast readout system for tomography". In: *Journal of Synchrotron Radiation* 24 (2017), pp. 1250–1259.

[Momose2003] A. Momose et al. "Demonstration of X-Ray Talbot Interferometry". In: *Japanese Journal of Applied Physics* 42 (2003), p. L866.

[Morgan2012] K. S. Morgan, D. M. Paganin, and K. K. W. Siu. "X-ray phase imaging with a paper analyzer". In: *Applied Physics Letters* 100 (2012), p. 124102.

[Muller2018] Mark Müller et al. "Nucleus-specific X-ray stain for 3D virtual histology". In: *Scientific Reports* 8 (2018).

[Munro2019] Peter R. T. Munro. "Rigorous multi-slice wave optical simulation of x-ray propagation in inhomogeneous space". In: *J. Opt. Soc. Am. A* 36.7 (2019), pp. 1197–1208.

[Nanci2017] A. Nanci. *Ten Cate's Oral Histology - E-Book: Ten Cate's Oral Histology - E-Book*. Elsevier Health Sciences, 2017.

[Olivo2021] Alessandro Olivo. "Edge-illumination x-ray phase-contrast imaging". In: *J. Condens. Matter Phys.* 33.36 (2021), p. 363002.

[Ourselin2001] S Ourselin et al. "Reconstructing a 3D structure from serial histological sections". In: *Image and Vision Computing* 19.1 (2001), pp. 25–31.

[Paganin1998] D. Paganin and K. A. Nugent. "Noninterferometric Phase Imaging with Partially Coherent Light". In: *Phys. Rev. Lett.* 80 (12 1998), pp. 2586–2589.

[Paganin2002] D. Paganin et al. "Simultaneous phase and amplitude extraction from a single defocused image of a homogeneous object". In: *Journal of Microscopy* 206.1 (2002), pp. 33–40.

[Paganin2006] David Paganin. *Coherent X-Ray Optics*. Oxford University Press, 2006.

[Paganin2019] David M. Paganin and Kaye S. Morgan. "X-ray Fokker–Planck equation for paraxial imaging". In: *Scientific Reports* 1 (2019), p. 17537.

[Pascolo2018] L. Pascolo et al. "Morphological and chemical information in fresh and vitrified ovarian tissues revealed by X-ray Microscopy and Fluorescence: observational study". In: *Journal of Instrumentation* 13.06 (2018), p. C06003.

[Zaslansky2010] Peter Fratzl Paul Zaslansky Simon Zabler. "3D variations in human crown dentin tubule orientation: A phase-contrast microtomography study". In: *Dental Materials* 26.1 (2010), e1–e10.

[Pavlov2021] Konstantin M. Pavlov et al. "Directional dark-field implicit x-ray speckle tracking using an anisotropic-diffusion Fokker-Planck equation". In: *Physical Review A* 104 (2021), p. 053505.

[Pfeiffer2008] F. Pfeiffer et al. "Hard-X-ray dark-field imaging using a grating interferometer". In: *Nature Materials* 7 (2008), pp. 134–137.

[Pichat2018] Jonas Pichat et al. "A Survey of Methods for 3D Histology Reconstruction". In: *Medical Image Analysis* 46 (2018), pp. 73–105.

[Richardson1996] M. O.W. Richardson and M. J. Wisheart. "Review of low-velocity impact properties of composite materials". In: *Composites Part A: Applied Science and Manufacturing* 27.12 PART A (1996), pp. 1123–1131.

[Rus2020] Janez Rus et al. "Qualitative comparison of non-destructive methods for inspection of carbon fiber-reinforced polymer laminates". In: *Journal of Composite Materials* 54.27 (2020), pp. 4325–4337.

[Samei1998] Ehsan Samei, Michael J. Flynn, and David A. Reimann. "A method for measuring the presampled MTF of digital radiographic systems using an edge test device". In: *Medical Physics* 25.1 (1998), pp. 102–113.

[Schaff2015] F. Schaff et al. "Six-dimensional real and reciprocal space small-angle X-ray scattering tomography". In: *Nature* 527 (2015), p. 353.

[Schmeltz2024] Margaux Schmeltz et al. "The human middle ear in motion: 3D visualization and quantification using dynamic synchrotron-based X-ray imaging". In: *Communications Biology* 7.1 (2024), p. 157.

[Schmeltz2024b] Schmeltz, Margaux et al. "Multiscale 3D organization of human auditory ossicles unveiled by synchrotron small-angle X-ray scattering tensor tomography". In: *BIO Web Conf.* 129 (2024), p. 27003.

[Schoonjans2011] Schoonjans, Tom and Brunetti, Antonio and Golosio, Bruno and del Rio, Manuel Sanchez and Sole, Vicente Armando and Ferrero, Claudio and Vincze, Laszlo. "The xraylib library for X-ray-matter interactions : recent developments". eng. In: *SPECTROCHIMICA ACTA PART B-ATOMIC SPECTROSCOPY* 66.11-12 (2011), 776–784.

[Senck2018] Sascha Senck et al. "Microcrack characterization in loaded CFRP laminates using quantitative two- and three-dimensional X-ray dark-field imaging". In: *Composites Part A: Applied Science and Manufacturing* 115.August (2018), pp. 206–214.

[Sharma2017] Yash Sharma et al. "Design of Acquisition Schemes and Setup Geometry for Anisotropic X-ray Dark-Field Tomography (AXDT)". In: *Scientific Reports* 7 (2017), p. 3195.

[Sharma2016] Yash Sharma et al. "Six dimensional X-ray Tensor Tomography with a compact laboratory setup". In: *Applied Physics Letters* 109 (2016), p. 134102.

[Shi2022] Z. Shi et al. "Fabrication of a fractal pattern device for focus characterizations of X-ray imaging systems by Si deep reactive ion etching and bottom-up Au electroplating". In: *Applied Optics* 61 (2022), pp. 3850–3854.

[Shoukroun2022] D Shoukroun et al. "Edge illumination X-ray phase contrast imaging for impact damage detection in CFRP". In: *Materials Today Communications* 31.February (2022), p. 103279.

[Skjonsfjell2016] Eirik Torbjørn Skjønsfjell et al. "Retrieving the spatially resolved preferred orientation of embedded anisotropic particles by small-angle X-ray scattering tomography". In: *Journal of Applied Crystallography* 49 (2016), pp. 902–908.

[Smith2022] R. Smith et al. "X-ray directional dark-field imaging using Unified Modulated Pattern Analysis". In: *PLOS ONE* 17 (2022), e0273315–.

[Soutis2005] C. Soutis. "Fibre reinforced composites in aircraft construction". In: *Progress in Aerospace Sciences* 41.2 (2005), pp. 143–151.

[Stockhausen2021] Kilian E. Stockhausen et al. "Collagen Fiber Orientation Is Coupled with Specific Nano-Compositional Patterns in Dark and Bright Osteons Modulating Their Biomechanical Properties". In: *ACS Nano* 15.1 (2021), pp. 455–467.

[Strobl2014] M. Strobl. "General solution for quantitative dark-field contrast imaging with grating interferometers". In: *Scientific Reports* 4 (2014), p. 7243.

[Teague1983] Michael Reed Teague. "Deterministic phase retrieval: a Green's function solution". In: *J. Opt. Soc. Am.* 73.11 (1983), pp. 1434–1441.

[Vogel2015] J. Vogel et al. "Constrained X-ray tensor tomography reconstruction". In: *Opticts Express* 23 (2015), pp. 15134–15151.

[Wang2015] Hongchang Wang, Yogesh Kashyap, and Kawal Sawhney. "Hard-X-Ray Directional Dark-Field Imaging Using the Speckle Scanning Technique". In: *Physical Review Letters* 114 (2015), p. 103901.

[Wang2016] Hongchang Wang, Yogesh Kashyap, and Kawal Sawhney. "Quantitative X-ray dark-field and phase tomography using single directional speckle scanning technique". In: *Applied Physics Letters* 108.12 (2016), p. 124102.

[Wang2021] Hongchang Wang and Kawal Sawhney. "Hard X-ray omnidirectional differential phase and dark-field imaging". In: *Proceedings of the National Academy of Sciences* 118.9 (2021), e2022319118.

[Wang2009] Zhen-Tian Wang et al. "Quantitative grating-based x-ray dark-field computed tomography". In: *Applied Physics Letters* 95.9 (2009), p. 094105.

[Weitkamp2005] Timm Weitkamp et al. "X-ray phase imaging with a grating interferometer". In: *Optics Express* 13 (2005), pp. 6296–6304.

[Wronkowicz2018] Angelika Wronkowicz, Krzysztof Dragan, and Krzysztof Lis. "Assessment of uncertainty in damage evaluation by ultrasonic testing of composite structures". In: *Composite Structures* 203.June (2018), pp. 71–84.

[Yashiro2010] W. Yashiro et al. "On the origin of visibility contrast in x-ray Talbot interferometry". In: *Optics Express* 18 (2010), pp. 16890–16901.

[Yu2016] B. Yu et al. "A comparison of different approaches for imaging cracks in composites by X-ray microtomography". In: *Philosophical Transactions of the Royal Society A: Mathematical, Physical and Engineering Sciences* 374.2071 (2016).

[Zanette2014] I. Zanette et al. "Speckle-Based X-Ray Phase-Contrast and Dark-Field Imaging with a Laboratory Source". In: *Phys. Rev. Lett.* 112 (25 2014), p. 253903.

[Zanette2015] I. Zanette et al. "X-ray microtomography using correlation of near-field speckles for material characterization". In: *Proceedings of the National Academy of Sciences of the United States of America* 112 (2015), pp. 12569–12573.

[Zdora2021] M. -C. Zdora. *X-ray phase-contrast imaging using near-field speckles*. Springer Cham, 2021.

[Zdora2018] M.-C. Zdora. "State of the Art of X-ray Speckle-Based Phase-Contrast and Dark-Field Imaging". In: *Journal of Imaging* 4 (2018), p. 60.

[Zdora2015] Marie-Christine Zdora et al. "Simulations of x-ray speckle-based dark-field and phase-contrast imaging with a polychromatic beam". In: *Journal of Applied Physics* 118.11 (2015), p. 113105.

[Zdora2017] Marie-Christine Zdora et al. "X-ray Phase-Contrast Imaging and Metrology through Unified Modulated Pattern Analysis". In: *Physical Review Letter* 118 (2017), p. 203903.

[Zhou2018] T. Zhou, H. Wang, and K. Sawhney. "Single-shot X-ray dark-field imaging with omnidirectional sensitivity using random-pattern wavefront modulator". In: *Applied Physics Letters* 113 (2018), p. 091102.

[Zhou2015] Tunhe Zhou et al. "Speckle-based x-ray phase-contrast imaging with a laboratory source and the scanning technique". In: *Optics Letters* 40.12 (2015), pp. 2822–2825.